Advances in Printing and Media Technology

Vol. XLVII(VII)

Edited by Cathy Ridgway

Darmstadt
MMXXI

Advances in Printing and Media Technology

Proceedings of the 47th International Research Conference of iarigai
Athens, Greece, 19–23 September 2021

Edited by Cathy Ridgway, Oftringen, Switzerland

Scientific Committee

Ian Baitz (Toronto, Canada)
Irena Bates (Zagreb, Croatia)
Fritz Bircher (Fribourg, Switzerland)
Anne Blayo (Grenoble, France)
Roger Bollström (Oftringen, Switzerland)
Tomislav Cigula (Zagreb, Croatia)
Tim Claypole (Swansea, Wales)
Edgar Dörsam (Darmstadt, Germany)
Nils Enlund (Helsinki, Finland)
Patrick Gane (Helsinki, Finland)
Gorazd Golob (Ljubljana, Slovenia)
Martin Habekost (Toronto, Canada)
Gunter Hübner (Stuttgart, Germany)
Fabio Ippolito (Oftringen, Switzerland)
Yuri Kuznetsov (St Petersburg, Russia)
Magnus Lestelius (Karlstad, Sweden)
Mladen Lovreček (Zagreb, Croatia)
Branka Lozo (Zagreb, Croatia)
Natalia Lumby (Toronto, Canada)
Lidija Mandić (Zagreb, Croatia)
Thomas Mejtoft (Umeå, Sweden)
Erzsébet Novotny (Budapest, Hungary)
Anastasios Politis (Athens, Greece)
Janet Preston (St Austell, England)
Fons Put (Turnhout, Belgium)
Anayath Rajendrakumar (Chennai, India)
Tomáš Syrový (Pardubice, Czech Republic)
Martti Toivakka (Abo/Turku, Finland)
Li Yang (Stockholm, Sweden)

Contents

Preface

Dear participants of the 47th iarigai conference

Dear colleagues and friends of the Graphic Communication, Print, Media and Packaging fields,

Some two years ago, we have undertaken the responsibility for the joint organization of iarigai and IC conferences in Athens, Greece. Meanwhile, COVID-19 appeared, changing and challenging our lives with unprecedented situations. We have accepted the challenge and we have undertaken the high risk to organize the conferences, despite the lockdowns and restrictions in personal contacts and travel.

With vaccination progressing, but still challenged by COVID-19, we finally managed to organize the conferences in a hybrid form. The most positive message is that, we were able to meet in person and at physical space and interact with our colleagues from around the world of print media science, research and technology.

Therefore, we at HELGRAMED, The Hellenic Union of Print Media Engineers, in cooperation with GRAPHMED-LAB, the Hellenic Graphic-Media Research Lab, University of West Attica, are proud that we could be able to organize the conferences, despite the negative impact of the pandemic.

In the conference proceedings of the 47th annual conference of iarigai with the title "Printing in the Digital Era", you will find the high quality extended abstracts from our colleagues that participated in person or from distance and presented their scientific work at the conference.

On behalf of the entire organizational team and the colleagues from iarigai board, we do hope to meet again in person at the next iarigai conference in 2022!

Prof. Dr. Anastasios E. Politis
Director of the iarigai and IC conferences

September 2021, Athens Greece

Links:
HELGRAMED: <http://www.helgramed.gr/>
University of West Attica: <https://www.uniwa.gr/en/>
iarigai: <https://iarigai.com>

A deep learning approach for the classification task of gravure printed patterns

Pauline Brumm[1,2], Nils Lindner[1], Tim Eike Weber[1], Hans Martin Sauer[1,2] and Edgar Dörsam[1,2]

[1] Technical University of Darmstadt, Department of Mechanical Engineering, Institute of Printing Science and Technology,
   Magdalenenstr. 2, 64289 Darmstadt, Germany

[2] Collaborative Research Center (CRC) 1194 – Interaction between Transport and Wetting Processes, Project C01, Germany

E-mails: brumm@idd.tu-darmstadt.de; lindner@idd.tu-darmstadt.de; timweber@idd.tu-darmstadt.de;
         sauer@idd.tu-darmstadt.de; doersam@idd.tu-darmstadt.de

Short abstract

Manual classification of gravure printed patterns is time-consuming and biased by the human observer. The suitability of supervised deep learning approaches for automatic classification of printed patterns into three classes of ink splitting, namely lamella splitting, point splitting and transition regime, is studied. We conduct gravure printing experiments in a wide parameter range. The digitized printing results are labeled by a human observer according to a given classification scheme and, after pre-processing, serve as a large dataset for training of several convolutional neural networks (CNNs) based on well-known architectures. Non-optimized CNN models achieve validation accuracies > 89.3 %, optimized CNN models > 91.9 %, up to 95.2 % for the best model based on DenseNet-161. We find that the transition regime is most likely to be misclassified. In conclusion, deep learning is evaluated as a suitable method for automatic gravure pattern classification of large amounts of samples due to the high validation accuracies. For future studies, unsupervised machine learning approaches are proposed since the greatest limitation of the developed deep learning approach is the need for labeled data.

Keywords: gravure printing, machine learning, hydrodynamic pattern formation, ink splitting, convolutional neural networks

1. Introduction and background

Hydrodynamic pattern formation phenomena in the gravure printing nip during ink splitting have not been fully understood yet. According to Hübner (1991), two classes of ink splitting can be distinguished on the phenomenological level: lamella splitting and point splitting. Lamella splitting often comes along with viscous fingering phenomena which in general show themselves as stripes or finger-like, dendritic structures on the printed product, spoiling the homogeneity of printed ultra-thin layers as required for functional printing, e.g. printed electronics. Point splitting results in dot patterns as known from halftones in graphical printing. Brumm, et al. (2021a) recently have shown the existence of an intermediate regime between point and lamella splitting, which they call transition regime. To prove the existence of the transition regime, they developed a classification scheme so that they were then able to manually classify a large number of printed samples into the three classes: lamella splitting, point splitting and transition regime (see Figure 1). Thus, they located the transition regime in the analyzed printing parameter range by manual classification.

Manual classification, or more general 'manual assessment' of printed samples, is very time-consuming and also inherits a subjective bias which is caused by the human observer. In this research, a highly automated, supervised deep learning approach shall be developed which, after successful training of the deep learning models, replaces the time-consuming manual classification of gravure printed patterns. The classification results shall be used to understand the complex wetting processes and the hydrodynamic pattern formation in gravure printing by identifying cause-effect correlations between the printing parameters and the

resulting pattern formation. An automatic classification approach enables the classification of an arbitrarily large number of samples in the future. Thus, fundamental empiric knowledge about the relationship between printed pattern and utilized printing parameters (raster width, tonal value, printing velocity, ink viscosity etc.) can be created. This knowledge helps to develop a guide for gravure printing users and researchers who want to understand in which printing parameter space which type of pattern formation appears so that they can choose the most suitable set of printing parameters for the intended application.
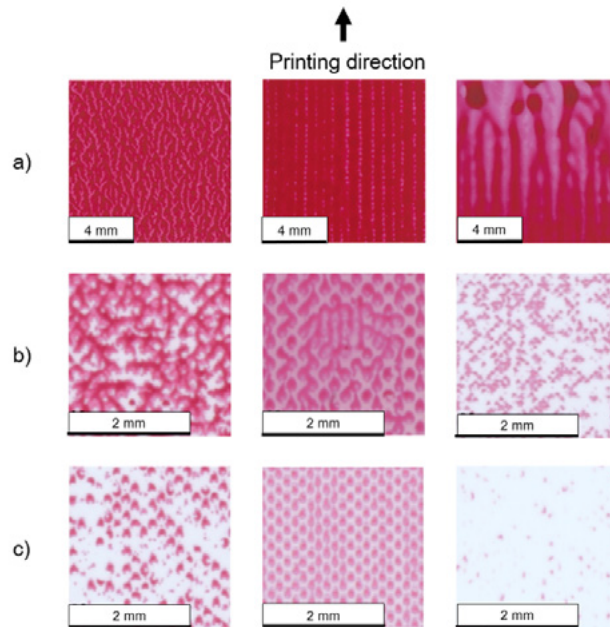
Figure 1: Pattern formation phenomena in gravure printing;
examples for: lamella splitting (a), transition regime (b) and point splitting (c)

We assume that the transition regime inherits great potential for functional printing applications such as printed electronics or security feature printing. For example, we state that the knowledge of the transition regime's location in printing parameter space helps printing closed homogeneous surfaces with smallest quantity of printing ink. This is because the transition regime marks the parameter range where adjacent printed raster dots are at the onset of mutual coalescence and are ready to form a closed thin layer of ink on the substrate. In addition, the transition regime is of special interest since it shows complex types of pattern formation which are not fully understood yet.

In the printing industry, the use of artificial intelligence is a topic of recent research. For example, Villalba-Diez, et al. (2019) recently have looked at deep learning for quality control of gravure cylinder production and Zhang, et al. (2019) have developed a deep learning method for the classification of printing defects. In other fields like medicine (e.g. medical imaging), engineering (e.g. autonomous driving, face recognition) or biology (e.g. classification of plants), artificial intelligence is already more widely spread.

For the analysis of pattern formation phenomena in printing, deterministic image processing algorithms have mostly been used up to now, for example, Fast Fourier Transform or template filtering for finger pattern analysis (Bornemann, 2014; Brumm, Sauer and Dörsam, 2019; Schäfer, 2020) or determining pattern uniformity via the mean grayscale level and its deviation (Hamblyn, 2015). For dot patterns, algorithms for finding missing dots have been developed (Heeschen and Smith, 2000; Eerola, et al., 2007; Vartiainen, et al., 2008). Deterministic image processing algorithms have the advantage that they are 'white boxes' whereas deep learning methods are 'black boxes'. However, it is very difficult to develop rule-based deterministic algorithms which classify printed patterns into lamella splitting, point splitting and transition regime according to characteristic features extracted through image processing like number of areas in the image,

grey level distribution etc. This is why we choose an intelligent deep learning approach for this paper and we pose the following research question: Is deep learning a suitable approach for the classification of gravure printed patterns?

2. Materials and methods

2.1 Printing experiments

2.1.1 Printing setup
Printing experiments were carried out using a lab-scale sheet fed gravure printer (Superproofer 220, GT+W, Rödermark, Germany) short 'Superproofer' as well as the gravure unit of an industrial-scale web-fed label printing press (Gallus RCS 330, Gallus Ferd. Rüesch AG, St. Gallen, Switzerland) short 'Gallus'. As printing forms, electromechanically engraved, chrome-plated copper printing cylinders with 45° raster angle and mostly 120° stylus angle were used (other stylus angles were 130° and 140°), obtaining a broad range of raster frequencies (40, 48, 54, 60, 70, 80, 90, 100, 120, 140 lines per cm) and tonal values (5, 10, 20, 30, 40, 50, 60, 70, 80, 90, 95, 100 %). The printing form layout mainly consists of 120 squares of size 13 mm × 13 mm for the Superproofer and 108 squares for the Gallus. Printing speeds were varied in a large range (20, 30, 45, 60, 75, 90, 160 m/min).

As substrates, we used paper (UPM Finesse matte-coated H) with a weight of 100 g/cm^2, coated transparent foil (Hostaphan® GN 4660A) and white foil (Melinex® 339). As printing fluids, water-based gravure inks in a red (Sun Chemical R0001235761) and a blue (Sun Chemical B0001117761) version were used as well as a diluted version of the red water-based ink (about 1:1 printing ink and distilled water).

2.1.2 Sample digitization
The printed samples were digitized using a flatbed scanner (EPSON Perfection V800 Photo) with the software SilverFast Ai Studio 8 at a nominal resolution of 2400 dots per inch. Color calibration was performed with a Kodak IT8 calibration target. The digitized samples were saved in a lossless TIFF format, with 16-bit lightness values per RGB color channel. All samples can be downloaded from <https://doi.org/10.48328/tudatalib-528.2>, as provided by Brumm, et al. (2021b).

2.2 Manual pattern classification

Manual pattern classification ('labeling') into the three classes lamella splitting, point splitting and transition regime was performed by a human observer according to a classification scheme as developed by Brumm, et al. (2021a). The results for manual pattern classification of selected Superproofer samples are already presented in their work. Here, we only briefly present the classification scheme underlying the manual pattern classification.
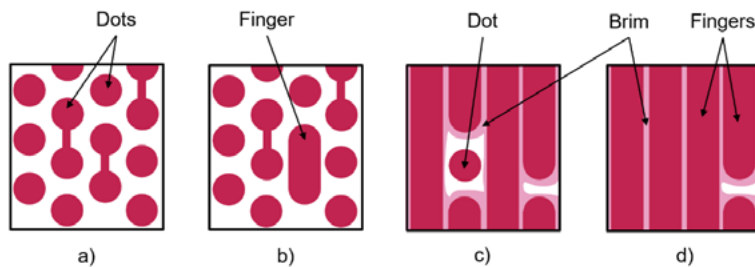
Figure 2: Classification scheme for: point splitting (a), transition regime (b, c) and lamella splitting (d), as described in Brumm, et al. (2021a)

If a printed field constantly shows gravure-raster-related patterns ('dots') (Figure 2a), it is classified as *point splitting*, and if it shows lamella-type patterns ('fingers') (Figure 2d), it is classified as *lamella splitting*. A field is classified as *transition regime*, if it shows dots as well as fingers. Only one finger amongst many dots (Figure 2b) or one dot amongst many fingers (Figure 2c) make a field be classified as transition regime. Fields with numerous coexisting dots and fingers are also classified as transition regime. The definition of the terms dots, fingers and brim is explained in detail in (Brumm, et al., 2021a).

2.3 Automatic pattern classification using deep learning

2.3.1 Development of an approach for automatic pattern classification

The deep learning approach was developed in the programming language Python, using PyTorch as a deep learning framework as well as other program libraries like OpenCV or Numpy for other tasks e.g. pre-processing of the digitized printed samples. A supervised learning approach using convolutional neural networks (CNNs) was chosen. Supervised learning means that labeled images are needed as a dataset for training, validation and testing of the CNNs. In contrast, unsupervised learning works with unlabeled images.

2.3.2 Pre-processing of the printed samples

A fully-automated pre-processing of the digitized printed samples was implemented in order to obtain a suitable dataset for the deep learning approach developed in this paper. The fields on the samples were identified using edge detection, binarization and dilation and erosion operations, and they were sorted according to their printing parameters. 8 031 of total 8 172 fields were detected via the implemented pre-processing algorithm, 4 139 fields from the industrial-scale Gallus and 3 892 fields from the lab-scale Superproofer. Detection sometimes failed due to very low tonal values or smeared ink. Only a cutout (11 mm × 11 mm, 1 040 px × 1 040 px) from the center of each field (13 mm × 13 mm) was used, since the edges showed different pattern formation phenomena than the center of the fields.

2.3.3 Implementation and optimization of CNNs

For the implementation of ten different CNN models for the classification of gravure printed patterns, four well-known pre-trained CNNs were chosen as basic architectures:

- DenseNet-161
- MobileNetV2
- VGG-19
- ResNet-50

Additionally, optimization of all architectures was performed. Data augmentation was added for some models, meaning that the input images during data loading were randomly rotated or mirrored to increase data diversity to prevent overfitting of the model, see Figure 3. The probability for each transformation was 50 %. Overfitting means that the model rather learns by heart than to generalize the problem.
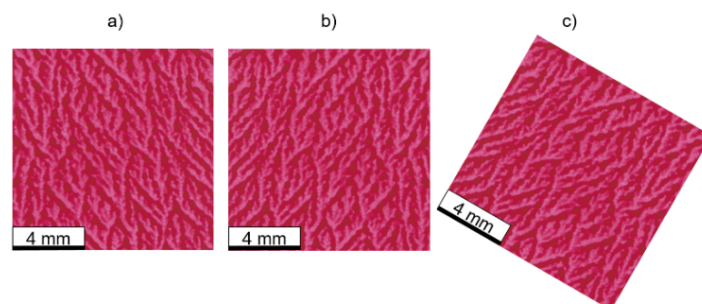
Figure 3: Data augmentation: original image (a), example for weak (b), and strong data augmentation (c)

2.3.4 Training, validation and testing

From the 8 031 pre-processed fields, those fields showing obvious defects such as a wrong cutout position or missing label were sorted out. All fields printed in blue color (379) were also sorted out and not used for training and validation to prevent the model from having a bias due to different color representations. They were reserved as test data for a future trial concerning the influence of color. The remaining fields comprised all three classes of point splitting, lamella splitting and transition regime, however, at distinct fractions. Unbalanced datasets lead to biased classification results (Buda, Maki and Mazurowski, 2018). Thus, dataset balancing was performed before training the CNNs, taking the most underrepresented class, the point splitting class, as reference. Finally, 5 400 fields with balanced distribution over the three classes (1 800 samples per class) were chosen randomly from all fields, from which 80 % were randomly assigned as training data, 10 % as validation data and 10 % as test data. Training data were used for training of the CNNs, validation data for optimization and test data to determine the final accuracy of a model on unseen data.

The chosen pre-trained CNNs expect RGB input images of size 224 px × 224 px, meaning that the 1 040 px × 1 040 px fields were downscaled so that spatial resolution was decreased by 78 %. Training was performed using CUDA (compute unified device architecture) on a graphics processing unit (GPU) NVIDIA Tesla T4, which was accessed via Google Cloud Platform Compute Engine, a commercial cloud computing service.

3. Results and discussion

3.1 Performance metrics of the deep learning models

Manual classification served as a basis for the development of a supervised deep learning approach. Table 1 lists properties as well as performance metrics of all ten developed CNN models with a training duration of 25 epochs. It turns out that even the non-optimized models achieved accuracies over 89.3 %. Weak data augmentation (horizontal flip) led to better results for some models, but strong data augmentation (horizontal and vertical flip and rotation by 30° clockwise and counter-clockwise) resulted in decreased accuracy. Probably, the high diversity of input data prevented generalization of the model. The model with the highest accuracy is #3, which achieved an accuracy of 95.2 % on the validation dataset and needed 57 minutes for training. The accuracy on the test dataset was determined as 93.5 % (not in Table 1), which confirms the good performance of the model.

Table 1: Properties and performance metrics of all developed models

Model	Underlying basic architecture	Optimized architecture	Maximum accuracy on validation dataset in %	Data augmentation	Duration of training in minutes
#1	DenseNet-161	No	93.5	No	52
#2	DenseNet-161	Yes	94.3	No	53
#3	DenseNet-161	Yes	95.2	Yes, weak	57
#4	DenseNet-161	Yes	91.3	Yes, strong	61
#5	MobileNetV2	No	92.2	No	15
#6	MobileNetV2	Yes	93.7	No	16
#7	ResNet-50	No	92.6	No	42
#8	ResNet-50	Yes	93.0	No	44
#9	VGG-19	No	89.3	No	59
#10	VGG-19	Yes	91.9	Yes, weak	62

The accuracy and loss curves for the training and validation dataset of model #3 over all 25 epochs are presented in Figure 4. The curves imply that a larger amount of training epochs could increase the accuracy even more, since the curves show no sign of overfitting so far. For example, a possible sign of overfitting would be a clear saturation of the validation accuracy curve with a turning point that is followed by decreasing accuracy.
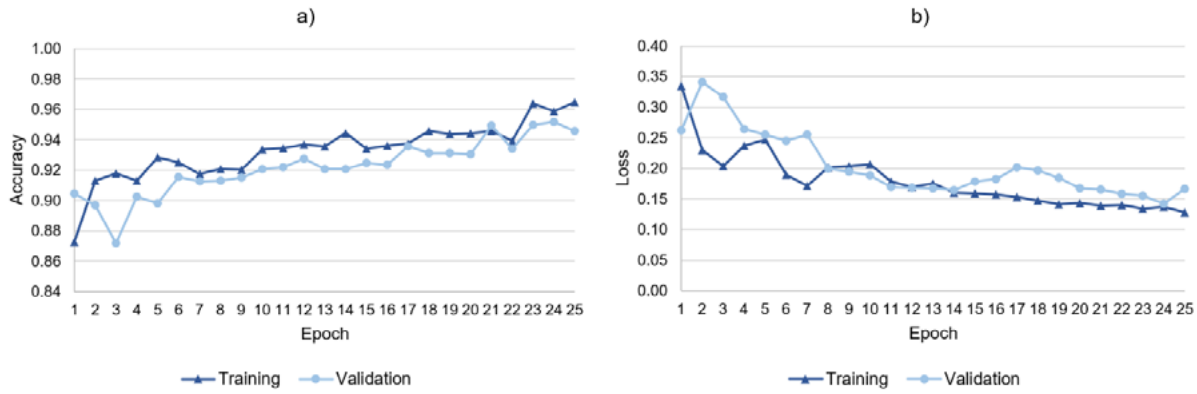
Figure 4: Accuracy (a) and loss curves (b) for model #3 for training and validation data; the lines between the data points serve only as a guide for the eye

Another metric for the performance of a CNN is a confusion matrix, as given in Figure 5 for model #3. It shows the correct class ('labels') in the rows and the predicted class ('predictions') in the columns of the matrix. The number of correctly classified fields can be found on the main diagonal. The other elements of the matrix show how many fields were misclassified and what type of misclassification it was. Figure 5 shows that lamella splitting fields were never classified as point spitting fields and vice versa. This indicates that the model can very well distinguish point and lamella splitting. In contrast, transition regime fields were nine times classified as lamella splitting and eight times as point splitting leading to the conclusion that the model has most difficulties in correctly classifying transition regime fields. Besides, the model misclassified lamella splitting fields seven times and point splitting fields twice as transition regime. Thus, the differentiation between point splitting and transition regime and lamella splitting and transition regime is not as clear as the differentiation between point and lamella splitting.
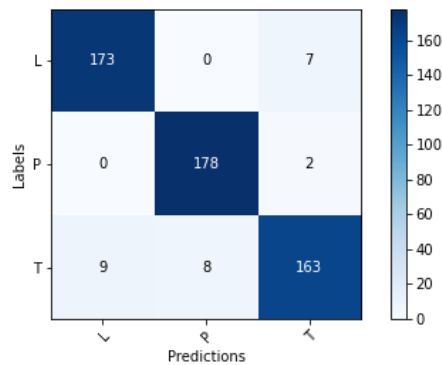
Figure 5: Confusion matrix for model #3 for validation data:
L = Lamella splitting, P = Point splitting, T = Transition regime

3.2 Limitations of the approach

The greatest limitation of the developed supervised deep learning approach is the fact that manually labeled images are required for training of the CNN models. However, once trained, a CNN is able to classify an arbitrarily large amount of data. Although the accuracy of the best model (#3) is very high, it is clearly

below 100 %, and erroneous assignments, distinct from the human observer during manual labeling, will occur. This makes the developed approach only suitable if those misclassifications are tolerated within the intended application e.g. research or commercial use with zero defects strategy. This has to be clarified before using such a deep learning approach. Certainly, the computing time and power for training is also a limiting factor when no GPU is available and when samples with higher resolution shall be trained.

3.3 Main findings

The main findings from this research are:

- Validation accuracies of non-optimized, pre-trained, well-known CNNs 'off the shelf' are very good already (> 89.3 %). Optimization leads to increased validation accuracies (> 91.9 %, up to 95.2 % for the best model based on DenseNet-161), but it has to be emphasized that optimization is a challenging, iterative task.
- Training of the CNNs on a commercial cloud computing platform takes a reasonable amount of time (about one hour for the best model) for the intended research application of correlating printing parameters to pattern formation phenomena.
- The transition regime is most likely to be misclassified.
- The main limitation of the deep learning approach is the need for labeled data.

4. Conclusions and outlook

In conclusion, we answer our research question with: Yes, deep learning is a suitable approach for the classification of gravure printed patterns, since it enables the automatic classification of a large amount of samples with very good accuracies.

Most misclassifications happen regarding the transition regime class. To avoid these misclassifications, several approaches are imaginable in future research: First, the classification scheme for manual classification could be updated to make the differentiation between the three classes more distinct and thus more learnable for the CNN models. Second, the number of epochs could be increased and it could be analyzed if this leads to higher accuracies without overfitting of the model. Third, the CNNs' could be altered and retrained so that 1 024 px × 1 024 px input images are possible. At the moment, the CNNs use input images with 78 % less spatial resolution than the images that the human observer uses for manual classification.

In future research, unsupervised learning methods should also be examined e.g. clustering or unsupervised CNNs, in order to get rid of the need for manually labeled data which is a main limitation of the supervised deep learning approach. The influence of printing ink color on the deep learning process is also a topic of further investigation.

References

Bornemann, N., 2014. *Characterization and Investigation of Large-Area, Ultra-Thin Gravure Printed Layers*. Dissertation. Darmstadt, Technische Universität Darmstadt. Available at <https://tuprints.ulb.tu-darmstadt.de/3847> [Accessed 19.07.2021].

Brumm, P., Sauer, H. M. and Dörsam, E., 2019. Scaling behavior of pattern formation in the flexographic ink splitting process. *Colloids and Interfaces*, 3(1): 37. https://doi.org/10.3390/colloids3010037.

Brumm, P., Weber, T. E., Sauer, H. M. and Dörsam, E., 2021a. Ink splitting in gravure printing: localization of the transition from dots to fingers. *Journal of Print and Media Technology Research,* 10(2), pp. 81–93. https://doi.org/10.14622/JPMTR-2016.

Brumm, P., Weber, T. E., Lindner, N., Sauer, H. M. and Dörsam, E., 2021b. *Collection of digitized gravure printed samples for the analysis of hydrodynamic pattern formation*. TUdatalib. https://doi.org/10.48328/tudatalib-528.2.

Buda, M., Maki, A. and Mazurowski. M.A., 2018. A systematic study of the class imbalance problem in convolutional neural networks. *Neural Networks*, 106, pp. 249–259. https://doi.org/10.1016/j.neunet.2018.07.011.

Eerola, T., Kamarainen, J.-K., Lensu, L. and Kälviäinen, H., 2007. Visual print quality evaluation using computational features. In: G. Bebis, R. Boyle, B. Parvin, D. Koracin, N. Paragios, S.-M Tanveer, T. Ju, Z. Liu, S.Coquillart, C. Cruz-Neira, T. Müller and T Malzbender, eds. *Advances in Visual Computing. ISVC 2007: Lecture Notes in Computer Science, vol 4841*. Lake Tahoe, NV, USA, 26-28 November 2007. Berlin, Heidelberg, Germany: Springer, pp. 403–413. https://doi.org/10.1007/978-3-540-76858-6_40.

Hamblyn, A., 2015. *Effect of plate characteristics on ink transfer in flexographic printing*. Ph.D. thesis. Swansea University.

Heeschen, W.A. and Smith, D.A., 2000. Robust digital image analysis method for counting missing dots in gravure printing. In: *2000 International Printing & Graphic Arts Conference*. Savannah, GA, USA, 1–4 October 2000. TAPPI, pp. 29–35.

Hübner, G., 1991. *Ein Beitrag zum Problem der Flüssigkeitsspaltung in der Drucktechnik*. Dissertation. Technische Hochschule Darmstadt. https://doi.org/10.25534/tuprints-00013550.

Schäfer, J.K., 2020. *In situ Untersuchung der hochdynamischen Grenzflächeninstabilität im Zylinderspalt*. Dissertation. Technische Universität Darmstadt. https://doi.org/10.25534/TUPRINTS-00014204.

Vartiainen, J., Sadovnikov, A., Kamarainen, J.-K., Lensu, L. and Kälviäinen, H., 2008. Detection of irregularities in regular patterns. *Machine Vision and Applications*, 19(4), pp. 249–259. https://doi.org/10.1007/s00138-007-0096-9.

Villalba-Diez, J., Schmidt, D., Gevers, R., Ordieres-Meré, J., Buchwitz, M. and Wellbrock, W., 2019. Deep learning for industrial computer vision quality control in the printing industry 4.0. *Sensors*, 19(18): 3987. https://doi.org/10.3390/s19183987.

Zhang, E., Li, B., Li, P. and Chen, Y., 2019. A deep learning based printing defect classification method with imbalanced samples. *Symmetry*, 11(12): 1440. https://doi.org/10.3390/sym11121440.

Challenges for the printing industry in the modern digital and meta-pandemic era

Georgios Gamprellis[1,3,4,6], *Anastasios E. Politis*[1,2,3,5], *Yannis Sofias*[1,7], *Antonios Tsigonias*[1,3,6], *Gerasimos Vonitsanos*[5], *Marios Tsigonias*[1,3,4,5,6] *and Kenneth L. Macro*[2]

[1] University of West Attica (UNIWA), Athens, Greece

[2] California Polytechnic State University, San Luis Obispo, USA

[3] HELGRAMED - Hellenic Union of Graphic Arts and Media Technology Engineers, Greece

[4] National Printing Office, Athens, Greece

[5] Hellenic Open University (EAP), Patra, Greece

[6] GARDEN – Graphic Arts Research, Development and Engineering Institute, Athens, Greece

[7] Heidelberg Hellas, Athens Greece

E-mails: gampgeo@gmail.com; politismedia@gmail.com; yannis.sofias@heidelberg.com; antonio_tsigonias@yahoo.gr;
        mvonitsanos@eap.gr; tsigonias@yanoo.gr; kmacro@calpoly.edu

Short abstract

The ever-changing global economic conditions (global financial crisis, pandemic COVID-19, etc.) combined with the rapid increase in internet use and social media are urgently raising the question: "Is printing *decreasing*?" It is very easy for someone to make the mistake of answering in the affirmative immediately. The Printing Industry, comprised of vast network of sectors, is exhibiting a trend of stabilization and in some sectors an upward trend. Even sectors that would be expected to decline, such as newspaper printing or book publishing, show either a much lower-than-expected downward trend or a stabilization trend. In other areas such as the packaging printing or the labels printing the trend is clearly increasing and even with very high growth rates. The financial crisis of the early 2010s and the crisis caused by the COVID-19 pandemic have certainly dealt a blow to the Printing Industry, but not so severe as to lead to death. Instead, the Printing Industry must change and "exploit" the trend for digitization and automation that characterizes our time to their advantage. The data show that both print media and digital media will continue to coexist.

Keywords: printing industry, print media, digital media, digitalization, Industry 4.0, printing industry growth

1. Introduction

In recent years, ever-changing global conditions and the increasing use of digital media have had a tremendous impact on the Printing Industry sector, leading to an almost complete change in the field. In recent years, in addition to new technologies that promote the automation of the production of Printing Industry and new concepts and philosophies related to the management, organization and administration that were entered to the field of Printing Industry, the most important role is played by information and its management.

In this ever-evolving environment, the crucial question that arises but seeks an immediate answer is whether the Printing Industry, as we know it today, will continue to exist or whether *is Print decreasing?* And if the answer to this question is "no, Print is not decreasing", then will it exist in its traditional form, or will it have to change and adapt to the new conditions? This research will attempt to answer this crucial question.

2. General trends challenging human behavior

2.1 The Internet use

In 2016, three-quarters (76 %) of people in the US were online and during these years countries from many parts of the world caught up: in Malaysia 79 % used the internet; in Spain and Singapore 81 %; in France 86 %; in South Korea and Japan 93 %; in Denmark and Norway 97 %; and Iceland tops the ranking with 98 % of the population online. At a population of 334 252 this means that only 5 883 Icelanders were not online (Roser, Ritchie and Ortiz-Ospina, 2017). The speed with which the world is changing is incredibly fast. On any day in the last 5 years there were on average 640 000 people globally online for the first time. This was 27 000 every hour.

2.2 The social media use

The increase in the use of internet by the global population, as expected, brought a huge increase in the number of social media users (Facebook, Twitter, Instagram, etc.). In June 2016, there were an estimated 1.55 billion active users on the most popular social media platform, Facebook. As of April 26th, 2017 there were an estimated 700 million active users on Instagram (Zhan, et al., 2018) and at the first quarter of 2019, Twitter averaged 330 million monthly active users, a decline from its all-time high of 336 millions in the first quarter of 2018 (Statista, 2021a).

2.3 Reliability

It would be expected the huge increase in the use of the internet and social media by millions of people on a daily basis to make these media reliable in transmitting information. The average value of interpersonal trust for internet people was estimated at just 1.89 (on a 1 to 10 scale) with only 7.3 % of the sample giving values above 5. Particularly 44.16 % chose the value 0 and 48.6 % of the sample chose values from 1 to 5 (Tsekeris, et al., 2020). These figures show that people do not trust internet. According to Sirimanne cited in UNCTAD (2019), a staggering 75 % of those surveyed who distrust the internet cited Facebook, Twitter and other social media platforms as contributing to their lack of trust. While cyber criminals, cited by 81 % of those who distrust the internet, remained the leading source of distrust, a majority in all regions (62 % globally) indicated that a lack of internet security was also a critical factor (UNCTAD, 2019)

2.4 International economic conditions & the COVID-19 pandemic influence

Global foreign direct investment (FDI) collapsed in 2020, falling 42 % from USD 1.5 trillion in 2019 to an estimated USD 859 billion, according to UNCTAD. Such a low level was last seen in the 1990s and is more than 30 % below the investment trough that followed the 2008–2009 global financial crisis (UNCTAD, 2021).

European Commission's survey (Figure 1) about the High Growth Enterprises (HGE) showed that 21 % of HGEs are in the wholesale and retail trade sector, 20 % in manufacturing, 11 % in construction, and 10 % each in the administrative and support services; professional, scientific and technical activities; and accommodation and food services industries. (Flachenecker, et al., 2020)
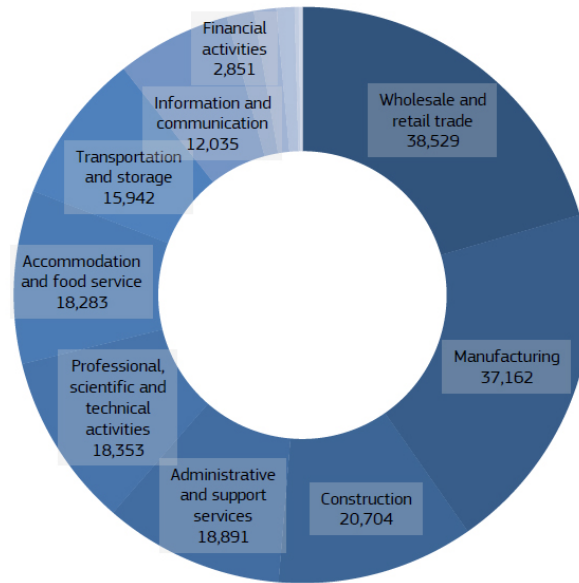
Figure 1: Number of HGEs across industries in the EU28 in 2017,
source: European Commission - JRC elaboration based on Eurostat (2020)

Due to COVID-19 pandemic, the World Trade Organisation (WTO) projects global merchandise trade (Figure 2) could decline by 13–32 % in 2020 (Azevêdo, 2020). According to the World Tourism Organisation, international tourist arrivals could fall by 60–80 % in 2020 compared to 2019 (UNWTO, 2020). Shifting consumption during recessions towards goods that are often subject to reduced rates or exemptions could further decrease consumption tax revenue (Simon and Harding, 2020).
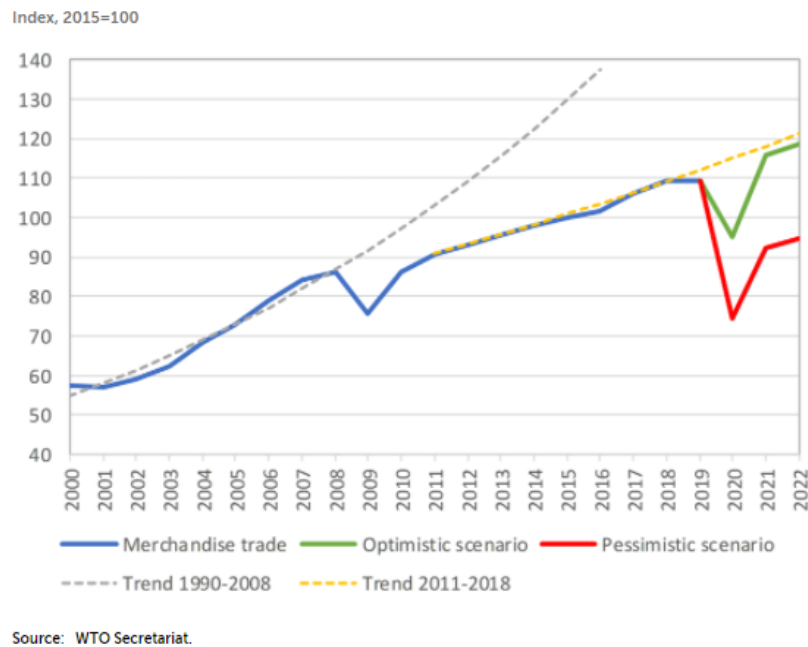
Figure 2: World merchandise trade volume, 2000-2022, source: Azevêdo (2020)

3. The print vs. digital media debate

As can be understood from the data presented in the previous section, the modern environment of human activity is characterized by the tendency of more and more activities to be digitized and carried out using digital media.

Activities such as the socialization of people, search for information, economy, trade, entertainment, etc. have now been transformed into processes of using digital media such as Facebook, Google, Web/Internet Banking, Amazon, YouTube etc. The same is true in the field of communication.

4. How print segments are affected

At a time when more and more people are using new technologies and are familiar with the use of the internet and electronic devices (computers, tablets, smartphones, etc.) and the global economic environment is in a difficult position due to the COVID-19 pandemic, as mentioned in the previous sections, it was perfectly reasonable and expected that the Printing Industry would be influenced like any other human activity.

In recent years, it has been recognized that the Printing Industry has declined over the past few decades. The global print market is shrinking in volume but growing in value over the period 2014–2024. Output measured in billions of A4 prints (or equivalents) was 49 973 in 2014 and forecast to decline very slightly to 49 654 by 2024. In value terms, print output grows from a total of USD 767.4 billion in 2014 to USD 862.7 billion in 2024 – a Compound Annual Growth Rate (CAGR) of +1.18 % (Smithers, 2019b; 2020).

4.1 Press – newspapers

According to Barthelemy, et al. (2011), recent data shows the "death of print" is, if even real, a limited phenomenon. Newspaper circulation declined −9.2 % in North America and −2.9 % in Europe between 2004 and 2009. By contrast, it increased +16.4 % in South America, +16.1 % in Asia and +14.2 % in Africa during the same period. Global print newspaper circulation declined −0.8 % from 2008 to 2009, but overall circulation was +5.7 % higher in 2010 than five years earlier (Barthelemy, et al., 2011).

According to Statista (2021b), the Newspaper & Magazines sector is projected to reach USD 157 567 million in 2021 (Figure 3). Revenue is expected to show a CAGR of −1 % in 2021–2025 resulting in a projected market volume of USD 149 154 million by 2025 (Statista, 2021b).
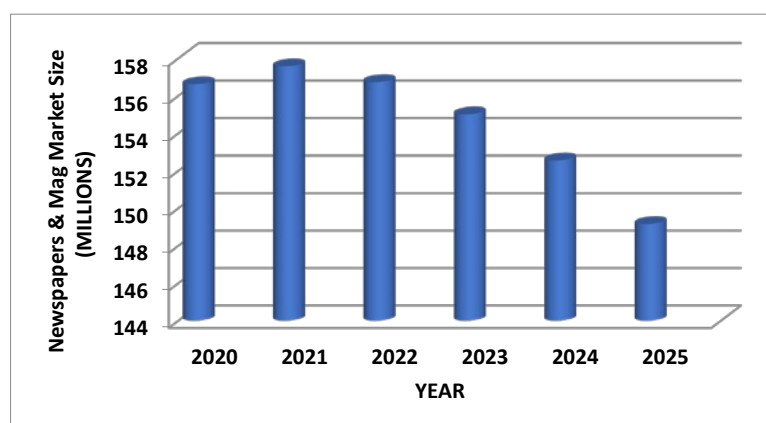
Figure 3: Estimation of annual growth in global newspapers & magazines market size, source: Statista (2021b)

4.2 Publications

The Federation of European Publishers (FEP) which represents 29 national associations of publishers from the European Union and the European Economic Area Member States, conducted a survey whose results clearly showed the increase in total sales (measured in billions) of books in European countries in

2019 compared to the previous four years, 2015–2018 (Turrin, 2021) According to Grand View Research (2018), the global books market size was valued at USD 115.0 billion in 2016 and is expected to grow at a CAGR of +0.9 % over the forecast period (Figure 4). The increasing consumer spending supported by increasing income is expected to boost market growth. Furthermore, increasing innovation in the market, which is anticipated to enhance the reading experience, is expected to boost the demand over the forecast period. (Grand View Research, 2018)
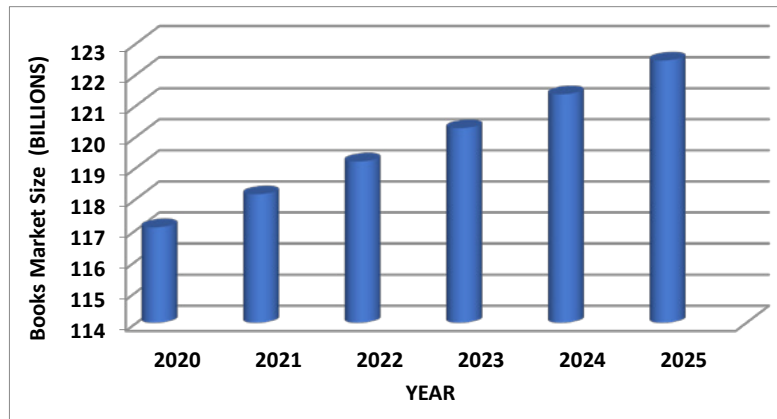
Figure 4: Estimation of annual growth in global books market size,
source: Grand View Research (2018)

Also, according to FEP's research (Figure 5), the majority of consumers who bought a book acquired it from a bookstore or a physical store and not from a digital store (e-shop) (Turrin, 2021). This is in stark contrast to the increase in the use of electronic devices, the internet and social media mentioned in a previous section of this research.
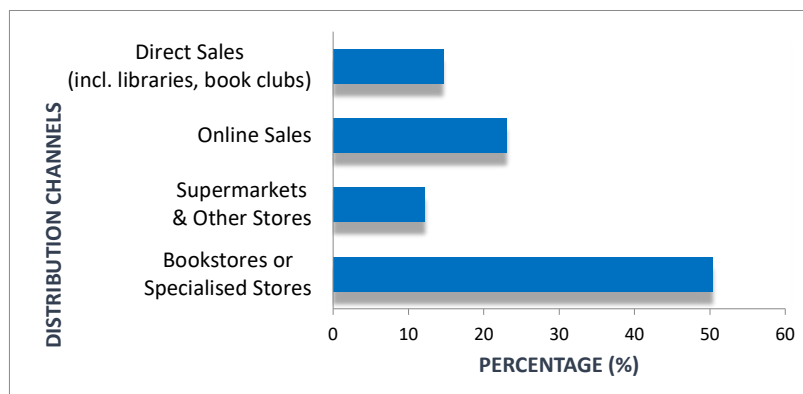
Figure 5: Book distribution channels in European countries (29 members),
source: Federation of European Publishers (Turrin, 2021)

Overall, however, the situation in the book publishing sector has deteriorated dramatically due to the COVID-19 pandemic. According to the Hellenic Statistical Authority (2011), in its annual report on the Greek economy during the period of economic recession (2009–2011) in Greece, the book publishing sector recorded a dramatic decrease of −30.6 %. During the period of the peak of the pandemic (B and C quarter of 2020) there was an extra decrease of the field by −17.8 % (Hellenic Statistical Authority, 2021). According to Eurostat, a similar decrease was recorded throughout the European Union (27 countries), while the largest decrease during the peak period of the COVID-19 pandemic was presented by Spain (Figure 6), in which in the second quarter of 2020 there was a contraction by −70 % compared to with the corresponding period in 2015 (Eurostat, 2020).
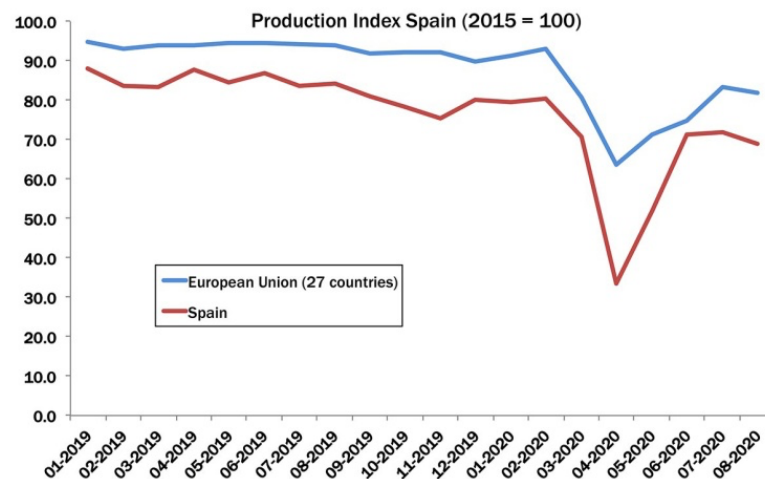
Figure 6: The decline of book publishing sector in Spain and European Union during the COVID-19 pandemic compared to 2015, source: Eurostat (2020)

4.3 Commercial prints

The Global Commercial Printing Market was valued at USD 400.46 billion in 2019, and it is projected to be worth USD 460.28 billion by 2025, registering a CAGR of +2.24 % during the period 2020–2025 (Figure 7). The commercial printing market is poised for remarkable growth over the next five years. (Wood, 2020a)
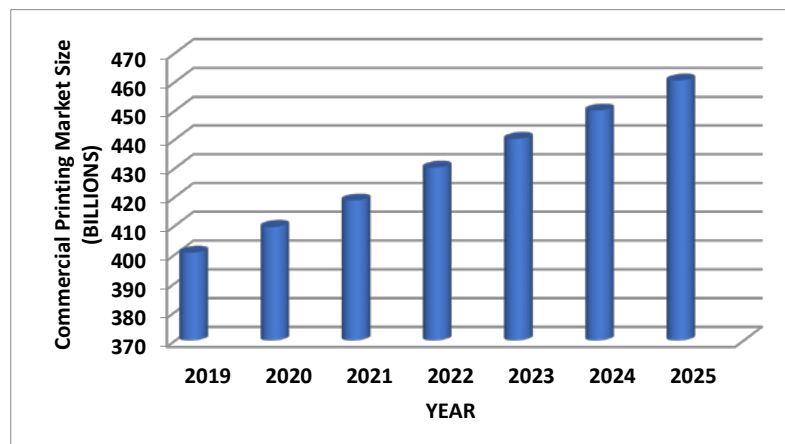
Figure 7: Estimation of annual growth in global commercial printing market size, source: Wood (2020a)

However, demand for commercial printing has reduced during the COVID-19 pandemic outbreak. Heidelberg (2020) released a report on the current state of the global print industry, during the COVID-19 pandemic outbreak. According to the report, during the COVID-19 pandemic outbreak, print production in China fell by up to 80 % compared to normal volumes but recovered as the infection curve fell and is now back to last year's levels, in both the commercial and the packaging/label segments. In addition, some printers witnessed increased demand for COVID-19 pandemic related signage from retailers, who want to assure customers that they are taking necessary safety precautions (Mordor Intelligence, 2020).

4.4 Packaging printing

Comprehensive research by Smithers Pira in its report on the Future of Global Packaging to 2022, shows that packaging demand will grow steadily at +2.9 % to reach USD 980 billion in 2022 (Smithers, 2017). The

global packaging printing market size is projected to grow from USD 352.1 billion in 2020 to USD 433.4 billion by 2025, at a CAGR of +4.2 % from 2020 to 2025. The packaging printing market is expected to witness significant growth in the future due to the increased demand for aesthetic printing solutions in end-use industries, such as food & beverage and pharmaceutical (MarketsandMarkets, 2021).
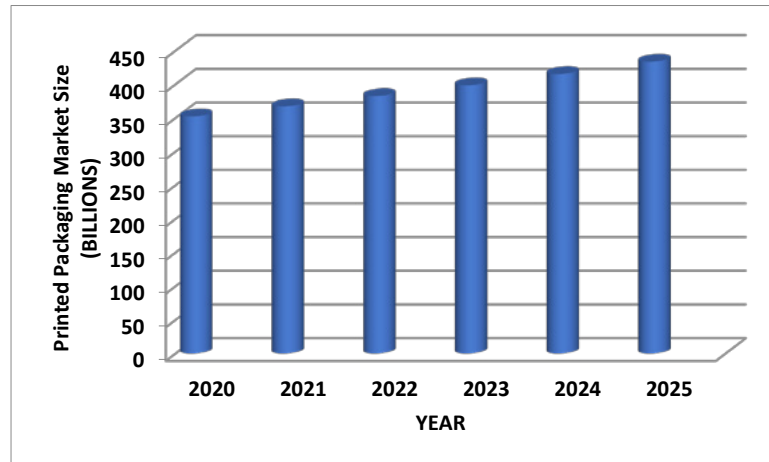
Figure 8: Estimation of annual growth in global packaging printing market size,
source: MarketsandMarkets (2021)

As Byström (2020) points out, during the COVID-19 pandemic crisis, there was a dramatic growth in online shopping that drove ten years of e-commerce growth in an eight-week period. Today, 38 % of UK consumers are now buying online at least once a week - in the US it is 26 %, Benelux 22 %, Australia 21 %, Germany 20 % and Sweden 20 % (Byström, 2020).

Furthermore, during the COVID-19 pandemic, states and local municipalities are practicing extreme caution to avoid the spread of the corona virus. Healthcare products, such as syringes, vials, and cartridges, are required on a large scale amidst this pandemic to fulfill the increasing global demand (Wood, 2020b). There will be an increase in the demand for packaging printing solutions for food & beverage and pharmaceutical applications (Figure 8), during COVID-19 pandemic (MarketsandMarkets, 2021).

These facts created a huge consumption growth that led to a growth of the packaging printing industry. The global packaging market size during the COVID-19 pandemic is projected to grow from USD 909.2 billion in 2019 to USD 1 012.6 billion by 2021 (Wood,2020b).

4.5 Labels printing

The global market for labels printing has been growing steadily from 2014 to 2019, at rates of +4.8 % in value and of +5.2 % in volume (A4 prints). Smithers latest market report "The Future of Label Printing to 2024", values the market to be worth USD 41.02 billion on volumes of 1.21 trillion A4 prints or equivalent in 2019 (Figure 9).

This is a +4 % increase on the 2018 value of USD 39.46 billion, and up +5.5 % on 2018 volumes of 1.15 trillion A4 prints or equivalent. The market will continue to increase up to 2024, at an annual average rate of +4.0 % in value to USD 49.90 billion, and by +5.5 % in volume to 1.59 trillion A4 prints or equivalent. (Smithers, 2019a)
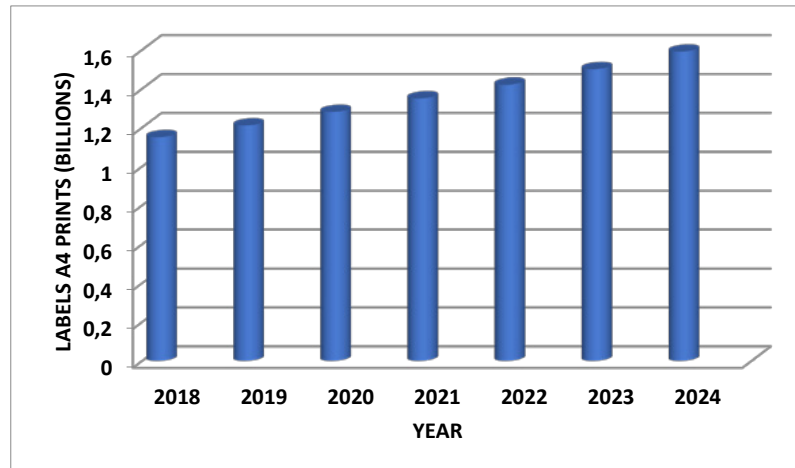
*Figure 9: Estimation of annual growth in volume of A4 prints or equivalent in global market
for label printing, source: Smithers (2019a)*

As Lejeune (2019), FINAT Managing Director, pointed out at the 2019 FINAT European Label Forum, the label stock demand between 1998 and 2018 shows an increase every year, even if this increase is small (Figure 10). An exception to this trend is the years 2009 and 2011 during which there was a deep recession in the economy in general. It is also very important to emphasize that the consequence of this continuous increase is the more than doubling of label stock demand between these 20 years (1998–2018).
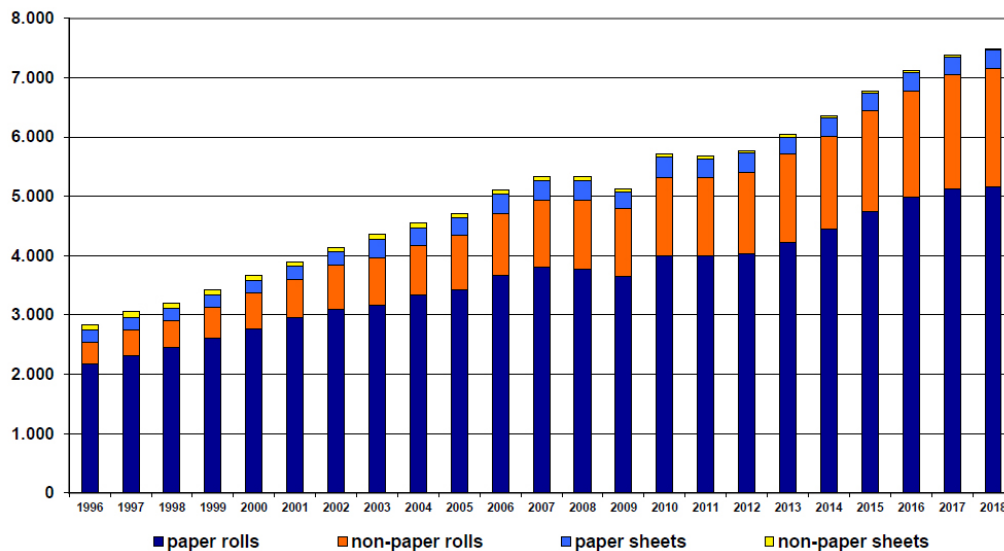
*Figure 10: Label stock demand 1998–2018,
source: FINAT (2019)*

4.6 Security printing

In recent decades, it is widely accepted that the use of the most well-known security document, the printed banknote, is declining day by day due to the growing number of electronic transactions or the use of "plastic money". A rise in card and mobile payments and a decline in cash purchasing is being seen in countries like Sweden. This will continue but will not be universal over the next five years.

It would be logical for someone to combine this fact with a reduction in the production of security prints. But this is not a fact, as there may be a reduction in printed banknote production but there is an increase demand for security prints for other purposes.

The personal ID segment has to react to the need for new printed solutions that can integrate online and mobile-based platforms. Simultaneously, new regulations and mandates are creating exciting future revenue streams in tax stamps and brand protection packaging (Whitcher, 2019).

The shift to polymer banknotes is progressing with over 20 countries and an increasing range of denominations is being issued. This shift will continue and counterfeits will increase, enabled by technology (Smithers, 2020).

The tourism sector is addressing growth due to factors such as the growth of budget airlines and an increase in the number of air travelers around the globe. Also, according to the World Tourism Organization, international tourist arrivals worldwide increased 6 % in 2018 to 1.4 billion. Consequently, the demand for visas and passports to avoid identity-related frauds is expanding. This is leading to extensive security printing involving proof certificates to prevent terrorist activities and maintain the integrity and security of national and international borders (Research and Markets, 2021).

Smithers latest market report, "The Future of Global Security Printing to 2024" forecasts the global security printing market value (Figure 11) will increase from USD 29.5 billion in 2019 to USD 36.0 billion by 2024, with a CAGR of 4.1 % (Smithers, 2020).
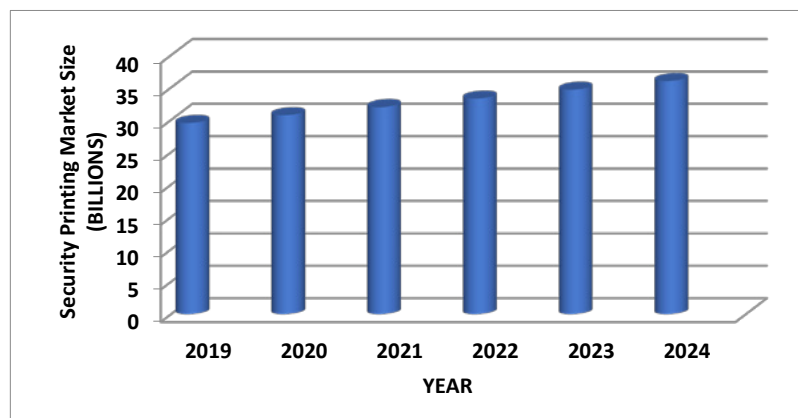
Figure 11: Estimation of annual growth in global security printing market size,
source: Smithers (2020)

4.7 Art market & printing reproduction

During COVID pandemic there was a decline in the turnover of large galleries and long-range markets where for the purchase of these products the buyer prefers to purchase the work in person. However, the overall market has recovered from the establishment of several smaller domains of domestic and international interest galleries that are smaller in purchasing power but with more artists under their supervision. In short, during the pandemic crisis, more works of lower commercial value were circulated, of more artists numerically (McAndrew, 2021). This market (Figure 12) declined only 20 % during 2020 and compared to the global financial crisis of 2009 is still at significantly higher levels (USD 50.1 billions in 2019 Vs 39.5 USD billions in 2009).
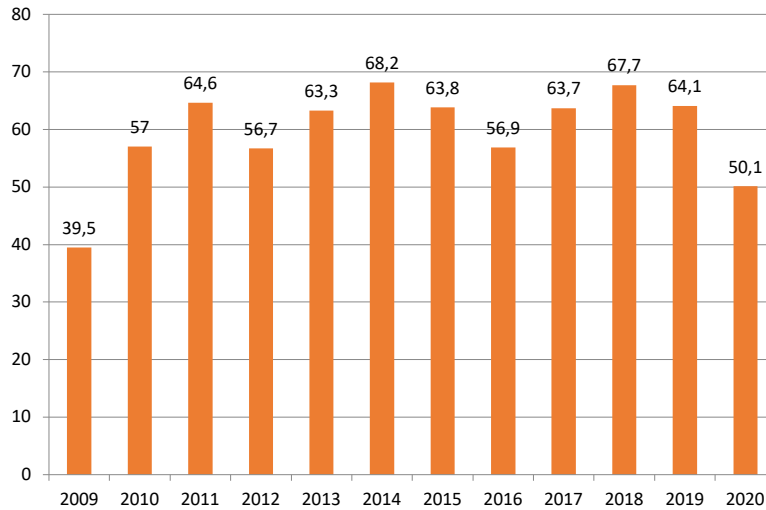
Figure 12: The Global Art Market (in billions $),
source: McAndrew (2021)

This can be interpreted as that in the coming years this market will have multiple purchasing power and after the end of the crisis a huge market will have been created from works of art and derivative copies of them which will have investment value. (McAndrew, 2021)

4.8 All printing industry segments

As shown in previous segments of this research, most of the Printing Industry segments will be expected to show an annual growth in the years coming (Table 1, Figure 13). The estimated annual growth for some of these Printing Industry segments will be higher than other, but in the end only the Press – Newspapers segment is expected to decrease.

Table 1: The estimated annual growth of the sectors of the printing industry

Printing Industry sectors	2020	2025	Estimated annual growth (%)
Press – Newspapers (millions)	157.57	149.15	− 1.00
Publications – Books (billions)	117.07	122.44	+ 0.90
Commercial Prints (billions)	409.40	460.28	+ 2.24
Packaging Printing (billions)	352.10	433.40	+4.20
Labels Printing (billions)	42.70	51.89	+ 4.00
Security Printing (billions)	29.50	36.00	+ 4.10
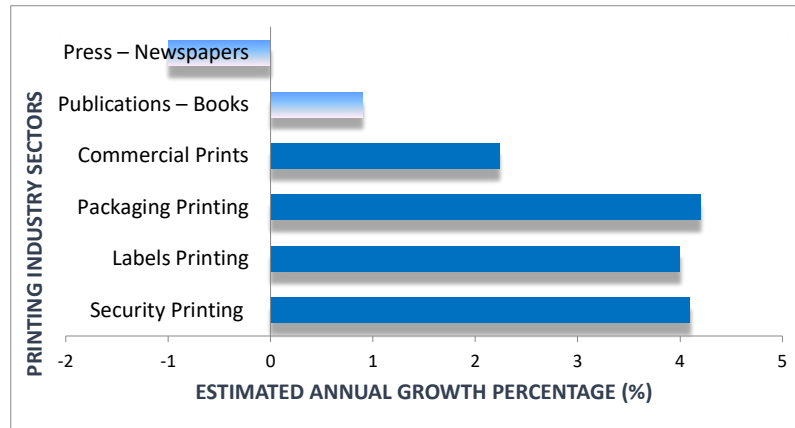
Figure 13: The estimated annual growth of the sectors of the printing industry

It seems that up to today, statements and predictions on the "decreasing" of print do not seem to be a reality. Our field and the related sectors show a rather stable condition in terms of turnover and production, at least in Europe and North America, whereas in other continents, such as Asia, print is booming (Politis, 2018b)

5. Evolution in the Printing Industry – challenges by digital transformation

With the data presented in the previous sections of this research composing the current era in the field of Printing Industry, the need for transformation and evolution seems more necessary than ever. In any case, the concepts of "transformation" and "evolution" accompany the course of the Printing Industry from the Gutenberg era, and the progress of the space is largely due to them.

The transformation and evolution in the Printing Industry is a continuous and uninterrupted process. Hence in recent years this acceleration is faster than ever.

On the one hand, this transformation and evolution were expressed with the development of technology in the field of Printing Industry production, which is faster than ever and leads with mathematical precision to the complete automation of all production processes. A good 90 % of global printing volume still comes from offset. However, when we talk about digital in the Printing Industry today in terms of production processes, we are not automatically referring to digital printing alone (Riva, 2020).

5.1 Industry 4.0

The original definition of Industry 4.0 comes from Smart industry or "INDUSTRIE 4.0" as it has been defined by the German Trade and Invest agency. It refers to the technological evolution from embedded systems to cyber-physical systems. The term Industry 4.0 has been coined at the 2011 Hannover Fair, a concept better known as the "Smart Factory". The 4.0 makes reference to be a fourth industrial revolution to come (Rüttimann and Stöckli, 2016; Politis, et al., 2019).

Put simply, INDUSTRIE 4.0 represents the coming fourth industrial revolution on the way to an Internet of Things, Data and Services. Decentralized intelligence helps create intelligent object networking and independent process management, with the interaction of the real and virtual worlds representing a crucial new aspect of the manufacturing and production process. As such, INDUSTRIE 4.0 represents a paradigm shift from "centralized" to "decentralized" production – made possible by technological advances, which constitute a reversal of conventional production process logic. Simply put, this means that industrial pro-

duction machinery no longer simply "processes" the product, but that the product communicates with the machinery to tell it exactly what to do. INDUSTRIE 4.0 connects embedded system production technologies and smart production processes to pave the way to a new technological age which will radically transform industry and production value chains and business models (e.g. "smart factory") (Politis, et al., 2019). The definition of Industrie 4.0 as proposed in 2011 was pretty lengthy. In a paper, entitled "Industrie 4.0 – Smart Manufacturing for the Future", GTAI (Germany Trade and Invest) looked at the questions what is smart industry (a synonym of Industry 4.0) and what Industrie 4.0 means (MacDougall, 2015; Politis, et al., 2019).

According to Politis, et al. (2019), Ostdick proposes 5 key elements of Industry 4.0 to better understand its place and overall value proposition in a global manufacturing stream: Greater levels of product customization, Integration of Advanced Analytics, Pushing beyond postmodern ERP, Embracing the Internet of Things, Increased reliance (and positive outcomes) on cloud technology (Ostdick, 2017; Politis, et al., 2019)

Drexler, suggests that new technologies, spanning mobile computing to cloud computing, have undergone vast development in the last decade and are now ready to be used as commercially available, interconnected systems within manufacturing – this is Industry 4.0. It holds the key to accessing real-time results and data that will catapult the industry into new levels of lean achievements (Drexler, 2016; Politis, et al., 2019).

5.2 Industry 4.0 and the Printing Industry

Automation and technological innovations have entered all sectors of Printing Industry, from the beginning of the process, which is the client's command to communicate his information (any form of information that can lead to any print or digital media) until the completion of the production of the communication he desires. This is also the case with the concept of Industry 4.0, which characterizes the manufacturing industry in general, including the Printing Industry. Industry 4.0 or the "Fourth industrial revolution" appears as an interesting global trend that defines the current trend of automation and data exchange (Ostdick, 2017; Politis, 2018a; Politis, et al., 2019).

As Politis claims, vendors, organizations and scientists from the Printing Industry and media – printing sectors could not stay out of the debate for manufacturing evolution caused by the Industry 4.0 trend. Numerous manufacturers are taking position within Industry 4.0. As such Industry 4.0 is classified / translated as Print 4.0, Finishing 4.0, Packaging 4.0 and Paper 4.0 (Politis, 2017).

In addition, according to Politis (2018a), Niemela (2016) argues that "Printing 4.0 megatrend applies for all Printing Industry / graphic communication fields, namely Design, Prepress, Print and Finishing, at an integrated and connected workflow based on full digitalization".

As Niemela points out, this means the integration of computer integrated manufacturing, networked production steps, low stock levels, just in time delivery, innovative workflow structures and Maximum flexibility (Niemela, 2016; Politis, 2018a).

Müller Martini (2021), presented Finishing 4.0 which includes the following elements: touchless workflow, uninterrupted print finishing, touchless manufacture of print products in a single pass, combination of high degree of automation with seamless connectivity, modification of product parameters during the job run without interrupting production and dynamic job change function. Müller Martini's Finishing 4.0 philosophy shows that it is possible to produce customized and variable print products cost-effectively and efficiently using means of mass production. In other words, it is possible to produce customized books, brochures and magazines with high added value at low prices per copy and stay competitive. The time is not only ripe to talk about connectivity and workflows in the graphic arts industry but also to offer specific solutions (Politis, 2018a).

Further, Heidelberg USA argues that "Industry 4.0 is a transformation that's sweeping every sector of manufacturing, and Heidelberg has solutions that can put its customers in the forefront of driving this transformation in printing. In this kind of print manufacturing, the essential raw material isn't paper or ink. Its data–data that connects machines to machines, machines to plant environments, plant environments to management systems, and management systems to customers. Each step of the process generates data, and all of it is captured and analyzed with one objective in mind: to make the entire manufacturing sequence as efficient and as profitable as it can be (Heidelberg, 2018; Politis, et al., 2019).

In addition, as it is stated in a brochure from Horizon, "In Printing 4.0, processes happen in holistic and borderless environment. The direct connection of the service provider with its customers offers sustainable potential" (Druckerei 4.0, 2015; Politis, 2018a). As Druckerei 4.0, it is understood the step towards fully automated production through the mechanical and electronic networking of printing and finishing systems as well as increased transparency of the entire production environment. (Druckerei 4.0, 2015; Politis, et al., 2019).

In a brochure from CEPI – the Confederation of European Paper Industries, the paper industry contributes in the Industry 4.0 discussion by stating that "Digital" is the major evolution for the paper industry. Industry 4.0 is a digital manufacturing revolution, leveraging the huge unrealised value potential available from the digitalisation of industrial processes, products, and services. Digitalisation is the main driver of the next industrial revolution. Everything that can be digitalized, will be digitalised. The complete process of papermaking will be revolutionized, from forests to end consumers (CEPI, 2015). The goal is to automate all conventional production processes in Printing Industry and to operate in a digital way.

5.3 Digitalization of printing industry

Digital transformation is progressing rapidly in the conventional sector. As a result, ever fewer companies today use routing slips that have been manually filled out, but instead rely on digitized job sheets. More and more machines are directly linked to the Management Information System (MIS) – just like job preparation and pre-press – which has several benefits (for example, real-time reporting) (Riva, 2020).

Many of the enterprises of Printing Industry will or plan to invest in the next few years a significant percentage of their total investments in types of software that will help them transform their activities based on full or partial digitalization. This trend is expressed by the intention to invest in software about cloud-based content management services, web to print, MIS etc. (Figures 14 to 17). This trend is common also in many sectors of the Printing Industry sectors.
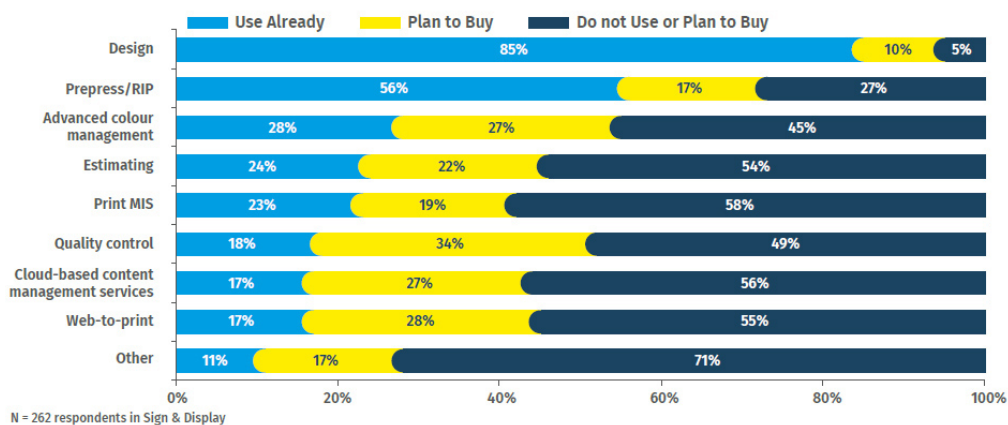
Figure 14: Printing Industry ownership or investment plans for the different types of software –
Sign & Display sector, source: FESPA (2018)
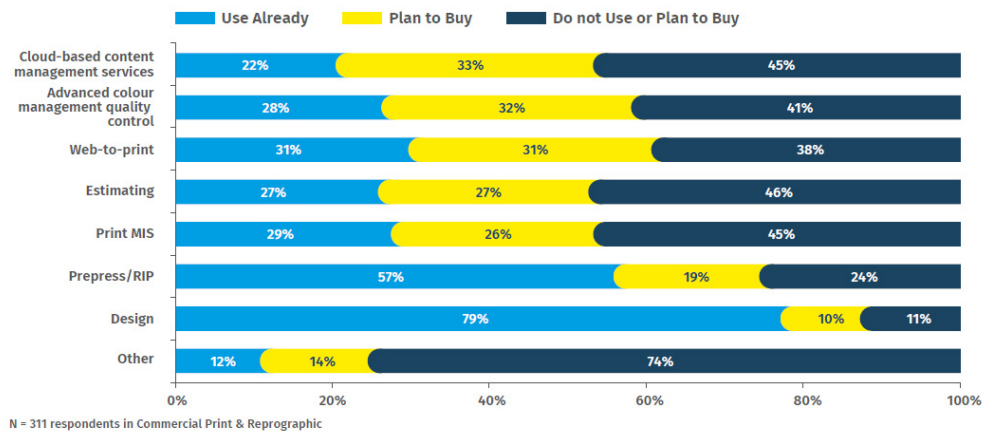
Figure 15: Printing Industry ownership or investment plans for the different types of software –
Commercial Print & Reprographic sector, source: FESPA (2018)
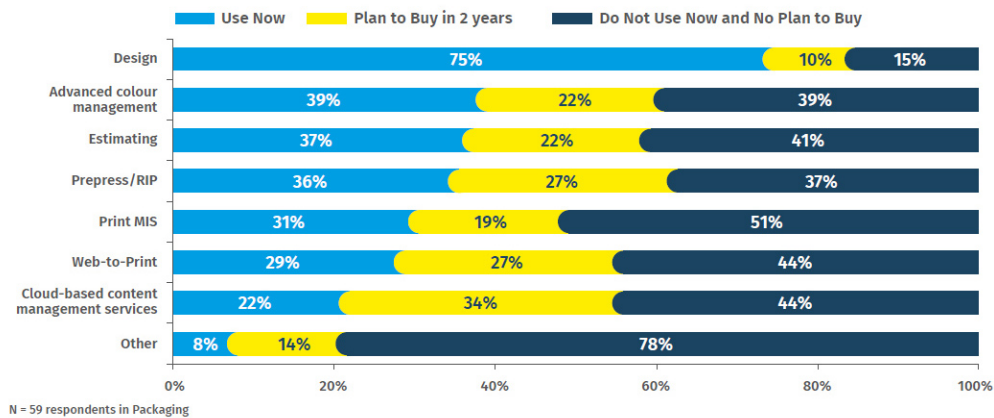
Figure 16: Printing Industry ownership or investment plans for the different types of software –
Packaging sector, source: FESPA (2018)
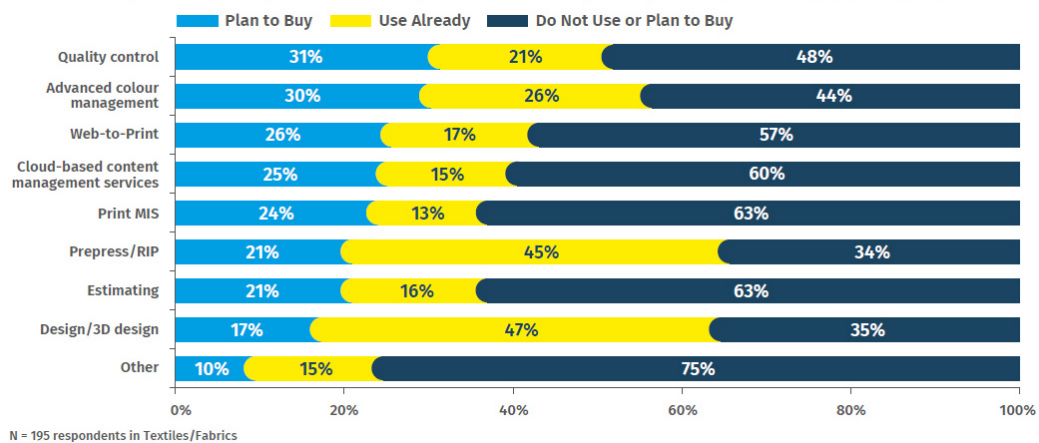
Figure 17: Printing Industry ownership or investment plans for the different types of software –
Textiles/Fabrics sector, source: FESPA (2018)

On the other hand, transformation and evolution are not limited to the production processes of the product, but continue to take place even deeper, in areas such as the philosophy of how a Printing Industry company operates and manages. According to Netland (2015), Lean Manufacturing represents a philosophy for the establishment of efficient operational management of all functions of an organization or company (Politis, et al., 2019).

According to Politis (2018b), Bohan (2017) states that printing companies today have to navigate the requirements of shorter run lengths, faster turnaround times and increasing costs, all while facing relatively stable print prices and higher consumables prices. With all of these challenges, it's virtually impossible to maintain, yet alone increase, profitability without making changes to your current business model or operations. The key to profitability and the solution to current challenges may be no further than workflow (Bohan, 2017; Politis, 2018b).

6. Conclusions

The main purpose of this paper was to investigate whether the printing industry is decreasing or not. As presented in the first sections of this research, the general trend of automation and digitization has prevailed everywhere and has "flooded" every aspect of human activity. The printing industry could not be an exception to this trend.

The vast majority of the printing industry segments, although one would expect the opposite, seem to be increasing in the coming years. The publications segment, the commercial printing segment, packaging printing segment, the label printing segment and the security printing segment will increase. On the contrary, only the newspaper printing segment is expected to show a decrease.

The estimated CAGR of important sectors of the printing industry, therefore, clearly shows that the printing industry is not declining, but in contrast is also expected to increase. Market analysts' estimations as presented in previous sections, show that the annual increases until 2025 will range from 1 % to 4.2 % depending on the printing industry segment.

It is also very important to notice (and perhaps is expected), that the highest estimated CAGR occur in segments whose final product can hardly serve the needs for which it was made, if it is in a digital form. Segments such as packaging printing or labels printing are increasing compared to segments where the final product may be in a digital form, such as a newspaper, a book or an advertising brochure.

At the same time, the COVID-19 pandemic is clearly making its mark on global economic activity and consequently, on the printing industry. As it turned out the COVID-19 pandemic affected in a repressive way CAGR of each segment of the printing industry, but this phenomenon seems to be temporary and markets and consumers seem to be adapting to it one way or another. As a result, according to estimations for the future of the printing industry, the estimated CAGR will have a positive sign and this phenomenon seems to be temporary and slowly reversing.

As mentioned before in this paper, the general trend of automation and digitization has prevailed everywhere. As a result, the printing industry is forced to proceed to the complete automation of its production processes. As presented in section 5.3, the process of automation and digitization of the printing industry has already begun and data shows that some sectors of the production process, such as prepress, are almost fully automated while others, such as post press to a lesser extent. In a significant degree, companies are willing to invest in the automation of these sectors as well.

In some segments of the printing industry, data shows that companies are using technologies that help digitize or automate their operations at rates ranging from 17 % to 31 %. In addition, and perhaps even more importantly, these companies are willing to invest in technologies that will contribute to the digitization and automation of their operation at rates of 17 % to 31 %. These numbers confirm the significant shift towards digitalization and automation of the printing industry.

Of course, it is not enough just to digitize or automate the production processes of the printing industry. This digitization must be included in the way the production is organized, in its workflow, in its administration and management. The principles and ideas of industry 4.0 must be applied to the printing industry in order this industry to continue to evolve.

This development proves that it cannot come from any other path than that of automation and digitization.

7. Further discussion/research

The adaptation of the printing industry to the age of automation and digitization raises other issues that deserve to be discussed and researched in the future.

When the printing industry has entered the digitization to a significant degree, then it is worth doing a study on the effects of this change. All productivity indicators should be measured in order to capture mathematically the benefit that the printing industry will have in all or some of its sectors as future research will show.

A future research, however, is important to be dedicated to the people of the printing industry as well. The workers in this industry have always been an integral part of it and have been of great importance for its development. It is necessary to research not only whether these people have the right background to enter the digitization, but also whether and how the digitization of the printing industry itself will integrate them in this new working context.

References

Azevêdo, D., 2020. Trade set to plunge as COVID-19 pandemic upends global economy. *World Trade Organization,* [online] 8 April. Available at: <https://www.wto.org/english/news_e/pres20_e/pr855_e.htm> [Accessed 11 February 2021].

Barthelemy, S., Bethell, M., Christiansen, T., Jarsvall, A. and Koinis, K., 2011. *The future of print media: Capstone report 2011*. [pdf] Available at: <https://www.sipa.columbia.edu/academics/capstone-projects/future-print-media> [Accessed February 2021].

Bohan, M., 2017, How Prinect Production Manager will reshape your business. *Heidelberg Connect,* [online] 28 November. Available at: <https://news.heidelbergusa.com/2017/11/prinect-production-manager-reshape/> [Accessed 13 February 2021].

Byström, M., 2020. COVID-19: From impact to action in the packaging industry. In: *COVID-19: From impact to action in the packaging industry: how to sustain agility and profitability in the packaging value chain in the new normal.* Gent, Belgium: ESKO, p. 5.

CEPI, 2015. Paper Industry 4.0 – what digital can do for the paper industry. *CEPI*, [online] 19 November. Available at: < https://www.cepi.org/paper-industry-4-0-what-digital-can-do-for-the-paper-industry/> [Accessed February 2021].

Drexler, S., 2016. The 5 factors of Industry 4.0. *ARC Advisory Group*, [blog] 15 August. Available at: < https://www.arcweb.com/blog/5-factors-industry-40> [Accessed February 2021].

Druckerei 4.0, 2015. *Druckerei 4.0: bereit f*ür *die Revolution?*. *HORIZON Druckverarbeitung*. [pdf] Available at: <https://www.horizon.de/fileadmin/user_upload/horizon.de/Dateien/Pdf/Horizon_nachdruck_2015-2.pdf> [Accessed February 2021].

Eurostat, 2020. *Digital economy and society statistics - households and individuals*. [online] Available at: <https://ec.europa.eu/eurostat/statistics-explained/index.php/Digital_economy_and_society_statistics_-_households_and_individuals> [Accessed 5 February 2021].

Turrin, E., 2021. European book publishing statistics 2019. *The voice of European publishers,* 18 January [online] Available at: <https://fep-fee.eu/European-Book-Publishing-1268> [Accessed 9 February 2021].

FESPA, 2018. *2018 FESPA print census report.* Dorking Surrey, U.K.: FESPA, pp. 34, 67, 79, and 92.

FINAT, 2019. *FINAT Radar 11 – 1ST Semester 2019.* The Hague, The Netherlands: FINAT, p. 6.

Flachenecker, F., Gavigan, J., Goenaga Beldarrain, X., Pasi, G., Preziosi, N., Stamenov, B. and Testa, G., 2020. *High growth enterprises: demographics, finance & policy measures.*, Luxembourg, Publications Office of the European Union, pp. 21, 23, and 27.

Grand View Research, 2018. Books sales worldwide. *Grand View Research.* [online] Available at: <https://www.grandviewresearch.com/industry-analysis/books-market> [Accessed 15 February 2021].

Heidelberg, 2018. Digital business models are the future: Heidelberg achieves 100 worldwide installations of Prinect Production Manager. *Heidelberg Connect,* [online] 4 October. Available at: <https://news.heidelbergusa.com/2018/10/digital-prinect-production-manager/> [Accessed 13 February 2021].

Heidelberg, 2020. Print Industry in Times of COVID-19 - Heidelberg Presents Print Media Industry Climate Report. *Heidelberg*, [online] 28 April. Available at: <https://www.heidelberg.com/global/en/about_heidelberg/press_relations/press_release/press_release_details/press_release_137920.jsp> [Accessed May 2021].

Hellenic Statistical Authority, 2011. *The Greek economy 2011*. Piraeus, Greece: ELSTAT, pp. 40-41.

Hellenic Statistical Authority, 2021. *The Greek economy 2021*. Piraeus, Greece: ELSTAT, pp. 32-33.

Lejeune, J., 2019. FINAT market update. In: *Business as usual? FINAT European Label Forum 2019.* Copenhagen, Denmark, June 2019. FINAT.

MacDougall, W., 2015. *Industrie 4.0: smart manufacturing for the future*. Berlin, Germany: Germany Trade and Invest.

MarketsandMarkets, 2021, Packaging printing market by printing ink (aqueous, UV-based), printing technology (flexography, gravure, digital), packaging type (labels & tags, flexible), application (food & beverages, cosmetics, pharmaceuticals), & region – global forecast to 2025. *MarketsandMarkets* [online] Avaliable at: <https://www.marketsandmarkets.com/Market-Reports/packaging-printing-market-153207109.html?gclid=CjwKCAjw8ajcBRBSEiwAsSky_ecQnTHgr4mN972nMDuCrB1C2b4npfF9cDby3B1AvIbF4UwiwTxc_BoC_scQAvD_BwE.> [Accessed 2 February 2021].

McAndrew, C., 2021. The Art Basel and USB global art market report. *Art Basel*, [online]. Avaliable at: <https://artbasel.com/about/initiatives/the-art-market> [Accessed February 2021].

Mordor Intelligence, 2020. Commercial printing market – growth, trends, COVID-19 impact, and forecasts (2021 – 2026). *Mordor Intelligence,* [online]. Available at: <https://www.mordorintelligence.com/industry-reports/commercial-printing-market> [Accessed 12 February 2021].

Müller Martini, 2021. What is Finishing 4.0? *Müller Martini*, [online]. Available at: <https://www.mullermartini.com/en/company/our-vision/finishing-4-0/> [Accessed February 2021].

Netland, T., 2015. Industry 4.0: what about Lean? *better operations* [online]. Available at: <http://better-operations.com/> [Accessed 27 March 2019].

Niemela, B., 2016. Der Druck startet durch und wird internationaler. *Deutscher Drucker*, 13.

Ostdick, N., 2017. 5 Key elements of Industry 4.0. *flexis* [blog], 20 April. Available at: <https://blog.flexis.com/author/Nick-Ostdick> [Accessed 30 March 2019].

Politis, A., 2017, The graphic-media communication science – fields, trends and the contribution of research organizations. In: *Evolution Innovation in Graphic-Media Science: Research, Industry Innovation and the Role of Education*. Athens, Greece, 22 March 2017. Hellenic Union of Graphic Arts and Media Technology Engineers (HELGRAMED).

Politis, A., 2018a. Industry 4.0: what does it mean for the graphic arts industry? In: C. Ridgway, ed. *Advances in Printing and Media Technology: Proceedings of the 45th International Research Conference of IARIGAI,* Warsaw, Poland, October 2018. Darmstadt: iarigai.

Politis, A., 2018b, Innovations in the graphic arts, media and packaging fields. In: *Proceedings of GRID18: 9th international symposium on Graphic Engineering and Design*. Novi Sad, Serbia, 8–10 November 2018. Novi Sad, Serbia: Faculty of Technical Sciences.

Politis, A.E., Macro, K.L., Gamprellis, G., Tsigonias, M. and Trochoutsos, C., 2019. Matching lean manufacturing and Industry 4.0 for the graphic communication – printing industry. In: C. Ridgway, ed. *Advances in Printing and Media Technology: Proceedings of the 46th International Research Conference of IARIGAI*, Stuttgart, Germany, 15–18 September 2019. Darmstadt, Germany: iarigai.

Research and Markets, 2021, Global security printing market (2021 to 2026) – growth, trends, COVID-19 impact, and forecasts. *GlobeNewswire,* [online] 16 February. Available at: <https://www.globenewswire.com/fr/news-release/2021/02/16/2176150/28124/en/Global-Security-Printing-Market-2021-to-2026-Growth-Trends-COVID-19-Impact-and-Forecasts.html> [Accessed 25 July 2021].

Riva, G., 2020. Digital transformation is also progressing rapidly in the conventional sector, *Muller Martini,* [blog] 3 March. Available at: <https://www.mullermartini.com/en/newsroom-en/blog/events/digital-transformation-is-also-progressing-rapidly-in-the-conventional-sector/> [Accessed 10 February 2021].

Roser, M., Ritchie, H. and Ortiz-Ospina, E, 2017. The Internet's history has just begun. *Our World in Data,* [online] Available at: <https://ourworldindata.org/internet> [Accessed 2 February 2021].

Rüttimann, B.G. and Stöckli, M.T., 2016. Lean and Industry 4.0 – twins, partners, or contenders? A due clarification regarding the supposed clash of two production systems. *Journal of Service Science and Management*, 9(6), pp. 485–500. http://dx.doi.org/10.4236/jssm.2016.96051.

Simon, H., and Harding, M., 2020. What drives consumption tax revenues? *OECDiLibrary,* [online] Available at: <https://www.oecd-ilibrary.org/taxation/what-drives-consumption-tax-revenues_94ed8187-en> [Accessed 11 February 2021]. https://doi.org/10.1787/22235558.

Smithers, 2017. Paper and board have key roles in the future of packaging. *Smithers* [online] Available at: <https://www.smithers.com/resources/2018/feb/paper-and-board-roles-in-the-future-of-packaging> [Accessed February 2021].

Smithers, 2019a. The global market for label printing will reach $ 49.90 billion in 2024. *Smithers* [online] Available at: <https://www.smithers.com/resources/2019/may/global-market-for-label-printing-will-reach-$49-9b> [Accessed 15 February 2021].

Smithers, 2019b. How is the digital and offset printing markets going to change? *Smithers* [online] Available at: <https://www.smithers.com/resources/2019/may/how-is-the-digital-print-market-going-to-change> [Accessed 15 February 2021].

Smithers, 2020, How Smithers forecasts the global security printing market to reach $36 billion in 2024. *Smithers* [online] Available at: <https://www.smithers.com/resources/2020/april/smithers-forecasts-global-security-printing-market> [Accessed 20 July 2021].

Statista, 2021a, Number of monthly active Twitter users worldwide from 1st quarter 2010 to 1st quarter 2019. *statista* [online] Available at: <https://www.statista.com/statistics/282087/number-of-monthly-active-twitter-users/> [Accessed 4 February 2021].

Statista, 2021b. Newspapers & magazines. *statista* [online] Available at: <https://www.statista.com/outlook/21500/100/newspaper-magazines/worldwide> [Accessed 16 February 2021].

Tsekeris, C., Dermetzis, N., Linardis, A., Iliou, K., Kondyli, D., Frangiskou, A. and Papaliou, O., 2020. *Investigating the Internet in Greece: findings from the World Internet Project*. Athens, Greece: Hellenic Observatory.

UNCTAD, 2019. Survey says people don't trust the Internet, what needs to change? *UNCTAD,* [online] 11 June. Available at: <https://unctad.org/news/survey-says-people-dont-trust-internet-what-needs-change> [Accessed 4 February 2021].

UNCTAD, 2021. Global foreign direct investment fell by 42 % in 2020, outlook remains weak. *UNCTAD,* [online] 24 January. Available at: <https://unctad.org/news/global-foreign-direct-investment-fell-42-2020-outlook-remains-weak> [Accessed 4 February 2021].

UNWTO, 2020. International tourist numbers could fall 60–80 % in 2020, UNWTO Reports. *UNTWO,* 7 May. [online], Available at: <https://www.unwto.org/news/covid-19-international-tourist-numbers-could-fall-60-80-in-2020> [Accessed 4 February 2021].

Whitcher, J., 2019. Secure printing is an industry-wide challenge. *WhatTheyThink,* [online] 4 April*.* Available at*:* <https://whattheythink.com/articles/94661-secure-printing-industry-wide-challenge/> [Accessed 20 July 2021].

Wood, L., 2020a. Global commercial printing market report 2020-2025 assessed by type, application and region. *CISION PR Newswire,* [online] 25 June. Available at: <https://www.prnewswire.com/news-releases/global-commercial-printing-market-report-2020-2025-assessed-by-type-application-and-region-301083732.html> [Accessed 8 February 2021].

Wood L., 2020b. $1 billion global packaging industry to 2021 – growing demand for FMCG and pharmaceutical packaging presents opportunities. *Globe Newswire,* [online] 12 May. Available from: <https://www.globenewswire.com/news-release/2020/05/12/2031745/0/en/1-Billion-Global-Packaging-Industry-to-2021-Growing-Demand-for-FMCG-and-Pharmaceutical-Packaging-Presents-Opportunities.html> [Accessed 3 February 2021].

Zhan, F., Laines, G., Deniz S., Paliskara, S., Ochoa, I., Guerra, I., Tayeb, S., Chiu, C., Pirouz, M., Ploutz, E., Zhan, J., Gewali, L. and Oh, P., 2018. Prediction of online social networks users' behaviors with a game theoretic approach. In: *5th IEEE Annual Consumer Communications & Networking Conference (CCNC)*. Las Vegas, NV, USA, 12–15 January 2018. IEEE. http://dx.doi.org/10.1109/CCNC.2018.8319308.

Printed batteries, properties of substrates and components, regarding bendability and barrier

Gunter Hübner, Michael Krebes, Frank Etzel, Larissa Nußbaum and Sabrina Thamm

Innovative Applications of the Printing Technologies (IAD), Stuttgart Media University, Nobelstr. 10, 70569 Stuttgart, Germany
E-mails: huebner@hdm-stuttgart.de, krebes@hdm-stuttgart.de, etzel@hdm-stuttgart.de, ln025@hdm-stuttgart.de, sw181@hdm-stuttgart.de

Short abstract

Printed batteries are devices with several layers printed on top of each other and comprise an electrolyte. The big advantage of these thin film batteries in comparison to button cells is the freedom of design and mechanical flexibility. Especially if the printed batteries are used in wearables such as skin patches, they must remain functionable during bending movements and must be sealed perfectly in order to avoid electrolyte leakage. The substrates must have sufficient barrier properties so that the electrolyte is kept wet inside the flexible pouch.

Keywords: printed batteries, foil substrates, mechanical properties, water vapour transmission rates

1. Introduction

At the Innovative Anwendungen der Drucktechnologien (IAD) printed batteries are subject of investigation and development for almost 15 years. In the previous work together with VARTA Microbattery GmbH as the main research partner the focus was on the basic design (stack or co-planar, see Figure 1) the printing and assembly technical and, of course, the chemical systems. Besides the simplest, the primary system Zn/MnO_2 (aka. zinc-carbon) a lot of research effort has gone into rechargeable systems such as NiMH and Zinc/Air (with modified zinc in order to make it rechargeable). The chemical systems and the printing technique used for these film batteries has been described earlier (Huebner and Krebs, 2015; Huebner, et. al., 2015). Now, that the printed batteries are at the step to get commercialised in a broader range it is important to have a closer look to mechanical properties such as bending ability and avoidance of leakages. Both are mainly influenced by the substrates used. The applications that drive the commercialisation where the IAD is involved are on one hand solutions for logistics where a parcel sends out a SMS if opened, (see video on Elmeric, n.d.), and on the other hand skin patches used for monitoring health and wellbeing, see projects such as OxiFlexIT (Dums, et al., 2021) and BEWELL (2020). The flexible skin patches contain printed batteries and necessary electronics. The printed batteries need to be produced as thin as possible to be flexible.
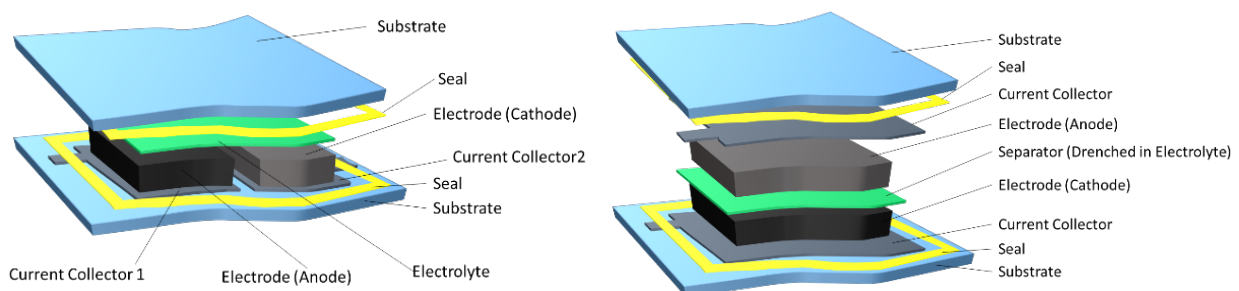
Figure 1: Basic design of printed batteries; left: co-planar, right: stack (Huebner and Krebs, 2015)

The printing process that is the most suitable is screen printing since the mass (layer thicknesses typical is ~150 μm) of the active electrode materials determine the battery capacity and the particles used are quite coarse (<25 μm).

2. Materials and methods

There are two basic designs of a printed battery, the stack and the co-planar one as shown in Figure 1. The differences are discussed thoroughly elsewhere (Huebner, et. al., 2015). In brief the co-planar is much easier to manufacture whereas the stack can deliver much higher peak (burst) currents. The challenge of the stack design is that a direct contact between the anode and cathode must be avoided and therefore a separator is used. The separator is drenched in electrolyte. In co-planar design, the electrolyte can easily be applied, e.g., by printing of a thickened electrolyte solution, the separator is not necessary. In both designs a top and bottom substrate is necessary. Also, in both designs current collector layers are necessary. Since they contribute very much to the inner resistivity of the battery they must be as conductive as possible. Therefore, silver is used for that purpose. However, silver is not electrochemically inert. Thus, the silver is covered by a layer of carbon black which prevents the contact between silver and the electrodes. Silver and carbon black pastes must be thermally treated after printing to achieve maximum conductivity. In stack design top and bottom substrates must withstand these treatment temperatures of 130 °C or above. In co-planar design the bottom substrate must be sufficiently heat-resistant solely. The top and bottom substrate must be sealed against each other using a glue or alternative materials can be used that can be heat-sealed (welded) without the need of additional material. However, the problem of sealing across the current lead-outs remains. All technologies that are known in packaging could potentially be applied for battery sealing.

The requirements for printed batteries substrates are almost the same for co-planar and stack design:

- Good printability
  The adhesion of the current collector paste (typically silver) and the sealing to the substrate must be very good.
- Dimensional and thermal stability
  After applying the current collectors (silver and/or carbon black layer) a thermal treatment is necessary to gain best possible conductivity. In sheet fed screen printing it is also important that the sheets do not curl too much.
- Barrier properties, sufficient leak tightness
  The electrolyte may not dry out (stop of ion transport is the death of the battery). Plastic foils comprising mono material often do not have sufficient barrier properties, therefore, compound foils comprising plastic and e.g., aluminium layer are preferable but have other drawbacks.
- Sealing/welding ability
- Sufficient mechanical stability while sufficient bendability
- Opaqueness
  Although transparency is not disadvantageous per se, the material should rather be opaque than transparent (the battery materials do not have nice looking colours and tend to tarnish during discharge). In the development phase, however, the possibility to observe tarnishing could be helpful in identifying problematic areas.
- Price
  In the moment of development of printed batteries in the lab, the price of the substrate plays a minor part. However, when it comes to mass production the price of the substrate becomes one of the most important factors because basic cost estimations reveal that the substrate has a major portion of the battery cost.

- "green" composition
  Recyclability would be very advantageous. A compound comprising different classes of materials such as plastic and metal is more difficult to recycle.

In recent years, investigations into printed batteries have mostly used standard PET, but other materials have also been tried. However, there are other promising candidates. Tables 1 and 2 list the choice of different substrates that have been investigated here. Table 1 lists the mono material foils and Table 2 the compound materials. PP stands for polypropylene, PE for polyethylene and TPU is thermoplastic polyurethane. BO means biaxial oriented.

Table 1: Mono material foils (monolayer)

Name	Description	Thickness [µm]	Pre-treatment at manufacturer	Orientation
PET Type D	BOPET	75	-	Biaxial
PET Type O	BOPET	70	One sided bonding agent	Biaxial
TPU	TPU	80	-	-
PET Type M 721	BOPET	50	One sided bonding agent	Biaxial
PET Type M 316	BOPET	20	One sided bonding agent	Biaxial
PET Type H	BOPET	50	-	Biaxial
BOPP Type S	BOPP	40	-	Biaxial
UPP	PP	40	One sided corona treatment	-

Table 2: Compound foils (multilayer)

Name	Description of compound layers	Thickness [µm]
PET/Al/PET	12 µm PET, 7 µm Aluminium, 12 µm PET	31
PET/Al/PE	12 µm PET, 9 µm Aluminium, 17 µm PE	38
PE/Pap/PE/Al/PE	36 µm PE, 81 µm Paper, 36 µm PE, 12 µm Aluminium, 36 µm PE	~200

Some of the monolayer materials have been treated by the manufacturer with a corona device or with an adhesion promoter to improve the adhesion of printing inks. This can be advantageous but also counterproductive. At the LOPEC 2019 fair where devices incorporating a printed battery were showcased on the so called demoline the top and bottom substrates, which were glued together with a printable adhesive delaminated after a few days. It could be shown that substrates without such an adhesion promoter did not suffer from this problem. The PET materials are all clear except for type H, which is slightly milky. Table 3 shows some other material properties that are based on observations. The welding property can be tested with a simple device shown in Figure 2.

Figure 2: Bar welding apparatus Rotek

Table 3: Material properties (with own observations)

Foil/Material	Welding possible	Printability (with pre-treatment)	Thermal stability
PET	no	good	good
TPU	yes	poor to medium	good
PP	yes	poor to medium	good
BOPP	our sample: no	poor to medium	good
PEHD	yes	poor to medium	medium
PET/Al/PET	no	good	good
PET/Al/PE	yes (on PE side)	on PET side good	poor
PE/Al/PE	yes	poor to medium	poor
PE/Pap/PE/Al/PE	yes	poor to medium	poor

The thermal stability property mentioned in Table 3 refers to the tendency to curl. Asymmetric compound materials tend to curl extensively during an oven treatment as can be seen in Figure 3.
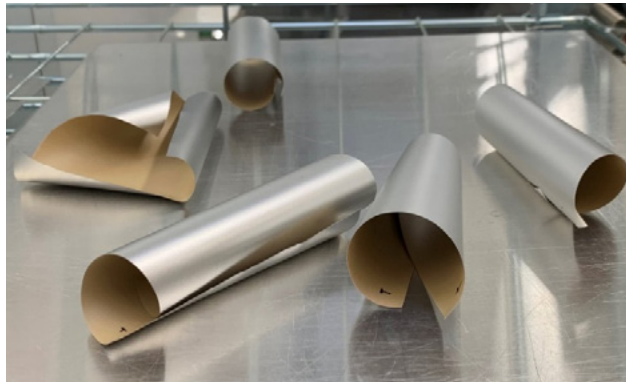
Figure 3: Curled samples after oven treatment PE/Pap/PE/Al/PE

The following mechanical properties of the candidates for substrates for printed batteries have been tested.

- Surface free energy (indicator for printability)
- Pre-shrink behaviour (dimensional stability)
- Tensile strength (modulus of elasticity)
- Bending stiffness

2.1 Surface free energy

The surface free energy was tested using a contact angle measuring device implementing the well-known OWRK method (Kaelble, 1979; Krüss, n.d.). Four test liquids were used water, glycerol, formamide and 1-bromo-naphthalene. The more test liquids are used the more accurate is the method.

2.2 Pre-shrink testing

For successive printing runs with intermediate thermal treatment, such as is necessary for silver and carbon layers, it is very important that the dimensional stability is sufficient for registration of the layers, adhesive, etc.

Thus, the materials were treated in this way:

- Mark distances of 100 mm in transverse and longitudinal direction
- Cut to 120 mm × 120 mm (6 specimen each)
- Place between two pieces of cardboard (to avoid extensive curling)
- Put in oven at 120 °C for 30 minutes.

Then the differences in length after the treatment were measured. For some of the materials only specimens of smaller dimensions were available. In these cases, 50 mm × 50 mm specimens were used with the disadvantage of lower accuracy.

2.3 Tensile strength (modulus of elasticity)

A Frank PTI tensile testing machine as shown in Figure 4 was used for the tensile strength measurements. The settings were:

- Pre tensioning with 1 N, speed: 650 mm/s, clamp spacing: 100 mm. Maximum distance 400 mm.
- The film samples were cut to a dimension of 140 mm × 15 mm, as the free clamping length is 100 mm, and the length of the clamping claws was 40 mm each. To obtain meaningful results, 10 samples of each material were tested.
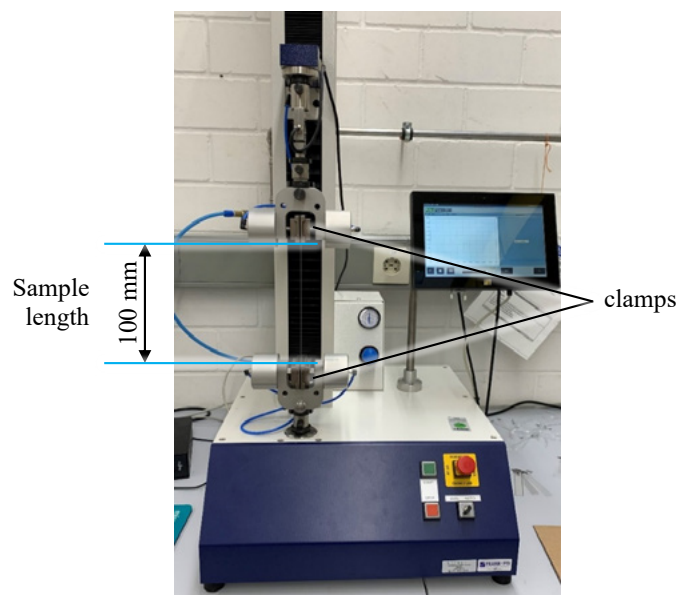
Figure 4: Frank PTI tensile testing machine

2.4 Bending stiffness

The bending stiffness is an important parameter if the battery is used for the skin patches. This investigation is carried out with fully finished batteries. Batteries of size 38 mm × 100 mm were assembled with each material. A compilation is shown in Figure 5.

Figure 5: Collection of printed batteries for bending test

Figure 6 shows the device used for the two-point bending tests and details can be seen in Figure 7.

Figure 6: Bending tester Frank PTI
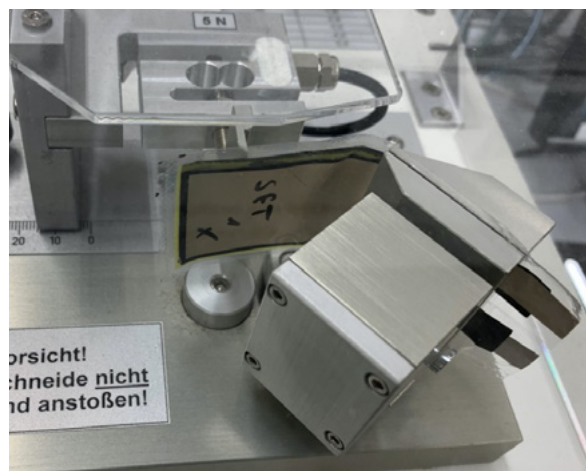
Figure 7: Sample clamped in bending tester Frank PTI (full deflection)

During the bending test, the clamp holding the sample is rotated at a defined angular velocity and during this movement the force exerted on a sensor touched by the sample is measured.

The settings were:

- Sample width: 38 mm
- Angular velocity until the initial force of 0.005 N is reached: 3°/s
- Angular velocity during measurement: 6°/s
- Maximum deflection angle: 50°
- Holding time: 5 s
- Initial distance between clamp tip and force sensor: 30 mm

The recording software draws a force-time diagram and indicates the bending stiffness and the torque (moment) needed to achieve the bending angle in Nmm.

2.5 Barrier properties

As already mentioned, the barrier properties of the substrates are very important. Numerous literature values can be found for the monomaterial films. Müller, et. al., (2011) has compiled the values in a very clearly arranged way (see Figure 8), whereas the values trace back to Langowski (2008) who also has made some considerations on compounds containing aluminium but for our specific multilayer compound materials no data could be found. Thus, the water vapour transmission rates (WVTR) were measured during this investigation. The measuring principle, following ASTM F1249 (American Society for Testing and Materials, 2013) of our lab device Systech is shown in Figure 9.
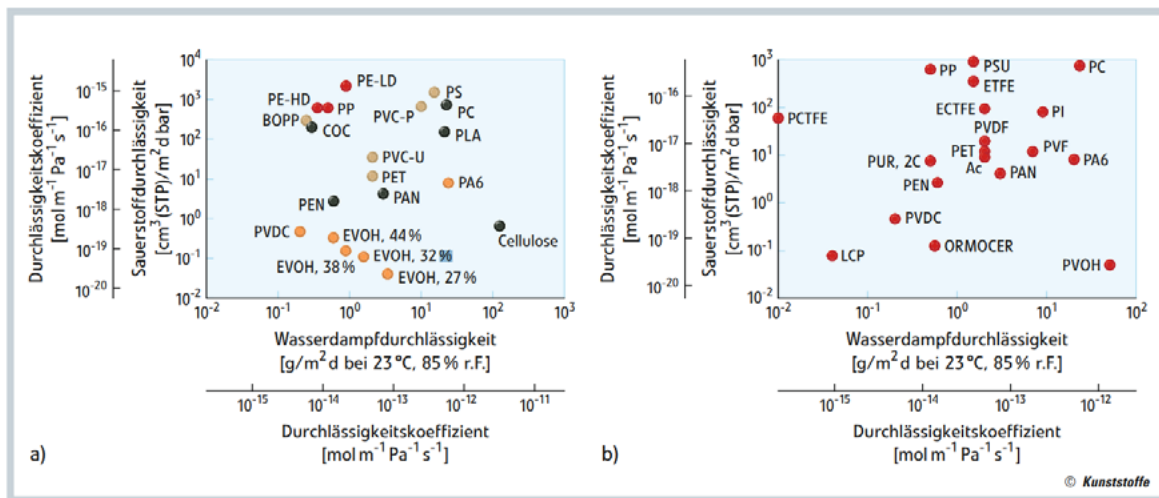
Figure 8: Oxygen and water vapour transmission rates;
materials used for food packaging (a); technical polymers (b)
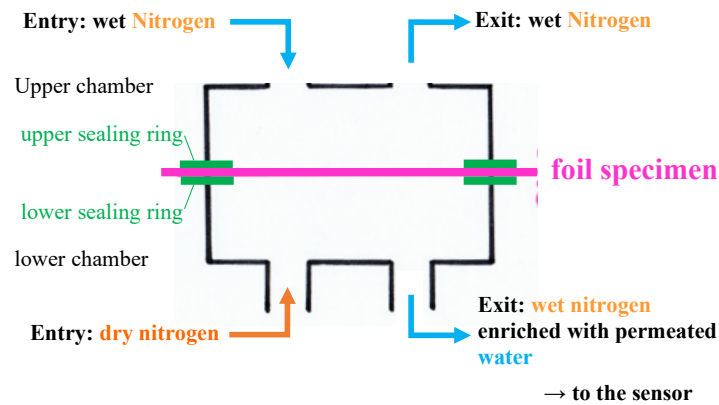
Figure 9: Principle of water vapour transmission measurement

Since the WVTR is depending on the thickness of the samples the results are normalized to 100 μm thickness after the measurement.

3. Results

3.1 Surface free energy

The reults obtained with the contact angle measurement and the OWRK-method are shown in Table 4 and in graphical representation in Figure 10.

Table 4: Contact angles and surface free energy of tested substrates

Material	Contact angle test liquids [°]				Surface free energy [mN/m]		
	Water	Glycerol	Formamide	1-bromo-napht-halene	total	dispersive	polar
PET Type D	77.7	64.2	51.1	16.3	44.39	39.43	4.96
PET Type O	76.9	65.3	50.5	2.9	45.19	40.42	4.77
TPU	76.5	89.6	61.5	21.0	35.99	31.89	4.11
PE/Pap/PE/Al/PE	73.7	80.4	72.1	40.0	32.21	24.09	8.12
PET Type M 7	71.3	63.0	45.4	26.8	44.24	36.25	7.99
PET Type M 3	73.4	61.1	47.3	16.8	45.59	38.91	6.68
BOPP Type H	73.1	65.2	59.0	3.2	47.47	41.43	6.04
OPP SFT RN	93.3	73.5	76.2	39.9	33.11	31.03	2.08
UPP	96.3	86.8	82.3	30.7	32.15	31.44	0.71
PET/Al/PET	69.8	66.5	35.6	27.1	45.44	37.51	7.93
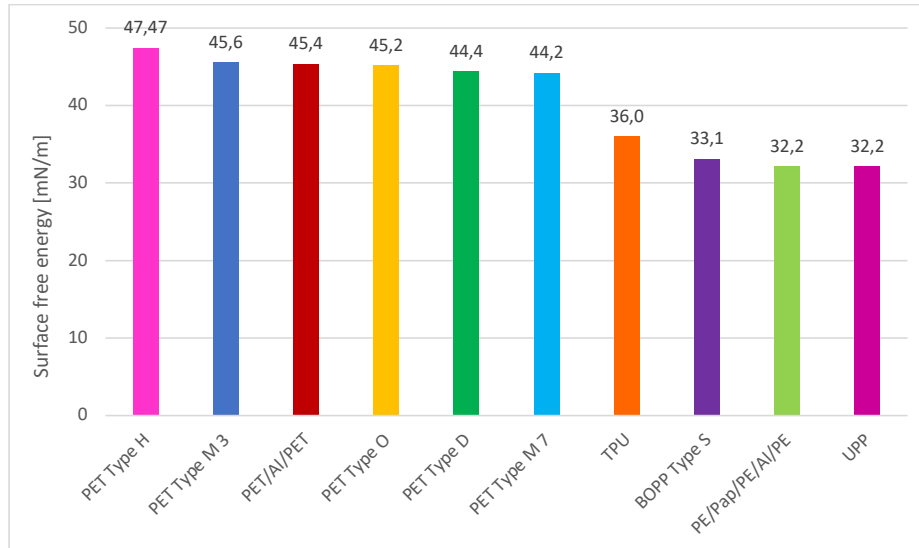
Figure 10: Surface free energy of tested substrates

In our lab we usually apply a pre-treatment of the substrates before the printing process. The standard treatment is a plasma treatment under ambient atmosphere with a device from the company Plasmatreat. Figure 11 impressively shows the effect of the treatment, but it can also be seen that the increase in surface free energy declines over time.
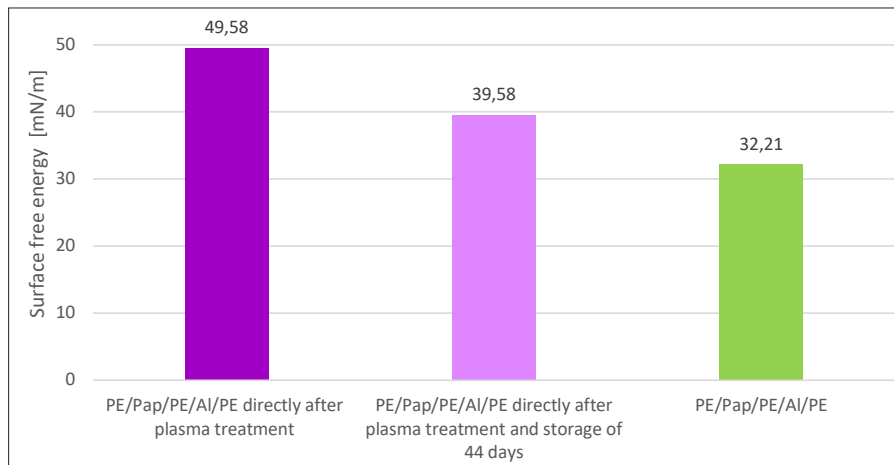
Figure 11: Surface free energy of the PE/Pap/PE/Al/PE substrate

3.2 Pre-shrink behaviour (dimensional stability)

With the method described in chapter 2 we measured the shrinkage during a thermal pre-treatment. The results are shown in Figure 12.

From Figure 12 it is clearly visible that the compound foils perform much better than the mono-layer foils. At least with the accuracy that our measurements provided, they showed zero shrink. PET is the second best choice, and the other polymers are worse.
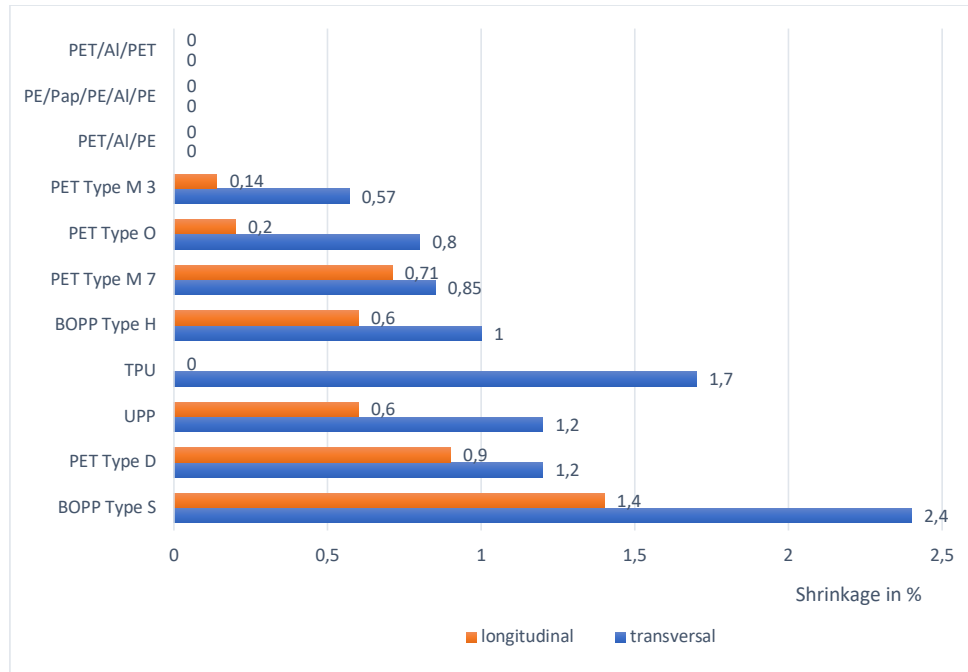
Figure 12: Pre-shrinking of materials

3.3 Tensile strength

The results obtained with the tensile testing device (Figure 4) are plotted in the diagram in Figure 13. The results are comparable to values found in the literature (Omnexus, 2021).
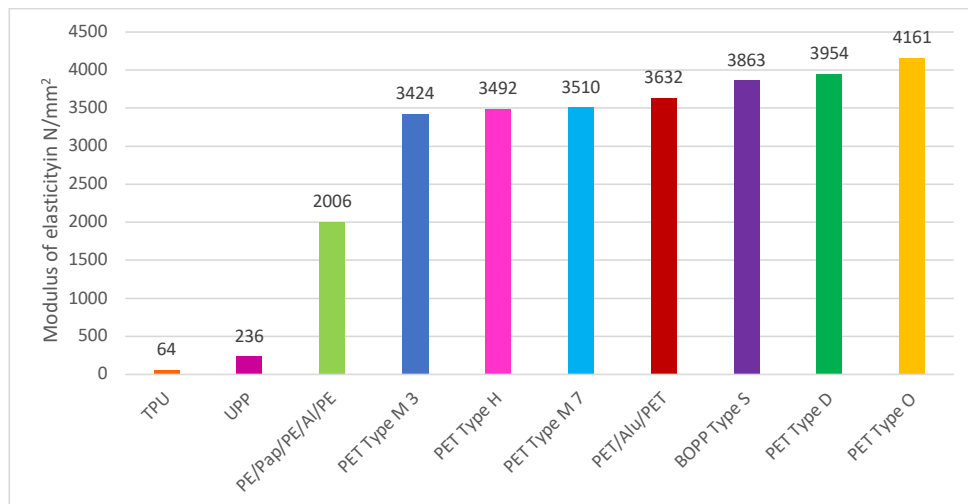
Figure 13: Modulus of elasticity of the tested substrates

In comparison to PET and BOPP the UPP and the TPU have much smaller tensile strengths. However, the measurement bears some difficulties and uncertainties. The Young's modulus of elasticity is the slope of the straight line in the beginning of the stress-strain curve. But as can be seen in the curve of TPU (Figure 14) there is barely a straight line, as TPU can be very strongly plastically deformed. However, the software of the measurement device reveals values derived at the very beginning of the curve.
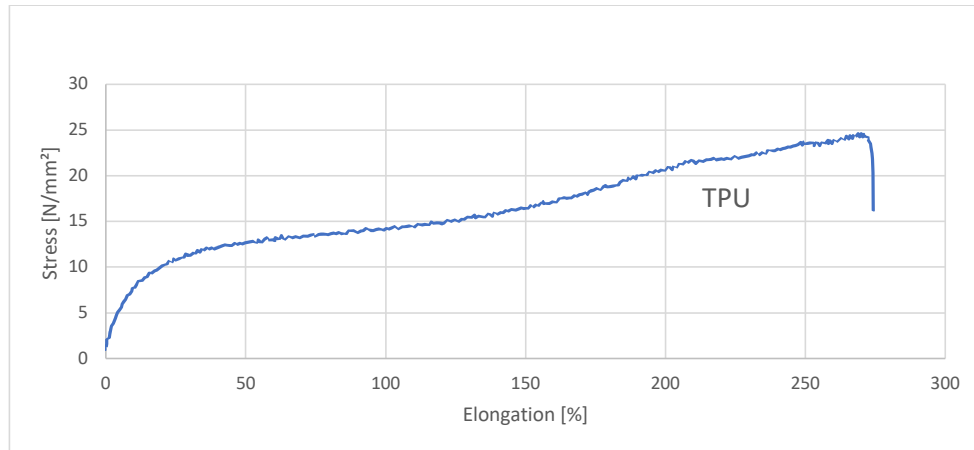
Figure 14: Stress-strain diagram for TPU

3.4 Bending stiffness

With some of the materials it was not possible to build a complete printed battery in this investigation. Therefore, in the results Table 5 for the bending stiffness values, only the materials for which a battery could be built are listed. It should be noted that there is quite a large scatter in the range of ± 5 % as the measurements were made on the assembled batteries and there is a large influence of the adhesive application. Figure 15 shows the corresponding diagram.

Table 5: Bending stiffness and bending moment

	Bending stiffness in Nmm	Bending moment in Nmm
PET Type D	4.6	15.4
PET Type O	3.8	12.9
PET Type M 7	2.3	7.6
PET Type M 3	0.7	2.5
PET Type H	2.1	6.9
BOPP Type S	1.3	4.3
PET/Al/PET	1.4	4.8
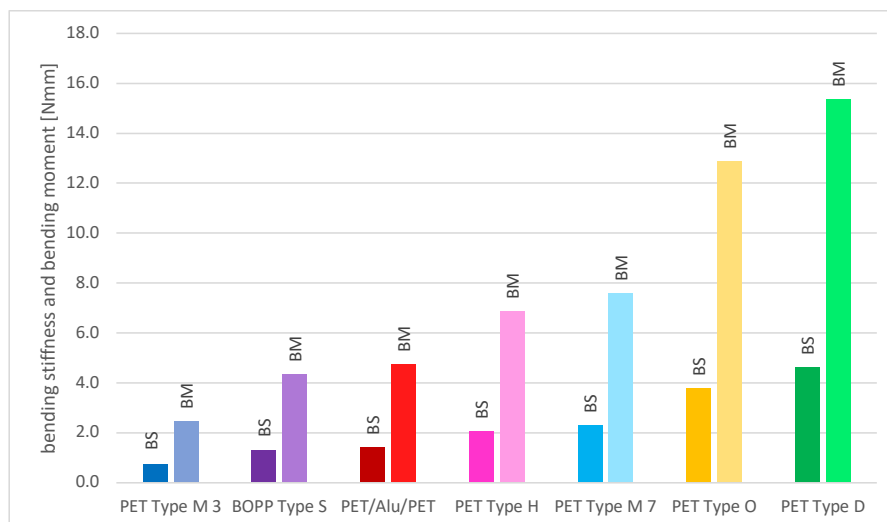
Figure 15: BS = bending stiffness and BM = bending moment

The "survivability" of the batteries was tested by checking the open circuit voltage (OCV) before and after the bend test measurements. For freshly assembled printed zinc/carbon batteries with zinc chloride as electrolyte, the OCV is slightly less than 1.7 V. After the bend test, the OCV was typically only about 0.01 V to 0.02 V lower. About 5 % did not "survive" the test by showing no more OCV or a very large voltage drop.

3.5 Water vapour transmission rates

The water vapour transmission rates (WVTR) values according to the measurements with the Systech device normalized to 100 μm thickness are shown in Figure 16.
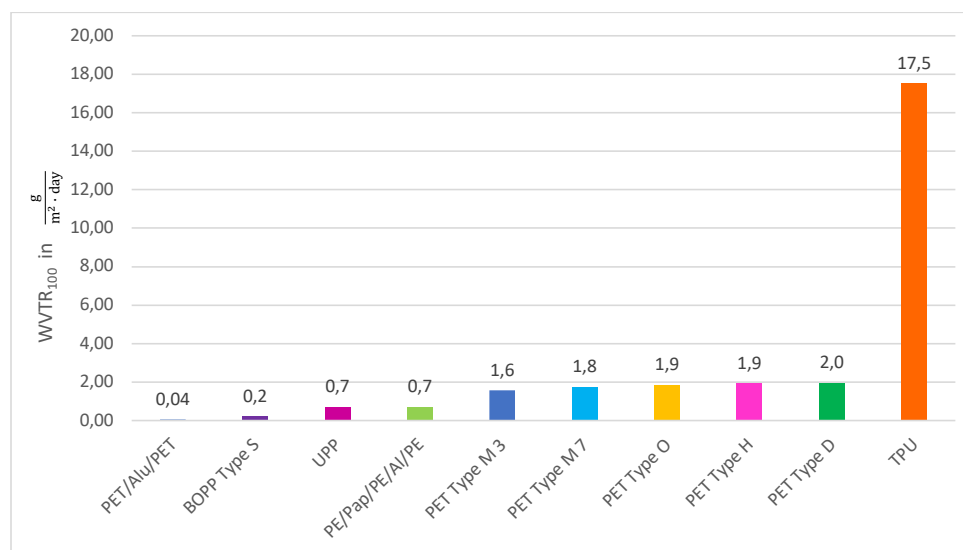
Figure 16: Water vapour transmission rates of different substrates

3.6 Water vapour transmission rates including current collector layers

From the previous results it can be seen that the TPU has very poor barrier properties in comparison to the other substrates. However, the TPU has the big advantage that it can snuggle up very well to curved parts of the skin for the wearable skin patch applications. Therefore, it was investigated how the current collector layers improve the barrier properties. Figure 17 shows the samples with the printed layers. The WVTR results are shown in Table 6.

It can be estimated that the current collector layers improve the barrier properties against water vapour in a way that batteries can be used for a sufficient long period also on this substrate.

Figure 17: TPU substrate with printed current collectors on top; left: silver, right: silver plus carbon

Table 6: Water vapour transmission rates of TPU incl. current collector layer

Substrate	$WVTR_{100}$
TPU	17.52
TPU incl. silver layer	0.28
TPU incl. Silver plus carbon layer	0.25

3.7 Weight decreases of final assembled batteries

A quite simple method to prove the barrier properties is just to measure the loss of weight of the freshly assembled battery over time. The weight of the assembled batteries was measured directly after the assembly and six days later. Under the assumption that the loss is linear, the values given in Figure 18 were calculated by normalizing to the unit .
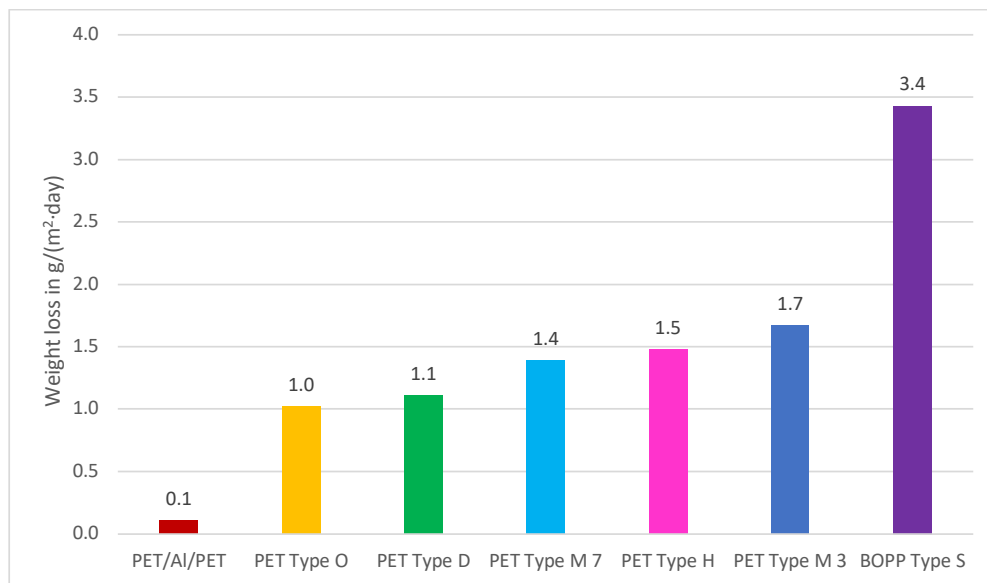
Figure 18: Weight loss over 6 days

4. Conclusion

By comparing the different substrates, it could be found in all tests that the PET/Al/PET performs the best. Although it is very thin, which is very positive for easy bendability for wearable applications, it has excellent barrier properties. Printing the current collector layers on top of the substrates increase the barrier effect. This will help not only in the case of TPU but for all candidates.

Summarizing it can be estimated that if substrates such as the PET/Al/PET are used, in printed batteries sufficient humidity can be preserved during the lifetime of the battery application.

References

American Society for Testing and Materials, 2013. *ASTM F1249-13 Standard test method for water vapor transmission rate through plastic film and sheeting using a modulated infrared sensor*. West Conshohocken, PA, USA: ASTM.

BEWELL, 2020. *Wearable sensors and actuators*. [online] Available at: < https://h2020bewell.eu> [Accessed July 2021].

Dums, F., Merz, M., Ulricj, T. and Gerlicher, A., 2021. *OxiFlexIT*. [online] Available at: < https://www.hdm-stuttgart.de/stage/projekt_detail/projekt_details?projekt_ID=3496> [Accessed July 2021].

Elmeric, n.d. *Electronics meets printing*. [video online] Available at: <www.elmeric.de> [Accessed July 2021].

Huebner, G. and Krebs, M., 2015. Printed, flexible thin film batteries and other storage devices. In: S. Logothetidis, ed. *Handbook of flexible organic electronics: materials, manufacturing and applications.* Oxford, Amsterdam: Woodhead Publishing, pp. 429–447, Ch. 18.

Hübner, G., Krebs M., Rassek, P. and Willfahrt, A., 2015. Printed batteries, overview, status, recent developments, future perspectives. In: P. Gane, ed. *Advances in Printing and Media Technology: Proceedings of the 42nd International Research Conference of iarigai*. Helsinki, Finland, September 2015. Darmstadt, Germany: iarigai, pp. 183–193.

Kaelble, D.H., 1970. Dispersion-polar surface tension properties of organic solids. *Journal of Adhesion*, 2(2), pp. 66–81. https://doi.org/10.1080/0021846708544582.

Krüss, n.d. *Methode nach Owens, Wendt, Rabel und Kaelble (OWRK)*. [online] Available at: <https://www.kruss-scientific.com/de-DE/know-how/glossar/methode-nach-owens-wendt-rabel-und-kaelble-owrk> [Accessed July 2021].

Langowski, H.-C., 2008. Permeation of gases and condensable substances through monolayer and multilayer structures. In: O.G. Piringer and A.L. Baner, eds. *Plastic packaging: interactions with food and pharmaceuticals*. 2nd ed. Weinheim, Germany: Wiley-VCH. https://doi.org/10.1002/9783527621422.ch10.

Müller, K., Botos, J., Bastian, M., Heidemeyer, P. and Hochrein, T., 2011. Schneller zum Ergebnis: Permeationsmessung von Folien. *Kunststoffe*, 101(7), pp. 75–80.

Omnexus, 2021. *Young's modulus*. [online] Available at: <https://omnexus.specialchem.com/polymer-properties/properties/young-modulus> [Accessed July 2021].

G. Hübner and M. Krebes: Spectral dependence of light scattering in human skin detected with a screen printed device for blood oximetry

2B

Spectral dependence of light scattering in human skin detected with a screen printed device for blood oximetry

Gunter Hübner and Michael Krebes

Innovative Applications of the Printing Technologies (IAD), Stuttgart Media University, Nobelstr. 10, 70569 Stuttgart, Germany
E-mails: huebner@hdm-stuttgart.de, krebes@hdm-stuttgart.de

Short abstract

In the research project OxiFlexIT that is governmentally funded, functionalities with printed components are produced and investigated. An autarkic sensor and a printed battery are on the same substrate. The sensor containing classical LEDs and photodetectors is used to measure the oxygen content of blood in larger areas on the human skin. The measurement is non-invasive. Tests have been carried out how the readings of the sensor will look like. They can be compared with existing theories on light scattering e.g. in paper. Photo current readings depending on the colour of the substrate (skin imitation) and underlying backings are analysed.

Keywords: screen-printing, printed functionalities, blood oximetry, light scattering

1. Introduction

The measurement of the blood oxygen content often called "blood oximetry" basically is done by detecting the colour change of the blood. In simple words the blood saturated with oxygen is red and the blood lacking oxygen is blue. In the project called OxiFlexIT funded by the German Ministry of Education and Research (BMBF) in co-operation with companies such as VARTA Microbattery GmbH, Lohmann GmbH, FM Siebdruck, Aspro GmbH, and the university of Heidelberg (faculty of medicine in Mannheim) a measurement system is investigated that is used as a flexible skin patch, which contains a printed battery and necessary electronics. The printed batteries will be produced as thin as possible to be flexible. The basic technique used for the printed batteries has been described earlier (Huebner and Krebs, 2015; Hübner, et al., 2015). The electronic circuits comprise of a broadcasting system to transfer the readings to a remote station where the treating doctor can monitor the status of the patient, perform statistics, or will be alarmed in critical situation. The sensor assembled and investigated here has two major components, first the light sources, which are LEDs in different colours and second photodetectors in an array with fixed distance to the light source. The intention is that this plaster is manufactured with very cheap but well-functioning components and due to hygienic reasons used as a single use item lasting about one day. Too much moisture and skin irritation should be avoided. The advantage of such an autarkic plaster is the exact, immovable location in comparison to already commercially available finger clamps (wire connected) or stiff (wrist-) bands.

The basic setup for these first feasibility tests is shown in Figure 1. The printed flexible strip comprises of the light source, here, a single infrared LED, only, at the left-hand side and 7 photodetectors (PDs), separated by 6 mm distance Δx each. Both, the LED and the PDs are surface mounted devices (SMDs). The conductive lines are printed with commercial silver screen printing ink.

In the second generation of the sensor there will be three LEDs, a red, a blue and an infrared one. The measured intensity of the red and blue will vary according to the oxygen content whereas the infrared one should not be affected and serves as reference.

Figure 1: Printed flexible strip on PET with mounted SMDs for testing purposes

Figure 2 shows the schematic view from the side if the strip is placed on the skin. The black areas indicate that there must be a cover that shades the setup from ambient light, and only four PDs are drawn to exemplify instead of seven.
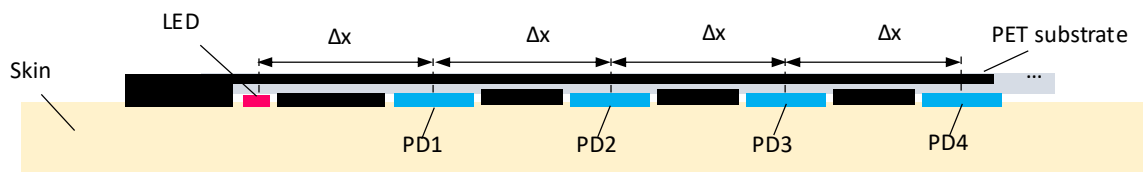
Figure 2: Printed flexible strip on PET with mounted SMDs for testing purposes

The principle of the measurement of the halo effect is depicted in Figure 3. The intensity of the impinged light decreases with the distance from the impingement point.
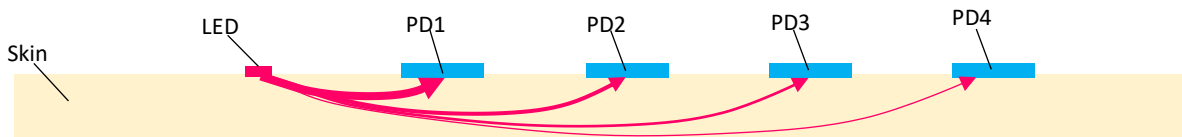
Figure 3: Light intensity decreases with distance from impingement point

Helfmann, et. al. described thoroughly the principle of these measurements (Helfmann, n.d.; Helfmann Gersonde and Netz, 2017).

2. Materials and methods

The measurements achieved with this printed strip and the schematic process shown in Figure 4 revealed a behaviour as principally expected.
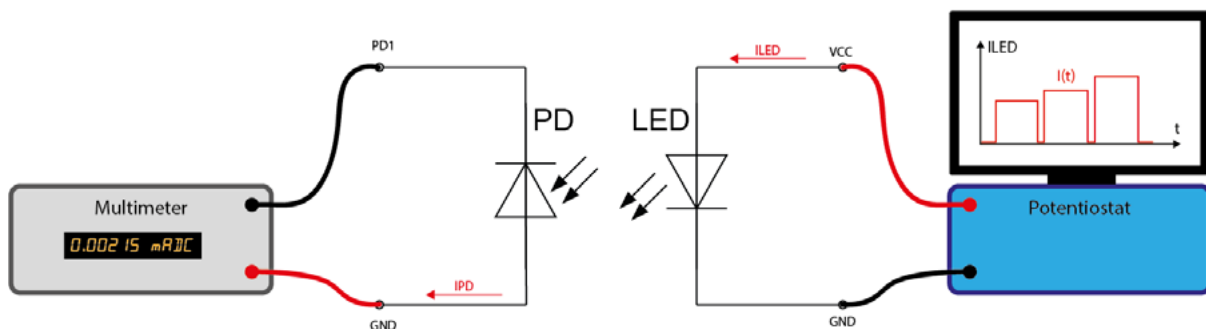
Figure 4: Driving the LED with a precise current level and measuring photo current with a multimeter

As can be seen in Figure 5 the photo current decreases with distance to the impingement point. In this case it was measured with the infrared LED.
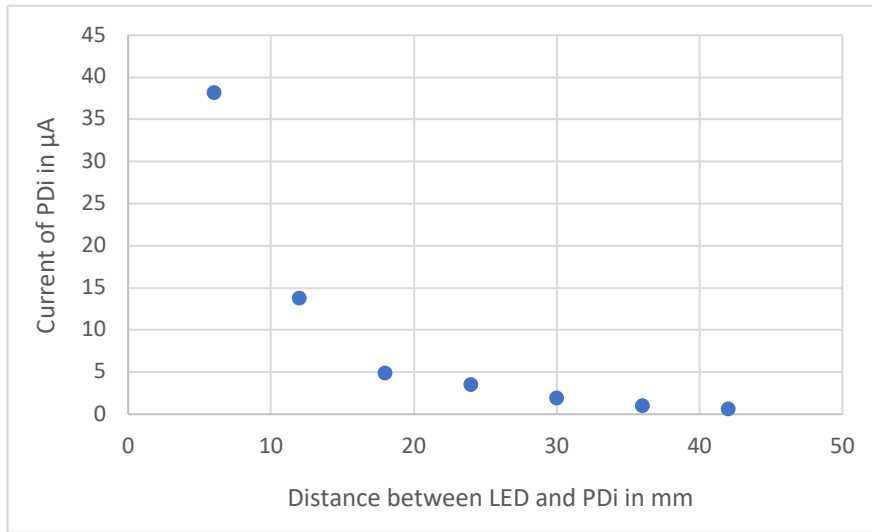
Figure5: Measured current (representing light intensity) vs. distance from impingement point

The seven PDs show a response to the light with a photo current that is in the range of µA.

In finding an algorithm for evaluating the measured results the question arises which mathematical dependence can be found that matches best with the measured values and does this correspond to the theory of the light travelling through the substrate (here the skin).

The basic interactions light undergoes during travelling through a matter are absorption and scattering. For a constant material medium, absorption remains the same according to that medium, and so predictable according to the Beer-Lambert decay expression, but light scattering can be a sensitive measure of changes occurring in respect to particles within the medium, either stationary or in motion.

Basic considerations on scattering can be found in several publications (e.g. Brar and Verma, 2011; Hahn, 2009), which summarize previous work (Bohren and Huffman, 1998; Stover, 2012). It is stated that the theoretical models of light scattering can be divided into three domains based on a dimensionless size parameter, α which is defined as:

$$\alpha = \frac{\pi D_p}{\lambda} \tag{1}$$

where πD_p is the circumference of a particle and λ is the wavelength of incident radiation. Based on the value of α, these domains are:

α ≪ 1:   Rayleigh scattering (small particle compared to wavelength of light);
α ≈ 1:   Mie scattering (particle about the same size as wavelength of light, valid only for spheres);
α ≫ 1:   geometric scattering (particle much larger than wavelength of light).

In our case the wavelength of the impinging radiation is well known (it is not the wavelength in vacuum or air but in the matter); however, it is very difficult to judge the size and shape of the involved particles.

In our industry some decades ago a lot of investigations were going on in order to find out about the light scattering in paper (e.g. Berg, 1997). The goal was to establish theories for light trapping in raster prints. At this time mainly for comparison of visual dot gain between AM and FM screening.

For paper, the order of magnitude is quite clear. The fibres are >>1µm, thus with the wavelength of visual light of about 0.4 to 0.7µm, $\alpha \gg 1$. In this case we therefore must deal mainly with geometric scattering.

The balance between forward and backward scattering was investigated already in the 1930s by Kubelka and Munk (1931). Berg (1997), and Ness and Göttsching (2000a; 2000b) developed scattering theories based on the Kubelka-Munk model and tried to prove them experimentally (Figure 6).
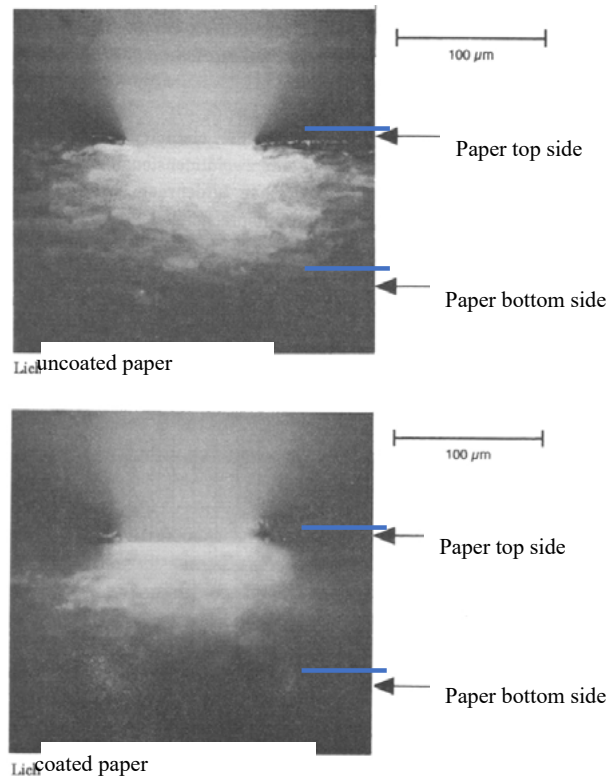
Figure 6: Photos of light scattering in uncoated and coated paper cross section, taken from Berg (1997)

Figures 7 and 8 show the findings of Ness and Göttsching investigating how the scattering function *s*(*r*) looks like in dependence of *r* the distance from the light impingement point. It is not the intention to discuss the theories of these authors here, but just to show the measurement results.
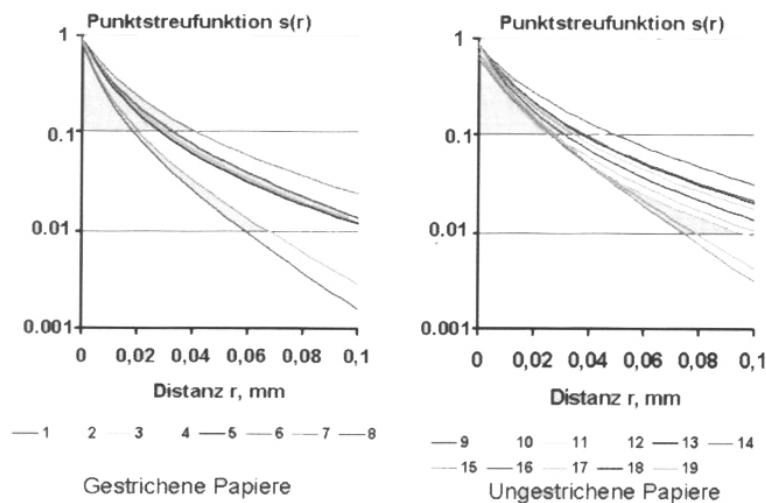
Figure 7: Measured normalized light scattering function in coated (left) and uncoated (right) paper, taken from Ness and Göttsching (2001a)
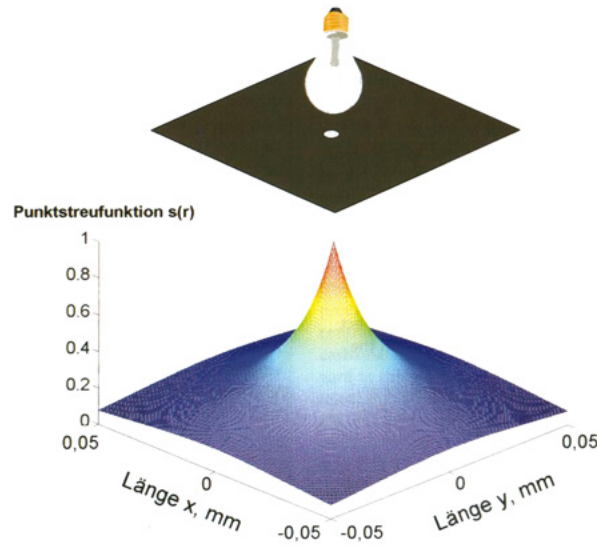
Figure 8: 3D-visualization of normalized light scattering function, taken from Ness and Göttsching (2001b)

If the wavelength of the light is approximately equal to the size of the particles that build the matter or are within it, then the theory established by Gustav Mie can be considered. The theory ranges back to the Maxwell equations and is for instance well described by Tweer (2002). He states that solutions of the established differential equations are the Bessel functions $j_n(\rho)$ as shown in Figure 9. Where ρ is the radius from the light impingement. Especially the curve for $n = 0$ looks reasonable for describing the declining of the light in the matter. However, negative values make no sense.
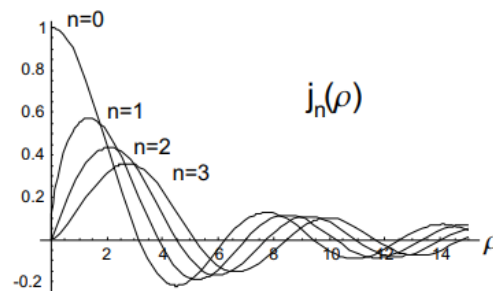
Figure 9: Spherical Bessel functions (Tweer, 2002)

For the application investigated in this research project, the measurement of light distribution in dermal tissue, it is not quite clear what can be assumed for the involved particle sizes. An obvious assumption is that there is a mixture of homogeneous bulk material (size of large molecules) with some particles and obstacles in the range of several micrometres. Thus, Helfmann, Gersonde and Netz (2017) according to Figure 10 distinguishes several types of light paths for travelling through this dermal tissue.
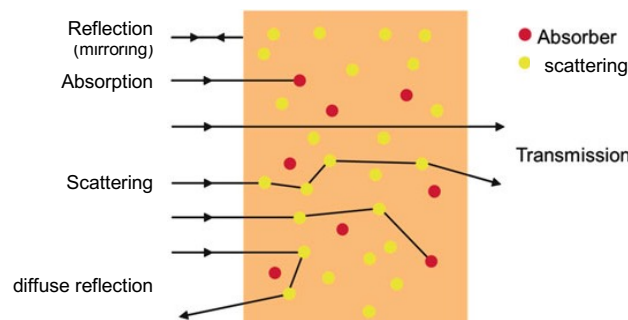
Figure 10: Possible light passes through dermal tissue, adapted from Helfmann (n.d.)

If we had pure isotropic homogenous material and simple transmission in one direction the intensity could be easily calculated by the Beer-Lambert law:

$$T = e^{-\mu r} \hspace{4cm} [2]$$

This would be a simple decay curve where T is the transmission rate, μ the absorption coefficient and r the radius from the light impingement. On the other hand, if there is no absorption and no obstacles the intensity should follow the power law:

$$I \sim \frac{1}{r^2} \hspace{4cm} [3]$$

But since there are so many influencing factors a full (complex) model was introduced by Chandrasekhar (1960). However, this model has no closed analytical solution. Therefore, Helfmann (n.d.) investigates the light scattering in dermal tissue experimentally with a setup using glass fibres placed in a circular shape around the light impingement point (see Figures 11 and 12).
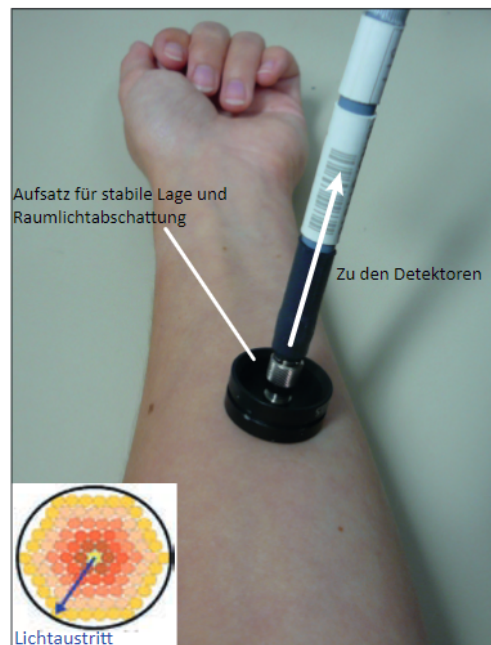
Figure 11: Glass fibre measuring setup for reflectance spectroscopy by Helfmann, taken from Helfmann (n.d.)

With this device he was able to detect the decline in light intensity and additionally found a dependence on the wavelength. There is a higher absorption rate with smaller wavelengths.
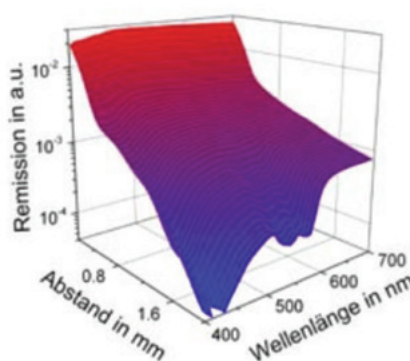
Figure 12: Reflectance spectroscopy on skin, taken from Helfmann (n.d.)

3. Results

In the development of the measuring device to be used in our project there were several steps. The very first measurement setup was constructed with one fixed location of the LED. The LEDs were sequentially exchanged, infrared (880 nm type Kingbright APT2012SF4C-PRV), red (660 nm type Lite ON LTST-C190CKT), blue (460 nm type Osram LD MVSG-JGLH-46-1) whereas the photodetector (PD) was manually moved away from the LEDs in steps of 5mm each.

Two photodetectors were used:
    PD1: Vishay VEMD8080
    PD2: Vishay VBP104S

It turned out that these two types have quite similar properties. Thus, later only PD2 was used.

The LED and the PD were covered with an 80 mm thick white foamed plastic. The results with the two different types of PDs are shown in Figures 13 and 14. The measurements were done twice, and the curves represent the average of that. Each PD has a dark current in the range of 0.1 µA. This value was measured and deduced from the photo current in the LED "on"-state. Since the photocurrent response from the blue LED is much higher than the red or infrared, it makes sense to normalise in a way that the maximum reading was set to 1. Figure 15 shows this result for PD2.
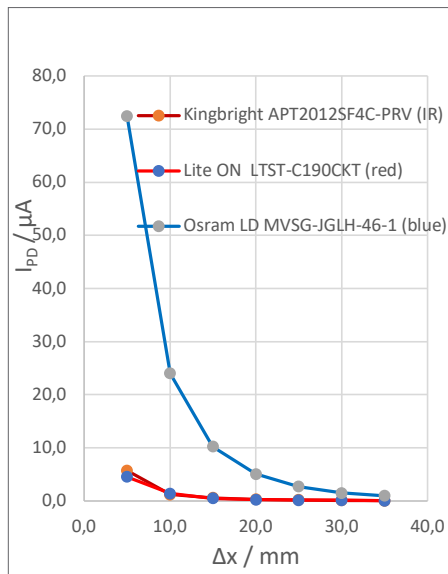
Figure 13: PD1 Photodetector current   Figure 14: PD2 Photodetector current
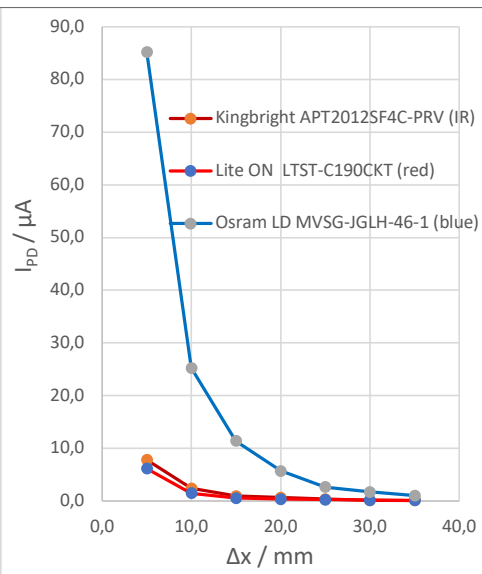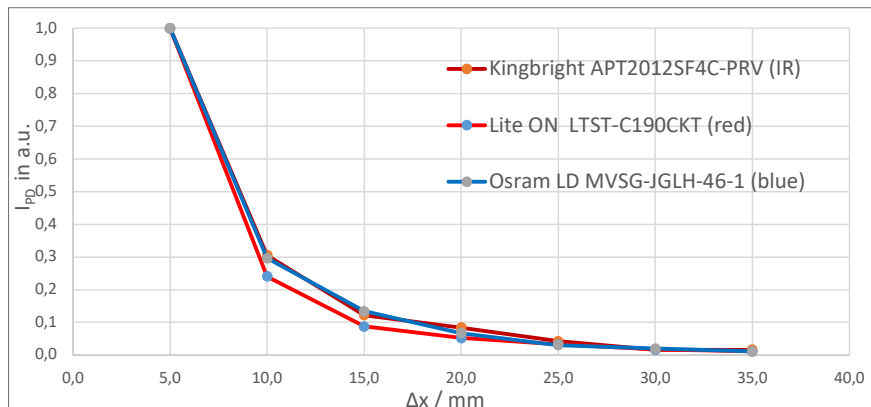
Figure 15: Normalized photodetector current for PD2

The curves in Figure 15 show quite similar behaviour for each different LED colour. Similar curves were found for PD1 (not shown). It can be assumed that deviations are caused by measuring uncertainties. In Figure16 two trend curves were fitted to the measurement curve for the IR LED using the capabilities of the Microsoft Excel software. It can be seen that the power-law gives a better fit than the exponential curve. The coefficient of correlation 0.97 is quite good but deviations in the range from 5 to 10 mm are clearly visible.
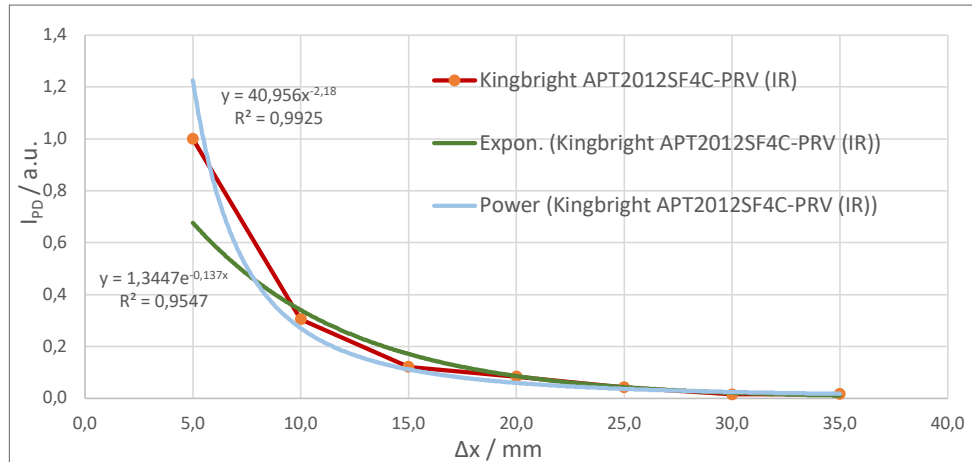
Figure 16: Trend curve fits for PD2 (normalized current vs. distance) covered with white plastic foam

After these preliminary investigations, the strip according to Figure 1 was used. Both PD types were tested in the strip with similar results. Figure 5 already showed the result with the PD2 type VBP104S. For these measurements, the white plastic foam was replaced by a skin imitation from URGO medical. The greasy skin imitation has a thickness of about 15 mm. The setup is shown in Figure 17.
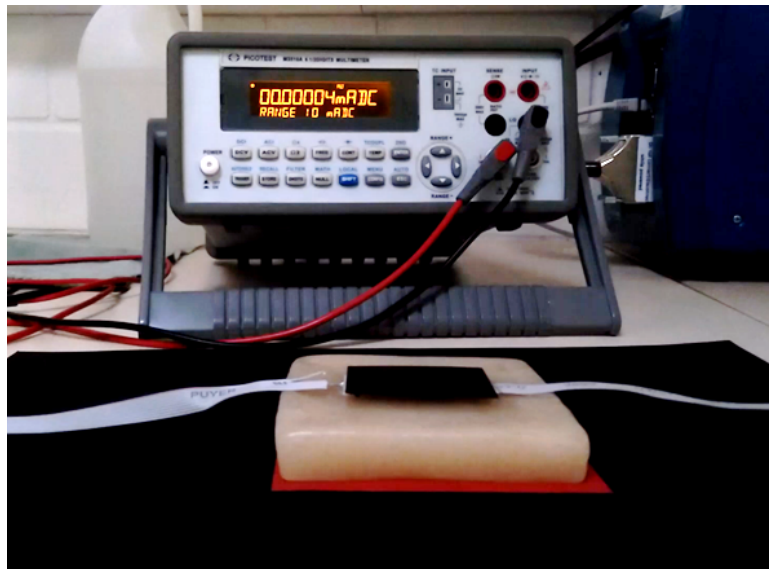
Figure 17: Measuring on skin imitation

Trend curve fits were again applied to try to match the resulting readings. As can be seen in Figure 18, although the coefficients of correlation are quite good for both, the exponential, and the power-law the functions cannot reflect very well the first 15 mm.

The chart shows trend curve fits with the following equations:

$$y = 1962.3x^{-2.076}$$
$$R^2 = 0.9849$$

$$y = 52.384e^{-0.109x}$$
$$R^2 = 0.9648$$
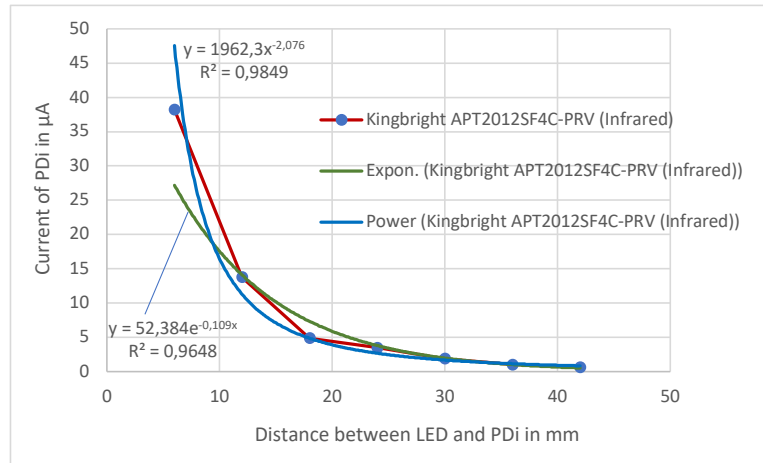
Figure 18: Trend curve fits for PD2 photodetector current on skin imitation

In another setup with the PDs closer to each other, but not closer to the light impingement than 5 mm, measurements were carried out with a coloured sheet of paper underneath the skin imitation (see Figure 17). Since the skin imitation is a kind of translucent material, the effect of the underlayer must be considered. Different power levels of the LED driver current (power level setting 1 to 3) were also tried out. The effect of different power levels (results in brighter light) is shown in Figure 19.
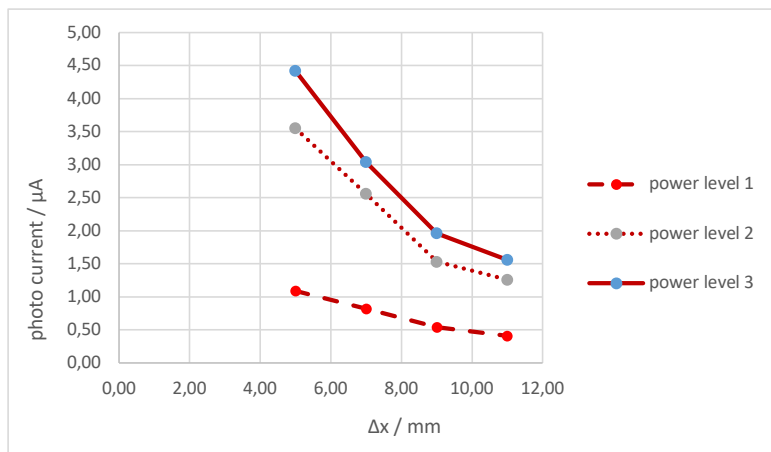
Figure 19: PD2 photo current at different power levels; red LED with white paper underneath
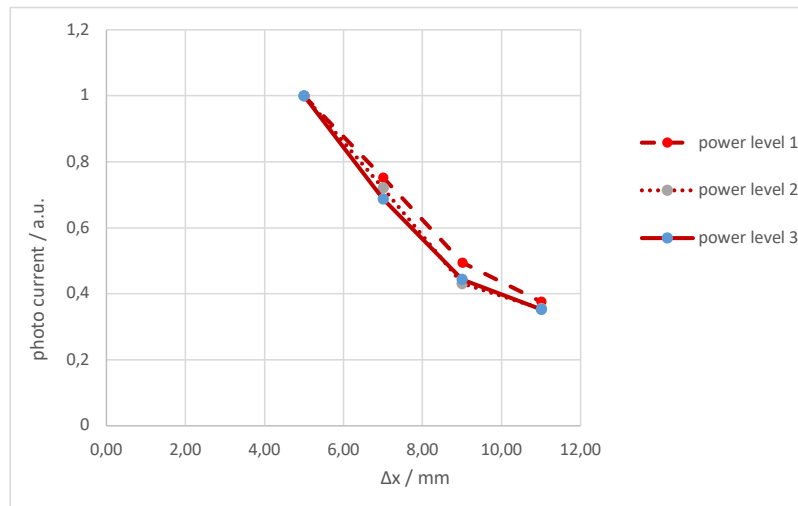
Figure 20: PD2 normalised photo current at different power levels; red LED with white paper underneath

It can be clearly seen that even after 11 mm the light is still quite intense. After normalisation (the maximum reading again set to 1) it is obvious that the declining slope looks similar for all power levels (see Figure 20). In tests with volunteering persons, it turned out very quickly that due to the light – and thus heat – insulating coverage the LEDs cannot be switched on for a longer period. The risk of overheating and burning of the skin is high.

Quite surprising is that even with a thickness of about 15 mm the light passes easily through the skin imitation. The influence of the underlying coloured paper sheets is shown in Figure 21. They have a significant influence on the reading. The readings were taken in 5 mm distance from the light impingement point and at the maximum power (brightness) level.
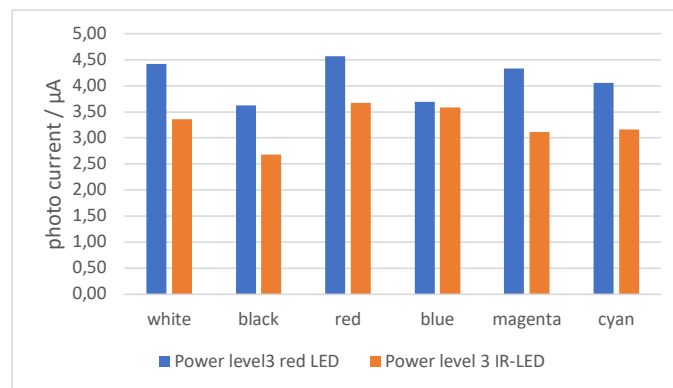
Figure 21: Photo current at 5 mm distance depending on the colour of underlying backing paper

In a momentarily last step, an attempt was made to eliminate the influence of the underlying backing. The setup is shown in Figure 22 where a black cylinder covered with a black passe-partout is used on top of the skin imitation. A weight is put on top to stabilize the setup.

Figure 22: Measurement on a "black hole" to avoid influence of underlaying backing

In Figure 23 the resulting photocurrent generated with the red LED at three different power levels is shown. It is quite remarkable that the values are in an order which could be regarded as almost linear.
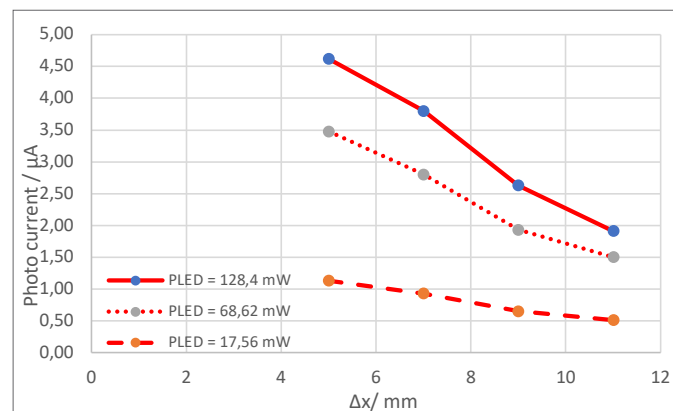
Figure 23: Photo current generated by red LED with different power levels on "black hole"-setup

52

It seems that we are already at the tail of the curves detected with other setups where the deviation is getting so small that any curve can be fitted onto the readings. In order to get more information, the PDs must be placed closer to the point of light impingement which will be done in the further investigations. Measurements on real human skin might also reveal completely different behaviour since at distances of a few millimetres other light absorbing obstacles e.g. bones must be expected to impinge on the results.

4. Conclusion

There are significant differences of the absorption characteristics depending on the wavelength of the impinged light.

The results of the measurements with the printed flexible device (Figure 1) providing an important basis for determining changes in blood oxygen saturation in deep tissue layers.

It is remarkable how far the light is being transported through the skin. It could be shown that the light travels about 50 mm through the skin.

References

Berg, F., 1997. *Isotrope Lichtstreuung in Papier: neue Überlegungen zur Kubelka-Munk-Theorie*. Doctoral thesis. Technische Universität Darmstadt.

Bohren, C.F. and Huffman, D.R., 1998. *Absorption and scattering of light by small particles.* New York, NY, USA: John Wiley & Sons.

Brar, S.K. and Verma, M., 2011. Measurement of nanoparticles by light-scattering techniques. *Trends in Analytical Chemistry*, 30(1), pp. 4–17. https://doi.org/10.1016/j.trac.2010.08.008.

Chandrasekhar, S., 1960. *Radiative transfer*. New York, NY, USA: Dover Publications.

Hahn, D.W., 2009. *Light Scattering Theory.* [pdf] University of Florida. Available at: <http://plaza.ufl.edu/dwhahn/Rayleigh%20and%20Mie%20Light%20Scattering.pdf> [Accessed 23 June 2021].

Helfmann, J., Gersonde, I. and Netz, U., 2017. Biomedizinische Optik (Biophotonik). In: R. Kramme, ed. *Medizintechnik: Verfahren – Systeme- Informationsverarbeitung*. Berlin, Germany: Springer, pp. 191–206. https://doi.org/10.1007/978-3-662-48771-6.

Helfmann, J., n.d. Ortsaufgelöste Rückstreuspektroskopie. [online] *STUDYLIB*. Available at: <https://studylibde.com/doc/2768304/ortsaufgelöste-rückstreuspektroskopie> [Accessed 23 June 2021].

Huebner, G. and Krebs, M., 2015. Printed, flexible thin film batteries and other storage devices. In: S. Logothetidis, ed. *Handbook of flexible organic electronics: materials, manufacturing and applications.* Oxford, Amsterdam: Woodhead Publishing, pp. 429–447, Ch. 18.

Hübner, G., Krebs M., Rassek, P. and Willfahrt, A., 2015. Printed batteries, overview, status, recent developments, future perspectives. In: P. Gane, ed. *Advances in Printing and Media Technology: Proceedings of the 42nd International Research Conference of iarigai*. Helsinki, Finland, September 2015. Darmstadt, Germany: iarigai, pp. 183–193.

Kubelka, P. and Munk, F. 1931. Ein Beitrag zur Optik der Farbanstriche. *Zeitschrift für technische Physik*. 12, pp. 593–601.

Ness, C. and Göttsching, L., 2000a. Neue Bildraster-Technologien und deren Anforderungen an den Bedruckstoff Papier. Teil 2: Methoden zur Beurteilung der Bildwiedergabe frequenzmodulierter Raster. *ipw. Internationale Papierwirtschaft*, 6, pp. T103–T108.

Ness, C. and Göttsching, L., 2000b. Neue Bildraster-Technologien und deren Anforderungen an den Bedruckstoff Papier. Teil 2 (Fortsetzung): Methoden zur Beurteilung der Bildwiedergabe frequenzmodulierter Raster. *ipw. Internationale Papierwirtschaft*, 7, pp. T109–T113.

Ness, C. and Göttsching, L., 2001a. Neue Bildraster-Technologien und deren Anforderungen an den Bedruckstoff Papier. Teil 3: Tonwertzunahme gedruckter Rasterflächen. *ipw. Internationale Papierwirtschaft*, 6, pp. 88–94.

Ness, C. and Göttsching, L., 2001b. Neue Bildraster-Technologien und deren Anforderungen an den Bedruckstoff Papier. Teil 3: Tonwertzunahme gedruckter Rasterflächen. *ipw. Internationale Papierwirtschaft*, 7, pp. 34–37.

Stover, J.C., 2012. *Optical Scattering Measurement and Analysis.* 3rd ed. Bellingham, WA, USA: Society of Photo-Optical Instrumentation Engineers (SPIE).

Tweer, R., 2002. *Vielfachstreuung von Licht in Systemen dicht gepackter Mie-Streuer: Auf dem Weg zur Anderson-Lokalisierung?* Doctoral dissertation. Universität Konstanz.

2B

M.A. Pedersen: Is it really true that Pantone extended gamut can reproduce 90 % of all Pantone spot colors?

Is it really true that Pantone extended gamut can reproduce 90 % of all Pantone spot colors?

Michael Abildgaard Pedersen

The Danish School of Media and Journalism, Department of Media Production and Management, Copenhagen
E-mail: map@dmjx.dk

Short abstract

This study seeks to confirm or refute the statement that Pantone Extended Gamut (XG) can reproduce 90 % of all Pantone Solid colors (PMS) by using seven process colors (CMYK+OGV). At the same time, it is investigated which colors within the 10 % that cannot be reproduced in this system. By using a comparison of Pantone's own "reference values" (CIELAB values) it appears that only 57.6 % of all PMS colors can be reproduced if the tolerance is ≤ 2 CIEDE2000 and only 82.7 % of all PMS colors can be reproduced if the tolerance is ≤ 3 CIEDE2000. The tolerance will have to be ≤ 3.7 CIEDE2000 in order to reproduce 90 % of all PMS colors. In an attempt to plot the two gamuts in a CIE a^* b^* projection diagram, it proves surprisingly difficult to identify the seven primary colors of XG. PMS Orange 021 is apparently not equal to XG Orange. PMS Green is apparently not equal to XG Green, and PMS Violet is apparently not equal to XG Violet. Likewise, it has not been possible to identify the secondary colors (overprints) of the XG Primary Colors. A suggestion for gamut plotting is proposed.

Keywords: Extended gamut, Pantone XG, CIELAB, CIEDE2000

1. Introduction and background

In the Graphic Arts Industry, it's a well-known fact that only 50 % of all Pantone Solid Colors can be reproduced by using the four process colors CMYK. Therefore, years of efforts have been made to expand the CMYK gamut. Either by producing more pigmented CMYK inks (CMYK+) or by expanding to six-colors Hexachrome (CMYKOG), seven-color Hi-Fi Color (CMYKRGB) or seven-color Opaltone (CMYRGBK).

In 2015, Pantone released a concept called Pantone Extended Gamut (XG) claiming to be able to reproduce 90 % of all Pantone colors by using the seven process colors Cyan, Magenta, Yellow, Black, Orange, Green and Violet (Pantone, 2021).

In 2019, a study by Ryerson University confirmed that Pantone XG *are able to reproduce more than 90 % of the Pantone spot color library on the Epson P9000 inkjet printer to < 2 CIEDE2000"* (Sharma, 2019)

The Pantone XG fan contains 1 729 PMS Colors matched by using the XG seven-color printing process. Nevertheless, when looking through the colors and comparing them with the original PMS spot colors, it turns out that many of the colors cannot be matched with a visually satisfactory result.

This raises several questions, for example:

If Pantone XG can match 90 % of all PMS Colors, which PMS colors cannot be reproduced and how would it be possible to identify those missing 10 %?

2. Materials and methods

Four abbreviations will be used in the rest of this Paper:

- XG meaning *Pantone Extended Gamut Coated* (Pantone, 2015)
- PMS meaning *Pantone Formula Guide Solid Coated* (Pantone, 2019)
- PCMS meaning *Pantone Color Manager Software v2.4.0.60 for Windows* (Pantone, 2020)
- CMYK meaning *Process Colors as defined in ISO 12647-2:2013 on* Coated paper (International Organization for Standardization, 2013).

Colorimetric data from all Pantone Colors (PMS and XG) were downloaded from PCMS. These were imported into excel, where additional colorimetric data were calculated (ΔL^*, Δa^*, Δb^*, ΔC^*, Δh^*, ΔH^*, ΔE_{ab} and ΔE_{00}). This way, data could be sorted by color difference.

A visual assessment was made of the individual Pantone color pairs PMS vs. XG in a viewing booth under daylight D50. Color pairs with a clearly color difference were noted and plotted into a CIE a^* b^* diagram. This was conducted by following Pantone's instructions (Pantone, 2015, p. ii).

The XG fan deck (printed in 2015) were purchased, unpacked, put to use in 2020 and measured in 2021. The XG Primary colors Orange, Green and Violet from the XG fan deck were measured by using an *X-rite eXact Advanced* spectrophotometer set in accordance with ISO 12647-2:2013, using measurement condition M1 (International Organization for Standardization, 2013).

The assessment of whether XG can reproduce PMS is based on a comparison of Pantone's own reference values for the two color systems.

When assessing color differences, a tolerance of ≤ 3 CIEDE2000 was used as the limit (Pedersen, 2016).

An attempt to identify XG's seven primary colors and their secondary colors was made in order to plot gamuts into the CIE a^* b^* diagram to identify possible gab areas between PMS and XG gamuts.

3. Results and discussion

3.1 Colorimetric Reference Value Comparison

By sorting the 1 729 data pairs by CIEDE2000, it appears that 82.7 % of the color pairs have a CIEDE2000 ≤ 3 (1 432 color pairs). Thus, XG cannot reproduce 90 % of PMS if the tolerance is ≤ 3.0 CIEDE2000. 327 color pairs have a color difference > 3.0 CIEDE2000 (19 % of all colors).

	A	B	C	D	E	F	G	H	I	J	K	L	M	N	O	P	Q	R	S	T	U	V
1	*Formula Guide Coated*	*L**	*a**	*b**	*C**	*h**		*Extended Gamut Coated*	*L**	*a**	*b**	*C**	*h**		*ΔL**	*Δa**	*Δb**	*ΔC**	*Δh**	*ΔH**	*DE**	*ΔE*2000*
2	PANTONE 7476 C	30,67	-19,67	-9,94	22,04	206,81		PANTONE 7476 XGC	30,75	-19,62	-10,02	22,03	207,04		-0,08	-0,05	0,08	0,01	0,23	0,1	0,1	0,1
3	PANTONE 7719 C	39,15	-37,39	-8,50	38,34	192,81		PANTONE 7719 XGC	38,99	-37,36	-8,42	38,30	192,70		0,16	-0,03	-0,08	0,04	0,10	0,1	0,2	0,1
4	PANTONE 7718 C	41,82	-43,38	-10,96	44,74	194,18		PANTONE 7718 XGC	41,84	-43,00	-11,07	44,41	194,44		-0,02	-0,38	0,11	0,34	0,26	0,2	0,4	0,2
5	PANTONE 2303 C	69,71	-16,94	43,29	46,49	111,37		PANTONE 2303 XGC	69,90	-17,17	43,46	46,73	111,55		-0,19	0,23	-0,17	0,24	0,18	0,1	0,3	0,2
6	PANTONE 2162 C	67,62	-0,67	-8,54	8,57	265,51		PANTONE 2162 XGC	67,53	-0,60	-8,81	8,83	266,09		0,09	-0,07	0,27	0,26	0,57	0,1	0,3	0,2
7	PANTONE 7545 C	34,69	-4,14	-11,59	12,31	250,34		PANTONE 7545 XGC	34,42	-4,20	-11,65	12,39	250,17		0,27	0,06	0,06	0,08	0,17	0,0	0,3	0,2
1722	PANTONE 246 C	49,00	71,34	-33,51	78,82	334,84		PANTONE 246 XGC	46,96	50,73	-18,36	53,95	340,10		2,04	20,61	-15,15	24,86	5,26	6,0	25,7	7,0
1723	PANTONE 2572 C	66,79	35,38	-31,00	47,04	318,78		PANTONE 2572 XGC	67,24	21,70	-17,86	28,10	320,55		-0,45	13,68	-13,14	18,94	1,77	1,1	19,0	7,1
1724	PANTONE 253 C	43,03	67,21	-40,90	78,68	328,68		PANTONE 253 XGC	43,76	45,28	-23,48	51,00	332,59		-0,73	21,93	-17,42	27,68	3,91	4,3	28,0	7,4
1725	PANTONE 251 C	72,78	34,32	-23,57	41,63	325,52		PANTONE 251 XGC	72,06	20,95	-11,62	23,95	330,99		0,72	13,37	-11,95	17,68	5,47	3,0	17,9	7,4
1726	PANTONE 2385 C	53,51	69,32	-28,77	75,05	337,46		PANTONE 2385 XGC	53,17	49,04	-11,60	50,39	346,69		0,34	20,28	-17,17	24,66	9,23	9,9	26,6	7,7
1727	PANTONE 2375 C	65,62	51,44	-24,20	56,85	334,81		PANTONE 2375 XGC	64,70	32,72	-11,21	34,59	341,08		0,92	18,72	-12,99	22,26	6,27	4,9	22,8	7,7
1728	PANTONE 2582 C	50,46	52,73	-44,34	68,89	319,94		PANTONE 2582 XGC	52,82	32,58	-26,57	42,04	320,79		-2,36	20,15	-17,77	26,86	0,85	0,8	27,0	8,1
1729	**PANTONE Purple C**	47,52	68,89	-42,48	80,93	328,34		**PANTONE Purple XGC**	47,71	42,73	-21,86	48,00	332,91		-0,19	26,16	-20,62	32,94	4,57	5,0	33,3	8,7
1730	PANTONE 252 C	58,63	53,59	-36,40	64,78	325,81		PANTONE 252 XGC	59,68	30,92	-17,66	35,61	330,26		-1,05	22,67	-18,74	29,18	4,44	3,7	29,4	9,2

Figure 1: Colorimetric data in Excel sorted by CIEDE2000 (showing five of the 1 729 color pairs)

In order to claim that XG can reproduce 90 % of PMS colors, a tolerance of ≤ 3.7 CIEDE2000 have to be the limit. This way, 1 556 PMS colors can be reproduced by XG leaving 173 colors, which cannot.

By maintaining the limit of ≤ 3 CIEDE2000 there will be 297 PMS colors that cannot be reproduced by XG and the Excel sheet shows which PMS colors are out of XG gamut.

Other observations show that the largest color difference is 9.2 CIEDE2000 (PMS 252), the smallest color difference is 0.1 CIEDE2000 (PMS 7476 and 7719) and 19.2 % (322 colors) have a CIEDE2000 ≤ 1.

3.2 Gamut sizes

To get the first indications of the difference in gamut sizes between the two gamuts, the range of each gamut is shown in Table 1.

Table 1: Comparison of the two color space's (PMS and XG) colorimetric extreme values

	The span of the PMS gamut	The span of the XG gamut
L*	from 7.90 (Black6C) to 92.10 (600C)	from 9.48 (7447XGC) to 92.03 (600XGC)
a*	from −78.99 (3405C) to 80.21 (226C)	from −77.70 (2252XGC) to 77.34 (219XGC)
b*	from −75.99 (072C) to 110.86 (Yellow C)	from −70.22 (2371XGC) to 95.13 (1505XGC)
C*	from 0.20 (CoolGray4) to 110.90 (Yellow C)	from 9.69 (7547XGC) to 98.39 (3405XGC)

It seems that XG is less chromatic in the yellowish areas. The most chromatic color in PMS is Yellow C while the most chromatic color in XG is orange 1505 XG. A mapping of the gamuts might provide further information.

3.3 Gamut mapping

In order to plot an XG gamut as a polygon in a CIE *a*b** projection diagram a minimum 12 data points would be desirable. Six primary colors (CMYOGV) and six secondary colors (Y+O, O+M, M+V, V+C, C+G, G+Y). This will create a 12-sided polygon.

3.3.1 Primary XG Color identification
Surprisingly it has not been possible to find precise and specific information on the XG Primary Colors *Orange XG, Green XG* and *Violet XG*. Neither in the XG fan deck nor at Pantone Inc.

A search for CIELAB-values (the "Reference values") from the PCMS results in confusion information and the subsequent measurements of the colors in the XG fan deck causes further confusion.

One would assume that it would be relatively easy to figure out which seven Pantone XG primary inks to use. It would be logical to use the four common CMYK Process Colors, PMS Orange 021, PMS Green and PMS Violet. However, it does not seem to be these inks sets.

Page 1XG in the XG fan deck (Pantone 2015), shows the seven *Pantone XG Bases Colors*. The four process colors CMYK are simply named *Process Yellow C*, *Process Magenta C*, *Process Cyan C* and *Process Black C* (XG is not a part of the names)*. The additional base colors are named *XG Orange C, XG Green C* and *XG Violet C*.

On page iii, in the XG fan deck it states that the Primary XG-CMYK colors must comply with ISO 12647-2:2004/Amd 1:2007. This information is surprising since ISO 12647-2 came in a new edition (International

Organization for Standardization, 2013) in 2013 (ISO 12647-2:2013) prior to the production of the XG fan deck in 2015. In this research, the new edition of ISO is used.

This however, defines four of the seven XG Process Colors (CMYK) (Table 2) and at the same time sets the limits for how many PMS colors can be reproduced in this part of the XG gamut when it comes to PMS colors created by CMYK combinations, including its overprint RGB.

Table 2: Colorimetric values of XG CMY Primaries (CIELAB values taken from ISO 12647-2:2013, Table 5, premium coated paper, white backing, measurement condition M1)

Color	L*	a*	b*	XG Hue angle	C* (calculated)
Cyan	56	−36	−51	233°	62.43
Magenta	48	75	−4	357°	75.11
Yellow	89	−4	93	93°	93.09

Consequently, a yellow PMS spot color must have a maximum chroma (*C**) of 93.09 and other yellowish spot colors must have a smaller chroma (*C**) to be within this XG-CMY-gamut. This means that PMS Yellow (*C** 110.87) and PMS Yellow 012 (*C** 109.07) cannot be reproduced in this XG-CMY gamut and thus cannot be reproduced in XG.

Having the three chromatic CMY XG-Process Colors defined, we need to define the three additional XG Process Colors; XG Orange, XG Green and XG Violet.

On page iii, in the XG fan deck (Pantone, 2015) there are additional information about the color's metric hue angles (Orange 58°. Green 180° and Violet 311°). A search for these three additional primary colors inside the XG fan deck (Table 3) results in the following confusing observations: One would assume that the primary color *XG Orange* should consist of 100 % Orange and no other XG colors and it should have a hue angle of 58°. None of the colors inside the XG fan deck complies with this. The only XG color named orange is *Orange 021 XG* (Pantone, 2015, p. 23). This however, is created by a combination of 27 % Magenta + 100 % Orange in the XG fan deck, it has a hue angle of 54° and therefore the primary XG Orange doesn't seem to be PMS Orange 021.

It turns out that another orange color 1505 XG is the only XG color to meet the requirement (O: 100 % + no other XG colors) and it has a hue angle of 59°. Thus, PANTONE XG Orange could be equal to PMS 1505 C. According to the PMS fan deck, PMS 1505 is created by 50 % Orange 021 + 50 % Transparent White!

Table 3: The XG Orange and Orange 021 comparison of different target values

	L*	a*	b*	C*	h*	PMS Orange 021	PMS 1505
XG Orange Measured on page 1XG	66.02	56.06	91.01	106.89	58.37	7.1 ΔE_{00}	0.9 ΔE_{00}
Orange 021 XG Values from PCMS	50.82	61.70	86.47	106.22	54.49	2.0 ΔE_{00}	
PMS Orange 021 Values from PCMS	60.81	65.69	85.06	107.47	52.32		

Likewise, we would assume that the primary XG Green should consist of 100 % Green and no other XG colors. It should have a hue angle of 180°. However, none of the 1 729 XG colors has these specifications! The closest color is 2240 XG (86 % Green (*h** 181)) or 3275 XG (23 % Cyan + 92 % Green (*h** 185)). In fact, XG

Green is defined with the combination; C: 26 % + Y: 17 % + G: 100 % (Pantone, 2015, p. 177). Even though it has a correct hue angle of 179.5° it does not make sense that a primary process color should be made from a screening combination of three other primary process colors. Nevertheless, the target values from PCMS indicate that PMS Green is the Primary XG Green (Table 4).

Table 4: The XG Green and PMS Green comparison of different target values

	L^*	a^*	b^*	C^*	h^*	PMS Green	PMS 2240	PMS 3275
XG Green Measured on page 1XG	62.20	−74.87	0.67	74.87	179.49	4.0 ΔE_{00}	4.2 ΔE_{00}	3.6 ΔE_{00}
Green XG Values from PCMS	57.82	−76.17	0.67	76.17	179.50	0.3 ΔE_{00}		
PMS Green Values from PCMS	57.74	−77.18	0.20	77.18	179.85			

Finally, the primary process color XG Violet should consist of 100 % Violet and no other XG colors. It should have a hue angle of 311°. However, XG Violet is defined as 37 % Cyan + 100 % Violet (Pantone, 2015, p. 96) it has a hue angle of 307.70°. Thus, PMS Violet doesn't seem to be the XG Primary Violet. Pantone 266 XG is defined as 80 % Violet (XG p. 94), it has a hue angle of 308.68° and is thereby the closest XG color to 100 % Violet. A comparison of the CIELAB target values from *XG Violet* and *PMS Violet* from PCMS results in a CIEDE2000 of 3.3 and thereby indicate that PMS Violet could be the primary process color XG Violet even if it exceeds the limit of 3 CIEDE2000. However, when comparing the measurement of the XG Violet from the fan deck and the target values from PCMS there is a difference of 6.1 CIEDE2000 as seen in Table 5. This in fact indicates that PMS Violet cannot even be reproduced in XG even though Violet is a primary color in XG!

Table 5: The XG Violet and PMS Violet comparison of different target values

	L^*	a^*	b^*	C^*	h^*	PMS Violet	PMS 266
XG Violet Measured on page 1XG	25.94	52.05	−59.31	78.91	311.27	6.1 ΔE_{00}	10.6 ΔE_{00}
XG Violet Values from PCMS	22.92	49.26	−63.74	80.56	307.70	3.3 ΔE_{00}	
PMS Violet Values from PCMS	18.75	54.58	−69.48	88.35	308.15		

3.3.2. Secondary Colors
Secondary colors are usually made of two primary colors (100 %+100 %). In the XG fan deck, only one color is made from two primary inks (2371 XG: V: 100 % + C: 100 % (Pantone, 2015, p. 109)) none of the other 1 729 XG colors is made solely from two solid primaries.

Thus, in order to plot the gamut edge, alternative secondary colors must be specified. It should be colors that lie between two primary colors, which have the highest possible chroma (C^*) and having a mixing ratio as close to 50/50 as possible. A proposal is shown in Table 6.

Table 6: Possible alternative Secondary Colors for plotting XG

The color between:	XG Name	XG Process combination	L*	a*	b*	C*
Yellow and Orange	XG 2013	Y: 100 % + O: 54 %	75,48	32,35	92,03	97.55
Orange and Magenta	XG 2347	O: 100 % + M: 83 %	49,51	72,43	67,72	99,16
Magenta and Violet	XG 2405	M: 100 % + V: 49 %	38,69	65,70	−12,99	66,98
Violet and Cyan:	XG 2371	V: 100 % + C: 100 %	18,72	42,30	−70,22	81,98
Cyan and Green	XG 320	C: 90 % + G: 75 %	52,48	−62,53	−24,25	67,06
Green and Yellow	XG 2423	Y: 100 % + G: 91 %	61,74	−71,90	47,15	85,98

This way, it is now possible to plot an XG gamut into the CIE *a*b** projection diagram (Figure 2, bold line). For the sake of comparison, other gamuts have been plotted in Figure 2. In an earlier study, the PMS gamut was specified (Pedersen, 2019) and is plotted as a bold dotted line. The CMYK gamut (thin line) relate to ISO 12647-2:2013 and the RGB gamuts (thin dotted lines) were plotted by using CIELAB values from the primary RGB and their secondaries.
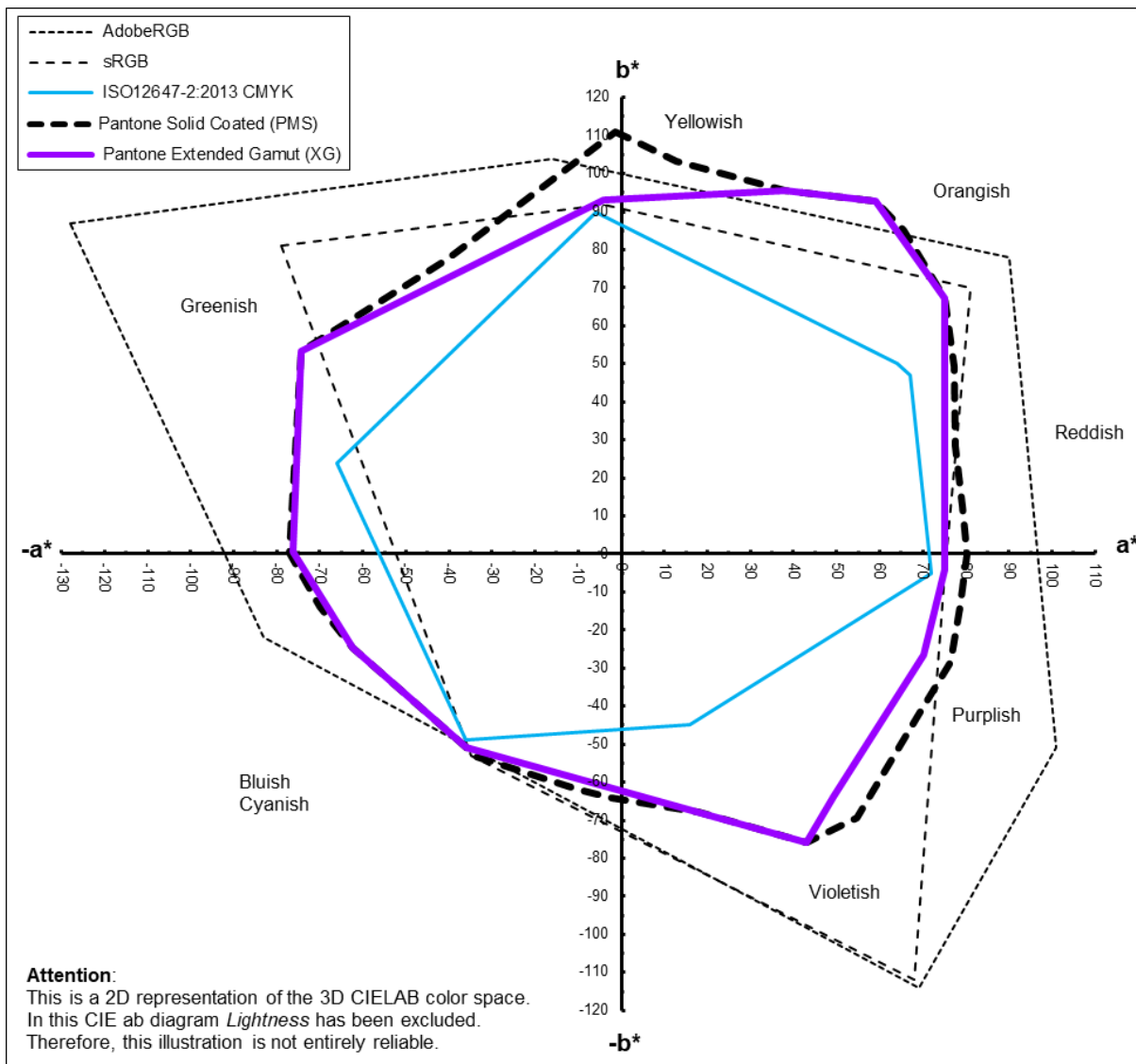
Figure 2: Comparison of five different color spaces and the gaps between PMS and XG

Figure 2 confirms some of the assumptions discussed in section 3, regarding the yellowish area. In addition, it also shows a gap between PMS and XG in the purplish area. By consulting all reference values from PCMS imported into the Excel spreadsheet it shows that colors with the largest color difference are placed in this purplish area. Some examples below:

- PANTONE 252   (9.2 CIEDE2000)
- PANTONE Purple   (8.7 CIEDE2000)
- PANTONE 2582   (8.1 CIEDE2000)
- PANTONE 2375   (7.7 CIEDE2000)
- PANTONE 2385   (7.7 CIEDE2000)
- PANTONE 251   (7.4 CIEDE2000)
- PANTONE 253   (7.4 CIEDE2000)
- PANTONE 2572   (7.1 CIEDE2000)
- PANTONE 246   (7.0 CIEDE2000)
- Forty other PMS colors in this area have a difference between 5.0 and 6.9 CIEDE2000.

4. Conclusions

The question of whether Pantone Extended Gamut (XG) can reproduce 90 % of all PMS colors depends largely on which tolerance limit is used and on which basis the comparison is made.

When the Ryerson study determines that 90 % of all PMS colors can be reproduced to a color difference of ≤ 2 CIEDE2000 (Sharma, 2019, p. 4), this is based on an assessment of the ability of different software solutions to separate digital colors into the seven process colors and a subsequent digital print production.

In the present study, an assessment and a comparison has primarily been made of Pantone's own target values for the two color systems (CIELAB target values from PMS Solid Coated vs XG Coated).

On this basis, the conclusion is that according to Pantone's own target values it is not possible to reproduce 90 % of all the PMS colors. According to these data, only 82.7 % of the colors can be reproduced to a limit of 3 CIEDE2000. If the tolerance limit is to be lowered to ≤ 2 CIEDE2000, as the Ryerson study has used, only be 57.6 % of all PMS colors can be reproduced.

As for the 10 % of the color pairs with highest color difference, the majority are located in the purplish area while some highly chromatic red and yellow colors also outside the gamut.

References

International Organization for Standardization, 2013. ISO 12647-2:2013 *Graphic technology — Process control for the production of half-tone colour separations, proof and production prints - Part 2: Offset lithographic processes.* Geneva: ISO Central Secretariat.

Pantone, 2015. *Pantone extended gamut coated the plus series: 1,729 PANTONE MATCHING SYSTEM colors matched using a seven-color printing process.* New Jersey: Pantone LLC.

Pantone, 2019. *Pantone formula guide solid coated:ink colors and formulas for packaging, print and graphics.* New Jersey: Pantone LLC.

Pantone, 2020. *Pantone color manager software* (2.4.0.60 for Windows). [computer program] New Jersey: Pantone LLC. Available at: <https://www.pantone.com/customer-service/software-download> [Accessed 2020].

Pantone, 2021. *Extended gamut coated guide*. [online] Available at: <https://www.pantone.com/extended-gamut-coated-guide> [Accessed January 2021].

Pedersen, M.A. 2016. Why most Brand Manuals fail when it comes to defining Brand Colors. And how to determine acceptable Color Deviations for specific Brand Color. In: G. Patrick, ed. *Advances in Printing and Media Technology: Proceedings of the 43th International Research Conference of iarigai*. Toronto, Canada, August 2016. Darmstadt: iarigai. pp. 91–100.

Pedersen, M.A. 2019. Reinventing the wheel. An attempt to create an objective technical color wheel for Pantone colors by using hue angles (h_{ab}) as the deciding factor. In: C. Ridgway, ed. *Advances in Printing and Media Technology: Proceedings of the 46th International Research Conference of iarigai*. Stuttgart, Germany, 15-18 September 2019. Darmstadt: iarigai. pp. 29–41.

Sharma, A. 2019. *Ryerson University expanded gamut study 2019: evaluation of spot color reproduction in multicolor printing – Version 2.7.9.* Toronto: Ryerson University.

S. Theerathammakorn and C. Koopipat: Customers' color preferences for Mango (*Mangifera indica* L.) var. Nam Dok Mai ...

2B

Customers' color preferences for Mango (*Mangifera indica* L.) var. Nam Dok Mai and impact on buying decision based on color attributes of printed images

Supawadee Theerathammakorn[1] *and Chawan Koopipat*[2]

[1] School of Science and Technology, Sukhothai Thammathirat Open University, Thailand
[2] Department of Imaging and Printing Technology, Chulalongkorn University, Thailand
E-mails: s_thee49@yahoo.com; Chawan.k@chula.ac.th

Short abstract

Printed color images of food products on packaging tend to play an important role in drawing the attention of customers and activating their purchase decisions for those products. Making the right choice when it comes to customers' preferred color for a product is essential for packaging designers and marketers in order to influence the purchase decision of those customers. *Mangifera indica* L. var. Nam Dok Mai is a commercial tropical fruit in Thailand. Utilizing the CIELAB color system, the color attributes (i.e., hue, saturation, and brightness) of mango images were evaluated to investigate color preference of customers and production of stimuli. A psychophysical experiment was conducted based upon the feelings of "deliciousness" and "taste" since these feelings appear to impact purchase decisions. Findings from a multivariate analysis of variance (MANOVA) indicate that color and favorite flavor had a significant effect on feelings influencing purchase decision. An analysis of variance (ANOVA) test revealed that color preference significantly affected taste and purchase decisions, yet did not demonstrate any significant effect on perceived deliciousness. Therefore, making a purchase decision for the Nam Dok Mai Si-Thong (NDMST) mango appears to significantly depend upon the favorite flavor of the customer. In addition, the results of the ANOVA test on CIELAB, saturation, and hue angle of the NDMST mango images indicate that the three color attributes of redness ($a*$), saturation, and hue angle had significant impact on perception of taste. The findings also reveal that the three color attributes of redness, saturation and hue angle had significant impacts on taste preference for buying decisions. Redness represents the preferred color for people who like sweet taste while green is the right color for people who prefer a sweet-sour one. Saturation of sweet and sour (SS) taste presents more than that of sweet (SW) taste. The favorite tastes of SW and SS are classified by hue angle at 90 degrees of yellow color. The SW taste shows hue angle at less than or equal to 90 degrees, while the SS taste displays at more than 90 degrees.

Keywords: color preference, CIELAB, purchase decision, Mango

1. Introduction and background

Mangifera indica L. or mango cv. Nam Dok Mai is a main commercial fruit in Thailand, which is exported to many countries due to its flavor, color, and smell (Matulaprungsan, et al, 2019; Booranasrisak, et al., 2017). Both fresh and processed versions are found in markets. The Nam Dok Mai Si-Thong (NDMST) mango peel increases in yellowness as it ripens, depicting an orange color at the lower pole (sometimes referred to as golden mango) which corresponds to a higher sugar content (i.e., sucrose, glucose, and fructose) with maximum sucrose of approximately 141.52 ± 0.11 μg/mg 120 days after flowering (Booranasrisak, et al., 2017). In general, most farmers harvest Nam Dok Mai mangoes before they are fully ripe due to various flavor preferences (e.g., sour, sweet-sour, and sweet), which are indicated by different types of coloring on the mango peel. Jha, Chopra and Kingsly, (2007) found that maturely ripened mangoes satisfied participant taste, while those mangoes predicted to be immature or overly mature were mostly refused by participants.

Former studies have revealed that expectations of manufacturers and customers are dissimilar when it comes to the mechanism driving a purchase decision based on fruit packaging (Schifferstein, et al., 2013; Shankar, Levitan and Spence, 2010; Ndom, Elegbeleye and Ademoroti, 2011; Huang and Lu, 2015). Manufacturers tend to mainly concentrate on product features such as color, shape, texture, design, etc. (Ndom, Elegbeleye and Ademoroti, 2011; Huang and Lu, 2015; Delwiche, 2012; Padda, et al., 2011; Lee, et al, 2013), while customers appreciate freshness, a delicious look, taste, etc. Therefore, the packaging needs to be "right" in order to drive more customers to buy. A purchase decision on fruit, especially packed fruit, is influenced by the experiences of the customers (Huang and Lu, 2015; Delwiche, 2012). For example, Schifferstein, et al. (2013) indicate that the duration of a product on a supermarket shelf is significantly influenced by vision when the customer is at the purchasing stage. Taste after opening the package and consuming the food was the second most significant factor. Ndom, Elegbeleye and Ademoroti (2011) found that color mixed with food coloring affects the taste and flavor perception of a drink. The researchers found that customers rarely classified the taste of a fruit-flavored beverage when the color did not correspond with the expected taste. Hence, it is inferred that people perceive a product to be of higher quality when the color of the product is in harmony with their expectations of the product taste.

The ecological valence theory (EVT) of color preference says that people's preference for a given color is closely related to the affective value that people associate with that color (Schloss and Palmer, 2015). Color preference is learned through developing experiences with differently colored objects. For example, yellow bananas and red strawberries are greatly preferred to blue ones. Color of food may be the most obvious visual cue regarding flavor, yet customer expectations through associative learning are decided by other visual cues as well, e.g., gloss and shape (Delwiche, 2012). Cognitive behavioral responses to fruit should be considered when it comes to the elucidation of packaging color and cognitive (dis)similarity, which affects not only the ability to balance cognitive and behavioral responses to stimuli, but also cognitive behavioral responses to fruit (Huang and Lu, 2015).

Consequently, whenever colorful images of any foods, especially familiar ones, are perceived, they may trigger signals to our brains (Boldbaatar, 2017) directing us to experience flavor perceptions e.g., delicious, sweet, sour, etc. (Ndom, Elegbeleye and Ademoroti, 2011; Huang and Lu, 2015; Padda, et al., 2011; Wie, et al., 2014; Köster and Mojet, 2015). Using color which is positively perceived by a customer leads to a decision to purchase the product (Wie, et al., 2014; and Köster and Mojet, 2015). The color on the package design affects the initial appeal of a product, which is then followed by the action of a purchase decision, especially when the color is consistent with the expectation of the customer (Wie, et al., 2014).

Therefore, this study aims to investigate color preference for *Mangifera indica* L. var. Nam Dok Mai and how the feelings of customers are affected in terms of deliciousness and taste, ultimately leading to a purchase decision.

2. Materials and methods

Owing to the fact that this research aims to investigate color preference of NDMST mango, the experiment started with photographing NDMST mango fruits from two mango farms in Chachoengsao Province every week for four weeks, from the beginning of flowering until harvest. The digital image files were measured and a single image was selected that provided the closest CIELAB match to the average of CIELAB data. The image file was prepared by adjusting hue, saturation, and lightness as object stimuli in order to find the color attributes relating to customers' feelings that would most probably lead to a purchase decision on a NDMST mango.

2.1 Object stimuli

Thirty-five ink jet print images of mango cv. Nam Dok Mai were utilized as object stimuli in this study. The print images were prepared from a mango cv. NDMST reference image file utilizing the CIELAB value closest to the average of all 105 CIELAB values (five positions measured by Adobe Photoshop CS6 using RGB color space) of each of 21 digital mango images as shown in Figures 1 and 2.
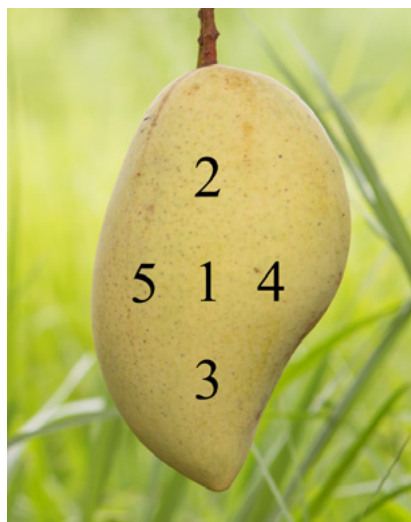
Figure 1: The five positions measured on a digital mango image by Adobe Photoshop
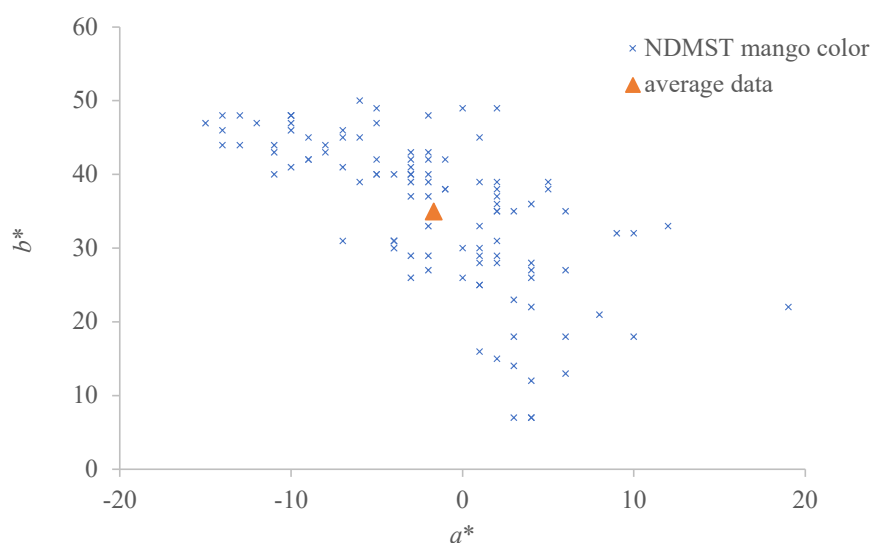
Figure 2: CIE a*b* of the five positions on each of 21 digital mango fruit images from the two farms (round dot) and the average of CIE a*b* (triangle mark)

Twenty-one of 24 images (three rotten mango fruits in the fourth week) were photos of three mango fruits of each farm with a color checker captured every week, wrapped with black paper (to protect against fruit flies), from 80 days after flowering until harvest, four weeks later. This period covers the days of most highly-satisfying taste (days 91–110) (Schifferstein, et al., 2013; Watanawan, et al, 2014). The two mango farms in the study are mango exporting farms located in Chachoengsao Province, Thailand. The closest CIELAB of the image to the average CIELAB was used as a reference color and adjusted in hue, saturation, and brightness by using Adobe Photoshop CS6. This adjustment was made because color preference is mostly presents in three dimensions - hue, saturation, and brightness (Schloss and Palmer, 2015). Figure 3 shows the hue adjustment window in Photoshop. Each image was adjusted at the same point dimension

x, y (50.11, 23.08) in the mango image area. The hue-adjusted images were prepared in 6 colors of Red, Green, Blue, Cyan, Magenta, and Yellow by sliding the relevant icon. The adjusting color image at each time was calculated as the CIELAB color difference or ΔE^*_{ab} around 3 (Dharavath and Basim, 2018).
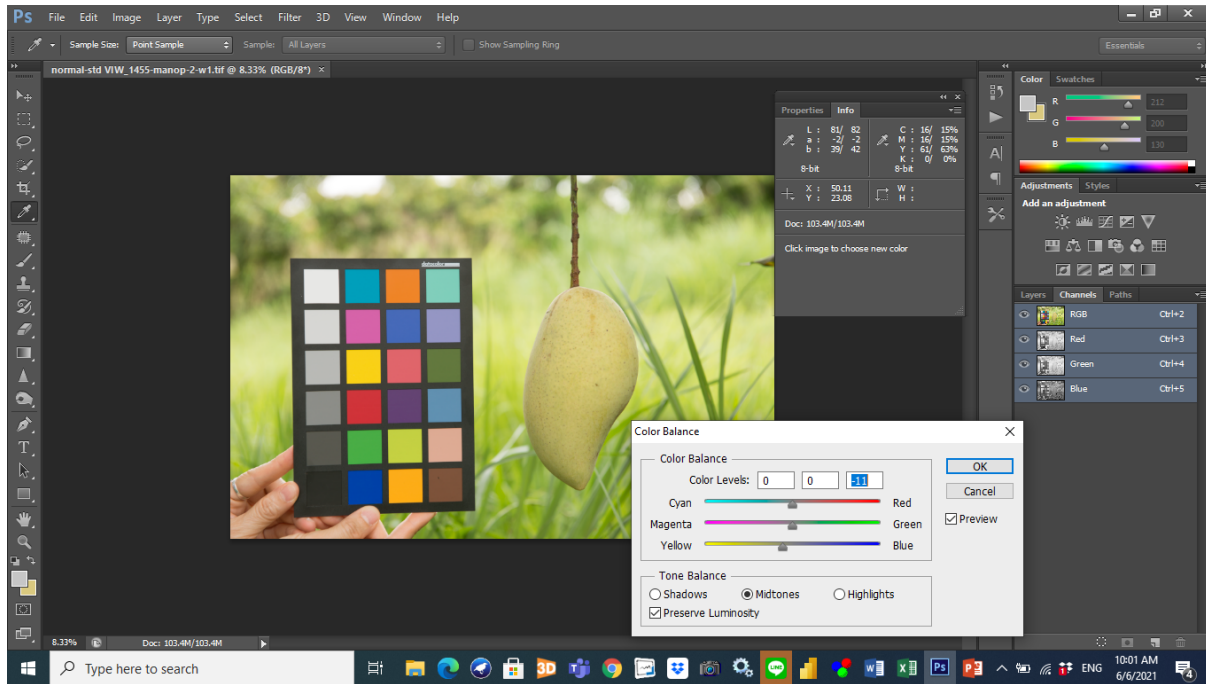
Figure 3: Hue adjustment window in Photoshop with sliding icon

The adjusting color and normal images were adjusted for saturation and brightness by sliding the relevant icon in the saturation and brightness windows in the same manner used for hue adjustment. Then the CIELAB of each image at each time of adjustment was calculated until ΔE^*_{ab} was around 3 as well. Following this, all 35 files were created (i.e., seven files from hue variations of six colors plus one control, 28 files of plus and minus in seven hue shades of saturation and brightness, respectively). Table 1 presents details of all 35 images in terms of picture number, code, color attributes and ΔE^*_{ab}. The Mean and SD of ΔE^*_{ab} of the 35 images are 3.02 and 0.89, respectively. To simulate the offset printer, which is commonly used for packaging printing, all 35 images were printed on coated paper, with a profile of coated paper Fogra39 (International Organization for Standardization, 2004) by Epson Stylus Pro 9000, using a color ink jet proof printer.

Table 1: Picture number, color attributes and ΔE^*_{ab} of the 35 NDMST digital images

Picture number	Code	Hue	Saturation	Brightness	Reference	ΔE^*_{ab}
1	Red−ad	Red	0	0	Normal	2.83
2	Red+S8	Red	+8	0	Red-ad	3.16
3	Red−S6	Red	−6	0	Red-ad	2.24
4	Red+Br5	Red	0	+5	Red-ad	4.24
5	Red-Br4	Red	0	−4	Red-ad	3.32
6	Green−ad	Green	0	0	normal	2.24
7	Green+S8	Green	+8	0	Green-ad	3.16
8	Green−S6	Green	−6	0	Green-ad	3.16
9	Green+Br5	Green	0	+5	Green-ad	2.24
10	Green−Br3	Green	0	−3	Green-ad	2.24

Picture number	Code	Hue	Saturation	Brightness	Reference	ΔE^*_{ab}
11	Normal	0	0	0	Normal	0.00
12	Nor+S7	0	+7	0	Normal	3.16
13	Nor−S7	0	−7	0	Normal	2.24
14	Nor+Br6	0	0	+6	Normal	5.48
15	Nor−Br5	0	0	−5	Normal	3.16
16	Cyan−ad	Cyan	0	0	Normal	2.83
17	Cyan+S8	Cyan	+8	0	Cyan-ad	3.16
18	Cyan−S7	Cyan	−7	0	Cyan-ad	2.45
19	Cyan+Br7	Cyan	0	+7	Cyan-ad	3.61
20	Cyan−Br4	Cyan	0	−4	Cyan-ad	2.45
21	Blue-ad	Blue	0	0	Normal	3.32
22	Blue+S8	Blue	+8	0	Blue	3.32
23	Blue−S8	Blue	−8	0	Blue	3.16
24	Blue+Br6	Blue	0	+6	Blue	2.45
25	Blue−Br4	Blue	0	−4	Blue	2.45
26	Mag−ad	Magenta	0	0	Normal	4.47
27	Mag+S6	Magenta	+6	0	Magenta	2.00
28	Mag−S9	Magenta	−9	0	Magenta	4.12
29	Mag+Br8	Magenta	0	+8	Magenta	3.32
30	Mag−Br4	Magenta	0	−4	Magenta	3.61
31	Yellow−ad	Yellow	0	0	Normal	3.16
32	Yellow+S7	Yellow	+7	0	Yellow	3.16
33	Yellow−S6	Yellow	−6	0	Yellow	3.16
34	Yellow+Br7	Yellow	0	+7	Yellow	3.32
35	Yellow−Br5	Yellow	0	−5	Yellow	3.16
					Mean	**3.02**
					SD	**0.89**

2.2 Observers

A total of 35 observers were organized into two groups. The first group contained 30 customers (twenty-six female and four male) with 23 % ranging from 21 to 30 years, 27 % ranging from 31 to 40 years, and 50 % over 40 years of age. All customers who participated in this study were familiar with mango cv. NDMST. Fifty-seven percent reported that their favorite flavor of mango cv. NDMST was sweet, and 40 % reported a sweet-sour taste as being their preferred flavor. Three percent reported that they prefer a sour taste. All participants took the FM100 Hue test to assess their color discrimination abilities (i.e., 77 % showed average discrimination, 23 % showed superior discrimination, and 0 % showed low discrimination). To evaluate color preference in relation to entrepreneurs, the second group consisted of five entrepreneurs (three female and two male) with 60 % over 40 years of age, and the remainder between the ages of 31 to 40. All of the entrepreneurs had sales experience with mangoes (an average of 19 years) and showed average color discrimination abilities.

2.3 Test procedure

Each participant viewed the 35 printed images one at a time under LED lighting with CCT at 6500 K and an illuminance level at 500 lux (Green, 2010). The viewing distance and angle were 30 centimeters and

0/45 degrees, respectively. Each NDMST print image was covered with a gray color paper mask (the shade was approximately Munsell N6 (L^* 58.25, a^* −0.82, b^* −1.64)) showing only the printed mango image during viewing. Each participant was asked to provide information about the following for each of the 35 images: his or her color preference of NDMST mango in terms of favorite flavor (only the first group), his or her feelings about "deliciousness" and "taste", and his or her "purchase decision". Following this, the participants evaluated how well each image conveyed their color preference for "deliciousness" utilizing a 5-point Likert scale ranging from 1 (least appealing) to 5 (most appealing). After this rating, each participant identified one of three tastes (i.e., sweet (SW), sour (S), or sweet-sour (SS)) and a purchase decision (i.e., yes or no) corresponding to their deliciousness feeling.

2.4 Statistical analysis

The mean and standard deviation of color preference were calculated for each image. A multivariate analysis of variance (MANOVA) and an analysis of variance (ANOVA) were applied to assess each color image and favorite flavor influencing deliciousness, taste, and purchase decision.

3. Results and discussion

As can be seen in Figure 4, the results of color preference show that 12 of 35 printed mango images (34.3 percent) scored high for deliciousness feeling (i.e., equal to or greater than 3.51), whereas the color preference of the entrepreneurs shows that 19 of 35 printed mango images (54.3 percent) provided the same feeling.

The printed mango images obtained from both groups show that taste covered the three flavors of mango Nam Dok Mai (i.e., sweet, sweet-sour, and sour). The highest score of 4.17 (customers, picture 27) and of 4.6 (entrepreneurs, picture 26) relates to sweet taste. There were five pictures preferred by both customers and entrepreneurs at high deliciousness, which also led to the same taste and customer buying decision, which were the pictures numbered 26, 27, 29, 34, and 35. These five printed images comprised two groups of tastes: sweet (SW) (pictures 26, 27, and 29), and sweet-sour (SS) (pictures 34 and 35). The 3 NDMST mango images corresponding to sweet taste were those with additional Magenta hue adjustment from the normal image, while the other two images, related to sweet and sour taste, were among those with yellow hue adjustment.
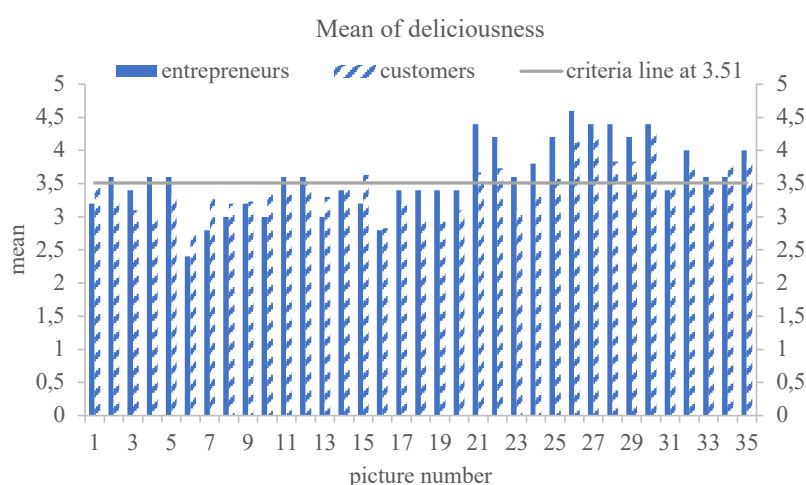

Figure 4: Mean of deliciousness scores from entrepreneurs and customers for the 35 printed mango fruit images

Since multiple dependent and independent variables were present in this study, MANOVA was applied to determine the factors influencing customer color preference. The results indicate that printed mango images and favorite flavor significantly influenced perception of deliciousness and taste, and the purchase decision, F (102, 2824.477) = 1.402, p = 0.005 and F (6, 1886.000) = 3.136 (Wilk's Lambda) p = 0.005, respectively. In addition, as shown in Table 2, the ANOVA results point out that the printed mango image significantly affected taste perception and purchase decision, but did not significantly impact perceived deliciousness (p = 0.000 and p = 0.002). Purchase decisions based upon the printed mango image also significantly depended upon the customers' favorite flavors (p =0.001).

Table 2: ANOVA Analysis on deliciousness, taste, and purchase decision of NDMST Mango based on printed images

Source	Dependent variable	Type III Sum of squares	df	Mean square	F	Sig.
Corrected Model	deliciousness	169.328[a]	104	1.628	1.675	.000
	taste	159.296[b]	104	1.532	3.618	.000
	purchase decision	39.469[c]	104	.380	1.631	.000
Intercept	deliciousness	3293.931	1	3293.931	3388.459	.000
	taste	1279.124	1	1279.124	3021.043	.000
	purchase decision	566.936	1	566.936	2435.952	.000
Pic-number	deliciousness	35.698	34	1.050	1.080	.348
	taste	40.191	34	1.182	2.792	.000
	purchase decision	14.849	34	.437	1.877	.002
Favorite flavor	deliciousness	2.503	2	1.251	1.287	.276
	taste	.065	2	.032	.077	.926
	purchase decision	3.298	2	1.649	7.085	.001
Pic-number * Favorite flavor	deliciousness	27.460	68	.404	.415	1.000
	taste	27.351	68	.402	.950	.593
	purchase decision	10.899	68	.160	.689	.974
Error	deliciousness	918.637	945	.972		
	taste	400.118	945	.423		
	purchase decision	219.936	945	.233		
Total	deliciousness	13472.000	1050			
	taste	5398.000	1050			
	purchase decision	2454.000	1050			
Corrected Total	deliciousness	1087.966	1049			
	taste	559.413	1049			
	purchase decision	259.406	1049			

a. R Squared = .156 (Adjusted R Squared = .063)

b. R Squared = .285 (Adjusted R Squared = .206)

c. R Squared = .152 (Adjusted R Squared = .059)

To find out the preferred color of the NDMST mango related to favorite taste and purchase decision, CIELAB of the five digital image files corresponding to the five highest-rated printed images was measured at 5 points on each NDMST mango image (as shown in Figure 1) by using Photoshop. Then saturation (C^*_{ab}), hue angle (h_{ab}), and saturation difference (ΔC^*_{ab}) were calculated from CIELAB. The color difference and saturation difference were compared to the CIELAB of the 'normal' picture (picture number 11). CIELAB of the five printed images was also measured at 5 points using a Techkon Spectrophotometer, adjusted at

D65 and 2 degrees observer. The significant differences between color attributes of the 5 NDMST mango digital and print images were analyzed using the ANOVA test. In Table 3, the average of CIELAB, C^*_{ab}, hue angle, and ΔC^*_{ab} of the five NDMST mango images from both digital and printed images are displayed. The favorite tastes of SW and SS are classified by hue angle at 90 degrees of yellow color. The SW taste shows hue angle at less than or equal to 90 degrees, while the SS taste displays at more than 90 degrees for both digital and print images. The saturation C^*_{ab} of sweet and sour taste presents more than that of sweet taste. The lightness CIE L^* value is lower for printed images than for digital ones. The CIE L^*, a^*, b^* values of NDMST mango digital images affecting favorite taste and purchase decision are 76.2 ± 1.64, 0.96 ± 2.53, and 35.44 ± 3.03 respectively.

Table 3: Average CIELAB, C^*_{ab}, h_{ab}, and ΔC^*_{ab} of the 5 NDMST mango images corresponding to favorite taste and leading to purchase decision from both digital images and printed images, including those values for the 'normal' picture (number 11)

Image type/ flavor	Picture number	L^*	a^*	b^*	C^*_{ab}	Hue angle	ΔC^*_{ab}
Digital/SS	11 (normal)	75.80	−1.20	37	37.02	91.86	0
Digital/SW	26	75.6	2.8	34	34.12	85.29	−2.90
	27	75.8	3	36.2	36.32	85.26	−0.70
	29	77.4	2.6	31	31.11	85.21	−5.91
Digital/SS	34	78.2	−2	37.2	37.25	93.08	0.23
	35	74	−1.6	38.8	38.83	92.36	1.81
Mean ± SD		76.2 ± 1.64	0.96 ± 2.53	35.44 ± 3.03	35.53 ± 3.00	88.24 ± 4.10	−1.49 ± 3.00
Print/SS	11 (normal)	72.132	−3.04	36.43	45.68	94.77	0
Print/SW	26	71.916	0.46	35.99	32.88	89.19	−12.80
	27	72.62	0.66	38.58	35.69	88.93	−9.99
	29	73.9	0.06	33.53	30.04	89.88	−15.64
	34	73.632	−3.15	34.88	44.78	95.15	−0.90
	35	70.554	−3.24	37.89	48.39	94.89	2.72
Mean±SD		72.52 ± 1.36	−1.04 ± 1.98	36.17 ± 2.09	38.35 ± 7.88	91.61 ± 3.14	−7.32 ± 7.88

Figure 5 displays CIE a^* and b^* values of the five NDMST mango images corresponding to sweet taste (pic-26-SW, pic-27-SW, and pic-29-SW) and sweet and sour taste (pic-34-SS and pic-35-SS) from both digital (top plot) and print image (bottom plot). The redness of the image leads to customer perceptions of sweet favorite taste, while greenish adjustment leads to perception of sweet and sour taste.
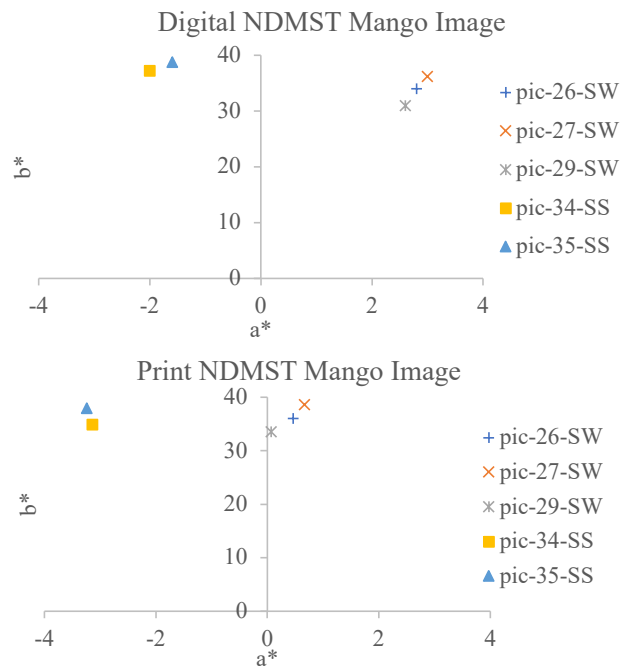
Figure 5: CIE a* and b* of the 5 NDMST mango images from both digital (top) and print (bottom) images

Figure 6 shows the plot of the average values of CIELAB, C^*_{ab}, and hue angle of digital and print NDMST mango images. The variation of CIE a^*, C^*ab and hue angle influence on favorite taste from SW (top plot) to SS (bottom plot). The saturation of digital image of SS taste is more pronounced when images are printed.
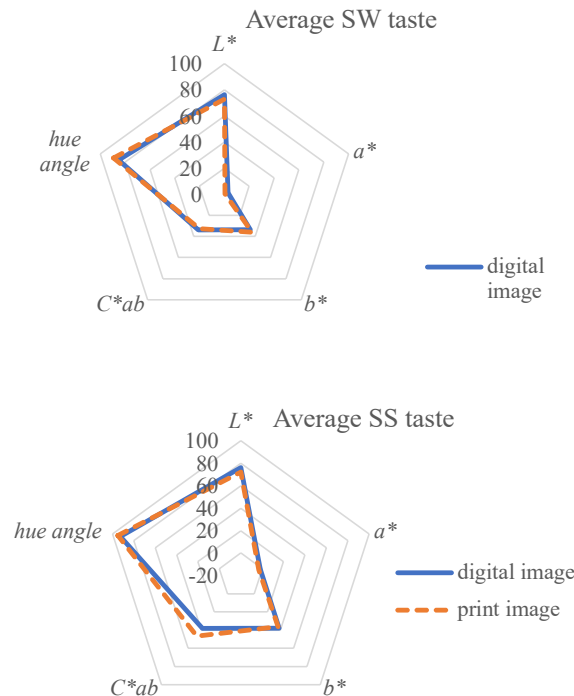
Figure 6: Average values of CIE L*, a*, b*, C^*_{ab}, and hue angle of the NDMST mango images for both digital and print images associated with favorite sweet taste (top) and sweet and sour taste (bottom)

According to the ANOVA test on CIELAB, C^*_{ab}, and h_{ab} of the five NDMST mango images, the results indicate that the three color attributes of redness (a^*), saturation, and hue angle had significant impact on perception of taste, $F(1,8) = 29.340$, $p = 0.001$, $F(1,8)=13.756$, $p =.006$, and $F(1,8) = 26.756$, $p = 0.001$,

respectively. In addition, the lightness of CIELAB had a significant impact on perceptions of printed images, $F(1,8) = 14.862$, $p = 0.005$.

The findings of this study support that color preference involves feelings based on the favorite flavor of the customer, is related to the coloring of the mango based on saturation, and ultimately leads to a purchase decision. The perception that redness corresponds to sweetness is consistent with the findings of Spence (2019) that most people in the world feel that red-colored drinks taste the sweetest compared to blue, green, orange, purple, and yellow.

4. Conclusions

This study indicates that color and favorite flavor are the most important factors when considering taste and purchase decision. Color – adjusted in hue, saturation, brightness, and primary color – leads to a visual perception that influences human perception of deliciousness and taste. Furthermore, color, perception, and feelings about deliciousness and taste, along with recognition and emotion based in memory and experience lead to the final purchase decision (Theerathammakorn, Hansuebsai and Hoshino, 2019). This study will help packaging designers to select the optimal color for images of the NDMST mango on packaging that provides meaningful visual clues to customers, who have different taste preferences. By better understanding how the color of images influences customer perception of the mango product, designers can help ensure that customers get the expected taste when they make a purchase decision. Nonetheless, the generalizability of this study is limited as this study only examines one specific type of mango (cv. Nam Dok Mai Si-Thong). The relationship between saturation, CIELAB, and taste for various mango cultivars and other kinds of fruit should be examined in future studies.

References

Boldbaatar, G., 2017. Neuromarketing study on Mongolian consumers' buying decision process. *Proceedings of Mongolian Academy of Science*, 57(4), pp. 97–108. https://doi.org/10.5564/pmas.v57i4.928.

Booranasrisak, T., Jaresitthikunchai, J., Phaonakrop, N. and Roytrakul, S., 2017. Shotgun proteomics analysis of fruit sweetness and ripening in Nam-Dokmai mango (Mangifera indica L.) peel. *Genomics and Genetics*, 10(3), pp. 54–61.

Delwiche, J.F., 2012. You eat with your eyes first. *Physiology & Behavior*, 107(4), pp. 502–504. https://doi.org/10.1016/j.physbeh.2012.07.007.

Dharavath, H.N. and Basim, S.C., 2018. Color quality comparison of electrophotographic vs. inkjet printing processes in a color managed digital printing workflow. *Visual Communications Journal*, 54(2), pp. 4–9.

Green, P., 2010. Standards for illumination of digital prints and photographs. *Journal of Physics: Conference Series*, 231: 012016. In: A. Fricker and P. Green, eds. *4th International Conference on: Preservation and Conservation Issues in Digital Printing and Digital Photography*. London, UK, 27–28 May 2010. https://doi.org/10.1088/1742-6596/231/1/012016.

Huang, L. and Lu, J., 2015. Eat with your eyes: package color influences the expectation of food taste and healthiness moderated by external eating. *The Marketing Management Journal*, 25(2), pp. 71–87.

International Organization for Standardization, 2004. ISO 12647-2:2004, *Graphic technology – Process control for the production of half-tone colour separations, proof and production prints – Part 2: Offset lithographic processes.* Geneva, Switzerland: ISO.

Jha, S.N., Chopra, S. and Kingsly, A.R.P., 2007. Modeling of color values for nondestructive evaluation of maturity of mango. *Journal of Food Engineering*, 78(1), pp. 22–26. http://dx.doi.org/10.1016/j.jfoodeng.2005.08.048.

Köster, E.P. and Mojet, J., 2015. From mood to food and from food to mood: a psychological perspective on the measurement of food-related emotions in consumer research. *Food Research International*, 76(2), pp. 180–191. https://doi.org/10.1016/j.foodres.2015.04.006.

Lee, S.-M., Lee, K.-T, Lee, S.-H and Song, J.-K., 2013. Origin of human colour preference for food. *Journal of Food Engineering,* 119(3), pp. 508–515. https://doi.org/10.1016/j.jfoodeng.2013.06.021.

Matulaprungsan, B., Wongs-Aree, C., Penchaiya, P., Boonyaritthongchai, P., Srisurapanon, V. and Kanlayanarat, S., 2019. Analysis of critical control points of post-harvest diseases in the material flow of Nam Dok Mai mango exported to Japan. *Agriculture,* 9(9): 200. https://doi.org/10.3390/agriculture9090200.

Ndom, R.J.E., Elegbeleye, A.O. and Ademoroti, A.O., 2011. The effect of colour on the perception of taste, quality and preference of fruit flavoured drinks. *IFE PsychologIA,* 19(2), pp. 167–189. https://doi.org/10.4314/ifep.v19i2.69520.

Padda, M.S., do Amarante, C.V.T., Garcia, R.M., Slaughter, D.C. and Mitcham, E.J., 2011. Method to analyze physico-chemical changes during mango ripening: a multivariate approach. *Postharvest Biology and Technology,* 62(3), pp. 267–274. https://doi.org/10.1016/j.postharvbio.2011.06.002.

Schloss, K.B. and Palmer., S.E. 2015. Color preference. In: M.R. Luo, ed. *Encyclopedia of color science and technology*. New York; NY, USA: Springer Science + Business Media. https://doi.org/10.1007/978-3-642-27851-8_70-13.

Schifferstein, H.N.J., Fenko, A., Desmet, P.M.A., Labbe, D. and Martin, N., 2013. Influence of package design on the dynamics of multisensory and emotional food experience. *Food Quality and Preference*, 27(1), pp. 18–25. https://doi.org/10.1016/j.foodqual.2012.06.003.

Shankar, M.U., Levitan, C.A. and Spence, C., 2010. Grape expectations: the role of cognitive influences in color-flavor interactions. *Consciousness and Cognition*, 19(1), pp. 380–390. https://doi.org/10.1016/j.concog.2009.08.008.

Spence, C., 2019. On the relationship(s) between color and taste/flavor. *Experimental Psychology,* 66(2), pp. 99–111. http://dx.doi.org/10.1027/1618-3169/a000439.

Theerathammakorn, S., Hansuebsai, A. and Hoshino, Y., 2019. Effect of color attributes on the buying decision model for Durio zibethinus L. *Color Research and Application*, 44(2), pp. 296–306. https://doi.org/10.1002/col.22337.

Watanawan, C., Wasusri, T., Srilaong, V., Wongs-Aree, C., and Kanlayanarat, S., 2014. Near infrared spectroscopic evaluation of fruit maturity and quality of export Thai mango (Mangifera indica L. var. Namdokmai). *International Food Research Journal*, 21(3), pp. 1109–1114.

Wie, S.-T., Ou, L.-C., Luo, M.R. and Hutchings J.B., 2014. Package design: colour harmony and consumer expectations. *International Journal of Design*, 8(1), pp. 109–126.

Development of Egyptian blue pigment for the production of silk-screen printing ink

Eirini Pavlou[1,2,7], *Antonios Tsigonias*[1,3,4], *Galina Xanthopoulou*[5], *George Vekinis*[5], *Thomas Katsaros*[6], *Marios Tsigonias*[1,3,4,7] *and Anastasios E. Politis*[1,3,7]

[1] Hellenic Union of Graphic Arts and Media Technology Engineers (HELGRAMED)

[2] Bank of Greece, Printing Work Department, Greece

[3] Graphic Arts Technology Study direction, University of West Attica, Greece

[4] Graphic Arts Research Development and Engineering Institute (GARDEN Institute)

[5] NCSR Demokritos, Advanced Ceramic and Composites Materials Laboratory

[6] Byzantine and Christian Museum of Athens

[7] Hellenic Open University, School of Applied Arts

E-mails: eirinipav@gmail.com;antonio_tsigonias@yahoo.gr; g.xanthopoulou@inn.demokritos.gr; g.vekinis@inn.demokritos.gr; thomasthkatsaros@gmail.com; tsigonias@yahoo.gr; politismedia@gmail.com

Short abstract

Colors and pigments are not an issue of modern times. Ancient societies have used materials thousands of years ago, to produce color items and artifacts. Research conducted, has revealed various inorganic fossils and materials, used by our ancestors for coloring. The interest of the scientific community on the subject is constantly high, originating from different scientific fields and disciplines. In this project we have experimented on producing a ceramic pigment, based on an ancient recipe for the production of the Egyptian lbue pigment/color. The objective of the research was to investigate whether the pigment produced, was appropriate to be used for the production of silk-screen printing ink by printing a fine printing of an artwork.

Keywords: Egyptian blue pigment, solution combustion synthesis – SCS, colorimetry, ink formulation, silk-screen printing, visible induced luminescence – VIL

1. Blue pigments in Antiquity

In Antiquity, blue was the color of the heavens, the kingdom of the gods, as well as the color of water, the annual flood and the primeval flood. Although ancient Egyptians used semi-precious stones such as azurite for jewelry, technology was advanced enough to make the world's first artificial pigment, known since medieval times as Egyptian blue. Depending on the powdering degree, the color can range from a rich, dark blue (coarse ground) to a light, ethereal blue (very fine ground). Blue used to color the hair of gods (specifically lapis lazuli, or darker Egyptian blue) and the face of the god Amun – a practice that extended to those Pharaohs associated with him (Figure 1).

Figure 1: Amun-Ra (center) in the temple of Amada

1.1 Egyptian blue

The first artificial pigment, Egyptian blue, was made in the early 3rd millennium BC in Egypt and then spread to Greece and the Roman Empire. This pigment was produced of a mixture of copper, calcium, silicon and the production process has remained secret for many centuries. Depending on the materials and conditions of manufacture, the shade of Egyptian blue varies. It is observed that during powdering the larger the grain size, the darker the shade of the produced color. Specifically, Egyptian blue is produced after successive heating to a high temperature of 850–1 000 °C of a mixture of materials containing copper (e.g. malachite), a set of calcareous materials (mainly pulverized limestone) and quartz in the form of sand. (Tite, Bimson and Cowell, 1984). At this high temperature, raw materials melt and interact, forming crystals of a copper mineral that produce the blue color. Using X-ray diffraction, Egyptian blue was identified as the mineral Cuprorivate, with the chemical formula $CaCuSi_4O_{10}$ (Hatton, Shortland and Tite, 2008).

1.2 The Egyptian blue in Antiquity

Plinius mentions (Levidis, 1994): according to the ancient recipe "*we will now refer separately to blue because a while ago we gave this name to Jasper (Ocean) because of the blue color. The best species is the Scythian, followed by the Cypriot and the last is the Egyptian. It is often imitated by painting other stones and they were very famous for it in the kings of Egypt. In the Egyptian history it was recorded who painted stones by this way. The cyan is divided into male and female. Sometimes there is in the cyan (azurite) a golden powder that differs from that which exists in Sappirus because there gold takes the form of spots. Sappirus (lapis lazuli) is blue and rarely purple. The best comes from Persia; Sappirus (lapis lazuli) that are blue (azurite) are considered male.*" (Figure 2).

Figure 2: Sappirus color of pigment from blue to purple

Theophrastus (1965, 1993) states: "*Since natural and artificial Milton (cinnabaris) exist, there are also natural and artificial Egyptian cyan. There are three varieties of cyan: Egyptian, Scythian and Cypriot. The Egyptian, the artificial one, as a pure pigment is better, the Scythian dissolves better in water. And those who tell the story of the Egyptian Kings note the name of the king that first produced artificial blue in imitation of the native one... and those who rub the colors say that from the same Cyan(os) four colors could be produced. The first is made from the thinnest grains and is very light and the second from the thicker ones (very dark).*" (Figures 3 and 4).
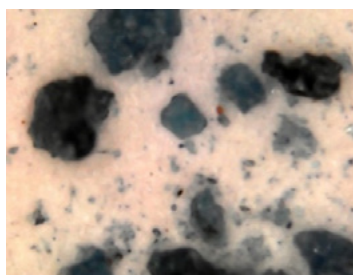

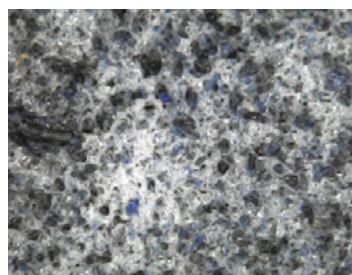*Figure 3: How granulometry affects the color of Egyptian blue*

Figure 4: Egyptian blue used as painting color

Theophrastus (1965, 1993) uses temporarily the word cyan to describe a mineral gemstone and sometimes one or more cyan pigments. The Cypriot cyan should be the azurite native base copper carbonate $2CuCO_2 + Cu(OH)_2$ found in most copper mines.

According to Vitruvius (2010) *"Egyptian cyan is a compound of copper, silicon, calcium and oxygen ($CuCaSi_4O_{10}$). It is produced by baking silica sand, copper, calcium carbonate and sodium salts (soda), at a temperature of around 840 °C."* It is believed that the copper used was in the form of malachite – mineral carbonated carbon and not metallic.

Some researchers consider Vitruvius's description incomplete because it lacks the essential calcium carbonate that is needed to make Egyptian blue. But it seems that sand, especially Egyptian, contains calcium carbonate. Vitruvius' information that the place of invention was Alexandria is incorrect because its use is already known from 3000 BC in Egypt.

Egyptian cyan was found in the frescoes of Knossos (Figure 5) (approx. 1700–1400 BC), in those of Santorini (1600–1500 BC), Mycenae (1400–1100 BC) and Vergina (4th century BC). Recently, evidence for late Hellenistic (first century BCE) Egyptian blue production was brought to light through the excavations of the Greek Archaeological Service on the Aegean island of Kos (Kostomitsopoulou Marketou, et.al., 2020).

Figure 5: "Toreador" fresco painting technique using Egyptian blue at the palace of Minoan, Knossos Crete

The observation made by Theophrastus (1965, 1993) and followed by Plinius that the shade of blue changes in relation to how the color has been rubbed, that is, whether it is coarse or fine-grained, concerns the Egyptian cyan and azurite (Levidis, 1994). In both cases the coarse-grained color is dark while the fine-grained one has a light shade. In color samples from Mycenaean murals analysis showed that a gray color was very finely ground Egyptian cyan (Figure 6).
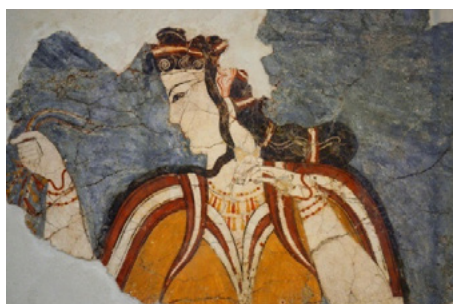
Figure 6: A fresco of a Mycenaean woman, 1400–1200 BCE

However, it seems that the production technology for Egyptian blue was lost (or extremely localized) and that there was almost a thousand years in which Egyptian blue dropped out of recorded art history. Essentially, it was forgotten, probably caused by the decline of the Roman Empire, with the consequent loss of the necessary knowledge and technologies. It seems that this was coupled with a misunderstanding arising over the method of manufacture described by Vitruvius (2010) in De Architectura in the first century BC. Vitruvius had made no specific mention of the need for calcium carbonate (lime), probably because the particular sand used in the samples available to him happened to have the right limestone content.

With sand from elsewhere, however, the method he described was totally ineffective, and the knowledge was lost (Lazzarini, 1982).

2. Reproducing Egyptian blue

In this study two different techniques of Egyptian blue production are investigated. The first one is based on the revival technique of the ancient recipes provided in the first part of this paper. The second one is based on a modern production method (solution combustion synthesis – SCS) that provides energy efficiency benefits (Pavlou, at al., 2015). This is achieved firstly with the use of nitrates allows the so-called self-propagating high temperature combustion, in a shorter time than other methods. Secondly, because the creation of gels instead of solid pellets requires less additional processing by mechanical methods (e.g. pellet crushing).

Both procedures, aim to improve the production of Egyptian blue from the basic reactive chemicals, by using the least possible energy dissipation and at the same time exploring the possibility of using these pigments such as ingredients and components of silk-screen inks.

2.1 Revival of the Egyptian blue ($CaCuSi_4O_{10}$) production according to ancient Greek and Roman references.

By studying, recording and cross-referencing data from several recipes, from ancient times to today, on the preparation of Egyptian blue we come to the following suggestions for the production of Egyptian blue pigment.

In order to experiment with the recipe, a certain methodology has been developed, based on the step-by step experimental activity and by the application of scientific results from previous research conducted so far. Six recipes were used in this study and they are presented in Table 1.

Table 1: Recipes of the six (6) experimental production of Egyptian blue pigment

Recipe	Cooper metal (80 μm 99.5 % pure)	$CaCo_3$	Na_2Co_3	NaCl on the top	SiO_2	H_2O	Temperature	Heating time
1	1.3 g	1.4 g	2.0 g	0.8 g	4.2 g	2 ml	750 °C	4 h
2	1.5 g	1.5 g	3.5 g	0.8 g	4.5 g	2 ml	750 °C	4 h
3	2.0 g	1.5 g	2.5 g	0.8 g	4.0 g	2 ml	750 °C	4 h
4	1.4 g	1.4 g	2.0 g	0.8 g	4.4 g	2 ml	750 °C 770 °C	3 h 2 h
5	1.4 g	1.4 g	2.0 g	0.8 g	4.4 g	2 ml	860 °C	1 h 20 min
6	1.4 g	1.4 g	1.4 g	0.8 g	4.4 g	2 ml	860 °C	1 h 20 min

2.2 Production of ceramic blue pigments with solution combustion synthesis of redox mixtures

Further in the research, the ancient knowledge of producing Egyptian blue, has been transferred to the SCS method, a new technic of pigment production by self-propagating high temperature synthesis (SHS) with mixtures of nitrates metals. Copper-based inorganic photoluminescent pigments were produced by SCS and their photoluminescence and coloring properties were investigated. Nanosized pigments were synthesized by the combustion of aqueous solution containing stoichiometric and non-stoichiometric amounts of metal nitrates (Table 2) in the following procedure under two steps:

Step 1: Mixing of the materials (Table 2, Figure 7):

Table 2: Composition recipe of two step solution combustion synthesis

Material	Weight Percentage
$Cu(NO_3)_2$	25.0 %
$Ca(NO_3)_2$	24.6 %
Na_2SiO_3	50.4 %

Step 2: Mixing of the total amount (volume) of the above-mentioned synthesis of materials, with the addition of 40 % Urea (as a fuel) + 3.6 % H_2O, at 700 °C until the ignition and remain for 2 h in the oven at 850 °C (Panagopoulou, Karanasios and Xanthopoulou, 2016).
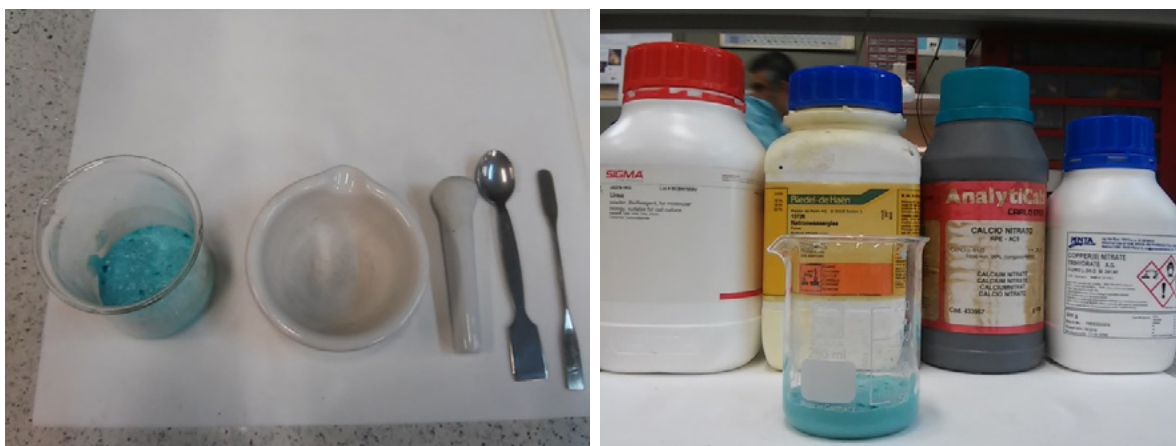
Figure 7: Accessories, chemicals & materials for pigment production

3. Ceramic powder treatment

The produced ceramic material with the SCS method had a very light and spongy texture while being brittle (Figure 8). In order to alternate the spongy ceramic material into powder form it was pulverized in an agate mortar, a process that took a couple of minutes in a laboratory environment. No special or industrial equipment that are used commonly to pulverize ceramic rocks that are used widely in industrial applications was necessary for this pulverization method. The produced powder was then passed through three sieves (Figure 9) of different granulometry (400 µm / 120 µm / 30 µm) and the mass of the powder with a mechanical diameter of less than 30 µm was collected. The material left in the sieves was reprocessed in the mortar until it reached the desired granulometry.

Figure 8: Pure pigment productions
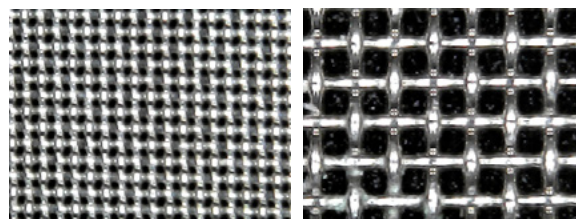
Figure 9: Different meshes of sieving process

During sifting and separation process it was observed a slight difference in color shade of the material from sieve to sieve. This could be explained by the different interaction of light waves to the particle size of the powder. Depending on the granulometry, the reflected light changes and the stimuli produced varies from

dark gray to cyan. As the size of the open area of the sieve decreases, the treated pigment provides a clearer blue shade. These phenomena had been verified during the production of Egyptian blue in ancient world as reported by Theophrastus, Vitruvius, Dioscorides and Vestorius (Vestorian blue). The same phenomena are observed to the murals in Mycenae or at Knossos palace in Crete.

By the use of the visible induced luminescence imaging technique (VIL) we may identify both samples as identical since they both have the same IR luminosity despite the fact that they react different under visible light source.

4. Ink Formulation

In order to test the pigment, it was necessary to formulate the printing ink. To speed up the process, our research team decided to formulate a silk-screen printing ink and test it by applying the ink via a hand-operated screen-printing machine. The artificial powder (between 400 μm and 120 μm) that was produced by SCS method was mixed with carriers and silk-screen printing additives and a dark blue-gray ink (Figure 10) was prepared which was printed from 120/58, W, PW, 18N silk-screen printing mesh. Due to the size of pigment particles a transparency is observed in the final ink that depends on the absorption phenomena.

Figure 10: Tanks with produced ink

Printed images provide beautiful tints from a sweet gray to a bluish gray depending on the volume concentration of the ceramic powder dispersions (Figure 11). Mixing a small amount (volume fraction from 10 % to 20 %) of the produced ceramic powder with other screen-printing inks, a grainy and earthy-like ceramic texture appears, resulting a visual and tactile ceramic feeling. By the use of the VIL, Egyptian blue was detected and identified on the printed substrate.

Figure 11: Color changes depending on the size of the grain while pulverising the colorant

4.1 Ink modification and reformulation

Since ceramic powder grained as a coarse one, a bluish gray color was produced and we tried to modify our ink by the use of smaller powder particles. This time the artificial powder (less than 30 μm) that was produced by SCS method was mixed with carriers and silkscreen printing additives and a blue ink was prepared which was printed from 120/58, W, PW, 18N silk-screen printing mesh.

5. Screen preparation and sensitization

For the testing process it was ensured that the proper printing guidelines for the specific printing process should be followed. As it was decided to print an artwork by hand in handcrafted screen-printing press, both the prepress and the printing steps should be followed by the book. The frame and printing mesh were prepared in order to sensitize them by Diazo photo-emulsion. The emulsion used was intended for high-quality production, solvent and water-resistant stencils and had proper viscosity (6 800 mPa·s) for fine meshes. The selected mesh & frame that were used for the printing test are suitable for printing fine half-tones, designs and artworks. Colorimetry proved the repeatability of the color reproduction on prints.

5.1 The printed artwork

The artwork, to be reproduced by the Egyptian blue ink, represents the printing press Daemon (Titivilus) and it is engraved on linoleum plate (Figure 12). Titivilus is known for its involvement in most typographical and non-typographical errors throughout publishing and printing science. The best of the few original prints, were scanned, resized, digitized and processed to produce a positive readable film. Artwork was converted into two different files in order to render the form and the counter form of Titivilus after a minimal imprint was applied to the boundaries of the two areas (trapping).

Figure 12: Prototype & printing result by industrial & Egyptian ink

With this technique Titivilus could be hidden under a blue background, which would bring its image to the near-infrared (NIR) spectrum. Additionally, the Egyptian blue ink has different luminosity in the near IR spectrum compared to the industrial pantone ink so this characteristic separates the different areas of the blue printed background surface. The Egyptian blue ink produced, was tested by printing spot areas on which the color was identified with a Gretag Macbeth Spectro-Eye Spectrophotometer under 2°/D65/ No Filter conditions while color difference (ΔE_{00}) was calculated using the CIEDE2000 equation.

The same color ($\Delta E_{00} \leq 3.0$) was then produced by industrial silk-screen printing inks. Both inks were used to print the Titivilus form and its counter form so that in the visible spectrum the overall image appears as an overall flat rectangular blue surface. Titivilus is essentially hidden from our eyes in visible light. Titivilus finally appears only under near infrared (830 nm) spectrum.

5.2 Final formulation of printing ink

Two inks had been produced for the printing of Titivilus: one industrial ink, visually similar to the one measured and produced following the Egyptian Blue CIELAB values, and the actual Egyptian Blue ink based on the ceramic pigment.

The ceramic pigment ink (with a particle size of less than 30 μm) was produced using the pigment and industrial printing rheology additives, optimizers and antistatic fluids. After several experimentations the following recipe was characterized as the optimal one and is described on the Table 3 below.

Table 3: Composition recipe of Egyptian blue ink

Base/binder	Super Gloss Vinyl	70 g
Colorant	Ceramic Kyano/Egyptian Blue	20 g
Retarder	Thixogel retr.	5 g
Solvent	102 M Diluents	5 g
Total		100 g

6. Printing of Titivilus with both industrial and ceramic-based inks

The produced copies were printed on opal paper 250 g/m² in a handcrafted Vi.Sta silk-screen printing machine. Each copy was placed in the corner signs in order to achieve perfect registration. After drying, samples (indicative of 5 random copies) were measured (CIELAB colorimetry) in 3 specific areas (α, β, γ) and the CIE L*a*b* values are noted in Table 4 and marked in Figure 13.

*Table 4: Colorimetric measurement of Egyptian blue (CIE L*a*b* color space)*

Sample 1	Sample 2	Sample 3	Sample 4	Sample 5	Average CIE *L* a* b* Final Values
$L\alpha$: 53.52	$L\alpha$: 55.70	$L\alpha$: 55.35	$L\alpha$: 55.22	$L\alpha$: 55.24	
$L\beta$: 52.15	$L\beta$: 55.42	$L\beta$: 55.37	$L\beta$: 55.27	$L\beta$: 55.50	
$L\gamma$: 52.17	$L\gamma$: 54.94	$L\gamma$: 56.87	$L\gamma$: 54.74	$L\gamma$: 55.00	
$LS1$: 52.61	$LS2$: 55.35	$LS3$: 56.19	$LS4$: 55.07	$LS5$: 55.24	*L* Egyptian: 54.80
$a\alpha$: −9.55	$a\alpha$: −9.42	$a\alpha$: −9.14	$a\alpha$: −9.53	$a\alpha$: −9.58	
$a\beta$: −9.63	$a\beta$: −9.72	$a\beta$: −9.49	$a\beta$: −9.27	$a\beta$: −9.66	
$a\gamma$: −10.04	$a\gamma$: −9.59	$a\gamma$: −9.50	$a\gamma$: −9.48	$a\gamma$: −9.59	
$aS1$: −9.74	$aS2$: −9.57	$aS3$: −9.37	$aS4$: −9.42	$aS5$: −9.61	*L* Egyptian: −9.54
$b\alpha$: −48.82	$b\alpha$: −46.94	$b\alpha$: −46.85	$b\alpha$: −47.49	$b\alpha$: −47.29	
$b\beta$: −50.11	$b\beta$: −47.72	$b\beta$: −47.38	$b\beta$: −46.99	$b\beta$: −47.79	
$b\gamma$: −49.73	$b\gamma$: −47.72	$b\gamma$: −46.32	$b\gamma$: −47.54	$b\gamma$: −47.85	
$bS1$: −49.55	$bS2$: −47.46	$bS3$: −46.85	$bS4$: −47.34	$bS5$: −47.64	*L* Egyptian: −47.76

Figure 13: Specific areas of the reproduction where CIELAB values were measured

The form of Titivilus was printed by the Egyptian blue ink while the counter-form was printed with the Industrial ink.

Table 4 shows a stable repetition of the printing production with Egyptian blue ink and the stability of the ink structure based on the good dispersion of the pigment in the binder of the produced ink.

In order to produce the industrial ink, one basic condition had to be met: the color difference between the industrial ink and the Egyptian blue – ceramic ink, should be at $\Delta E_{00} < 3.00$.

When a $\Delta E_{00} < 5$ has been achieved (with the comparison with the reference print of the Egyptian Blue ink), the recipe was recorded and gradually corrected (Figure 14). At this point, 5 printed samples have been measured at the same areas α, β, γ. Their CIELAB values and their difference with the measured points of the Egyptian samples are presented in Table 5.

Figure 14: Comparison between Lab values of Egyptian blue and industrial printing ink

Table 5: production of industrial ink in CIELAB color space

Sample 1	Sample 2	Sample 3	Sample 4	Sample 5
Lα: 59.23	*Lα*: 55.84	*Lα*: 56.88	*Lα*: 57.40	*Lα*: 56.12
Lβ: 59.28	*Lβ*: 55.03	*Lβ*: 57.52	*Lβ*: 56.88	*Lβ*: 55.12
Lγ: 60.32	*Lγ*: 55.08	*Lγ*: 58.09	*Lγ*: 57.10	*Lγ*: 55.03
LS1: 59.61	*LS2*: 55.32	*LS3*: 57.32	*LS4*: 57.12	*LS5*: 55.42
aα: −9.55	*aα*: −10.86	*aα*: −12.72	*aα*: −11.45	*aα*: −10.83
aβ: −9.63	*aβ*: −10.61	*aβ*: −11.94	*aβ*: −11.54	*aβ*: −10.81
aγ: −10.04	*aγ*: −10.98	*aγ*: −12.42	*aγ*: −11.44	*aγ*: −10.99
aS1: −9.74	*aS2*: −10.81	*aS3*: −12.28	*aS4*: −11.47	*aS5*: −10.87
bα: −48.82	*bα*: −44.17	*bα*: −45.08	*bα*: −44.00	*bα*: −43.90
bβ: −50.11	*bβ*: −44.55	*bβ*: −43.72	*bβ*: −44.84	*bβ*: −45.16
bγ: −49.73	*bγ*: −45.09	*bγ*: −43.74	*bγ*: −43.93	*bγ*: −45.44
bS1: −48.22	*bS2*: −44.60	*bS3*: −44.17	*bS4*: −44.25	*bS5*: −44.83

As it is observed in Table 5, the S5 industrial ink derived from Table 4, meets the condition where ΔE_{00} is under 3 and in particular it has been measured at $\Delta E_{00} = 2.76$. The S5 industrial ink recipe was recorded and used for the screen-printing reproduction of the counter form of Titivilus.

7. Verification of Egyptian blue printing by observation with VIL imaging technique

To detect photoluminescence of the printed Egyptian blue, an DSLR camera (Nikon D3200) was used with a special modification by removing the factory UV/IR cut filter (Verri, 2008; 2009).

Special infrared filters of the following types: Massa IR Filter 850 nm, Hoya IR Filter R72/720 nm and B+W 093/830 nm were alternatively installed to observe the infrared region. This methodology is applied in the detection of traces of egyptian blue in ancient Greek sculptures (Katsaros, 2017; Katsaros and Vasiliadis, 2019).
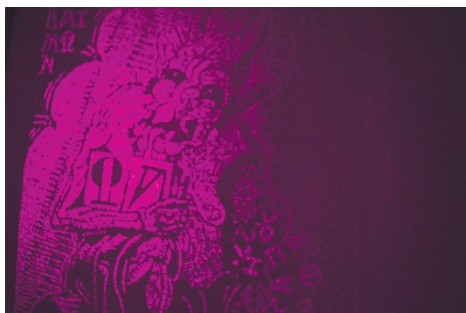
Figure 15: Identification of the Egyptian blue printed areas via VIL imaging technique

The optimum experimental results were obtained using the IR filter B+W of 830 nm. The most-strong fluorescense of egyptian blue had observed by use of the specific IR filter (830 nm). The used radiation source of the observation of silkscreen reproduction was the PAR64 LED/RGB with cool light bulbs.

The project has been quite successful, since VIL observation proved that both experimental process and scientific methodology applied were correct. For the observation and evaluation of the phenomenon of photo-luminescense we used the Color-Checker-Passport of Munsell for white balance (Verri, 2008). The use of Color Checker exludes the possibility of reflectance and the white brightness during the observation was derived by the fluoresecence of Egyptian blue in the area of infrared. Egyptian blue ceramic pigment was identified on several silkscreen prints due to the photo-luminescence characteristics. The other blue color on the silkprint with the same hue was remained dark in the background.

8. Conclusions

In this study it was proved that by following the SCS procedure it was possible to produce artificial Egyptian blue pigments with the same color characteristics as the one produced by the traditional techniques. This procedure proved to be quite effective in respect with economical, energy-efficient and environmental issues.

The formulated inks were used in screen printing technique and had been proven quite accurate for the purposes of artwork printing and anti-counterfeited printing due to their photo-luminescence abilities.

References

Hatton, G.D., Shortland, A.J., and Tite, M.S., 2008, The production technology of Egyptian blue and green frits from second millennium BC Egypt and Mesopotamia. *Journal of Archaeological Science*, 35(6), pp. 1591–1604. https://doi.org/10.1016/j.jas.2007.11.008.

Katsaros, T., 2017. *Aníchnefsi tou aigyptiakoú kyanoú me efarmogí tis technikís VIL (visible induced luminescence - imaging technique)*. [online] Available at: <https://fespahellas.gr/aigyptiako-kyano/> [Accessed 1 March 2021]. [In English: *Detection of the Egyptian blue using the VIL technique (visible induced luminescence - imaging technique*].

Katsaros, T. and Vasiliadis, C., 2019. Polychromy in Greek sculpture. In: O. Palagia, ed. *Volume 1 Handbook of Greek sculpture*. Berlin, Boston: De Gruyter. Ch. 22, pp. 690–724. https://doi.org/10.1515/9781614513537-022.

Kostomitsopoulou Marketou, A., Andriulo, F., Steindal, C. and Handberg, S. 2020. Egyptian Blue pellets from the First Century BCE Workshop of Kos (Greece): microanalytical investigation by optical microscopy, scanning electron microscopy-X-ray energy dispersive spectroscopy and micro-Raman spectroscopy. *Minerals*, 10(12): 1063. https://doi.org/10.3390/min10121063.

Lazzarini, L., 1982, The discovery of Egyptian blue in a Roman fresco of the mediaeval period (ninth century A.D.)*. Studies in Conservation*, 27(2), pp. 84–86. https://doi.org/10.1179/sic.1982.27.2.84.

Panagopoulou, A., Karanasios, K. and Xanthopoulou, G., 2016. Ancient Egyptian Blue ($CaCuSi_4O_{10}$) pigment by modern solution combustion synthesis method*. Eurasian Chemico-Technological Journal*, 18(1), pp. 31–37. https://doi.org/10.18321/ectj390.

Pavlou, E., Xanthopoulou, G., Tsigonias, M. and Vekinis, G., 2015, Solution combustion synthesis of luminescent pigments based on the systems Co-Al-Mg-Ba-O, Co-Al-B-O and Co-Ba-B-O for ink applications. In: *International Symposium on Self-Propagating High-Temperature Synthesis – SHS.* Antalya, Turkey. https://doi.org/10.13140/RG.2.1.4585.6081.

Levidis, A., ed., 1994. *Peri tis archaias Ellinikis zografikis: 35o vivlio tis "Fysikis istorias", by Pliny the Elder*. Translated from Latin by A. Levidis and T. Roussos. Athens, Greece: Agra Publications. [In English: *About ancient Greek painting 35th book of "Natural history", by Pliny the Elder*].

Theophrastus, 1965. *De lapidus*. Translated and edited by D.E, Eichholz. Oxford: Clarendon Press.

Theophrastus, 1993. *Peri lithon*. Translated by A. Katerinopoulou. Athens, Greece. [In English: *On stones*].

Tite, M.S., Bimson, M. and Cowell, M.R., 1984. Technological examination of Egyptian blue. In: J.B. Lambert, ed. *Archaeological chemistry – III: Advances in Chemistry Series No. 205*. Washington, DC: American Chemical Society. Ch. 11, pp. 215–242. https://doi.org/10.1021/ba-1984-0205.ch011.

Verri, G., 2008. The use and distribution of Egyptian blue: a study by visible-induced luminescence imaging. In: K. Uprichard and A. Middleton, eds. *The Nebamun wall paintings*. London, UK: Archetype, pp. 41–50.

Verri, G, 2009. The spatially resolved characterisation of Egyptian blue, Han blue and Han purple by photo-induced luminescence digital imaging. *Analytical and Bioanalytical Chemistry*, 394(4), pp. 1011–1021. https://doi.org/10.1007/s00216-009-2693-0.

Vitruvius, M., 2010. *Perí Architektonikís, Vivlía I-V, VI-X*. Translated by P. Lefas. Athens, Greece: Pletharon. [In English: *On Architecture, Books I-V, VI-X*.].

Carbon black and reduced graphene oxide water-based conductive inks

Apostolos Koutsioukis[1]*, Theodora Philippakopoulou*[2]*, Maria Anastasopoulou*[2]*, Dimitra Giasafaki*[3]*, Christina Mitzithra*[3]*, Theodore Steriotis*[3]*, Georgia Charalambopoulou*[3]*, Vasilios Georgakilas*[1] *and Vassiliki Belessi*[2,4]

[1] Department of Materials Science, University of Patras, Rio, 26504 Greece

[2] Department of Graphic Design and Optical Communication, University of West Attica, Agiou Spyridonos Street, 12243 Egaleo, Athens, Greece

[3] National Centre for Scientific Research "Demokritos", 153 41 Aghia Paraskevi Attikis, Greece

[4] Laboratory of Electronic Devices and Materials, Department of Electrical and Electronic Engineering, University of West Attica, Egaleo, Greece

E-mails: t.steriotis@inn.demokritos.gr; viegeorgaki@upatras.gr; vbelessi@uniwa.gr

Short abstract

This article describes the preparation and characterization of high-quality gravure printable inks based on Carbon Black and reduced Graphene Oxide composites (CB-rGO) composites combined with suitable mixtures of commercial resins. The water-based CB-rGO printing inks showed very good stability, electrical conductivity and printable properties.

Keywords: carbon black, reduced graphene oxide, water-based conductive inks, gravure

1. Introduction and background

Graphene is a flat monolayer of carbon atoms tightly packed into a two-dimensional (2D) honeycomb lattice (Novoselov, et al., 2004). It is known for its high electrical conductivity, mechanical strength and optical properties as well as chemical and thermal stability. It offers significant advantages for a wide range of applications: flexible and wearable electronics, smart sensing, supercapacitors, batteries, conductive inks, protective coatings etc. The most prevalent approach for bulk production of graphene is the reduction of graphene oxide (GO) to obtain the so-called reduced graphene oxide (rGO). GO is a nonconductive hydrophilic carbon material produced by the oxidation of graphite under strong acidic conditions (Dreyer, et al., 2010).

Carbon black (CB) is pure elemental carbon (> 97 %) in the form of near-spherical colloidal particles produced by incomplete combustion or thermal decomposition of hydrocarbons (Buxbaum and Pfaff, 2005) and is one of the most broadly applied black pigments (Donnet, Bansal and Wang, 1993). In printing ink industry, it is widely used also as an additive to adjust the viscosity of inks towards optimum print quality; the finer the CB particles the higher the deep black color and the greater the tinting strength. CB is also combined with various material groups (carbon and non-carbon) in order to improve their mechanical, electrical and optical properties (Yang, et al., 2020). Generally, it is useful for improving conductivity (e.g. in batteries), optimizing viscosity, static charge control and UV protection in coatings, polymer and printing industry.

Most CB grades have an electrical volume resistivity in the range of 10^{-1} $\Omega \cdot cm$ to 10^2 $\Omega \cdot cm$. Special CB grades, the so-called conductive CBs, are used in applications that require low resistivity levels at low CB concentrations (Spahr, Gilardi and Bonacchi, 2017). Various combinations of CB with other carbon materials such as graphite, graphene or rGO have been studied in conductive inks. Phillips, et.al. (2017) developed screen printable carbon inks consisting of graphite, CB and a vinyl polymers and reported that an optimal conductivity (0.029 $\Omega \cdot cm$) was achieved at a graphite to CB ratio of 2.6. Yang, et.al. (2020) de-

scribed the preparation of carbon inks with graphene sheets and CB by a one-pot ball-milling method and the composite ink with a mass fraction of 10 % graphene sheets showed optimized rheological properties for screen printing. The resistivity of the composite coating was 0.23 Ω·cm, which was 30 % of that of a pure CB coating (0.77 Ω·cm) (Yang, et al., 2020). In another work, the electrical conductivity and rheology of screen-printing graphene conductive inks were improved by introducing CB as conductive filler in a way to counteract conductivity reduction due to polymer addition in the ink formulation. The conductivity of the printed patterns was increased by adding CB into the graphene ink formulation and reached the highest values (which were 8–14 times higher than those with graphene only) when the CB content was 15 % (Liu, et al., 2021).

Mixtures of CB and rGO (CB-rGO) have been proposed for preparing supercapacitors (Rapisarda, et al., 2020; Wang, et al., 2014; Yan, et al., 2010) but also for the electrochemical determination of rutin (Lu, et al., 2015) or dopamine and paracetamol (Baccarin, et al., 2017; Ibáñez-Redín, et al., 2018).

However, few works have addressed the use of CB-rGO composites in the formulation of conductive inks. For example, a mixture with a mass ratio CB/rGO ~ 1/5 was proposed for the fabrication of an ink-jet ink with sodium carboxymethyl cellulose as a binder and dispersant (Ji, et al., 2018). The authors claimed that CB particles prevented agglomeration of rGO sheets due to their distribution on the surface of the sheets, and in turn the rGO sheets can bridge the CB particles promoting thus the formation of conductive paths (Ji, et al., 2018; Shukla, et al., 2015).

It is clear that there are some requirements to be met for materials used as pigments in water-based conductive inks. Primarily, the pigments should be highly conductive, with long-term electrical conductivity stability, water dispersible, stable in storage, easily prepared and of low cost (Belessi, et al., 2018). Such pigments are advantageous to be printable by various methods and with high speed, after the tuning of their rheological profile, the selection of the appropriate resins/solvents system and the loading of solids. Concerning, the conductive printing inks formulations should have simultaneously long-term storage stability and long-term electrical conductivity stability with the last to be an important property for the lifetime of the printed devices (Chen, et al., 2018). An important parameter affecting electrical resistance is the percentage of the non conducting constituents in the liquid ink and the dried printed ink film. Apparently, there is an optimum amount of organic matter that is required compared to the conducting ingredients. Besides viscosity, other major properties to be considered during the formulation of conductive inks are surface tension and the wettability of the printing substrate by the ink. In order to afford functional and reliable inks, the forming printed lines should be conductive (regardless whether a post-printing thermal treatment may be necessary or not), as thin as possible, of high resolution and if possible printable in many copies with accuracy and precision. Good adhesion, resistance to weathering conditions (e.g. light, moisture) or acids/alkalis in combination with the demand of leaving the printing machine in an excellent working condition after usage are also important and unquestionable parameters.

In this work, we report a simple preparation method for water-based conductive inks using hybrids of rGO-CB and commercial resin emulsions, in order to enable the upscaled production of conductive composites, with good wettability, flow characteristics, dispersibility, storage stability and low cost. A key property for achieving this goal is the excellent dispersibility of the functionalized rGO used in this study that contributes to a homogeneous and stable CB-rGO suspension. The as prepared conductive inks were printed with the gravure printing process. Selected samples and the optimal ink formulation were extensively characterized by a wide range of methods.

2. Materials and methods

2.1 Materials

Graphite (powder, synthetic, particle size < 20 μm) and 2,4-diaminobenzenesulfonic acid (tech., 90 %) were purchased from Aldrich. Commercial water-based CB printing ink (NFD 029 S 0000), CB powder (4 < pH < 5, no ash content, 94 g/m^2, low oil absorption ability, tint strength 110 %) and the water-based resin emulsion were kindly provided from Druckfarben Hellas S.A. The water-based resin emulsion is a product under development that contains mainly a mixture of styrene–acrylate and acrylic resins named as R-UDP. The solid content of the R-UDP was measured at appr. 42 %. IGT C 2846 paper (coated and calendared) was used as printing substrate.

2.2 Preparation of materials and inks

2.2.1 Preparation of graphene oxide
The GO was synthesized by the modified Staudenmaier method (Poh, et al., 2012).

2.2.2 Functionalization and reduction of graphene oxide
The highly conductive and dispersible functionalized rGO was prepared according to the method reported in Belessi, et al. (2019).

2.2.3 Preparation of CB-rGO slurries
The CB and rGO water dispersions were mixed to produce nine batches of CB-rGO slurries with various CB concentrations (mass fraction of 40, 50, 60, 70, 75, 80, 85, 90, 100 %) as presented in Table 1, in a way to have for each of them the same starting CB content in the same volume of water. The as prepared aqueous CB-rGO slurries were shaken overnight (vortex) and used only for performing the electrical measurements.

2.2.4 Preparation of CB-rGO ink formulations at different resin ratios
For the preparation of CB-rGO ink formulations, the mass fraction of 70 % CB (CB$_{70}$-rGO) sample in the all carbon mixture was opted in favor of the others, for mixing it with a commercial resin emulsion (Zanh Cup 2/DIN4 94′′) and water at two different ratios of total solids, carbon/resin 50/50 and 70/30, respectively. The ink samples were named CB$_{70}$-rGO(50/50) and CB$_{70}$-rGO(70/30), respectively. The inks were prepared by mixing appropriate amounts of the water-based resin emulsion with CB, rGO powders and homogenizing them by a combination of sonication (Branson 3 800, 110 W, 40 kHz) and vortex (Vortexer LLG-uniTEXER with universal attachment, 3 000 rpm) for 5 min. In some cases, industrial equipment (Scandex disperser) was used to optimize ink homogenization. The stage of homogenization plays a decisive role both in the properties of conductive inks and the printing results. Before printing, both the resin emulsion and the selected ink samples CB$_{100}$(70/30), CB$_{70}$-rGO(70/30) and CB$_{70}$-rGO(50/50) were separately applied with the wired K-Bars (RK Print Coat Instruments Ltd., United Kingdom) numbered as 0 and 1 (4 μm and 6 μm wet film deposition, respectively) onto IGT C 2846 paper substrate.

2.2.5 Preparation of CB ink formulations at different resin ratios
Two CB ink formulations were prepared by mixing the CB powder with R-UDP and water at total solids carbon/resin ratios of 50/50 and 70/30; the respective ink samples were named CB$_{100}$(50/50) and CB$_{100}$(70/30).

2.2.6 Preparation of samples for electrical measurements
For the electrical measurements, 30 μL of each of the 9 samples (containing the same mass of the CB-rGO slurry) were deposited on paper as a spot with a surface area of 0.35 cm^2 (200 μg carbon on the spot). The same procedure was followed for measuring the selected ink samples CB$_{70}$-rGO(70/30) and CB$_{70}$-rGO(50/50)

after depositing them on common paper. The samples were compressed at 2 tn according to a previously used protocol (Belessi, et al., 2019).

2.3 Characterization of materials and inks

Field emission scanning electron microscopy (SEM) images were collected on a Hitachi 6600 FEG microscope operating in the secondary electron mode and using an accelerating voltage of 5 kV. The optical spectra were recorded with a Hitachi Digilab, Model U2800-DoubleBeam-UV/Vis. Sheet resistance (R_s) values, of the as deposited CB-rGO slurries and inks were measured by a 4-point probe system (Pro4 Resistivity System, Lucas Labs) and a Keithley 2400 Source Meter. A Zahn flow cup viscometer size 2 (code 2102) was used to measure the viscosity of the R-UDP emulsion. A rotational rheometer (Malvern Kinexus Pro) was used for the rheological characterization of selected inks adapting a cone (40 mm diameter and 4° angle) and plate geometry. The range of shear rate was kept between 0.01 s^{-1} and 1 000 s^{-1} with 10 points per decade interval (i.e. 50 points for each flow curve). Shear rate ramp tests were carried out by monitoring shear viscosity and shear stress as a function of variable shear rate. The temperature was kept constant at 25 °C.

2.4 Gravure printing

The printing tests were carried out using the IGT G1-5 printability tester (IGT Testing Systems). For gravure printing the 402.226 cylinder (60, 80, 100, and 140 lines cm^{-1}, screen angle 53º, stylus angle 130º, and cell volume 16, 11, 9, and 7 ml m^{-2}) was used. The printing force between the engraved disc and the substrate was 200 N and the printing speed was 0.2 m/s.

3. Results and discussion

Even specially treated CB is not dispersible in aqueous solutions (Figure 1, left) and forms aggregates thus making the use of special additives, e.g. surfactants, necessary in order to increase its wettability and dispersibility. In this work, it was found that the addition of a small amount of rGO (a mass fraction of 5 %) improves substantially the dispersibility of CB in water (Figure 1) probably due to the adsorption of rGO nanosheets around CB particles. The CB-rGO hybrid is hydrophilic and can be used in pigmented conductive printing inks with adequate wettability and dispersibility.
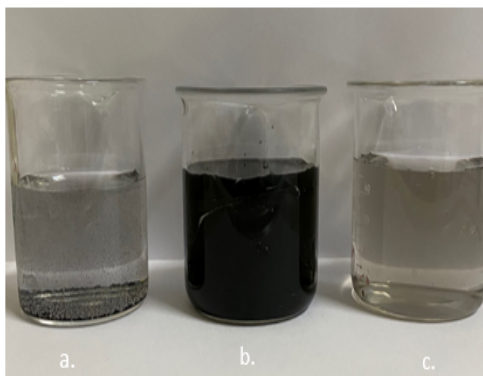
Figure 1: Aqueous dispersions (1.1 mg/ml) of (a) CB (b) CB-rGO hybrid and (c) rGO
after 30 min sonication and 1 day stay

Figure 2 shows the UV-Vis spectra of CB, CB$_{70}$-rGO and rGO dispersions in water as well as the stability of CB$_{70}$-rGO in water. The UV-Vis spectrum of pure CB showed one characteristic absorption broad band at 270 nm due to π−π* transitions. Also, rGO showed two characteristic absorption bands, at 250 nm due to

the π–π* transitions of the aromatic system and at 290 nm due to the n–π* transition of C=O bonds. The hybrid CB_{70}-rGO_{30} showed two bands at 270 nm and 290 nm, due to the coexistence of the two components. A characteristic decrease as regards the scattering that was observed in the UV spectrum of the hybrid material CB_{70}-rGO_{30}, in comparison with that of the pure CB, indicates the improved dispersibility of the hybrid. Furthermore, the stability of the CB_{70}-rGO_{30} aqueous dispersion against agglomeration and sedimentation was evaluated by recording the transmittance of a diluted dispersion for 5 days (Figure 2, right) and was found that the transmittance remained almost stable.
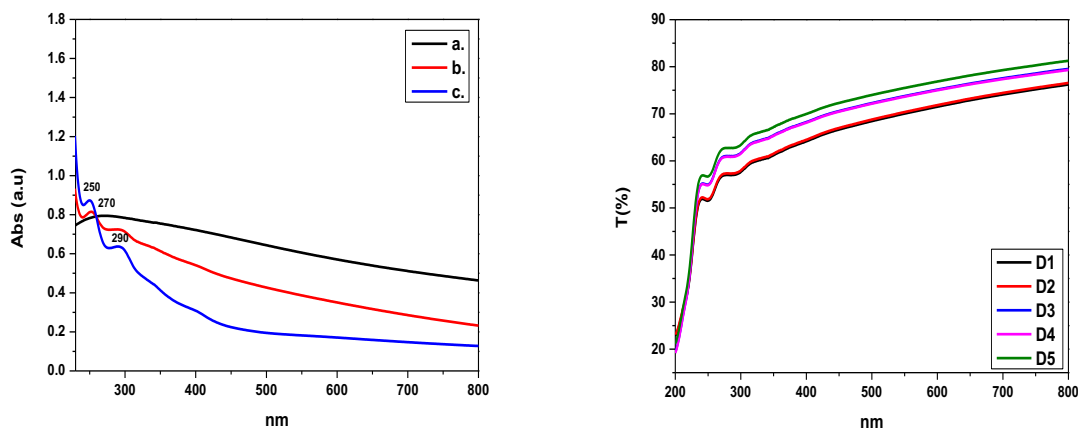

Figure 2: (left) UV-Vis spectra of (a) CB dispersion in water (b) CB_{70}-rGO_{30} dispersion in water (c) rGO dispersion in water and (right) stability of CB_{70}-rGO_{30} in water; day dependence of the transmittance at 550 nm

The electrical behavior of CB-rGO hybrids was studied as a function of CB concentration (Table 1, Figure 3). The R_s of the commercial CB was measured to ~3600 Ω·sq^{-1} (Table 1) and reduced remarkably, after the addition of rGO, as presented in Figure 3. The rate of R_s decrease is significant when increasing the rGO percentage up to 30%. For higher rGO concentrations, R_s decreases further but with a very low rate (Table 1, Figure 3). This trend is attributed to the formation of less resistive pathways between the CB nanoparticles and rGO nanosheets, whereas it seems that an rGO percentage of 30 % is rather sufficient for the formation of such low resistive pathways and a further increase does not offer additional substantial improvement. Our previous studies (Belessi, et al., 2019; Georgakilas, et al., 2015) in accordance with other research works (Hauptman, et al., 2011) have shown that dispersibility has a clear and important effect on the electrical conductivity of the materials, either composites or not. The specific type of CB used in this work is of low structure, and as such it has a low number of particles per aggregate, exhibits weak aggregation and simultaneously it is preferable for the formulation of gravure inks where low viscosity (and medium-sized CB particles) is necessary. Generally, the lower the structure of CB, the lower the conductivity (Buxbaum and Pfaff, 2005). Based on the above, the CB_{70}-rGO sample was selected as the most suitable one for further mixing with resins used in printing industry, as it combines satisfactory conductivity and lower printing cost.
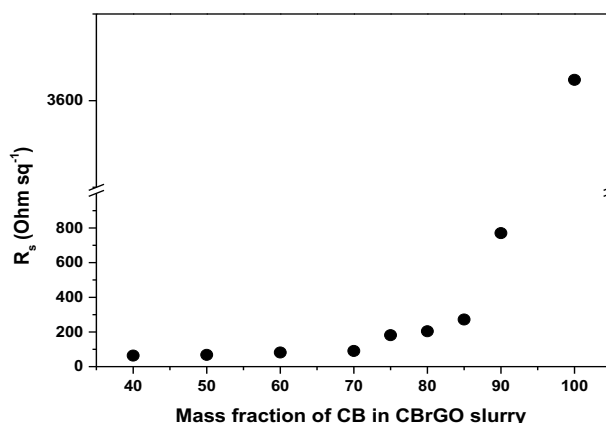
Figure 3: Sheet resistance (R_s) as a function of a mass fraction % of CB in the CB-rGO slurry

Table 1: R_s values of the CB-rGO samples as a function of a mass fraction % of CB and selected inks CB_{70}-rGO(70/30) and CB_{70}-rGO(50/50)

	Mass fraction % of CB	R_s ($\Omega \cdot sq^{-1}$)	Ink CB_{70}-rGO (50/50) R_s ($\Omega \cdot sq^{-1}$)	Ink CB_{70}-rGO (70/30) R_s ($\Omega \cdot sq^{-1}$)
CB_{100}	100	3624		
CB_{90}-rGO	90	770		
CB_{85}-rGO	85	272		
CB_{80}-rGO	80	204		
CB_{75}-rGO	75	181		
CB_{70}-rGO	70	91	312	122
CB_{60}-rGO	60	81		
CB_{50}-rGO	50	68		
CB_{40}-rGO	40	63		

Figure 4 includes representative SEM images of the CB_{70}-rGO hybrid (Figure 4, left) and the CB_{70}-rGO(70/30) ink, showing high homogenization between CB clusters (composed of spherical particles) and rGO nanosheets in the resin (Figure 4, right). This uniform distribution of the rGO sheets between the abundant CB particles provides electrical contact between the planes of rGO sheets and/or CB clusters, leading to R_s ~ 122 $\Omega \cdot sq^{-1}$ for the CB_{70}-rGO(70/30) ink (Figure 5b). The R_s for the CB_{70}-rGO(50/50) was almost 312 $\Omega \cdot sq^{-1}$ (Figure 5c).

Figure 4: SEM images of CB_{70}-rGO_{30} slurry in water (up and left), CB_{70}-rGO(70/30) ink (up and right), gravure printed pattern of CB_{70}-rGO(70/30) ink (down)

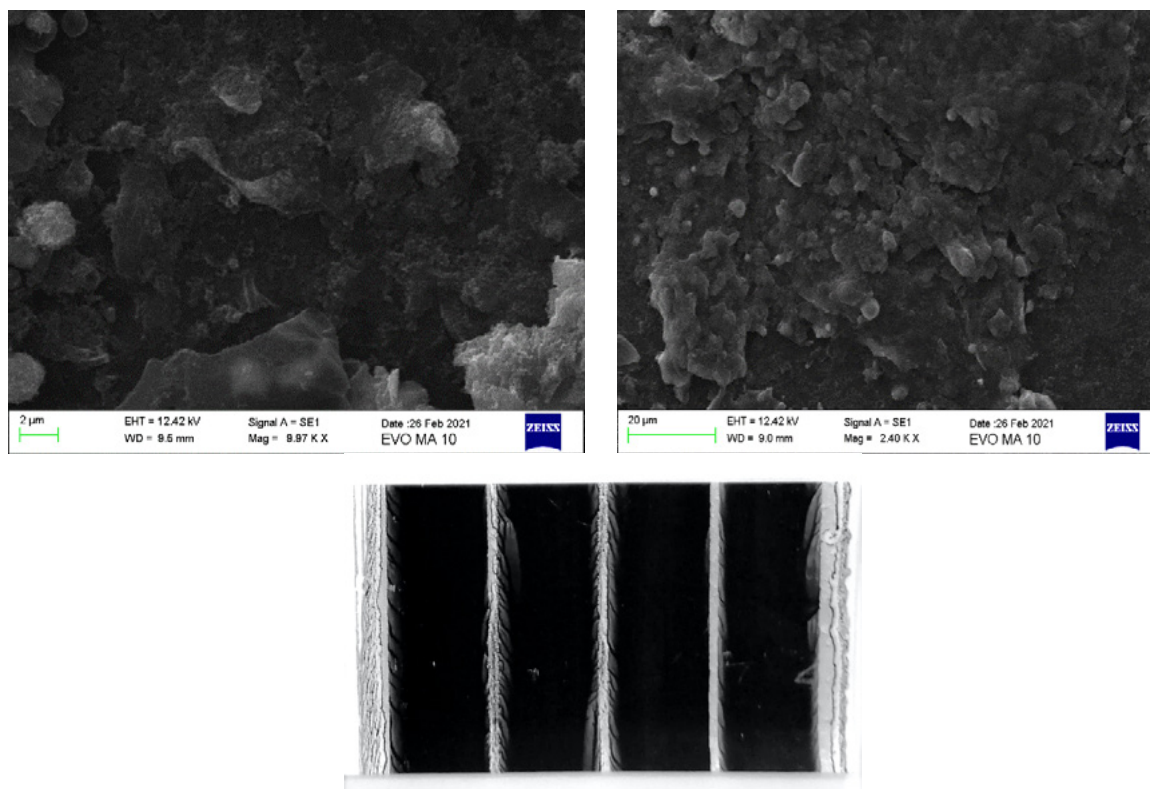*Figure 5: The R_s measurements of: (a) CB_{70}-rGO slurry, (b) CB_{70}-rGO(70/30) ink, and (c) CB_{70}-rGO(50/50) ink*

As expected from the SEM results, all tested inks (Table 2) applied with K-Bar 0 and 1 gave similar, encouraging results. Comparing all the gravure printed patterns, we observed that the printing properties follow the order: NFD 029 S 0000 > CB_{100}(70/30) ≥ CB_{70}-rGO(70/30) >> CB_{70}-rGO(50/50) (Table 2). It is obvious that the low-structure CB used in this work can achieve high quality of jetness and gloss on the coated and calendered paper and simultaneously improves significantly the printing properties of the rGO-CB inks. The importance of the ratio of total solids carbon per total solids resin for the print quality becomes evident from the images of Table 2 and Figures 6 and 7. The great printing result of CB_{70}-rGO(70/30) ink is also due to the connections between the rGO sheets and CB particles. Viscous fingering is observed for the CB_{70}-rGO(50/50) ink in the printed film (parallel to the print direction) that becomes more evident as the cell volume decreases (Table 2, Figure 6). These formation defects are commonly seen in functional printing (Hartwig, et al., 2018; Baker, et al., 2014; Sauer, Bornemann and Dörsam, 2011; Casademunt, 2004).

Also, CB_{70}-rGO(70/30) was estimated to yield the lowest resistance with a value of 3 kΩ (V/I) by a digital multimeter, which was used to measure the resistance of all the printed patterns while keeping the probe distance constant at 1 cm. The typical R_s values show that CB_{70}-rGO materials/inks can find applications as micro-heating devices (Barmpakos, et al., 2021a), temperature (Barmpakos, et. al., 2021b), strain (Le Borgne, et al., 2019) and tactile sensors (Miao, et al., 2019) as well as radio frequency (RF) antennas printed on flexible substrates.

The study of the rheological properties of all inks showed that they exhibit shear thinning properties (Figure 6), i.e. the viscosity decreases as shear rate and shear stress increase. For inks, shear thinning is desirable and occurs over a wide range of applied shear since under storage conditions shear rates are very low, while at the printing head shear rates are very high (Zhang, Sullivan and Bose, 2020). The commercial ink shows a lower shear thinning rate than the prepared inks, which can be attributed to the rheology additives used (Figure 8). Between the CB_{70}-rGO(70/30), CB_{70}-rGO(50/50) inks, the one with the higher resin content (50-50) shows higher viscosity values, as expected.

Table 2: Scanned images of all the gravure printed patterns

Samples	KB0 and KB1 4 µm and 6 µm wet film deposition	Gravure printed patterns Cell volume (ml·m⁻²)			
		16	11	9	7
NFD 029 S 0000 Commercial water-based printing ink					
CB$_{100}$(70/30)					
CB$_{70}$-rGO(70/30)					
CB$_{70}$-rGO(50/50)					

Print direction

Figure 6: Representative detail of the gravure printed pattern with the CB$_{70}$-rGO(50/50) ink for cell volume 9 ml·m⁻²
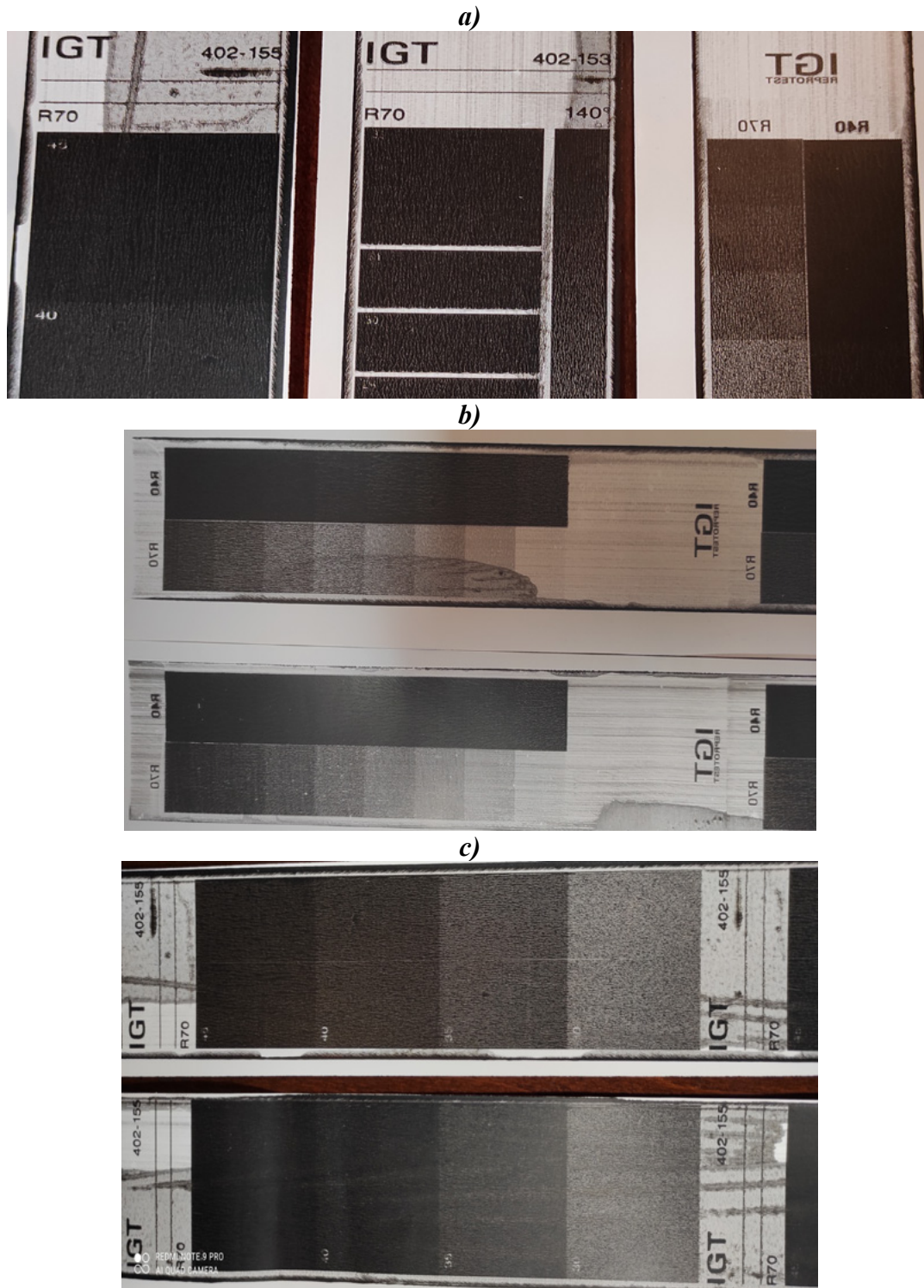
Figure 7: (a) Several patterns printed by gravure printing with the CB_{70}-rGO(70/30) ink on IGT C 2846 paper using the 402-155, 402-153 and 402-100 cylinders with cylinder pressure 200 N and print speed 0.2 m/s (b, c), the same pattern printed with the (Upper) CB_{70}-rGO(50/50) and (Down) CB_{70}-rGO(70/30) inks
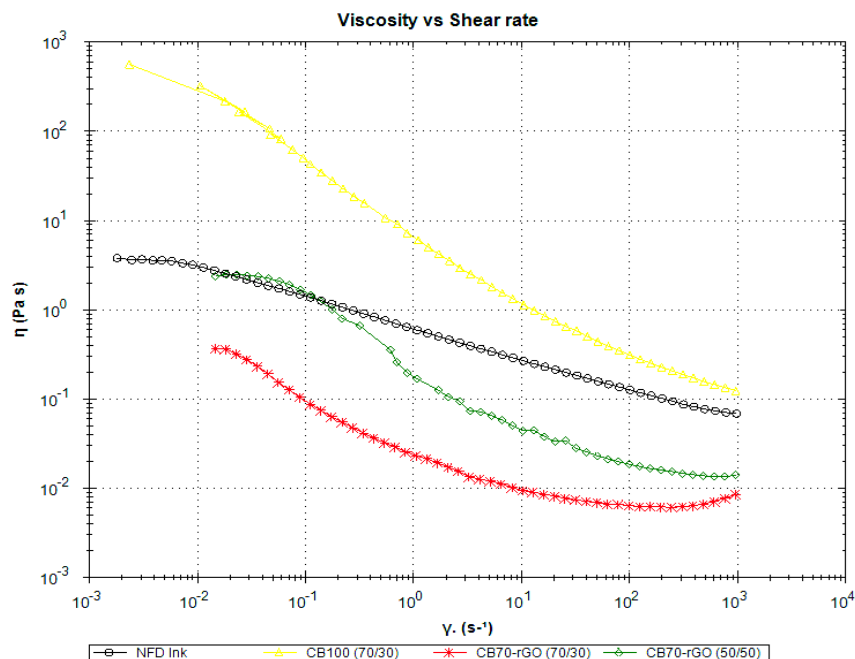
Figure 8: Viscosity (η) versus shear rate (γ), for the NDF commercial ink, the prepared $CB_{100}(70/30)$, CB_{70}-rGO(70/30) and CB_{70}-rGO(50/50) inks

4. Conclusions

The as prepared CB-rGO composites and especially the sample CB_{70}-rGO(70/30) satisfies many require-ments (e.g. dispersibility, conductivity) for conductive ink applications. The final conductive gravure ink possesses good flow characteristics, good conductivity, storage stability while its cost is low. In terms of the printed patterns, high quality of jetness, hiding power and gloss on the coated and calandered paper was achieved.

Acknowledgments

References

Baccarin, M., Santos, F.A., Vicentini, F.C., Zucolotto, V., Janegitz, B.C. and Fatibello-Filho, O., 2017. Electrochemical sensor based on reduced graphene oxide/carbon black/chitosan composite for the simultaneous determination of dopamine and paracetamol concentrations in urine samples. *Journal of Electroanalytical Chemistry*, 799, pp. 436–443. https://doi.org/10.1016/j.jelechem.2017.06.052.

Baker, J., Deganello, D., Gethin, D.T. and Watson, T.M., 2014. Flexographic printing of graphene nanoplatelet ink to replace platinum as counter electrode catalyst in flexible dye sensitised solar cell. *Materials Research Innovations*, 18(2), pp. 86–90. https://doi.org/10.1179/1433075X14Y.0000000203.

Barmpakos, D., Belessi V., Schelwald, R. and Kaltsas, G., 2021a. Flexible Graphene-based inkjet- printed heaters. In: *Micro and Nano Engineering Conference 2021*. Turin, Italy, 20–23 September 2021. (Accepted for presentation).

Barmpakos, D., Belessi, V., Schelwald, R. and Kaltsas, G., 2021b. Evaluation of inkjet-printed reduced and functionalized water-dispersible graphene oxide and graphene on polymer substrate – application to printed temperature sensors. *Nanomaterials*, 11(8): 2025. https://doi.org/10.3390/nano11082025.

Belessi, V., Georgakilas, V., Petridis, D., Steriotis Th., Nomikos, S., 2018. Conductive inks with applications to functional printing. *Hyfen* (In English: *Hyphen*), 11(17), pp. 103–116.

Belessi, V., Petridis, D., Steriotis T., Spyrou, K., Manolis, G.K., Psycharis, V. and Georgakilas, V., 2019. Simultaneous reduction and surface functionalization of graphene oxide for highly conductive and water dispersible graphene derivatives. *SN Applied Sciences*, 1: 77. https://doi.org/10.1007/s42452-018-0077-9.

Buxbaum, G. and Pfaff, G. eds., 2005. *Industrial inorganic pigments*. 3rd ed. Weinheim, Germany: Wiley-VCH, pp. 163–194.

Casademunt, J., 2004. Viscous fingering as a paradigm of interfacial pattern formation: recent results and new challenges. *Chaos*, 14(3): 809, pp. 809–824. https://doi.org/10.1063/1.1784931.

Chen, Q., Zhong, Y., Zhang, Z., Zhao, X., Huang, M., Zhen, Z., He, Y. and Zhu, H., 2018. Long-term electrical conductivity stability of graphene under uncontrolled ambient conditions. *Carbon,* 133, pp. 410–415. https://doi.org/10.1016/j.carbon.2018.03.056.

Donnet, J.-B., Bansal, R.C. and Wang, M.-J., 1993. *Carbon black: science and technology*. 2nd ed. New York, NY, USA: Marcel Dekker.

Dreyer, D.R., Park, S., Bielawski, C.W. and Ruoff, R.S., 2010. The chemistry of graphene oxide. *Chemical Society Reviews*, 39(1), pp. 228–240. https://doi.org/10.1039/B917103G.

Georgakilas, V., Demeslis, A., Ntararas, E., Kouloumpis, A., Dimos, K., Gournis, D., Kocman, M., Otyepka, M. and Zbořil, R., 2015. Hydrophilic nanotube supported graphene–water dispersible carbon superstructure with excellent conductivity. *Advanced Functional Materials*, 25(10), pp.1481–1487. https://doi.org/10.1002/adfm.201403801.

Hartwig, T., Siesel, T., Sauer, H.M., Dörsam, E., 2018. Controlling film formation of functional organic materials in gravure printing by using temperature-controlled substrate carriers. In: *19th International Coating Science and Technology Symposium*. Long Beach, CA, USA, 16–19 September 2018.

Hauptman, N., Klanjšek Gunde, M., Kunaver, M. and Bešter-Rogač, M., 2011. Influence of dispersing additives on the conductivity of carbon black pigment dispersion. *Journal of Coating Technology Research*, 8(5), pp. 553–561. https://doi.org/10.1007/s11998-011-9330-5.

Ibáñez-Redín, G., Wilson, D., Gonçalves, D. and Oliveira Jr, O.N., 2018. Low-cost screen-printed electrodes based on electrochemically reduced graphene oxide-carbon black nanocomposites for dopamine, epinephrine and paracetamol detection. *Journal of Colloid and Interface Science*, 515, pp. 101–108. https://doi.org/10.1016/j.jcis.2017.12.085.

Ji, A., Chen, Y., Wang, X. and Xu, C., 2018. Inkjet printed flexible electronics on paper substrate with reduced graphene oxide/carbon black ink. *Journal of Materials Science: Materials in Electronics*, 29, pp. 13032–13042. https://doi.org/10.1007/s10854-018-9425-1.

Le Borgne, B., Chung B.-Y., Tas M.O., King S.G., Harnois M. and Sporea R.A., 2019. Eco-friendly materials for daily-life inexpensive printed passive devices: towards "do-it-yourself" electronics. *Electronics*, 8(6): 699. https://doi.org/10.3390/electronics8060699.

Liu, L., Shen, Z., Zhang, X. and Ma, H., 2021. Highly conductive graphene/carbon black screen printing inks for flexible electronics. *Journal of Colloid and Interface Science*, 582(Part A), pp. 12–21. https://doi.org/10.1016/j.jcis.2020.07.106.

Lu, L., Zhang, F., Xia, J., Wang, Z., Liu, X. and Yuan, Y., 2015. Conductive carbon black-graphene composite for sensitive sensing of rutin. *International Journal of Electrochemical Science*, 10(2), pp. 1646–1657.

Miao, P., Wang, J., Zhang, C., Sun, M., Cheng, S. and Liu, H., 2019. Graphene nanostructure-based tactile sensors for electronic skin applications. *Nano-Micro Letters,* 11: 71. https://doi.org/10.1007/s40820-019-0302-0.

Novoselov, K.S., Geim, A.K., Morozov, S.V., Jiang, D., Zhang, Y., Dubonos, S.V., Grigorieva, I.V. and Firsov, A.A., 2004. Electric field effect in atomically thin carbon flms. *Science*, 306(5696), pp. 666–669. https://doi.org/10.1126/science.1102896.

Phillips, C., Al-Ahmadi, A., Potts, S.-J., Claypole, T. and Deganello, D., 2017. The effect of graphite and carbon black ratios on conductive ink performance. *Journal of Materials Science*, 52(16), pp. 9520–9530. https://doi.org/10.1007/s10853-017-1114-6.

Poh, H.L., Šaněk, F., Ambrosi, A., Zhao, G., Sofer, Z. and Pumera, M., 2012. Graphenes prepared by Staudenmaier, Hofmann and Hummers methods with consequent thermal exfoliation exhibit very different electrochemical properties. *Nanoscale*, 4(11), pp. 3515–3522. https://doi.org/10.1039/C2NR30490B.

Rapisarda, M., Damasco, A., Abbate, G. and Meo, M., 2020. Carbon black and reduced graphene oxide nanocomposite for binder-free supercapacitors with reduced graphene oxide paper as the current collector. *ACS Omega*, 5(50), pp. 32426-32435. https://doi.org/10.1021/acsomega.0c04530.

Sauer, H.M., Bornemann, N., Dörsam, E. 2011. Viscous fingering in functional flexo printing: an inevitable bug? In: *Proceedings of the Large-Area, Organic & Printed Electronics Convention (LOPE-C)*. Frankfurt, Germany, 28–30 June 2011.

Shukla, S., Domican, K., Karan, K., Bhattacharjee, S. and Secanell, M., 2015. Analysis of low platinum loading thin polymer electrolyte fuel cell electrodes prepared by inkjet printing. *Electrochimica Acta*, 156, pp. 289–300. https://doi.org/10.1016/j.electacta.2015.01.028.

Spahr, M.E., Gilardi, R. and Bonacchi, D., 2017. Carbon black for electrically conductive polymer applications. In: R. Rothon, ed. *Fillers for polymer applications*. Cham, Switzerland: Springer, pp. 375–400. https://doi.org/10.1007/978-3-319-28117-9_32.

Wang, Y., Chen, J., Cao, J., Liu, Y., Zhou, Y., Ouyang, J.-H. and Jia, D., 2014. Graphene/carbon black hybrid film for flexible and high rate performance supercapacitor. *Journal of Power Sources*, 271, pp. 269–277. https://doi.org/10.1016/j.jpowsour.2014.08.007.

Yan, J., Wei, T., Shao, B., Ma, F., Fan, Z., Zhang, M., Zheng, C., Shang, Y., Qian, W. and Wei, F., 2010. Electrochemical properties of graphene nanosheet/carbon black composites as electrodes for supercapacitors. *Carbon*, 48(6), pp. 1731–1737. https://doi.org/10.1016/j.carbon.2010.01.014.

Yang, X., Li, X.-M., Kong, Q.-Q., Liu, Z., Chen, J.-P., Jia, H., Liu, Y.-Z., Xie, L.-J. and Chen, C.-M., 2020. One-pot ball-milling preparation of graphene/carbon black aqueous inks for highly conductive and flexible printed electronics. *Science China Materials*, 63(3), pp. 392–402. https://doi.org/10.1007/s40843-019-1210-3.

Zhang, Y., Sullivan, J.P. and Bose, A., 2020. Rheological and microstructural characterization of aqueous suspensions of carbon black and reduced graphene oxide. *Colloids and Surfaces: A Physicochemical and Engineering Aspects*, 592: 124591. https://doi.org/10.1016/j.colsurfa.2020.124591.

Glucomannan for food packaging biofilms: faceting of the polymer film

Kholoud Al-Ajlouni, Paul D. Fleming and Alexandra Pekarovicova

Chemical and Paper Engineering, Western Michigan University, USA
E-mails: kholoudsaleh.alajlouni@wmich.edu, dan.fleming@wmich.edu, a.pekarovicova@wmich.edu

Short abstract

Glucomannan, a natural hemicellulose that comes from the roots of a plant called Konjac, is a promising material for food packaging and printed electronics films. Unlike petroleum-based films, glucomannan films are biodegradable, safe, and eco-friendly. Glucomannan films should be transparent, clear, create water vapor and oxygen barrier and have good mechanical properties. In this work, the films were formulated from three constituents: glucomannan, surfactant and a plasticizer. Mixing the ingredients was done at a constant temperature at 35 °C and 6 000 rpm. Upon drying in an Environmental Chamber (50 °C and 11.4 % RH and 18–36 hours); after 3 hours, the films, showed shape transformation and surfactant freezing and depositing on the glucomannan-water interface. This deformation structure had shapes that looked like polygons and long fibers. This is faceting of the droplets of glucomannan gel solution during the slow cooling process or so called interfacial freezing phenomena. Faceting of the glucomannan gel droplets reduced the film's clarity, strength, and vapor's permeability, these deformed films are not suitable for packaging nor for printed electronics. We found that for a successful film formation, controlling the reaction temperature of the components at 40 °C and the drying conditions in an Environmental chamber (57 °C and 35 % relative humidity) is necessary.

Keywords: glucomannan, faceting, transparent, stretch wrapping biofilms, packaging, Surfynol 104H

1. Introduction and background

Wrapping films used in packaging of food, electronics, or other items are stretch elastic films that keep items firmly bound during storage or transportation. Commonly, they are made from linear low-density polyethylene (LLDPE) or other petroleum-based chemicals. Biofilms are synthesized from natural biomasses; they are eco-friendly, biodegradable, and they degrade naturally and faster (Rhim and Ng, 2007; Honarvar, Hadian and Mashayekh, 2016). One of possible materials to create these biofilms is glucomannan. Glucomannan is a hemicellulose mainly extracted from the roots of Konjac or elephant yam plant; it is a hetero polysaccharide which contains different saccharides, such as mannose and glucose. Its backbone consists of linked β-D-1→4-D-manopyranose and D-glucose, which are often acetylated (Scheller and Ulvskov, 2010) as shown in Figure 1.
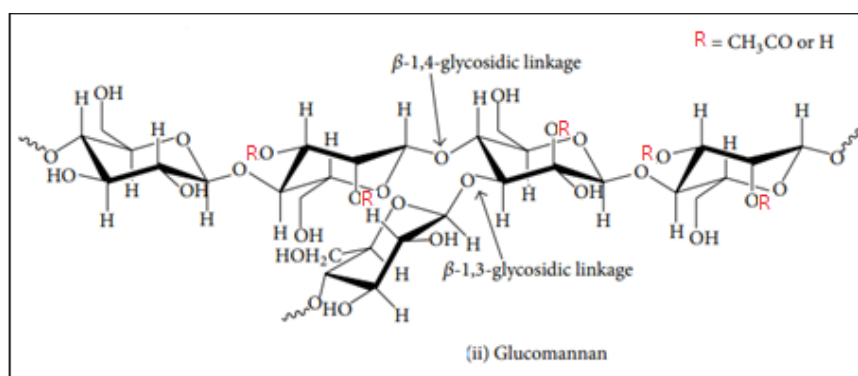
Figure 1: The chemical structure of glucomannan (Lee, Hamid and Zain, 2014)

Packaging films from hemicelluloses are safe, inexpensive and considered as oxygen barriers; however, they lack proper mechanical and water barrier properties (Jonas, 2006). To reinforce the strength, composite films from glucomannan and polymers such as cellulose (Kalia, et al., 2011), micro or Nano-fibrillated cellulose NFC (Lavoine, Desloges and Bras, 2014; Ma, Pekarovicova and Fleming, 2018), or different hemicelluloses (Wang, et al., 2017; Nair, Alummoottil and Moothandasserry, 2017) are added.

For packaging purposes, the rheology of the polymers influences the production and control processes because they behave as liquids and solids at the same time, as called viscoelastic (Triantafillopoulos, 1988). Printing labels on packaging films require smooth surfaces and free from 3D structures. Those requirements apply also for printed electronics (Ma, 2018).

Films were formulated from a polymer, surfactant, and plasticizer at 35 °C, then they must be casted and dried. Drying is an important step of the process, slow cooling of the formed gel could stimulate the transformation of polymer droplets in surfactant solutions into deformed solid shapes. In general, as the temperature is decreased, the droplets of the polymer-surfactant solution in water will undergo changes from spheres into polyhedra (Wong, et al., 2019; Marin, et al., 2020), platelets and finally platelets with a tail (Guttman, et al., 2016; García-Aguilar, et al., 2021; Denkov, et al., 2015). The interface of these deformed droplets had a frozen solid monolayer, once it is formed, it will not be further changed.

The market for bio-based film packaging is growing very fast because the need for biodegradable and sustainable films for packaging is globally recognized. Governments encourage companies to produce non-fossil- based packaging materials by tax exemption of the raw materials and trade regulations. Cellulose based films market is segmented into wrapping films, bags, labels, tapes and others. Several financial reports say that in 2007, the revenue of the packaging from cellulose films was $ 629.8 M and predicting to expand more at a compound annual growth rate of 4.9 % in the period 2018 to 2028, Figure 2.

Figure 2: Worldwide Market of Cellulose film Packaging in 2017, based on application (Cision, 2018)

Countries covered by this market are North America and Europe, which constitute over 40.4 % of the global market in 2018, South Asia, Middle East, Africa and some countries in South America. Examples of the packaging companies are: Bemis Company, Crown Holdings, Reynolds, Celanese corporation, Futamura Chemical Co., Eastman Chemical Company, Sappi limited and others (Cision, 2018). One kilogram of cellulose film ranges from US$ 3.75–4.50 produced by Hubei Golden Ring New Material Tech Co. Ltd, from China, and US$ 0.05 per meter by Masmak Kateryna Piasecka from Poland (Alibaba.com). Up to our knowledge films from hemicellulose, such as Glucomanan or xylan or composite films are still not commercially produced mainly because cellulose based films are stronger and have good barrier properties.

2. Materials and methods

2.1 Materials

Glucomannan from NOW Food Company; Sorbitol from Alfa Desar; Surfynol 104 PA from Air Products and Chemical Inc., and deionized water were used.

In this batch of experiments, a casting method was followed. The dose of the non-ionic Surfynol 104PA surfactant varied from 0 % to 40 % of the glucomannan on mass basis.

2.2 Film formation procedures

1. In a 500 ml beaker, glucomannan was dissolved in 100 ml of deionized, DI, water at room temperature, the beaker was placed in a water bath at 35 °C. A rotary mixer at a speed 6000 rpm was used to mix the solution for 15 minutes. The top of the beaker was covered to prevent evaporation of water.
2. Surfynol 104PA was added to the solution, according to Table 1, and mixed for 3 minutes, and finally Sorbitol was added and mixed for 3 more minutes.
3. For rheology testing, contact angles, surface tensions, samples of 5–10 ml of the gel solution were taken and kept in the water bath until testing. The rest of the gel solution was poured into a previously washed Petri dish by ethylene glycol, and then dried in an Environmental Testing Chamber at 50 °C and 11.4 % Relative Humidity (RH) for 3 hours.
4. The temperature was then changed to TAPPI conditions of 23 °C and 50 % RH for the rest of average drying time, 18–36 hours.
5. The film was peeled off and stored in a plastic bag before testing.
6. Some selected properties were measured, rheological, surface free energies, mechanical and barrier properties.

Table 1: Glucomannan film's formulations

Film	Glucomannan [g]	Surfynol 104 H [g]	Sorbitol [g]
1	1	0.10	0.2
5	1	0.20	0.2
13	1	0.40	0.2
15	1	0.00	0.2
16	1	0.05	0.2

2.3 Density measurement

Density is the first property to be measured for the gels and is needed for calculating the contact angle and the surface free energy; its value is plugged into the software of FTA 200 each time the concentration of the Surfynol 104 H was changed. Gardco stainless steel cups are metallic pycnometers having the exact volume of 8.32 ml at 20 °C. The cup is weighed, with and without the samples, and the density is calculated by dividing the mass difference (g) by 8.32 ml.

2.4 Rheological measurements

An Anton Paar instrument was used. The solution fills a 1 mm gap between two plates, and the rotational speed is selected to produce a shear rate, the rheometer determines the necessary shear stress to deform the gel. Viscosity is determined by the software as the quotient of shear stress and shear rate, different rheogram curves can be produced to illustrate the relation between rheology parameters. The dynamic

viscoelastic measurements of the glucomannan solutions were also carried out by the Anton Paar. The storage and loss shear moduli, G' and G^2, were measured under frequency sweep test, 0.1–628 Hz. The overall rigidity of the solutions is the sum of both moduli. If the storage modulus G' is higher than the loss modulus G^2, this means that the solution is more elastic than viscous, and vice versa. The relation between the two moduli is that $\tan d = G^2/G'$ which is a quick way to identify the overall behavior of the gel, if $\tan d < 1$ then the gel is more elastic than viscous. (Anton Paar, n.d.)

2.5 Surface tension and contact angles

Surface tension can be measured using the FTA 200 instrument, by the pendant drop analysis. A drop of the gel falls over a glass slide by a controlled needle pump, a camera captures 310 images of the falling drop and the software recorded it. The contact angle is selected from the images where the drop touches the surface of the substrate and has the shape of axisymmetric menisci and then calculated using the Young equation. The surface tension image is selected when the droplet is about to separate from the tip of the needle and land on the substrate (Chau, 2009).

2.6 Caliper of the glucomannan films

Caliper or thickness of the dry films is measured by automated Technidyne Profile plus instrument. The accuracy is ± 0.508 μm. The thickness of the film is important in determining the permeability and for tensile tests of the films.

2.7 Mechanical properties

Tensile strength, yield strain, and % elongation of the films defines the ability of the packaging films to stretching and ensuring a good seal. Packaging products, such as packing tape, are preferred to have higher tensile strength so that they can keep the products sealed and secured during shipping; stretching films also provide protection from damage. Samples of 100 cm by 15 cm were gripped in an Instron 430I and pulled apart, 500 N load and 2.5 cm/min speed, until it breaks. Software in a computer attached to the Instron, will give the values of tensile strength and % elongation, among other properties, during the process until it reaches the break point.

2.8 Barrier property

Packaging films should keep moisture and aroma inside food and packed materials, making a barrier from losing them is essential for both consumers and producers. The ability of a film to pass air and moisture through films defines air and water vapor permeability, testing films usually follow TAPPI standard methods. Permeability depends mainly on the porosity and thickness of the films and the fluid's pressure drop, which was first derived by Darcy's equation in the 19th century, it describes the transport of fluids through porous material. According to TAPPI T-555 (TAPPI, 2015), Messmer Instrument Parker Print Surf measures the PPS porosity of the films, and air permeability coefficient K is calculated from a relation proposed by Pal, Joyce and Fleming (2006).

$$K \,(\mu m^2) = 0.048838 \times Q \,(ml/min) \times L \,(m) \tag{1}$$

where Q denotes flow rate and L is flow length (thickness). However, permeability of water vapor can be tested by ASTM E96 using Thawing-Albert EZ- cup". Air permeability is a measure of barrier property of vapor and moisture inside the materials, if air cannot escape out of the packaging film, nor will gases or water vapors.

2.9 Transparency

Food packaging should be clear and transparent therefore it shows what inside it. The transparency is measured by the total transmittance, it depends on the type of polymer, and the thickness of the film. A SpectroScan Automated Scanner 36.62.11 was used to measure the transparency of the films.

3. Results and discussion

Characterization of biofilms is important to identify the polymers and their performances in food packaging and in printed electronics. Rheology parameters such as shear rate, shear stress and viscosity, have their influence on film's production and quality control processes (Picout and Ross-Murphy, 2003). They give a perception of the ease of flow of the polymeric films during film making and other flow dependent properties.

The formulation of glucomannan films was done using three components: glucomannan, surfactant Surfynol 104H and sorbitol as a plasticizer. Previous researches, selected the reaction temperature of the polymer with other components as 45 °C (Ma, Pekarovicova and Fleming, 2018) or 60 °C (Wang, et al., 2017) in the production of glucomannan films. In this work, we selected a lower temperature of 35 °C to reduce the energy consumption in industry. Upon casting, the glucomannan solution was like a gel, clear and homogenized but after cooling, the final dried film was distorted with solid structures, faceted, and grew tails, similar to those in Figure 3. The cooling rate of the films is affected by temperature, relative humidity, type of and concentration of the surfactant used. The surfactant reduced the surface tension of the solution and made evaporation of water faster, however, increasing the surfactant reached a value were its surface tension remained constant (Kajiya, et al., 2009). To understand what caused the faceting of the glucomannan gel, we studied the effect of the surfactant concentration on the stability of the films when reacting at 35 °C and undergoing a cooling process of 50 °C and 11.4 % RH.
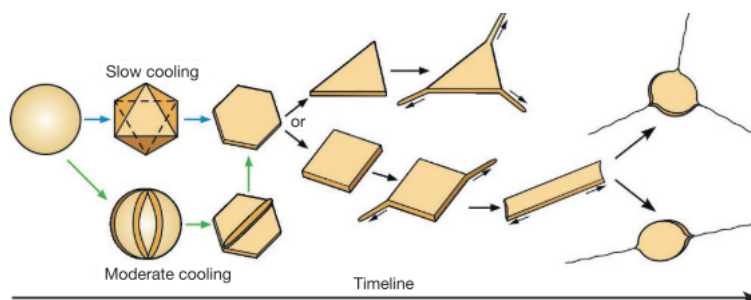
Figure 3: The timeline of shape transformations of an oil-droplet emulsion (Denkov, et al., 2015)

3.1 Density

The density of the gels of glucomannan was measured, Table 2. The density, is almost the same, the addition of the surfactant didn't change significantly the value of the density as expected; for example, the calculated value of the density, given by the calculator for Gluc. 0.2 g is 1.00581721 and for Gluc. 0.4 is 1.00466, but when rounding to 3 significant digits (the fewest significant number of the volume 8.32) the values become 1.00 g/cm^3 and 1.01 g/cm^3, respectively.

3.2 Rheology of the polymers

Biopolymers such as glucomannan are considered as viscoelastic materials, and they behave as Non-Newtonian shear-thinning solutions. When the viscosity is measured by the Anton Paar rheometer, parallel

plates were used in the measuring system (Anton Paar, n.d.). The viscous behavior of Glucomannan gels had been tested using Anton Paar rheometer, Figure 4 represents the viscosity against the shear rate for the faceted glucomannan gels. It is shown that the viscosity decreased as the shear rate increased, which indicates that these gels had a shear-thinning behavior, and the viscosity also decreased when the concentration of the surfactant increased. The surfactant Surfynol 104 H is a non-ionic surfactant, 25 % ethylene glycol; when absorbed at the air-water interface, the hydrophobic parts of the surfactant are aligned in air, thus breaking the interactions between water molecules, and thus reducing the surface tension which explains the reduction of the inner resistance to flow and thus lowering of the viscosity values. From the curves, the gel of viscosity of 0.1 g surfactant deviated from the trend of reduction of viscosity.
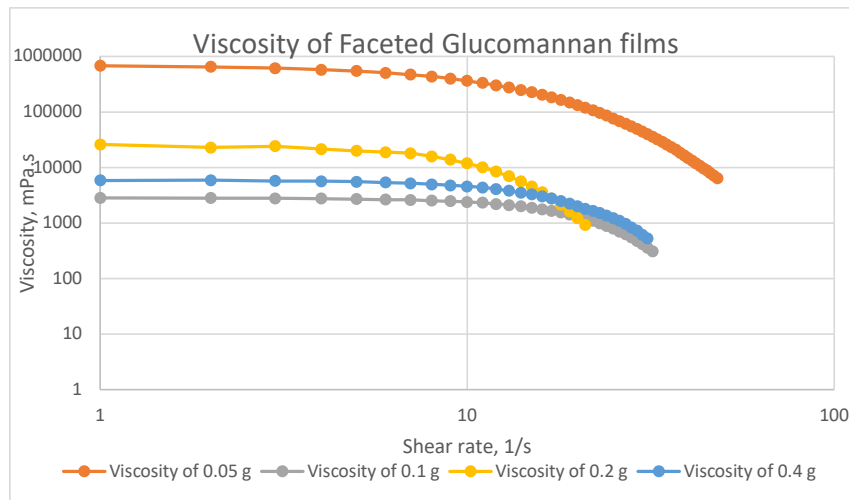
Figure 4: The viscosity and shear rate relationship for different glucomannan gels.

The viscoelastic behavior of the gel solutions of glucomannan showed that they behave as liquids at small angular frequencies and their delta $d < 1$, but they become elastic at higher frequencies. All of the glucomannan with surfactants gels experienced a turning point from viscous to elastic behavior at frequency ~ 7.5 rad/s, whereas the gel without surfactant became elastic at angular frequency ~ 0.13 rad/s. Figure 5 shows how the storage modulus G' and the loss modulus G'' depend on the angular frequency and the dual ability of the gels to act like liquids and solids as frequency changes.
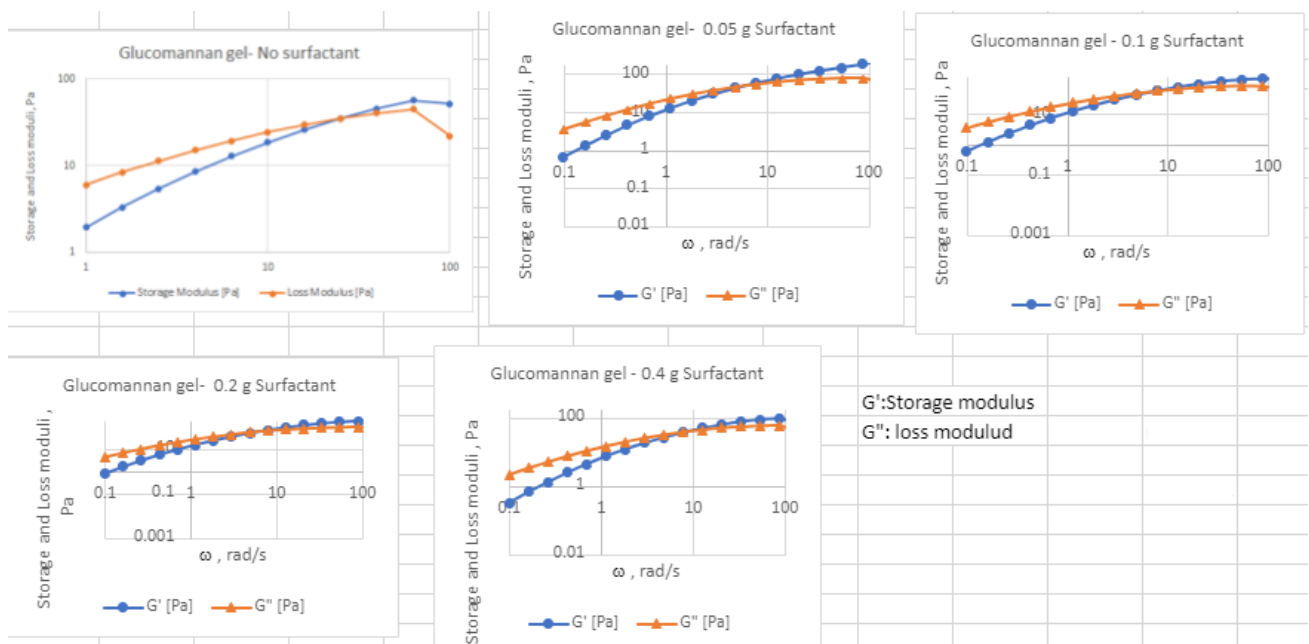
Figure 5: Frequency sweep for different glucomannan gels

3.3 Surface tension

The surface tension of the gel is an important property in printing applications, also the contact angle is vital in determining the surface free energy of substrates, and wetting properties of printed inks. The surface free energy of the substrate should be higher than that of the ink to assure good spreading of the ink during the printing process. Surfactants have hydrophilic and hydrophobic parts, which when becoming in contact with polymer, both hydrophobic parts make strong bonds causing the reduction of the solution surface tension, this allows the dissolution of the polymer in water; this gives the chance of other polymers or chemicals to react and produce a complex network that will improve the mechanical and thermal properties of the main polymer. The values of surface tension of glucomannan gels are illustrated in Table 2.

Table 2: Contact angle and surface tension of the glucomannan gels

Surfactant concentration [w/w %]	Density [g/cm^3]	Contact angle over glass [degree]	St. dev.	Surface tension [mN/m]	St. dev.
0	1	43.09	0.47	38.17	5.21
5	1	72.64	3.75	24.45	0.36
10	1	57.29	0.14	22.28	0.16
20	1.01	44.55	1.73	22.15	0.80
40	1	42.13	0.62	19.6	0.55

Figure 6 demonstrates pendant droplets of the glucomannan solutions, from the images captured by FTA 200. The surface tension of each was calculated from the shape of the pendant droplet.

Surface tension of 0.0 g surfynol in pure Glucomannan, 38.71 dy/cm.

Surface tension of 0.05 g surfynol in pure Glucomannan, 14.45 dy/cm.

Surface tension of 0.1 g surfynol in pure Glucomannan, 22.28 dy/cm.

Surface tension of 0.2 g surfynol in pure Glucomannan, 22.15 dy/cm.

Surface tension of 0.4 g surfynol in pure Glucomannan, 19.6 dy/cm.
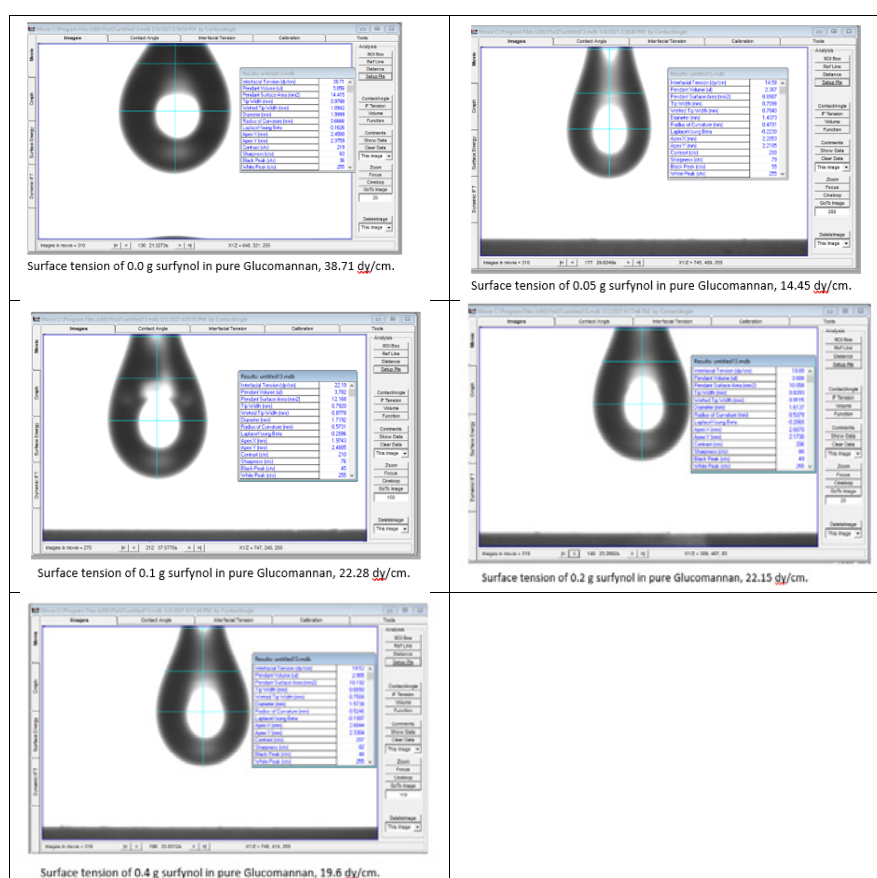
Figure 6: The surface tension of glucomannan solutions [mN/m]
at different surfactant concentrations, (g surfactant/g glucomannan)

3.4 Contact angles

Contact angle can be used to characterize the surface wettability and the surface free energy of the glucomannan solutions by using Young's equation: (Makkonen, 2016), Owens-Wendt (1969) (Owens and Wendt, 1969):

$$\gamma_{SV} = \gamma_{SL} + \gamma_{LV} \cos \theta \qquad\qquad [2]$$

where γ is interfacial tension, subscripts S, V, and L denote solid, vapor and liquid phases, and is contact angle; or AMF equations (Altay, et al., 2020). The classical view of the contact angle demonstrates where the force balance at the contact line between the 3 phases. The AMF method measures the surface tension of the liquid and the contact angle from the images of FTA 200 and then calculates the surface free energy of the solid surface introducing a new parameter, α, that satisfies the inequality $\gamma_{SV} + \gamma_{SL} - \gamma_{LV} > 0$, where $\gamma_{SV} = \cos \gamma_{LV} \cos^2 (\theta/2)/\alpha$ (Altay, et al., 2020). The contact angles in Table 2 show that the gel drops spread greater when more surfactant is added. The surface tension of the drops of the glucomannan solution are illustrated in Figure 7, it is also the same tendency of the contact angles. This behavior is vital in smooth printing of the glucomannan solution over a board in printed electronics and on printing labels on food packaging films.

Force balance at the contact line between the solid surface and the liquid and air. The surface tensions between each 2 phases are in equilibrium (Makkonen, 2016).

Contact angle of 0.0 g surfactant in pure Glucomannan, 43.09°.

Contact angle of 0.05 g surfactant in pure Glucomannan, 72.64°

Contact angle of 0.1 g surfactant in pure Glucomannan, 57.29°.

Contact angle of 0.2 g surfactant in pure Glucomannan, 44.55°.

Contact angle of 0.4 g surfactant in pure Glucomannan, 42.13°.

Figure 7: The contact angle of glucomannan gels over glass at different surfactant concentrations (g surfactant/ g glucomannan) from FTA 200 and contact angle theory demonstration (Makkonen, 2016)

3.5 Caliper of the glucomannan films

The thickness, caliper, of the films depends mainly on casting and drying conditions of the films. Faceted areas were thicker and hard, which made it difficult to stretch and easier to break. Figure 8 illustrates the different calipers of the biofilms and the petroleum-based film, polyethylene (PE) film.
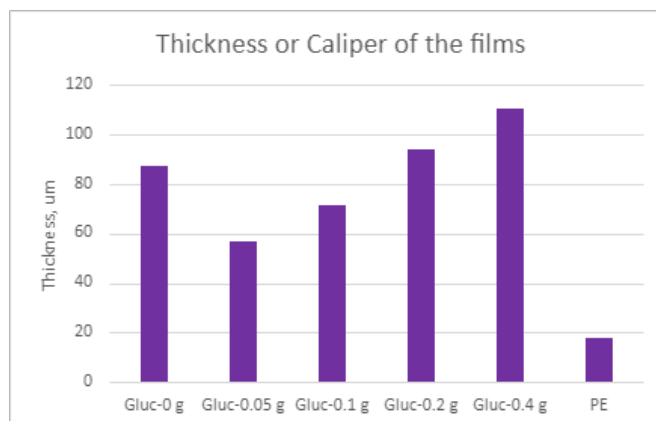
Figure 8: The thickness of glucomannan films compared with the PE film

3.6 Tensile strength and elongation of the films

Tensile strength and elongation of the films were measured as a result of applying 500 N force on both ends of stripes of the films, 10 cm × 1.5 cm until breaking point. The thickness of the films was not homogenized in each faceted film and affected the tensile strength at break of the films, the thinnest films showed more resistance to tensile stress. Elongation was also in the same pattern; more stretching was notable in thin films. Figure 9 shows the three relations together, it shows a comparison of the faceted films and a PE cling wrap from Glad company. The PE wrap film elongation was 7 folds of the highest elongation glucomannan films had, Gluc. 0.05, but the tensile strength at break was weaker.
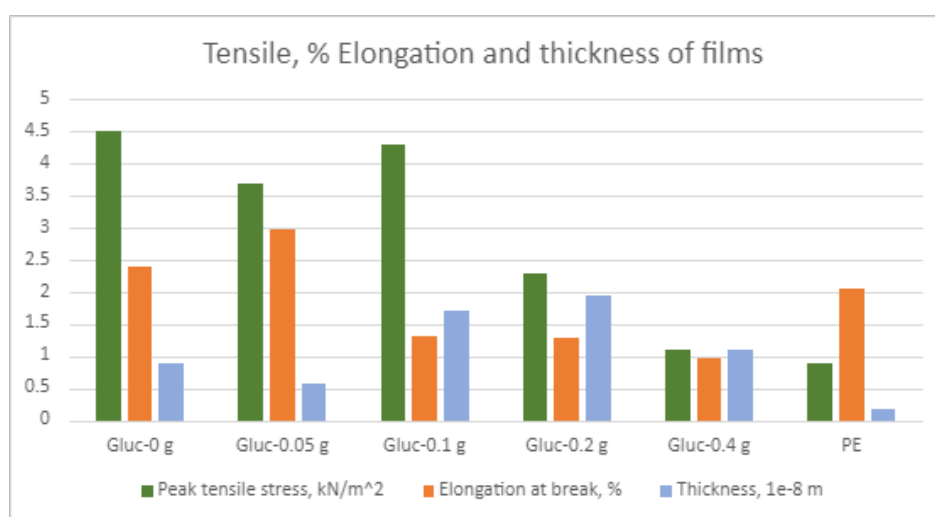
Figure 9: Tensile strength, % elongation of the films at break and the thickness of the glucomannan films, the % elongation of the PE is 20 %, but plotted as $1e^{-2}$ of the value for comparison purposes

3.7 Barrier properties

Air, gas, and vapor permeability is not favored in food packaging world as mention earlier, it should be at its minimum values. Following Pal, Joyce and Fleming (2006) to calculate air permeability, the thickness

and the PPS porosity should be measured first and then the air permeability can be calculated according to their equation. Figure 10 illustrates the porosity of the faceted films as well as PE film, the polyethylene film has the lowest permeability since it is the thinnest film and lower permeability coefficient. Between the faceted films the film Gluc. 0.05 g surfactant had low PPS porosity and caliper, which explains its tendency to be air-flow resistance and water vapor as a result.
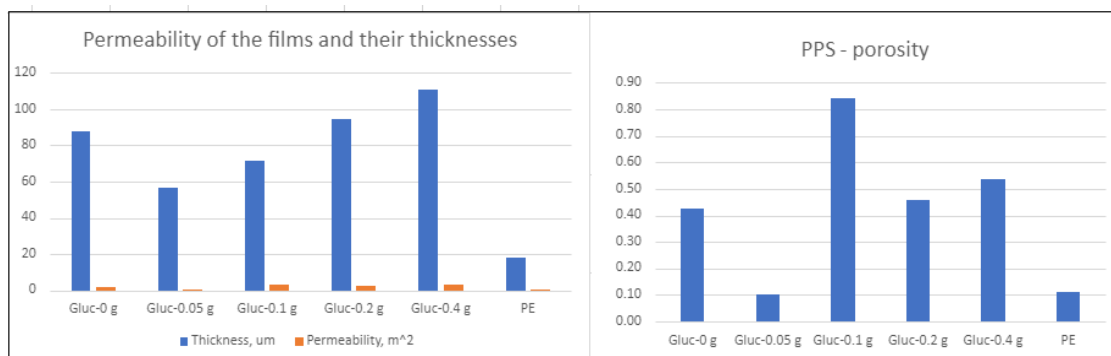
Figure 10: PPS-porosity and air permeability of the faceted films and PE film

3.8 Transparency

Although faceting produced thick areas, but the films were transparent to some extent. The PE film transparency was 99.5 % where the faceted film of 0.05 g surfactant gave a 75 % transparency, as in Figure 11.
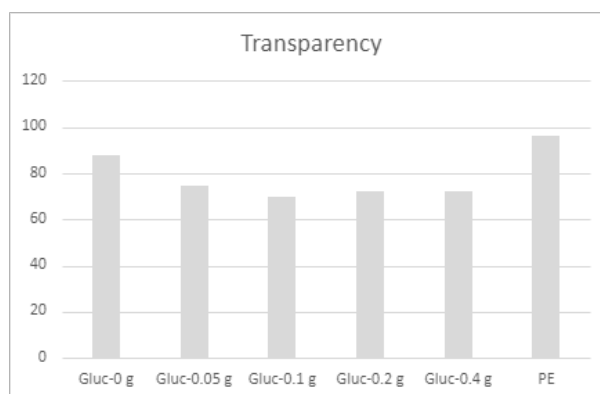
Figure 11: Transparency of glucomannan faceted films and PE film

3.9 Faceting and phase transformation

The dried films presented in Figure 12, exhibited a shape transformation, and solid polygons and fiber structures were formed. What happened at the glucomannan – water interface, is related to the surfactant freezing and depositing on the interface, due to a slow cooling rate and type of the surfactant (García-Aguilar, et al., 2021; Wong, et al., 2019). These changes occurred at a temperature above the melting point of the polymer, where the interfacial monomer crystallizes (Guttman, et al., 2016). As the surfactant concentration increased, the surface tension of the glucomannan solution dropped and faceting began, all the films (1, 5, 13 and 15) showed faceting but in distinct shapes. Film 5 showed the highest deformed droplets, because it was dried a longer time over the weekend, but the trend shows that the films had faceted areas when the surfactants were at 40 %, 20 %, 10 % and 5 % concentration (from the top left clockwise).

The last image shows a successful film, formulated from the same ingredients as the Film 1; it required raising the reaction temperature up to 40°C and the drying conditions (57 °C, 35 % RH for 3 hours) followed by 18 hours at TAPPI testing conditions for paper. The film was clear and there were no faceting

phenomena detected, it is ready for mechanical testing (Tensile strength, % elongation, roughness, caliper, and surface free energy) and water vapor and air permeability.
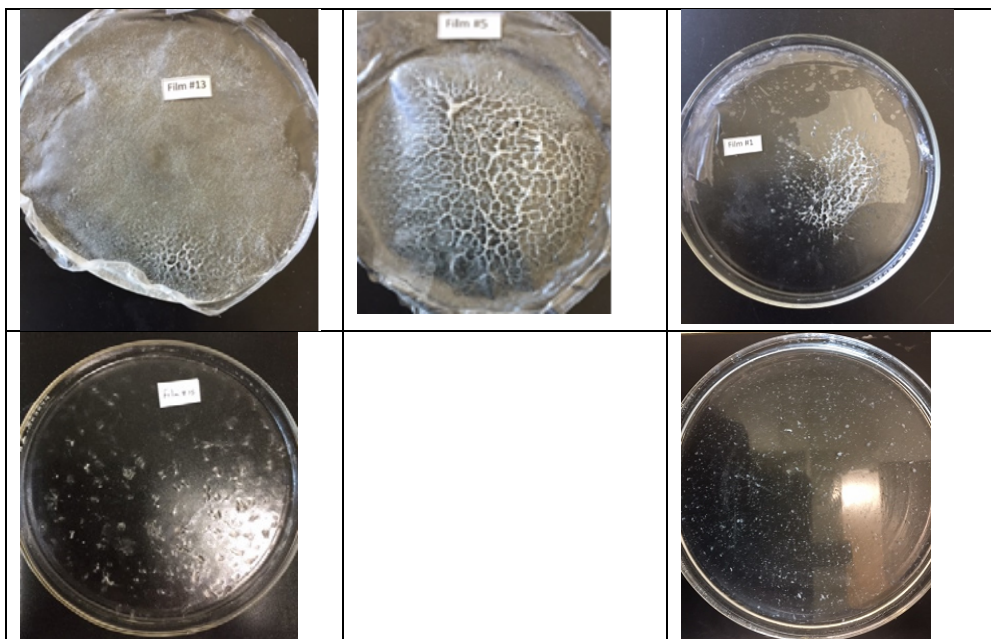
Figure 12: Glucomannan dried films, showing phase transformation at the polymer-water interface and a successful glucomannan film (last image to the right)

4. Conclusion

The glucomannan is a promising biofilm for food packaging because it is originated from an annual plant and is friendly to the environment. Controlling the reaction temperature and cooling rate during drying is crucial in producing glucomannan films to use them in the packaging industry, printing, and printed electronics. The films should be clear, have good mechanical and barrier properties, smooth, transparent, and easy to print on. Selection of the appropriate surfactant and its concentration, as well as selecting proper mixing reaction temperature and drying conditions helps also in reducing the interfacial freezing effect and therefore producing the proper biofilms. The market of cellulose wrapping biofilms is worldwide and is a big one, however, the hemicellulose biofilms, like Glucomannan and Xylan, is still in its early stages.

References

Altay, B.N., Ma, R., Fleming, P.D., Joyce, M.J., Anand, A., Chen, T., Keskin, B., Maddipatla, D., Turkani, V.S., Kotkar, P.R., Fleck, A., Rasheed, R. and He, D., 2020. Surface free energy estimation : new methodology for solid surfaces. *Advanced Materials Interfaces*, 7(6): 1901570. https://doi.org/10.1002/admi.201901570.

Anton Paar, n.d. *Rheological measurements.* [online] Available at: <https://wiki.anton-paar.com/en/basics-of-rheology/rheological-measurements/> [Accessed 5 April 2021].

Chau, T.T., 2009. A review of techniques for measurement of contact angles and their applicability on mineral surfaces. *Minerals Engineering*, 22(3), pp. 213–219. https://doi.org/10.1016/j.mineng.2008.07.009.

Cision, 2018. *Cellulose film packaging market: global industry analysis 2013–2017 and opportunity assessment 2018–2028*. [online] Available at: <https://www.prnewswire.com/news-releases/cellulose-film-packaging-market-global-industry-analysis-2013-2017-and-opportunity-assessment-2018-2028-300762706.html> [Accessed April 2021].

Denkov, N., Tcholakova, S., Lesov, I., Cholakova, D. and Smoukov, S.K., 2015. Self-shaping of oil droplets via the formation of intermediate rotator phases upon cooling. *Nature*, 528, pp. 392–395. https://doi.org/10.1038/nature16189.

García-Aguilar, I., Fonda, P., Sloutskin, E. and Giomi, L., 2021. Faceting and flattening of emulsion droplets: a mechanical model. *Physical Review Letters*, 126(3): 038001. https://doi.org/10.1103/PhysRevLett.126.038001.

Guttman, S., Sapir, Z., Schultz, M., Butenko, A.V., Ocko, B.M., Deutsch, M. and Sloutskin, E., 2016. How faceted liquid droplets grow tails. *Proceedings of the National Academy of Sciences of the United States of America*, 113(3), pp. 493–496. https://doi.org/10.1073/pnas.1515614113.

Honarvar, Z., Hadian, Z. and Mashayekh, M., 2016. Nanocomposites in food packaging applications and their risk assessment for health. *Electronic physician*, 8(6), pp. 2531–2538. https://doi.org/10.19082/2531.

Jonas, H., 2006. *Hemicellulose as barrier material*. Licentiate thesis. KTH, School of Chemical Science and Engineering (CHE), Fibre and Polymer Technology, Stockholm.

Kajiya, T., Kobayashi, W., Okuzono, T. and Doi, M., 2009. Controlling the drying and film formation processes of polymer solution droplets with addition of small amount of surfactants. *Journal of Physical Chemistry B*, 113(47), pp. 15460–15466. https://doi.org/10.1021/jp9077757.

Kalia, S., Dufresne, A., Cherian, B.M., Kaith, B.S., Avérous, L., Njuguna, J. and Nassiopoulos, E., 2011. Cellulose-based bio- and nanocomposites: A review. *International Journal of Polymer Science*, 2011: 837875. https://doi.org/10.1155/2011/837875.

Lavoine, N., Desloges, I. and Bras, J., 2014. Microfibrillated cellulose coatings as new release systems for active packaging. *Carbohydrate Polymers*, 103, pp. 528–537. https://doi.org/10.1016/j.carbpol.2013.12.035.

Lee, H.V., Hamid, S.B.A. and Zain, S.K., 2014. Conversion of lignocellulosic biomass to nanocellulose: structure and chemical process. *Scientific World Journal*, 2014: 631013.chttps://doi.org/10.1155/2014/631013.

Ma, R., 2018. *Screen printed moisture sensor on barrier coated SBS board: the characterizations of the hemicellulose-based biofilms and their applications for smart packaging*. Doctor of Philosophy dissertation. Western Michigan University.

Ma, R., Pekarovicova, A. and Fleming, P.D., 2018. Biopolymer films from glucomannan: the effects of citric acid crosslinking on barrier properties. *Journal of Print and Media Technology Research*, 7(1), pp. 19–25. https://doi.org/10.14622/JPMTR-1802.

Makkonen, L., 2016. Young's equation revisited. *Journal of Physics: Condensed Matter*, 28(13): 135001. https://doi.org/10.1088/0953-8984/28/13/135001.

Marin, O., Tkachev, M., Sloutskin, E. and Deutsch, M., 2020. Polyhedral liquid droplets: recent advances in elucidation and application. *Current Opinion in Colloid and Interface Science*, 49, pp. 107–117. https://doi.org/10.1016/j.cocis.2020.05.006.

Nair, S.B., Alummoottil N.J. and Moothandasserry S.S., 2017. Chitosan-konjac glucomannan-cassava starch-nanosilver composite films with moisture resistant and antimicrobial properties for food-packaging applications. *Starch/Staerke*, 69(1–2): 1600210. https://doi.org/10.1002/star.201600210.

Owens, D.K. and Wendt, R.C., 1969. Estimation of the surface free energy of polymers. *Journal of Applied Polymer Science*, 13(8), pp. 1741–1747. https://doi.org/10.1002/app.1969.070130815.

Pal, L., Joyce, M.K. and Fleming, P.D., 2006. A simple method for calculation of the permeability coefficient of porous media. *Tappi Journal*, 5(9), pp. 10–16.

Picout, D.R. and Ross-Murphy, S.B., 2003. Rheology of biopolymer solutions and gels. *The Scientific World Journal*, 3, pp. 105–121. https://doi.org/10.1100/tsw.2003.15.

Rhim, J.-W. and Ng, P.K.W., 2007. Natural biopolymer-based nanocomposite films for packaging applications. *Critical Reviews in Food Science and Nutrition*, 47(4), pp. 411–433. https://doi.org/10.1080/10408390600846366.

Scheller, H.V. and Ulvskov, P., 2010. Hemicelluloses. *Annual Review of Plant Biology*, 61, pp. 263–289. https://doi.org/10.1146/annurev-arplant-042809-112315.

TAPPI, 2015. *Roughness of paper and paperboard (Print-surf method), Test Method T 555 om-15.* Peachtree Corners, GA, USA: TAPPI.

Triantafillopoulos, N., 1988. *Measurement of fluid rheology and interpretation of rheograms.* 2nd ed. [pdf] Livonia, MI, USA: Kaltec Scientific Supplies and Instruments LLC. Available at: <http://www.kaltecsci.com/rheology.pdf> [Accessed April 2021].

Wang, K., Wu, K., Xiao, M., Kuang, Y., Corke, H., Ni, X. and Jiang, F., 2017. Structural characterization and properties of konjac glucomannan and zein blend films. *International Journal of Biological Macromolecules*, 105(p1), pp. 1096–1104. https://doi.org/10.1016/j.ijbiomac.2017.07.127.

Wong, C.K., Martin, A.D., Floetenmeyer, M., Parton, R.G., Stenzel, M.H. and Thordarson, P., 2019. Faceted polymersomes: a sphere-to-polyhedron shape transformation. *Chemical Science*, 10, pp. 2725–2731. https://doi.org/10.1039/c8sc04206c.

G.-M. Koltsia and N. Karampekios: Research & development dimensions – the printing industry in Greece: a first empirical capture

3A

Research & development dimensions – the printing industry in Greece: a first empirical capture

Georgia - Maria Koltsia and Nikos Karampekios

The Department of Graphic Design and Visual Communication/ Technology of Graphic Arts, University of West Attica,
Aigaleo,12243, Athens, Greece
E-mails: georginakolt@gmail.com, 9739600@gmail.com

Short abstract

On the occasion of the technological development and the technological revolution in the printing industry, it is realized that there is a global need for new applications in printing. A fact that is captured by Charles Hardy in S-curves (or Sigmoid Curves) as a way of understanding the lifecycle of a technology. He used S-curves as a way to demonstrate the need for significant and regular reinvention and change. Evolution presupposes the existence of research and development activities in the printing industry. In examining literature and publications in the Graphic Arts sector in Greece, it is noted that despite the size of the industry that covers more than 9000 enterprises, the research and development (R&D) situation of the industry has not been recorded. This is a significant shortage because it is impossible to define the state of the industry in terms of R&D. In pursuing this gap, this paper attempts an initial exploration of the R&D activities in the Graphic Arts sector. The aim is to gain an initial understanding and insight into the relevant investments, human resources, staff training, funding and research synergies that the industry is involved in. It will also explore issues related to R&D inside and outside the business, as well as ways to acquire external knowledge from other businesses or sectors. Addressing these business dimensions will allow for easier understanding of the sector as well as it will be expedient for further consideration and reachable for future investment. The graphic arts sector, due to its complexity and multiple activities – its products, has been classified by the Hellenic Statistical Authority in the category of manufacturing. There are wider, societal benefits in identifying the scale of R&D of the industry. For example, it will enable a public policy based in evidence, able to take decisions that regulate individual issues further reinforcing the growth, development and extroversion of the industry.

Keywords: research and development, expenditure, Greece, basic research

1. Introduction

1.1 The printing industry

Worldwide: The printing industry is one of the largest industries in the global market with a turnover of $ 898 billion and, combined with other services, is heading for $ 3.8 trillion (Wiseguyreports.com, 2018; Global commercial printing industry, 2018). The latest available data from the European Commission (2019) show that the printing industry in the 28 European countries includes more than 120 000 companies and employs around 770 000 people.

Europe: Approximately 625 000 employees were working in the European printing industry in 2016. The European printing industry counted approximately 112 000 companies in 2016, which generated a turnover of around € 79.5 billion (Intergraf, 2020).

Greece: The printing industry represents 1.21 % of the total turnover of the 24 manufacturing industries. The manufacturing sector employs a total of 370.2 thousand people for 2017 with the printing sector employing 14.5 thousand employees in 2017 after the industry shrank from 17 000 in 2009 (Eurostat, n.d.).

1.2 The printing industry R&D

Worldwide: The increase in expenditures for research and development (R&D) are a solution in creating a suitable ground for the smooth adaptation of companies to the digital transformation. Investment in R&D is necessary and a tool for attracting innovative business activities. At the moment on the world map, events related to R&D in the field of printing, packaging and nanotechnology are held, with organizers usually governmental and non-governmental organizations and associations as well as participating companies, universities and research teams where their project and vision is announced with the biggest forces and investors in R&D are America and China (Unesco Institute of Statistics, 2021).

Greece: At the national level, it is quite difficult to capture the progress of the printing industry both in terms of its research dimension and in terms of its technological dimension because the industry has not been studied. This fact creates problems in understanding the industry and in recording its course. For this reason, seeking a first valuation of the industry, was made an attempt to capture R&D activities for the first time.

At the heart of the national R&D system is the GSRT, which is responsible for shaping and implementing R&D policy in Greece. Since November 2009, GSRT has been under the Ministry of Education. The latest available data indicate for R&D that total expenditure in Greece in 2017 is 2 038.43 million € (Metrics.ekt. gr., 2020). And they are increased by 284.25 million € compared to 2016. The increase in R&D expenditure results in the increase of the "R&D Intensity" index to 1.15 % in 2017 from 1.01 % in 2016 (increase by 0.13 percentage points). According to new data, Greece ranks 19th among EU Member States (Oecd.org., 2017).

1.3 The purpose of the paper

The primary purpose of this paper is to understand the R&D situation in the domestic printing industry. To enable this, a record of specific R&D dimensions of the sector is essential. Currently, no information can be found concerning the R&D capacity of the sector. This fact raises concerns about the industry. As such, this paper presents the first results on this and as such it is sought to fill the specific industry gap for the first time.

This is done through a survey analysis of information concerning both the human resources and its training as well as data concerning the companies themselves in terms of their financial dimension. This collection was done through primary research carried out with the creation of the questionnaire. Moreover, information related to the movements and activities of companies and their investments in R&D through funding from government agencies and programs and the partnership with other companies in the same industry, with university bodies, with governmental and non-governmental organizations and research centers.

This record will allow us to determine whether the ground is fertile for technological and scientific development as well as the attitude of Greece to the developments that take place and redefine both the importance of printing and the scope of the industry.

2. Methodology

As a first step, the finding and registration of companies in the field of Graphic Arts in Greece was carried out by the publishing house "Fotini Antonopoulou - Book of Graphic Arts". Since its original publication in 1987, the Graphic Arts Book has been the most complete record of the Graphic Arts sector in Greece.

The companies are selected by the Business Activity Codes of Greece, 1811 Printing of newspapers, 1812 Other printing activities, 1813 Media pre-printing and pre-registration services, 1814 Bookbinding and related activities, 1820 Playback of pre-recorded media.

As a second step, it was found that the population exceeded 9 000 companies. The companies with the highest sales for the years 2011 to 2016 were selected as the population. In order to obtain information about the respective companies, we used the ICAP Group listing (Icap.gr., 2017). This listing provides balance sheets for the graphic arts companies. Herein, the 60 companies with the highest sales were drawn for the 2011 to 2016 period. The reason why the companies with the highest sales have been selected for this period of time is that the industry in Greece lags behind in terms of relevant information for new applications as well as for research and development.

As a third step, the data search was performed based on the name of each company. The necessary information was the address of the headquarters of each company, the telephone number, the e-mail address of the messengers and the names of the managers of each company. At the same time, there were some companies of the same name, which led to matching the data concerning the sales of each company from another source (National Printing Office) so as to clean the data.

The most valid source for finding the above information was the business balance sheets. Therefore, the companies that were identified based on the sales figures obtained from the ICAP Group and based on the numbers listed in the published balance sheets of the electronic file of the National Printing Office were selected.

As a fourth step, after the identification of the population, the formulation of the Questionnaire of Research and Development Activities followed. The structure of the questionnaire was created based on the questionnaires published by the National Documentation Center, which is the national authority of the Greek Statistical System, produces the national indicators for Research, Development and Innovation in Greece that are sent to the European Statistical Authority (Eurostat, n.d.; Metrics.ekt.gr., 2018). The questions were customized so as to refer to the characteristics of the printing industry.

The questionnaire was created on four different online platforms completely. The online platform Survey Monkey was found to be more appropriate. The questionnaire was created under the title "Questionnaire of Research & Development Activities", where the final changes were made. The questionnaire consists of forty-six (46) questions and its completion time is 20 minutes.

As a fifth step, a link containing the questionnaire was sent to each email address. It was noted by name to the person in charge of the company. A cover letter explained the purposes of the email and included all the necessary details of the person sending the questionnaire, the purposes, etc. Upon completion of the process of sending the Questionnaire, the telephone communication with the companies followed to confirm that the questionnaire was sent and has been received by the competent authorities.

Subsequently, and after telephone communication with the secretariat and the managers of the companies, the questionnaire was sent again to some addresses that either neglected it, deleted it or did not find it. A total of 112 emails were sent to the 50 companies, most of which sent the questionnaire back to the companies and another 45 reminder messages to complete the questionnaire. At specific intervals of one week, there was a telephone communication to remind the business leaders of the questionnaire for its completion but also to resolve any questions and clarifications concerning either the content of the questionnaire.

3. Findings

3.1 General business data

The size of the companies that were asked to answer the questionnaire, based on the number of employees until the end of 2017, have employed from 10 to 500 people. Of the 10 companies (20 %) that responded to the questionnaire, 7 employ staff from 10 to 49 people.

Regarding business merger issues, the following are observed: during the period 2016 to 2018, there is a change in companies in terms of activity as of the companies that were called to respond, the 3 companies were merged or bought by other companies.

Greek companies mainly target the domestic market (Figure 1). Sales of goods and services largely focus throughout Greece. In several cases there is an export of products to other European countries. All companies address and distribute their products in the Greek market (10 companies), most of which have export activities in European countries at a high level (7 companies), and companies that trade in countries outside the European continent (1 company).
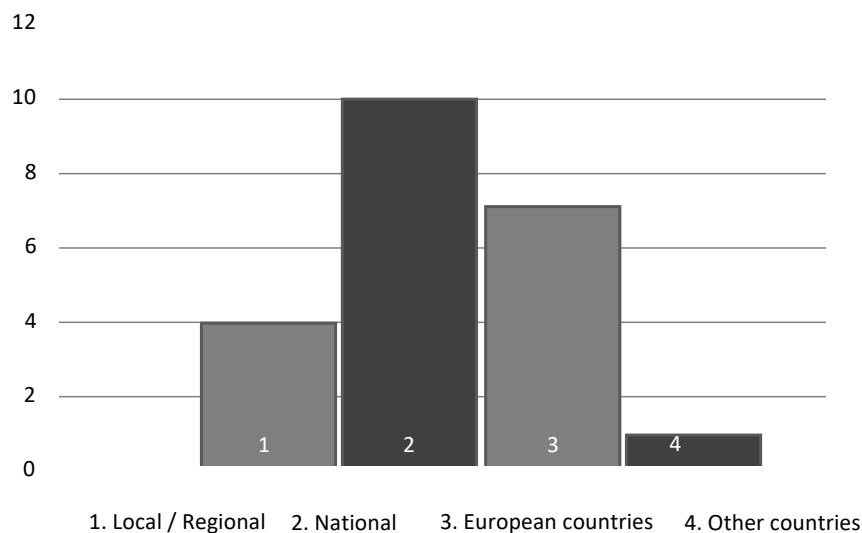
Figure 1: Sale of goods by geographic market

Subsequently (Figure 2), during the three years 2016 to 2018, several companies carried out development activities related to the purchase of machinery, equipment, software and buildings in order to produce new or significantly improved products or processes, in number 9 out of 10 companies. As a second option for 6 of the research companies comes the training for innovative activities In-house, or through outsourcing, training of your staff, especially for the development and / or introduction of new or significantly improved products and processes.
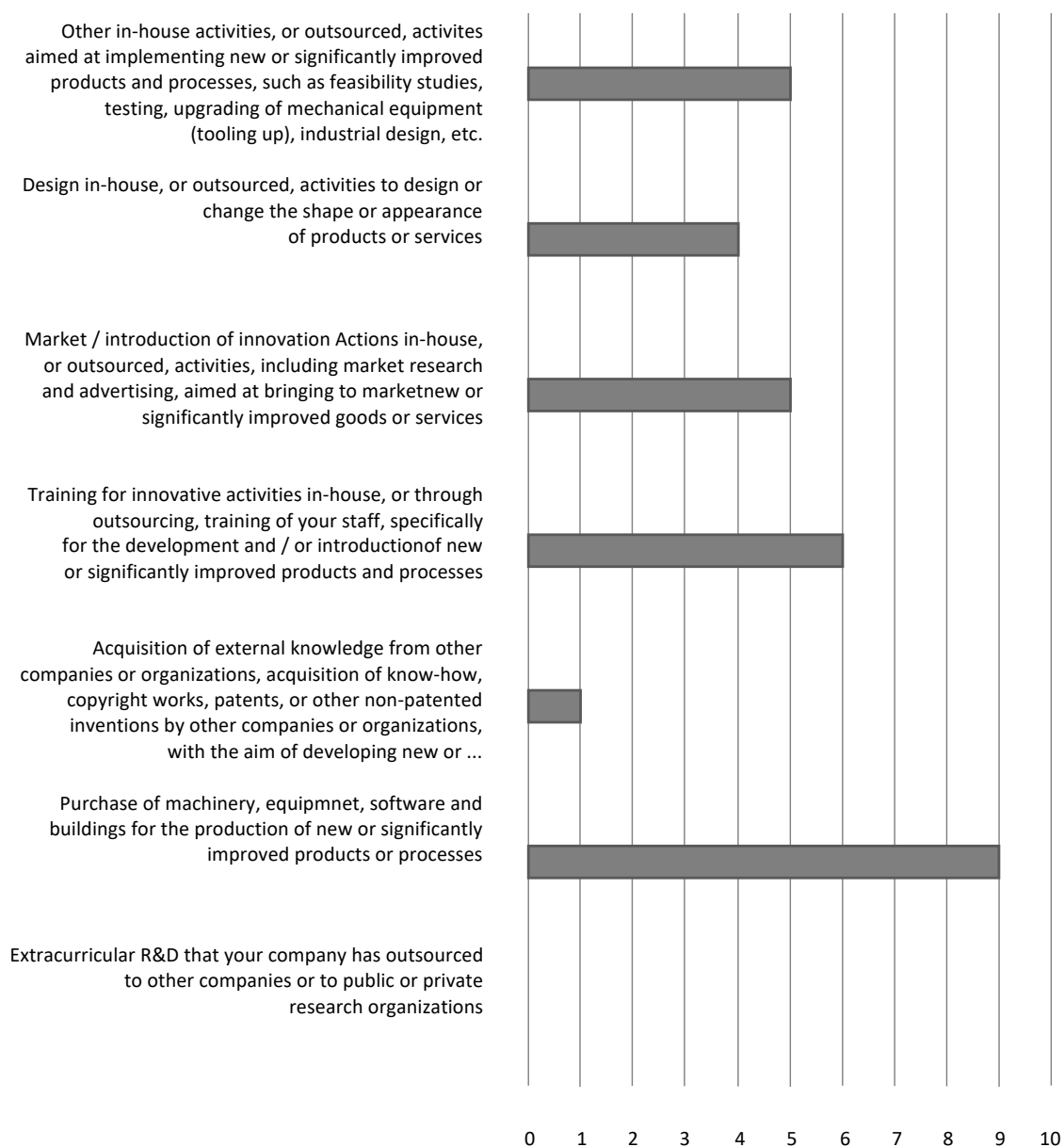
Figure 2: R&D activities for the years 2016–2018 percentage

3.2 Employed staff in R&D activities

With regard to salaried staff employed within the companies with R&D activities for the three years 2016 until 2018 it is observed that only 2 of the companies that responded to the survey employ R&D staff. With the number of researchers ranging from 1 to 2 people per company of which only one employs female researchers. Regarding the level of education of the staff engaged in R&D activities for the year 2016, no holders of Doctoral degrees were registered. Some independent centers like The Hellenic Organic & Printed Electronics Association (HOPE-A), has 23 employees and also the Nanotechnology Lab Ltfn has 13 employees. But there is no feather information about the genders and the level of education.

3.3 Internal costs for R&D activities

These costs are referred to as intramural expenditure and relate to R&D activities that are carried out either as part of the firm's ongoing activities, or as part of the implementation of research projects or pro-

grams, or after outsourcing but are implemented at the company's premises. R & D activities that are done by assignments to partners or agencies and are carried out outside the company (Figure 3).

Internal costs are current R&D expenditure and staff costs of the company engaged in R&D in which including gross remuneration, employer contributions, social security contributions, special remuneration, bonuses for R&D staff. The others current expenditure for R&D purposes including all other current non-staff costs (such as operating costs, rent, PPC costs, telephone expenses, travel expenses, consumables, books, magazines, library subscriptions, materials laboratories, and generally not included in the previous categories) during used to carry out in-house R&D activities.

Internal costs in 2016 for R&D activities on business premises range between 5 000 and 10 000 €. For the year 2017 the internal costs of personnel costs of the companies engaged in R&D remained at the same levels as in 2016 as well as the Other current expenses for R&D purposes. There was a difference in Capital expenditures where they increased up to 10 000 € compared to 2016, reaching up to 20 000 € for some companies. Capital expenditures refer to an amount spent on the acquisition or enhancement of a productive asset to increase a company's capacity or efficiency such as printing and finishing machines, factory facilities, equipment, buildings and not to depreciation amounts.

The corresponding estimates for the year 2018 are in the same context as in previous years and slightly increased, with the internal staff costs of R&D companies reaching up to 21 000 €. Other current expenditure for R&D purposes are at the same levels with the above and Capital expenditures showing upward trends of up to 200 000 €, for a few companies, after the purchase of fixed assets.
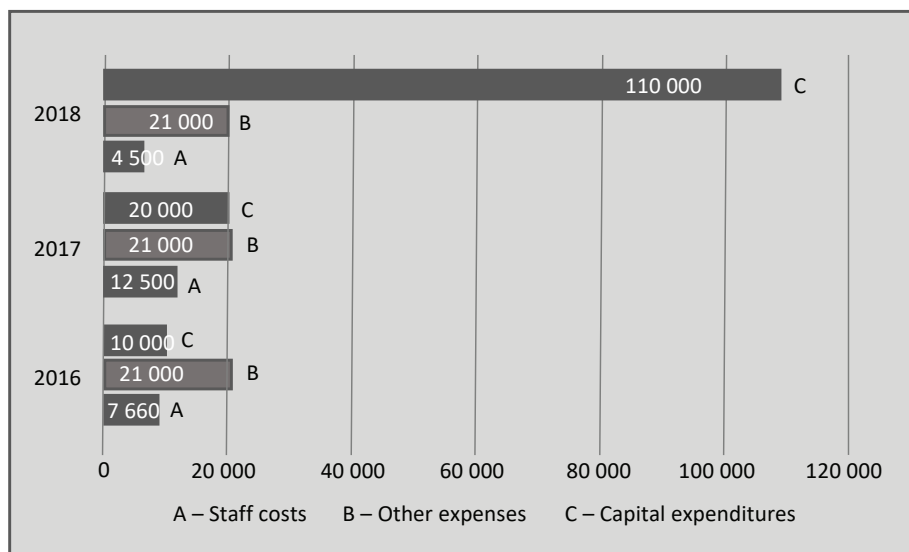
Figure 3: Internal R&D expenditure for the years 2016–2018 on average

Internal R&D expenditure based on the original source funding for 2 of the companies that developed R&D activities for year 2016 came from self-financing and ranged from 10 000 € to 30 000 €. For the year 2017 the distribution of costs to the respective companies based on the initial source of funding amounted to 20 000 € to 35 000 € and are equally product self-financing. The upward trends appeared in the year 2018 with 3 companies that receive funding and with the amounts reaching 100 000 € for financing from the State Sector, financing from companies at 100 000 € and self-financing to be at the same levels as in 2017 (Table 1).

Table 1: Internal R&D expenditure based on Source of Funding

Year	Number of companies	Self-financing	Public sector	Companies
2016	2	10 000	0	0
2017	2	20 000	0	0
2018	4	20 000	100 000	100 000

The 4 companies that claimed to have incurred internal R&D expenditure against type of Research and Development for the year 2016 and the year 2017 stated that 80 % of their expenses are related to Basic Research, which is experimental or theoretical work done with the main purpose of acquiring new knowledge about the fundamental characteristics of phenomena and observable events, without aiming at specific application or use. And 20 % of their spending on Applied Research, that is, in original research for the acquisition of new knowledge with a specific practice purpose or goal (Figure 4).
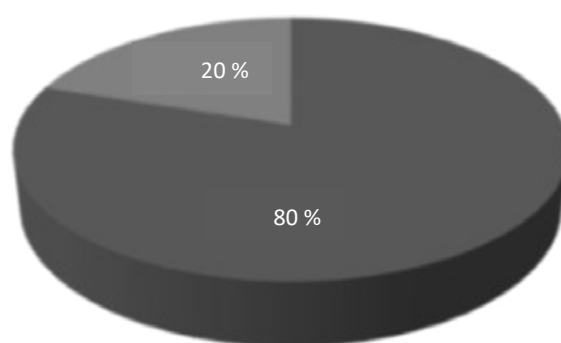
Basic research – 80 %   Applied research – 20 %   Experimental development – 0 %

Figure 4: Internal Expenditure on R&D by type of R&D for 2016, 2017, at %

3.4 External costs for R&D activities

External costs relate to R&D Activities that are not implemented in facilities of the company but in facilities of third parties, such as Universities, Research and Technology Centers, other companies, with assignments, tenders, subcontracting, etc. For the years 2016 and 2017 they were zero while for the year 2018 the estimates range at 15 000 € in 10 % of companies in Domestic companies.

3.5 Impact of legislation on E&A activities

Most companies claim that R&D legislation has created uncertainty about taxation and employment in social affairs. As well as that it did not create particular issues regarding the safety of employees.

Between 2016 and 2018, legislation or regulations affected E&A activities in just 3 of the companies motivating one or more E&A activities. At the same level were the companies that claimed that the legislation slowed down the start of E&A activities and stopped their development. Only 3 of the respondents claimed that the completion of R&D activities was delayed due to the legislation and 4 of the companies claimed that the cost of R&D activities increased due to the legislation.
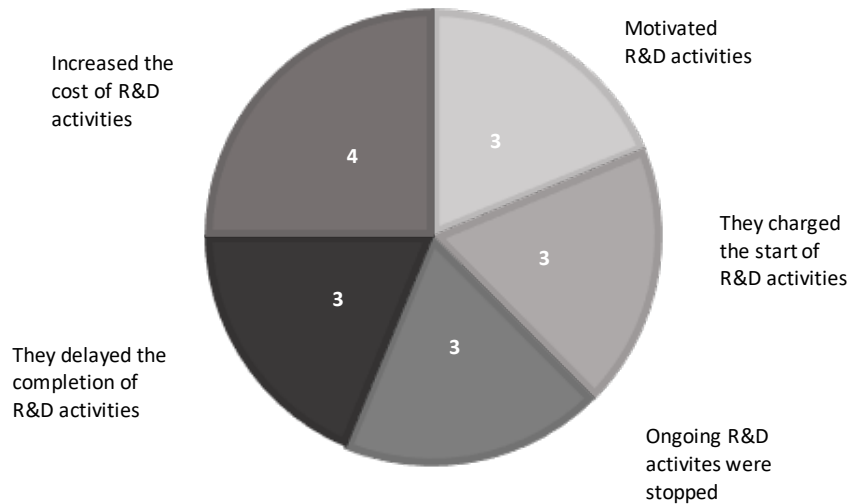
Figure 5: Ways of Impact of legislation on E&A activities

It is obvious that for most companies the laws and regulations do not hindered R&D activities, which may motivate Greek companies in the activity with Research and Development actions.

3.6 Basic business financial data

During the period from 2016 to 2018 for 2 companies there were stages of production of products (goods or services) which were implemented in another country by a third party. With 2 of the 4 companies having connections abroad to carry out production stages in EU countries and with one company operating in China, having a competitive advantage by acquiring external knowledge.
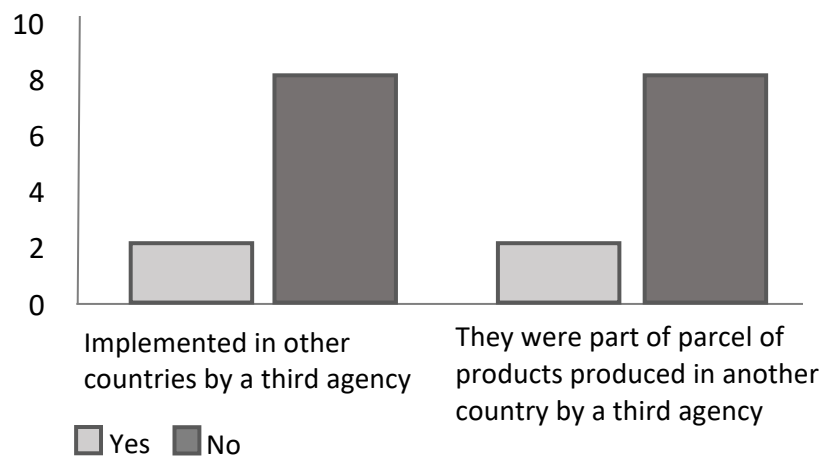
Figure 6: Stages of production of products in another country (2016–2018)

3.7 Strategies & Obstacles to achieve goals

The dominant strategy is to reduce costs, whether operating costs or the cost of materials, components or services purchased. The reduction of domestic (within operating) costs according to the results of the questionnaire (Figure 7) is of particular concern to businesses.

A – Development of new markets in Europe

B – Development of new markets of Europe

C – Reduction of internal operation costs

D – Reduce the cost of material, components of services purchased

E – Introduction of new significantly improved goods or services

F – Improving Marketing / promoting goods and services
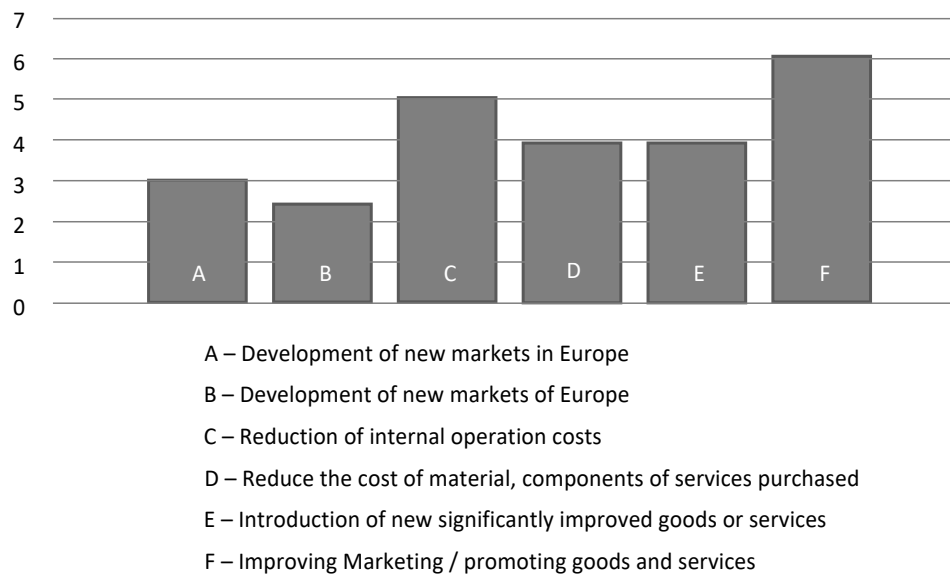
Figure 7: Goal Achievement Strategies 2016–2018

In the period 2016 to 2018 the following factors were obstacles for achieving the goals of the business. Strong price competition and competition as product quality, reputation or brand, has been one of the main issues facing businesses. The high cost of compliance with government regulations or legal requirements and limited access to sources of information (scientific & technical) also occupied Greek companies while the lack of demand, the dominant market share of competitors, the lack of specialized staff, the lack of adequate funding, high cost of access to new markets and competitors' innovations at last.

A – Strong price competition

B – Strong competition in term of product quality, price or brand

C – Lack of demand

D – Competitors innovations

E – Dominant market share of competitors

F – Lack of adequate funding

G – Lack of qualified staff
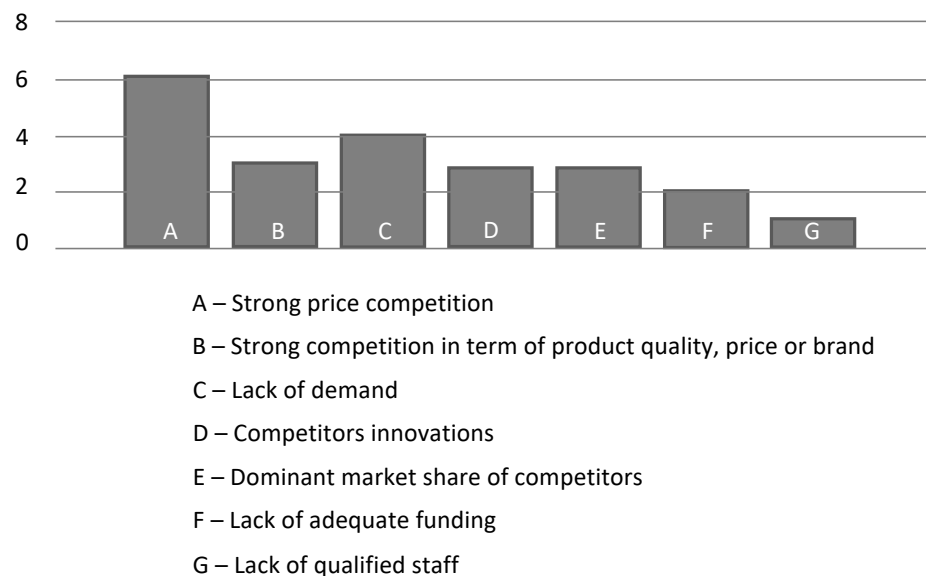
Figure 8: Obstacles to the achievement of Goals 2016–2018

4. Conclusions – suggestions

This work is a first attempt to capture the printing industry in terms of Research and Development Activities. It is a product of primary research and despite the fact that it is the first time that it takes place in the printing industry, the response rate was very low. This fact proves the ignorance of the industry as to the usefulness and necessity of recording such activities as well as the indifference of the industry to Research and Development.

According to the results of the questionnaire, during the three years from 2016 to 2018, several companies carried out development activities related to the purchase of machinery, equipment, software and buildings in order to produce new or significantly improved products or processes with a percentage. In general, in-house activities were carried out for the development and / or introduction of new or significantly improved products and processes, which refer to ink, coatings, substrates, and adhesives. Businesses do not invest in activities outside the business, which shows that they do not expect business extroversion and the acquisition of external knowledge.

The percentage of investment of the printing industry in Research and Development activities in the Graphic Arts sector is low. In 2018 they showed a small increase, it is a positive event for the development of the industry and its activity with research actions achieving the commercial utilization of the findings during the Research and Development.

Business competitiveness is achieved through Research and Development for operational issues but also for processes and products. Competition drives businesses to evolve. So, in order to overcome the obstacle of competition from companies, the solution is to carry out Research and Development activities, gaining a competitive advantage by the companies themselves.

The synergy of companies, universities and research centers strengthens the activity in Research and Development. Partnerships are the catalyst for growth through corporate funding and the provision of know-how and knowledge acquisition by academia and research centers, taking advantage of scientific research and development results, publicizing inventions, copyright, or even copyright and obtaining special permits.

By linking companies with universities, it is easy to train qualified staff with formal qualifications in key positions in companies from research centers and universities. In this way the system absorbs people with high formal qualifications, avoiding the flight of scientists abroad (Brain Drain).

Concluding, for reasons of regularity, the introduction of a two-year survey by the relevant national printing association would act as a catalyst for the valid recording of Research and Development activities in the sector. In a more general context, understanding the R&D-related characteristics of the printing industry would help recognize its strong and weak points as well as help sustain a transition to the era of digital transformation. In the future, it would be useful to identify strategies for achieving business goals because they are based on R&D. Due to the fact that the printing industry is commercial, the introduction of new or significantly improved goods or services, that is, innovations, is important and arises mainly through R&D activities. Equally important is the recording of innovations and patents that are patented in the industry, to determine the technological field.

References

European Commission, 2019. Internal market, industry, entrepreneurship and SMEs: printing industry. *European Commission*, [online] Available at: <https://ec.europa.eu/growth/sectors/rawmaterials/industries/forest-based/printing_en> [Accessed 2019].

Eurostat, n.d. *Eurostat: National accounts and GDP*. [online] Available at: <https://ec.europa.eu/eurostat/statistics-explained/index.php?title=National_accounts_and_GDP> [Accessed 2020].

Global commercial printing industry, 2018. *Global commercial printing industry – market research report*. [online] Available at: <https://www.ibisworld.com/global/market-research-reports/global-commercial-printing-industry/> [Accessed 2018].

Icap.gr., 2017. *ICAP Graphic arts.* [online] Available at: <https://www.icap.gr/Default.aspx?id=2016&nt=149&lang=1> [Accessed 20 October 2017].

Intergraf, 2020. *2019 Intergraf economic report: evolution of the European graphic industry*. Intergraf.

Metrics.ekt.gr., 2018. *Vasikoí Deíktes Érevnas & Anáptyxis gia dapánes kai prosopikó to 2017 stin Elláda.* [pdf] Available at: <http://metrics.ekt.gr/sites/metrics/files/RDstatistics_2017provisional_Greece_el.pdf> [Accessed 2018]. [In English: *Key research and development indicators for expenditure and personnel in 2017 in Greece*].

Metrics.ekt.gr., 2020. *Vasikoí Deíktes Érevnas kai Anáptyxis gia dapánes kai prosopikó to 2019 stin Elláda – Prokatarktiká stoicheía.* [pdf] Available at: <https://metrics.ekt.gr/sites/metrics-ekt/files/ekdoseis-pdf/2020/RDstatistics_2019_provisional_Greece_el.pdf> [Accessed 2020]. [In English: *Key research & development indicators for expenditure and personnel in 2019 in Greece – preliminary data*].

Oecd.org., 2017. *Ekthesi Axiológisis Synthikón Antagonismoú tou OOSA ELLADA 2017*. [pdf] Available at: <http://www.oecd.org/daf/competition/OECD-Competition-Assessment-Review-Greece-2017-gr.pdf> [Accessed 20 February 2017]. [In English: *Competition evaluation report of the OECD GREECE 2017*].

Unesco Institute of Statistics, 2021. *How much does your country invest in R&D?* [online] Available at: <http://uis.unesco.org/apps/visualisations/research-and-development-spending/> [Accessed February 2021].

Wiseguyreports.com, 2018. *Get market research, business prospects, industry analysis & commerce outlook reports.* [online] <Available at: https://www.wiseguyreports.com/> [Accessed 2018].

Showcasing functional inks and electronics through wearable art

Shu Chang[1], Christine Heusner[2], Marla Schweppe[3] and Gail Argetsinger[4]

[1] Department of Graphic Communications, The Wilbur O. and Ann Powers College of Business, Clemson University, Clemson, South Carolina, USA

[2] School of Media Sciences, College of Engineering Technology, Rochester Institute of Technology, Rochester, New York, USA

[3] School of Design, College of Art and Design, Rochester Institute of Technology, Rochester, New York, USA

[4] Department of Theatre and Music Studies, State University of New York, Brockport, New York, USA

E-mail: schang2@clemson.edu

Short abstract

Smart wearables is a transdisciplinary field that has increasingly attracted attention from many fields ranging from fundamental materials research to aesthetic designs. Wearables integrated with electronics and functional materials have been deemed smart due to their interaction with the human wearers. A smart wearable manufacturing process can include but is not limited to directly manufacturing a functional device on substrates, direct printing of interactive inks on substate, or attaching an existing functional device to the substrate. This work aims to integrate various smart functionality, through both inks and electronic devices, into one garment. The goal is to showcase the possibilities and demonstrate the numerous methods to incorporating smartness into wearables while enhancing the garment's design themes. This paper will also discuss the process and challenges encountered in hybrid and functional ink printing with textile as the substrate.

Keywords: interactive textile, smart textile, functional ink, smart wearable

1. Introduction

There has been a plethora of work examining making wearables smart. The term "smart" suggests incorporating electronic devices into wearables that facilitate some of our daily activities (Meoli and May-Plumlee, 2002). The incorporated electronic devices could be passive, active, or interactive. Examples include RF or microwave transmission lines (Huang, et al., 2016), or devices to conduct physiological monitoring (Screenilayam, et al., 2020), or integrated textile keypad or a global position system embedded in clothing (Meoli and May-Plumlee, 2002) for active, passive, or interactive functions respectively. Many industries have been exploring such wearables for their applications, including apparel, residential, military, and medical, to name a few (Meoli and May-Plumlee, 2002).

The second category of smart wearables belongs to the fabrication of functional materials on wearables, typically conducted through printing. Functional materials include, for example, conductive ink for printed electronics, functional inks for LED (Claypole, et al., 2019), functional inks for electroluminescence, as well as interactive color-changing inks with stimuli such as heat or light. Both traditional printing and planar additive manufacturing can be the fabrication method for at least parts of the wearable assembly. The essentials to construct wearables are as follows: manufacturing methods, functional materials, and integrating electronic devices (Xu and Wu, 2020).

This paper aims to establish the process of building the elements that make up the wearable garment focusing on the integration of materials, technologies, functions, and aesthetics. The paper explores the benefits and challenges of working with hybrid printing for functional effects on printed imageries. The wearable, designated Women of Rochester Dress (the Dress), highlights different representations of smart

wearables. The design of the Dress anticipates the advancement of wearable technologies and the smart feature panels on the Dress are incorporated as replaceable. The motivation behind this project was to pay tribute to the many remarkable women with connections to Rochester, New York, in celebration of the centennial of women's right to vote. The Dress is currently on permanent exhibition at the Women's Rights National Historical Park in Seneca Falls, New York.

2. Manufacturing, materials, and electronic components

2.1 Manufacturing of Women of Rochester Dress

Figure 1 depicts the process, materials, and components involved in creating the interactive Women of Rochester Dress. The Dress consists of a dress body and twenty-eight attachable panels. While the dress body's design was printed with inkjet, the interactive elements, such as smart inks and electronic devices, were implemented in the panels. The pie-shaped area labelled Print Technology in Figure 1 shows the four print technologies tested for the Dress graphics. In Figure 1, EP abbreviates the technology of electrophotography.
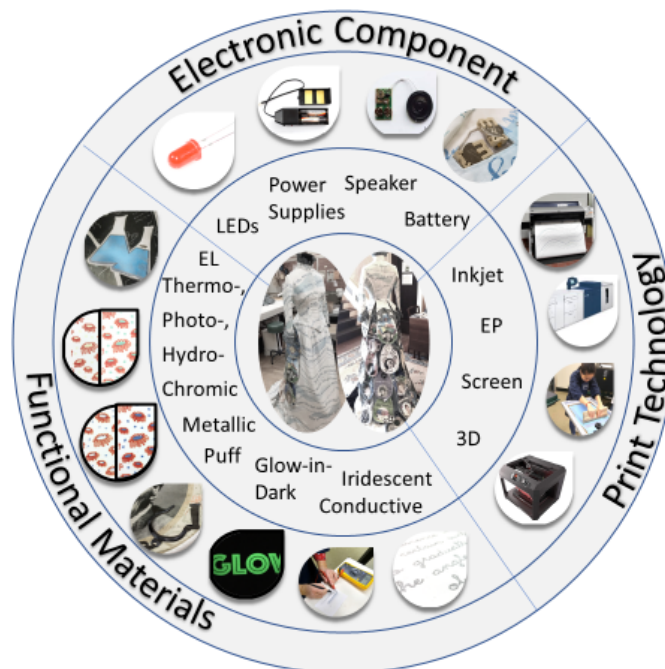
Figure 1: The print technologies, materials, and components used in creating the interactive Women of Rochester Dress

In this category of Print Technology, both inkjet printing and electrophotography were investigated as potential output devices for both the main dress body and the panel imageries. As the inkjet provided direct to garment printing, the electrophotography involved an extra step of an iron-on transfer. The look and feel of the inkjet printing to the fabric were superior to the iron-on transfers. Therefore, electrophotographic printing was not used in the final production of the Dress. Inkjet printing was completed with the Canon imagePROGRAF Pro4000 inkjet, using its recommended aqueous pigment ink for printing the imageries on the dress body and the base designs on the dress panels. Screen printings were flat-bed systems and were responsible for printing specialty inks, including various chromic, glow-in-dark, iridescent inks, the conductive, and electroluminescent layers. The specialty inks were over-printed onto the inkjet-printed panels, and thus the process of hybrid printing. The design called for all panels to have 3D printed buttons, which were produced with a Fused Deposition Modelling printer (MakerBot Replicator 2), except the button for Margaret Woodbury Strong, which was printed with the Stratasys J750 PolyJet.

After the initial stages of project planning, content creation, and design, the fabrication process of the Women of Rochester Dress consisted of nine steps: 1) inkjet printing the background design, 2) screen printing the specialty inks over the inkjet backgrounds, 3) 3D printing the buttons, 4) sewing panels and fabric holders for the electronic components, 5) connecting electronic circuitry into the panels, 6) building the wireframe for the skirt of the Dress, 7) sewing the dress, 8) sewing fasteners for the panels and the buttons, and 9) assembling all the panels to the Dress.

2.2 Substrate, electronic components, and ink

2.2.1 Substrate

The project also examined Cotton Twill, Rayon, Polyester, Satin Twill, Silk Satin, Vinyl Acetate, Canvas, and Chinese Dupion Silk. The Dupion silk, purchased from Jacquard Inkjet Fabric Systems with a FabriSign coating and a paper backing, was chosen for the ease of printing, sewing, and assembly *and* the superior image appearance. FabriSign coating was used to enable a wider color gamut and greater color saturation. The product recommendations indicated that this coating would lead to brighter yellows, darker blacks, richer blues, and stronger reds when used with water-based pigment inks on a wide variety of substrates. The FabriSign coating also improves digital prints' wash-fastness (Digital Fabrics, 2019).

2.2.2 Electronic components

As for the Electronic Components, the pie-shape area in Figure 1 depicts four electronic components integrated into the panels. The parts implemented in the panels were LEDs, a speaker, a screen-printed electroluminescent panel, and their respective power supplies and switches to complete the circuitry. The LEDs were in the design of two light bulbs in the Kate Gleason panel. The speaker with a recorded audio file of Renee Fleming's opera singing was placed behind the corresponding panel in a sewed fabric holder. The electroluminescent panel was in the form of two chemistry beakers for the Esther Conwell panel.

2.2.3 Inks

The Canon imagePROGRAF Pro 4000 uses the LUCIA PRO ink set, comprised of 11 inks and a chroma enhancer. The chroma enhancer was not used when printing to fabric as its recommended use was for gloss and semi-gloss substrates. The eleven-ink set includes Matte and Photo black, with Matte black used to print on the fabric. (Canon, n.d.)

The pie-shaped area labeled Functional Materials in Figure 1 depicts the nine functional inks tested for creating the special effects on the panels, with the electroluminescent ink abbreviated as EL. Table 1 below further details information and attributes of these inks. The nine inks were either purchased or donated from a variety of ink providers. The screen frames used were twenty inches by twenty-four inches with a mesh count of 100 threads per linear inch and 156 threads per linear inch, respectively. The squeegees used in the experimentations had a durometer of 70 Shore A. All screen inks were water-based, except the conductive and the electroluminescent inks.

There were a few inks that required special attention. For example, the photochromic ink was transparent before exposure to sun or UV light and consequently needed to avoid ink or dirt contaminants. Ink or dirt contaminants would cause discoloration of the clear photochromic ink. When hybrid printing hydro-chromic ink with other screen plastisol inks, the hydro-chromic ink changed the substrate dimensions when flash cured, which caused displacements in the registration positions for the subsequent prints. Hydro-chromic ink required either extra backing to support the substrate or last in the print order for multiple ink frames. Thermo-chromic is a fast-drying ink, so to prevent clogging, a retarder was added to the ink. The electroluminescent image consisted of an ITO polyester film, which was then printed with a phosphorescent layer, a dielectric layer, a silver conductive base layer, and an encapsulant (purchased from Gwent Group as a kit).

Table 1: Functional ink used for special effects on inkjet printed dress panels

Ink	Provider	Screen Mesh Count (no. threads per linear inch)	Comments
Glow-in-the-Dark or phosphorescent	Speedball	156	Ink is tacky after drying.
Puff additive to plastisol ink	International Coatings	156	Puff is an additive that can be added to the ink. When too much is added, it causes a bubbling effect and varying texture in ink.
Electro-luminescence	Gwent, Dupont	110	Four screens. The phosphor, dielectric, and conductive silver layers were all printed with at least two coats.
Photo-chromic	LCR Hallcrest, LLC.	110 and 156	This ink is transparent. It shows any traces of dirt or previously printed ink, which does not usually happen with opaque inks. Use a new or well-cleaned screen.
Hydro-chromic	Matsui	110	Ink dries quickly, causing the screen to clog. Flash cure can cause the substrate to curl and cause registration issues for the subsequent ink layer. No retarder was available for this ink.
Thermo-chromic	QCR Solutions Corp	110	Ink dries very fast while printing and results in clogging of screens, added retarder.
Iridescent	Speedball	110 and 156	No issues
Silver Metallic	Speedball	156	Highly viscous. Needed more pressure and lowering the angle of the squeegee. Added retarder.
Conductive	Dupont, flexible ink	156	Need near straight printed path without sharp turns or too many angles.

3. Results and discussion

Figure 2 shows the finished dress with all panels assembled. The Women of Rochester Dress consists of four separate entities: a skirt, a vest, 28 teardrop panels, and 28 buttons (one for each panel). Figure 2a shows the full dress from the front view. The Dress incorporated the names of over 100 women, including the creators of the Dress, in a wave pattern. The panels were in a teardrop shape, as shown in Figure 2b.
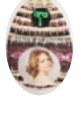

Figure 2: The Women of Rochester Dress: (a) front view of names distributed in wave patterns, and (b) back view of panels that highlighted the contributions

The panels were attached to the skirt with fasteners. The panels feature women with connections to up-state New York, who made a national or international impact through their contributions and were from diverse fields. Their contributions were the inspirations for the design of each panel.

Table 2 describes eight of the 28 panels, in terms of the women featured, their contributions, the implemented special effects, and how they interact with the audience. The eight women are Manuela Campanelli, astrophysicist; Kristen Wiig, actress; Harriet Tubman, abolitionist; Abby Wambach, soccer player; Adelaide Crapsey, poet; Renee Fleming, opera singer; Esther Conwell, chemist and physicist; and Kate Gleason, mechanical engineer.

Table 2: Select panel and their respective descriptions of the woman, implemented effects, and audience experiences

Panel	Name	Contribution	Implemented effect	Interaction
	Manuela Campanelli	Discoveries in relativity, gravitational waves, and black holes	Stars printed with phosphorescent ink which glows in the dark	Stars illuminate in darkness
	Kristen Wiig	American actress, comedian, and writer	Select dots printed with phosphorescent ink, which glows in the dark. 3D printed multi-color button	Dots illuminate in darkness
	Harriet Tubman	American abolitionist a "conductor" of the Underground Railroad	Puff additive to the ink expands the print to create raised handcuffs	Handcuffs are visually raised above other printed elements and are soft to the touch
	Abby Wambach	Two-time Olympic Soccer Gold Medallist and two-time FIFA World Cup Champion	The black, thermo-chromic ink on the soccer balls disappears with heat	Touch or breathe on the soccer ball for markings to disappear
	Adelaide Crapsey	American poet	Iridescent ink is used to illuminate the hand-written poem	View ink at different angles to see gradual color change
	Renee Fleming	American Operatic Soprano	Sound recording and speaker	Audio recording of her operatic singing can be switched on and off
	Esther Conwell	Pioneering American chemist and physicist, National Medal of Science winner	Electroluminescent beakers flash on and off. 3D multi-color button.	Switch to control battery power will turn on, off, or pulse glowing effect
	Kate Gleason	The first woman admitted to the American Society of Mechanical Engineers	Conductive ink circuitry for lighting LEDs implemented in the light bulb designs	LED lights can be switched on or off

For Manuela Campanelli's panel, the phosphorescent ink used in the panel features her research on the merging of black holes by having the stars illuminate in the darkness. The glow-in-dark ink was used again in the Kristen Wiig panel to create an actress's effect on a spot-lit stage. The puff ink produced the handcuffs for the Harriet Tubman panel. The handcuff images were raised and felt soft to the touch. The black-and-white soccer ball of Abby Wambach would lose its black marks when the ink is heated through touch or being breathed on. The iridescent ink emphasizes the personalized hand-written style of a poem by Adelaide Crapsey. A speaker implemented in opera soprano Renee Fleming's panel would play a recording when switched on.

The making of Esther Conwell and Kate Gleason panels are further detailed in Figure 3 and Figure 4, respectively. Figure 3 displays a 3D printed multi-color button in the shape of a chemistry beaker with the formula of polyethylene (Figure 3a) and a cut-out of two beakers fabricated with electroluminescent ink (Figure 3b). In Figure 3b, the two panels of Esther Conwell illustrate the "off" (left panel) and "on" (right panel) of the electroluminescent display, which shows the beaker illuminating when it is on. The lower image in Figure 3b displays a student testing the printed electroluminescent layer on a tightly woven fabric. An even layer of the ink required to create the uniform illumination could not be obtained on the tightly woven fabric. Consequentially, ITO film was used as a substrate for electroluminescent ink printing. From a design point of view, the ITO film provided a more realistic look-and-feel of a chemistry beaker.
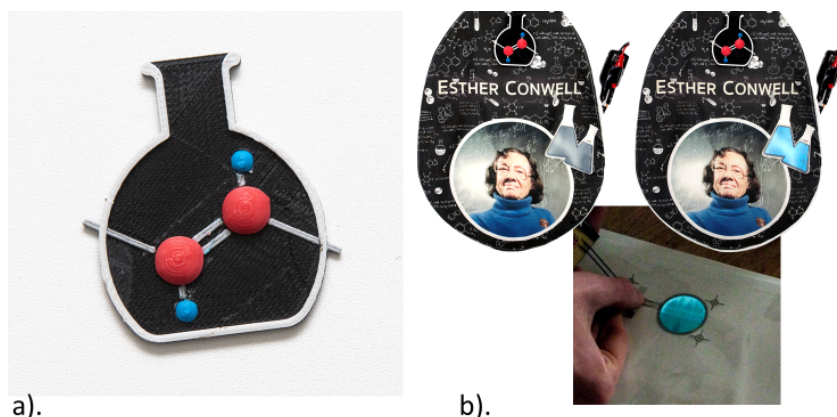
Figure 3: The panel of Esther Conwell includes (a) 3D printed button in the shape of a beaker
with the formula of polyethylene and b) two beakers of electroluminescent ink printed on ITO film;
the bottom image of (b) shows an attempt to print the electroluminescent layer on a tightly woven fabric

Figure 4 captures the dress panel representing Kate Gleason. The design features gears and rulers with two light bulbs lit up with LEDs (Figure 4a). The circuitry was completed with copper tape hidden between the front and back fabrics of the panel. Figure 4b shows the pocket designed and fabricated for the batteries and the switch to enable the circuitry.

Figure 4: The panel of Kate Gleason highlights her success as a pioneering woman engineer with
(a) LED light bulbs to emphasize innovations; image in (b) marks the hidden pocket for the circuitry

The Kate Gleason panel's original intent was to include the entire circuitry and all electronics on the panel's front as parts of the design. The process for producing this panel began by selecting workable conductive lines. Figure 5a shows a student testing the effectiveness of conductive lines. The lines were printed with Dupont flexible silver ink at different widths and lengths on various selected fabrics. The final line design was not too long or too narrow to ensure sufficient current supplied to illuminate the LEDs. After the conductive-track selection, the panel incorporated the tracks as part of the design. Figure 5b shows a test case for the inclusion of circuitry in the design. In Figure 5b, the conductive tracks are part of the lamp post;

while the tracks inside the house are positioned for a 3D printed door, it would act as the switch for the circuitry. The conductive tracks were printed below the over-printed screen images since the overlayer screen inks act to some degree as a passivation layer. The experiment shown in Figure 5b had sharp angles in the path, which were eliminated to minimize the conductive tracks' resistance as shown in Figure 5c.
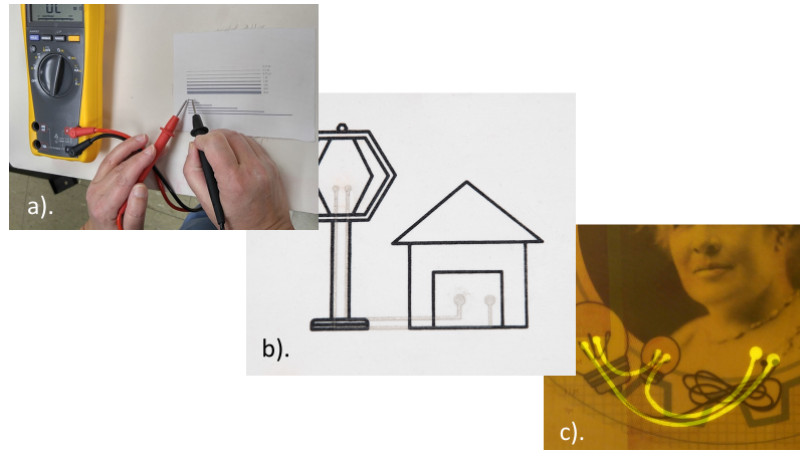
Figure 5: The process of incorporating the circuitry into the design: (a) choosing a conductive track, (b) experimenting with design, and (c) implementing in a design

For the Kate Gleason panel, curved tracks were eventually selected (yellow lines in Figure 5c). Although the design intention was successful, the printed conductive track was not used in the final product due to the constraints required to sew, assemble, and the Dress's hands-on display to a live audience. Such handlings caused damages to the circuit and limited the useful life of the panel.

The most challenging specialty ink to screen print was the hydro-chromic ink. Figure 6 illustrates issues occurring from the hydro-chromic ink. Figure 6a shows inkjet blue dots with red screen-printed flower petals and white hydro-chromic ink over the center of the flowers. After the sample had been wet multiple times, the imager underlines the bleeding of the red ink. Figure 6b shows light and dark blue fans printed with inkjet with white hydro-chromic ink printed over the top portion of the dark blue fans. The sample demonstrates the inconsistency in the coverage and texture of the ink. This is caused by ink's high viscosity and the ink's rapid drying while it was being printed.

a).   b).
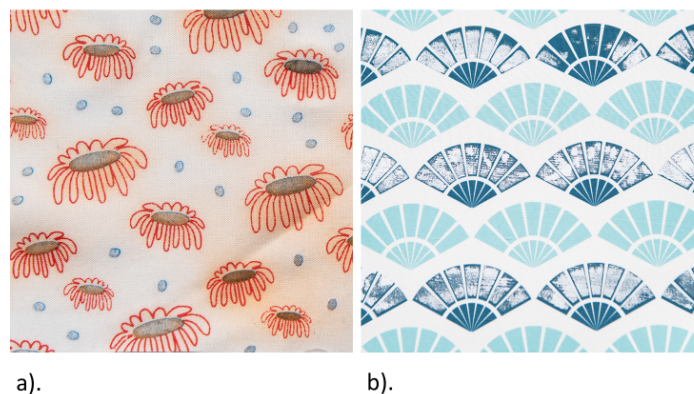
Figure 6: Challenges with hydro-chromic ink: (a) bleeding due to the presence of water, (b) clogging of the screen due to rapid drying of the ink

Figure 7 depicts examples of 3D buttons. Many of the buttons printed used multiple colors. The multiple colors were created by pausing the build process, replacing the filament with one of a different color, and then continuing the build with the new filament. This process required specific planning so that each new color was built upon the design below.
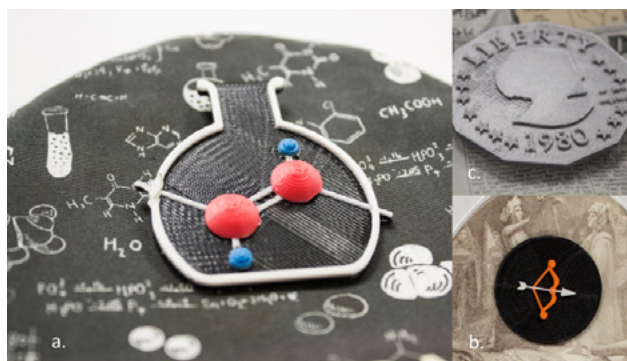
Figure 7: Multi-color 3D printed buttons

The Women of Rochester Dress project encountered common smart textile limitations as noted by previous research including cost, durability of materials, ability for materials to hold up to laundering, integration processes, technology and material limitations, and care and maintenance requirements (Meoli and May-Plumlee, 2002; Fernández-Caramés and Fraga-Lamas, 2018). Some of these limitations are avoided due to the nature of the Women of Rochester Dress being an art piece, that does not require mass production of the product and, while could be worn for show, its main function as wearable art means that the garment does not need to hold up to heavy wear, environmental effects or laundering.

One feature of the dress which specifically addressed the limitations of smart textiles was the detachable panels. All smart technology was implemented on a panel that could be removed via the button which attached the panel to the dress. This allows for the panel to be removed if the smart technology needs to be repaired or replaced, or if the garment required laundering. The removable panels also allowed the implementation of future panels that feature the state-of-the-art wearable technologies. The dress can be customized and for viewers of the garment to interact with the technology and smart effects on the panel with it removed from the larger garment.

4. Conclusions

The Women of Rochester Dress was completed by a cross-disciplinary group of graduate and undergraduate students and faculty. The dress project promoted experimentation with multiple sciences, technology, engineering, art, and design, and mathematic (STEAM) topics. The Dress illustrates what could be done through the integration of printing, materials, technology, and aesthetics to create a smart wearable that showcases the technologies and materials through wearable art. The integration of these diverse elements and skillsets allowed problem-solving across disciplines to achieve a shared goal. The resulting project is to inspire other women for years to come as it has become a permanent addition to the Women's Rights National Historical Park in Seneca Falls, New York.

References

Canon, n.d. *imagePROGRAF PRO-4000*. [online] Available at: <https://www.usa.canon.com/internet/portal/us/home/products/details/professional-large-format-printers/professional-photo-fine-art/imageprograf-pro-4000/> [Accessed February 2021].

Claypole, J., Holder, A., McCall, C., Winters, A., Ray, W. and Claypole, T., 2019. Inorganic printed LEDs for wearable technology. In: C. Ridgway, ed. *Advances in Printing and Media Technology: Proceedings of the of the 46th International Research Conference of iarigai. Stuttgart, Germany, 15–18 September 2019. Darmstadt: Germany: iarigai,* pp. 150–155.

Digital Fabrics, 2019. *Jacquard inkjet fabric systems*. [online] Available at: <https://www.inkjetfabrics.com/products/digital-fabrics> [Accessed February 2021].

Fernández-Caramés, T. and Fraga-Lamas, P., 2018. Towards the internet of smart clothing: a review on IoT wearables and garments for creating intelligent connected e-textiles. *Electronics*, 7(12): 405. https://doi.org/10.3390/electronics7120405.

Huang, X., Leng, T., Hsin Chang, K., Chin Chen, J., Novoselov, K.S. and Hu, Z., 2016. Graphene radio frequency and microwave passive components for low cost wearable electronics. *2D Materials,* 3(2): 025021. https://doi.org/10.1088/2053-1583/3/2/025021.

Meoli, D. and May-Plumlee, T., 2002. Interactive electronic textile development: a review of technologies. *Journal of Textile and Apparel, Technology and Management*, 2(2), pp. 1–12.

Screenilayam, S.P., Ul Ahad, I., Nicolosi, V., Acinas Garzon, V. and Brabazon, D., 2020. Advanced materials of printed wearables for physiological parameter monitoring. *Materials Today*, 32, pp. 147–177. https://doi.org/10.1016/j.mattod.2019.08.005.

Xu, S. and Wu, W., 2020. Ink-based additive nanomanufacturing of functional materials for human-integrated smart wearables. *Advanced Intelligent Systems*, 2(10): 2000117. https://doi.org/10.1002/aisy.202000117.

Wavelet-based watermarking in the finite field

Ignaty Adamantov[1], Valery Gorbachev[2], Maria Saveljeva[2] and Elena Yakovleva[2]

[1] ITMO University, St. Petersburg, Russia

[2] High School of Print and Media of St. Petersburg State University of Industrial Technology and Design, St. Petersburg, Russia

E-mails: botadeus@gmail.com; valery.gorbachev@gmail.com; savmary@mail.ru; 2305lena@mail.ru

Short abstract

It was found that the rounding errors due to storing of the watermarked image in graphical format can be significant. A scheme including wavelets coefficient replication is considered for visible and removal watermarking. A watermarking technique developed adopting the finite field GF(2) is found to be rounding error free.

Keywords: digital image, watermarking, finite field

1. Introduction and background

To protect digital images, numerous solutions have been proposed in the literature. The solutions are often based on image processing in the frequency domain, and the Discrete Wavelet Transform (DWT) technique is widely used (Khan, et al., 2019).

The aim of this work is to consider the accuracy of calculating with DWT. The calculating accuracy may be important for image-based watermarking. The reason is that there is a difference between the image data and the computing data encoding. Indeed, storing the image in graphical format usually supports integer encoding in contrast to computing which uses a larger set of rational numbers to achieve the computation. When rounding up to integer format, errors are introduced, recognised as rounding errors, and these can play a significant role in the accuracy of watermarking (Hu, Kwong and Huang, 2006; Gorbachev, et al., 2017). Such errors arise in various watermarking schemes, particularly in the scheme we consider in this work.

The scheme presented here allows embedding of a visible watermark that can be removed to retrieve the original. We found that storing watermarked images indeed results in significant errors, such that the visual quality of the retrieved original is degraded. To eliminate the rounding errors a solution adopting the finite field is introduced. It is based on the techniques developed for DWT in the field GF(2) (Gorbachev, et al., 2021) and results in rounding error free watermarking.

2. Materials and methods

For protection of media content, visible and removal watermarking is often used. The removal feature allows the legitimate user to remove the watermark if it is considered to impinge negatively on the desired visual perception. The main problem of this technique is how to retrieve the original after removal and storage. Considering a watermarking scheme based on replication, we focus on the common errors that restrict visual quality.

2.1 General scheme

In our scheme, a watermark M is embedded into a grayscale image F, and may be subsequently removed.

The main steps are as follows.

Before embedding, a replicated image F_2 is prepared from the original F. Image F_2 has two identical blocks or frequency bands in its frequency domain given by the DWT of F. Noting that the DWT of a grayscale image results in four blocks, known as approximation coefficients, namely amplitude, horizontal, vertical and diagonal details A, H, V and D, respectively, this results in the replicated image F_2 having two identical or replicated blocks, for example $\{AHVH\}$ instead of $\{AHVD\}$. Indeed, both images F and F_2 are visual undistinguishable. Then F_2 is watermarked by embedding a watermark M into one of the two replicated blocks, such that we now have F_M. The obtained watermarked image is stored in a graphical format. From the mathematical point of view this is a mapping onto integers $F_M \Rightarrow F_{RT}$, where "RT" refers to retrieved. The reason is that storing usually needs integer encoding in contrast to computing, which adopts a much large number set in computation. Then the legitimate user removes the watermark. The user retrieves image F_{RT} from F_M by replacing the watermarked blocks retrieved from its replica.

3. Experimental

In the experiment we study the rounding errors due to storing the watermarked image in graphical format. We consider a distortion measure known as Peak Signal to Noise Ratio (PSNR). This is a measure of distinguishability between two digital images. The greater the PSNR between two images A and B, $psnr(A, B)$, the more the images A and B are different. We calculated distortion measure between the original image F and the retrieved image before and after storing F_R and F_{RT}, namely $psnr(F, F_R)$ and $psnr(F, F_{RT})$. This, then, allows us to study the role of the rounding errors.

A database of 75 grayscale images was used. A binary watermark was embedded with a scale parameter q that is a measure of the strength or amplitude of watermark.

4. Results and discussion

Figure 1 presents two distortion measures averaged over 75 images against q.
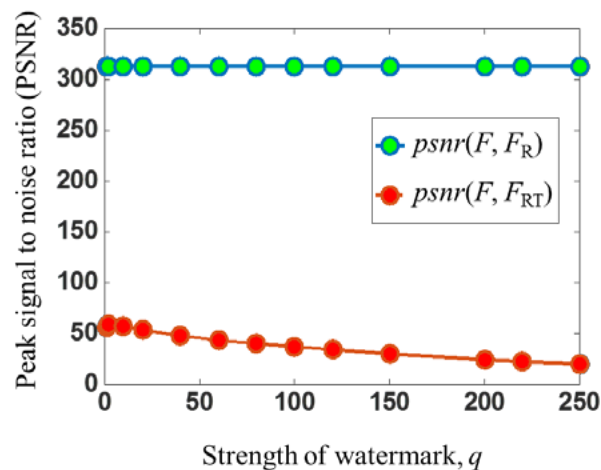
Figure 1: Distortion measure against against strength of watermark q

The Haar wavelet for replicating {*AHVH*} was used. It tells us that the rounding errors are significant and result in a difference up to 6 times between the respective PSNRs. Note, for two matrices *A* and *B*, described grayscale images *PSNR* is given by ratio , where is mean root square error. The findings are in accordance with visual perception.

Figures 2 and 3 show one of the watermarked images F_M and its retrieved version F_{RT}, displaying that the visual quality is not good.

Figure 2: Visual watermark

Figure 3: Retrieved original F_{RT}

4.1 Solution

To eliminate the rounding errors all calculations may be performed over a finite field that endows the arithmetic operation an integer encoding. For the considered scheme the calculation was made in the finite field GF(2), developed for DWT (Gorbachev, et al., 2021). We found that all transforms may be performed over this field GF(2). This results in the watermarking scheme being rounding error free. Such scheme allows us to retrieve an image matching the original of high quality, as is shown in Figure 4.

Figure 4: The retrieved original in the finite field GF(2)

5. Conclusions

The following conclusions can be drawn from the presented results:

1. A replicating frequency band of a grayscale image may be used for embedding visual and removal watermarking to protect the image.
2. This technique has rounding errors due to storing the watermarked image in a graphical format that supports integer encoding. These errors may be significant.
3. To eliminate the rounding errors, calculations may be performed in the finite field GF(2).

References

Khan, I.I., Ahmad, K., Rizvi, M.A. and Bin Ahmad, K.A., 2019. Increased PSNR with improved DWT digital watermarking technique. *International Journal of Innovative Computing and Applications*, 10(3/4), pp. 185–193. https://doi.org/10.1504/IJICA.2019.103390.

Hu, Y., Kwong, S. and Huang, J., 2006. An algorithm for removable Visible Watermarking. *IEEE Transactions on circuits and systems video technology*, 16(1), pp. 129–133. https://doi.org/10.1109/TCSVT.2005.858742.

Gorbachev, V.N., Denisov, L.A., Kainarova, E.M. and Metelev, I.K, 2017. A steganographic image-based approach for protection of pdf files. *Proceeding of the International Conferences Computer Graphics, Visualization. Computer Vision and Image Processing* 2017. Lisbon, Portugal, 20–23 July 2017. IADIS, pp. 285–289.

Gorbachev, V.N., Kazakov, A.Y. and Savel'eva, M.Y., 2021. Wavelet transform of the gray-scale image in a finite GF(2) field. *Journal of Optical Technology*, 88(2), pp. 87–93. https://doi.org/10.1364/JOT.88.000087.

Optical properties and appearance of fused deposition modelling filaments

Alina Pranovich[1], Sasan Gooran[1], Jeppe Revall Frisvad[2] and Daniel Nyström[1]

[1] Linköping University, Department of Science and Technology, Norra Grytsgatan 10, 60233, Norrköping, Sweden

[2] Technical University of Denmark, Department of Applied Mathematics and Computer Science, Richard Petersens Plads 321, 2800 Kgs. Lyngby, Denmark

  E-mail: alina.pranovich@liu.se

Short abstract

The appearance of 3D-printed objects is affected by numerous parameters. Specifically, the colour of each point on the surface is affected not only by the applied material, but also by the neighbouring segments as well as by the structure underneath it. Translucency of the 3D printing inks is the key property needed for reproduction of surfaces resembling natural materials. However, the prediction of colour appearance of translucent materials within the print is a complex task that is of great interest. In this work, a method is proposed for studying the appearance of translucent 3D materials in terms of the surface colour. It is shown how the thickness of the printed flat samples as well as the background underneath affect the colour. By studying diffuse reflectance and transmittance of layers of different thicknesses, apparent, spectral optical properties were obtained, i.e., extinction and scattering coefficients, in the case of commercially available polylactic acid (PLA) filaments for Fused Deposition Modelling (FDM) printers. The coefficients were obtained by fitting a simplistic model to the measured diffuse reflectance as a function of layer thickness. The results were verified by reconstructing reflected spectra with the obtained parameters and comparing the estimated colour to spectrophotometer measurements. The resulting colour differences in terms of the CIEDE2000 standard are all below 2.

Keywords: 3D printing, appearance, optical properties, PLA filaments, translucency

1. Introduction and background

Unlike in traditional 2D printing, it is possible to apply materials in layered structures in Fused Deposition Modelling (FDM) 3D printing. The technique is based on applying melted filament in a layer-by-layer manner. Although not originally used for the purposes of appearance reproduction, this possibility is being actively explored (Hergel and Lefebvre, 2014; Reiner, et al., 2014). Current FDM printers offer the possibility of combining several filaments within one print (Espalin, et al., 2014; Khondoker, Asad and Sameoto, 2018). Together with slicing and instrument path strategies (Kuipers, et al., 2018; Song, et al., 2019), it is possible to recreate different colour shades within the built surface. There is a rich variety of commercially available filaments for FDM printing of different colours and special effects (glossy, semi-transparent, etc). An important visual trait of any 3D material is its translucency, that is, its ability to let light penetrate the material and re-emerge from the surface after multiple subsurface scattering events. Typically, it is required to apply > 1 mm thick layers until the colour of the applied material saturates and the impression of the layer is not affected by the layers underneath. At the same time, available fused deposition modelling 3D printers are able to apply filament in layers as thin as 50 μm. A combination of layers of two different materials therefore has a potential to create a number of colours on the outer surface, depending on the layer order and their thicknesses (Babaei, et al., 2017). If intrinsic optical properties are known, it is possible to predict the diffuse reflectance of a print using an existing solution of the radiative transfer equation, like the Kubelka-Munk formulas (Kubelka and Munk, 1931; Kubelka, 1948) or multiflux models (Simonot, et al., 2016). It is also possible to use known optical properties for simulating/visualising the appearance of a surface using physically based rendering techniques (Pharr, Jakob and Humphreys, 2017).

This is called soft proofing. The main optical properties that affect the colour appearance of a print are extinction and scattering properties. 3D printing can directly provide samples for the purpose of estimating the optical properties, as the dimensions of the produced samples can be precisely controlled. The effect of the layer thicknesses on the colour appearance by preparing a set of straight layers and collecting spectral reflectance and transmittance values is being studied. These values are represented either by spectral reflectivity, or by CIELAB values. Reflectivity values of defined 3D printed samples can be sufficient for characterizing a printer with data driven approaches described by Chen and Urban (2021). However, the ability to reveal and use material parameters are necessary for the physical models. After collecting reflectance data of the samples of different thicknesses, the effect of material thickness for each wavelength is analysed. Spectral diffuse reflection that contributes to the visual perception of the surface can be measured with a spectrophotometer. This device is commonly used for 2D prints, where the paper with ink absorbed in it is being characterised. From the 3D printing perspective, it is not sufficient to only consider absorption of the ink, because of the multiple interactions within the volume and contribution of the environment to the final appearance. It is important to distinguish between the absorption and scattering by the used materials. The target of this work is to predict colour appearance of the printed layers of filament. This report shows how a prediction can be made and how the necessary optical properties can be obtained from collecting sets of spectral power distribution (SPD) measurements of differently thick printed layers.

2. Materials and methods

In this work, commercially available FDM filament Neon Pink PLA from Prima Creator was chosen. The samples were prepared with a Flashforge Creator 3 3D printer. For the SPD measurement, a Barbieri SPF LFP 2 series spectrophotometer was used. The parameters were set as follows: D50 illuminant, 8 mm aperture, 45°/0° light/view configuration for the reflectance measurement. Transmittance measurements were performed under D50 illuminant and 8 mm aperture. The spectral range of the measurement is 380-780 nm. For accurate spectrophotometer measurements, the sample thickness should not exceed 2 mm. As samples, 2 cm × 2 cm squares with varying thickness between 0.1 mm and 1 mm were printed. In order to 3D print the samples, 3D models were created and sliced, so that the instrument path could be generated. A sample can be built using different thickness of each applied filament layer, different pattern with which internal volume will be printed, and the density of infill. In our experiment, the slicing parameters were set as follows: first layer thickness 0.1 mm, each next layer 0.05 mm, volume fill pattern was chosen as lines with direction rotating by 90° at each layer, 100 % infill density. Figure 1 demonstrates appearance of the printed samples placed on the white paper.
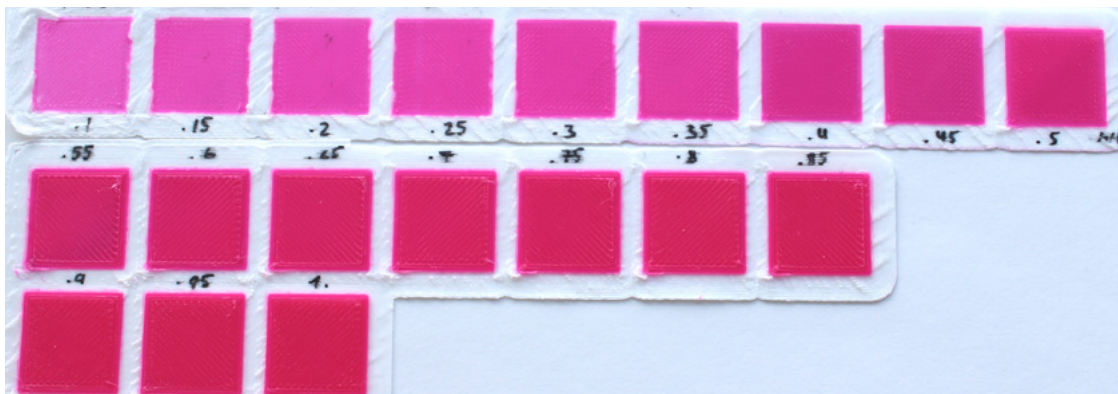
Figure 1: Printed samples of Neon Pink PLA of thicknesses 0.1 mm to 1 mm photographed on a white background; because of the material translucency, the background is affecting the surface colour, especially for the thin samples

After printing the samples, four sets of spectrophotometer measurements for each sample were performed. Reflection measurements were repeated for three different backgrounds below the sample: white paper, black paper and a mirror. The fourth set was transmission measurement. Each individual measurement was repeated five times each with a slightly different position and orientation of the sample, and the mean value was taken. This approach accounts for the imperfections on the surface caused by the printing process and compensates for the regular line patterns.

A practical model for predicting the variation in appearance for different backgrounds and different layer thicknesses is needed. To this end, a simple 1D light transport model was employed: light propagates upwards or downwards in the medium. The direction of the incident light is thus neglected, except for the fact that the reflectance of the background material is affected by the direction of incidence. If measured alone, mirror background results in almost perfect black SPD, as all incident light at a 45° angle of incidence will be reflected away, and nothing will be measured under 0°. However, when a layer of scattering material is included, part of the incident light will be scattered so that some of the light will be reflected to the normal direction. The amount of redirected light can be related to the thickness and scattering properties of the material. SPD of each sample was measured and then modelled with the following function accounting for extinction and diffuse reflection by the material:

$$R_{\mathrm{m}} = \int_{0}^{D} R e^{-2\alpha x} dx + R_{\mathrm{b}} e^{-2\alpha D} \qquad [1]$$

where R_{m} is the measured reflectivity, the apparent extinction coefficient of the material and D is the sample thickness. The exponential term represents extinction according to Bouguer's exponential attenuation law (Perrin, 1948), and R is the reduced coefficient representing diffuse scattering of the material. In our assumptions, R_{b} represents effective background reflectivity due to the bare background reflectance and the scattering in the material.

Measured transmittance data T_{m} were also modelled using the exponential attenuation law:

$$T_{\mathrm{m}} = e^{-\alpha D} \qquad [2]$$

All four sets of measured reflected and transmitted spectral distributions were modelled simultaneously with Equations [1] and [2]. The spectral dependency is described by spline functions. Parameter R and shared parameter α were fitted for each wavelength. For each background, an individual parameter R_{b} was fitted. After the material parameters were obtained, they were used as a benchmark to reconstruct spectral density by applying material parameters in Equation [1]. Obtained SPDs were used to compute CIELAB values which were compared to the originally measured ones in terms of CIEDE2000 standard.

3. Results and discussion

The spectral power distribution values collected during the measurements for each sample result in the colour perceived by the observer. The samples with thickness up to 1 mm are not opaque. Thus, the background below the sample affects the colour on the surface. This results in lighter shades in case of the white background and darker if the black background is used. Figure 2 demonstrates CIE *xy* chromaticity diagrams of samples with different thicknesses on different backgrounds. As the thickness increases, the background will contribute less to the top surface appearance. This can also be seen from Figure 3, where the evolution of the reflectance values with the sample thickness is shown for one chosen wavelength of the SPD. For three different backgrounds, a tendency of the colour of increasing thickness of the samples to saturate toward the common point can be seen.
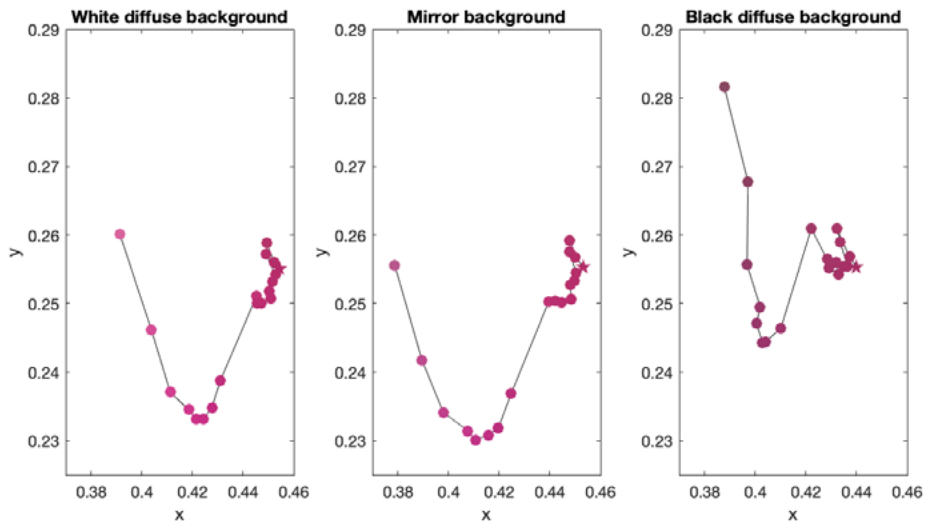
Figure 2: CIE xy chromaticity diagrams representing measured colour of the samples of Neon Pink filament of thickness 0.1 mm to 1 mm in steps of 0.05 mm; coordinates correspond to the CIE x and y values, the colour of the points represents RGB values calculated from the measured diffuse reflectance values, data for the 1 mm thick sample are marked with a star
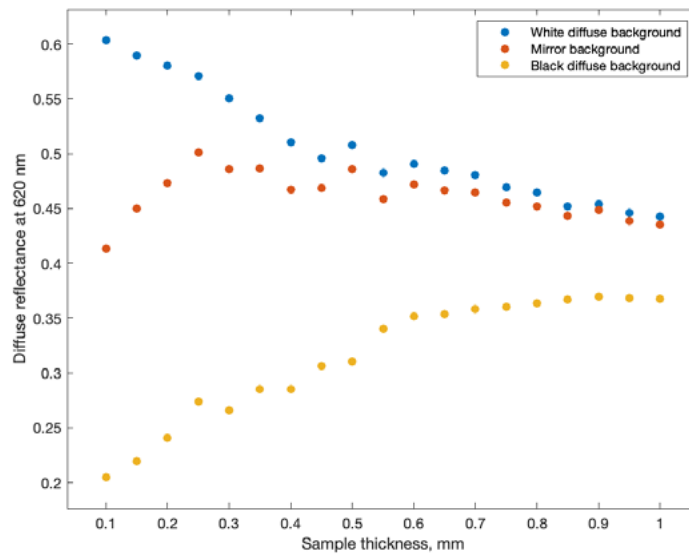
Figure 3: Diffuse reflectance at 620 nm with increasing sample thickness for all three backgrounds; as the thickness of the sample increases, the contribution of the background becomes less evident, and the values slowly approach a common saturation point

In Figure 4, the apparent extinction coefficient α and the apparent scattering coefficient R resulting from our fits is plotted. Notably, the spectral line shape of the fitted scattering coefficient resembles the (rescaled) derivative of the extinction coefficient with respect to photon frequency. This indicates that the approach is consistent with expectations of physically meaningful dispersion, according to the Kramers-Kronig relations (Jackson, 1975). The apparent scattering coefficient is mostly a result of polydispersity of the real part of the refractive index, while the apparent extinction coefficient is a result of both material extinction (the imaginary part of the refractive index) and scattering.
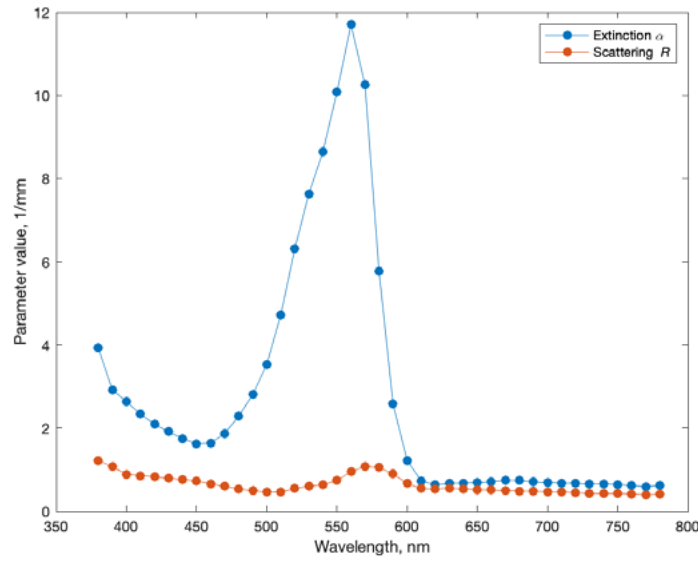
Figure 4: Effective extinction α and reduced scattering coefficient R obtained from the fit

The obtained extinction and scattering coefficients together with fitted effective surface response R_b were plugged into Equation [1]. By doing this, the diffuse reflectance values were reconstructed. Figure 5 demonstrates comparison between originally measured and reconstructed reflectance for the samples of the thickness of 0.1 mm, 0.5 mm and 1 mm on white diffuse background.

In order to quantitatively assess the difference, CIELAB values were calculated using the reconstructed reflectance spectra and assuming a D50 light source. Those values were compared to the originally obtained CIELAB values from the measurements in terms of CIEDE2000 standard. The results of comparison for all samples and each background are shown in Figure 6. As can be seen, the colour difference values are stochastically distributed across the mean value. No tendency with sample thickness can be observed, which indicates absence of a strong systematic error in our simplistic 1D radiative transfer model approach. There are discrepancies in the red spectral range, where the material is weakly absorbing. This can indicate insufficient consideration of the spatial distribution of the scattered light. The obtained values for colour difference below 2 show that the method is well suited for the main purpose, i.e., colour prediction.
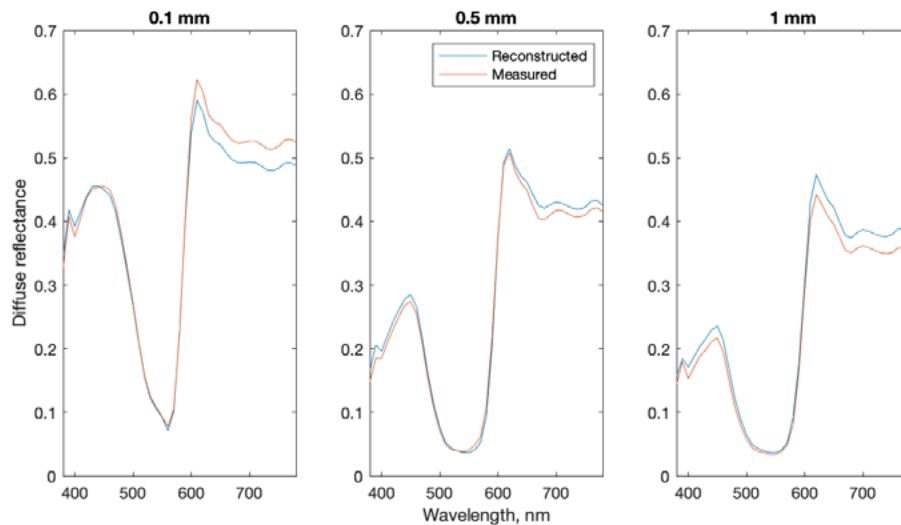
Figure 5: Comparison of the reconstructed diffuse reflectivity and the originally measured one for samples of the thickness of 0.1 mm, 0.5 mm and 1 mm on white diffuse background
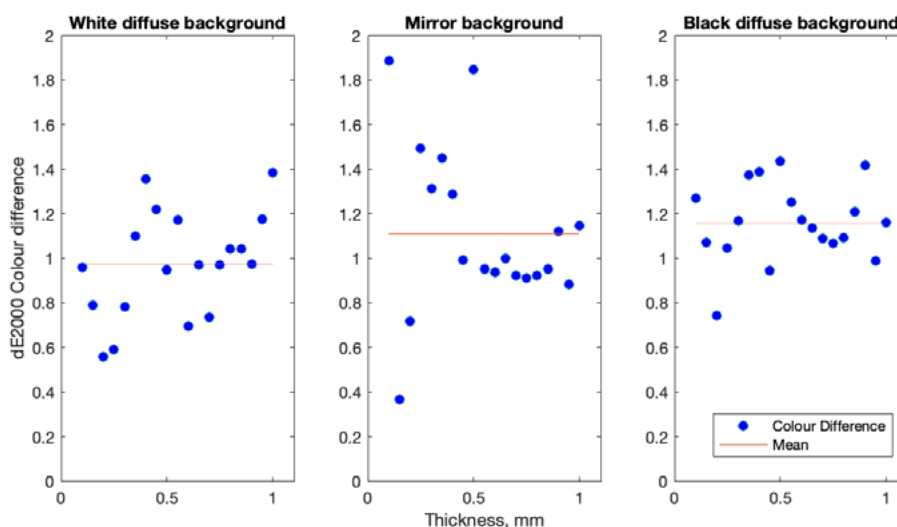
Figure 6: Colour difference between measured and reconstructed reflectivity values for all three backgrounds and each sample

4. Conclusions

In this work, a study of colour appearance of PLA filament with increasing thickness was made. A set of transmission and reflection measurements on three different backgrounds was used to obtain apparent extinction and scattering coefficients. The resulting coefficients are consistent with the expectations, i.e., the largest extinction of the pink material occurs in the green. Using a simplistic 1D radiative transfer model, it was possible to predict the spectral diffuse reflectance of layered PLA filaments and their combinations. This approach enables prediction based on physical assumptions as opposed to an approach based purely on machine learning. In this work, the samples were printed on an FDM 3D printer. This manufacturing method imprints certain surface artifacts caused by the instrument path. Therefore, the material parameters revealed during the experiment have apparent character. Further studies can be carried out in order to determine the effect of the volume and surface structure on the scattering and absorption properties of the samples. The method is not restricted to the PLA FDM samples, and it is possible to apply it on arbitrary materials produced by depositing layers of known thickness acceptable by the spectrophotometer. As a step of further work, one could assume that the scattering properties obtained in this work are valid in all directions. Our work is thus useful for studying the crosstalk between the neighbouring points of a print.

References

Babaei, V., Vidimče, K., Foshey, M., Kaspar, A., Didyk, P. and Matusik, W., 2017. Color contoning for 3D printing. *ACM Transactions on Graphics,* 36(4): 124. https://doi.org/10.1145/3072959.3073605.

Chen, D. and Urban, P., 2021. Deep learning models for optically characterizing 3D printers. *Optics Express,* 29(2), pp. 615–631. https://doi.org/10.1364/OE.410796.

Espalin, D., Ramirez, J.A., Medina, F., and Wicker, R., 2014. Multi-material, multi-technology FDM: exploring build process variations. *Rapid Prototyping Journal,* 20(3), pp. 236–244. https://doi.org/10.1108/RPJ-12-2012-0112.

Hergel, J. and Lefebvre, S, 2014. Clean color: improving multi-filament 3D prints. *Computer Graphics Forum,* 33(2), pp. 469–478. https://doi.org/10.1111/cgf.12318.

Jackson, J.D., 1975. *Classical electrodynamics.* 2nd ed. New York, NY, USA: John Wiley & Sons.

Khondoker, M.A.H., Asad, A. and Sameoto, D., 2018. Printing with mechanically interlocked extrudates using a custom bi-extruder for fused deposition modelling. *Rapid Prototyping Journal,* 24(6), pp. 921–934. https://doi.org/10.1108/RPJ-03-2017-0046.

Kubelka, P., 1948. New contributions to the optics of intensely light- scattering material, part I. Journal of the *Optical Society of America,* 38(5), pp. 448–457. https://www.osapublishing.org/josa/abstract.cfm?URI=josa-38-5-448.

Kubelka, P. and Munk, F., 1931. Ein Beitrag zur Optik der Farbanstriche. *Zeitschrift für technische Physik,* 12, pp. 593–601.

Kuipers, T., Elkhuizen, W., Verlinden, J. and Doubrovski, E., 2018. Hatching for 3D prints: line-based halftoning for dual extrusion fused deposition modeling. *Computers & Graphics,* 74, pp. 23–32. https://doi.org/10.1016/j.cag.2018.04.006.

Perrin, F.H., 1948. Whose absorption law? *Journal of the Optical Society of America,* 38(1), pp. 72–74. https://doi.org/10.1364/JOSA.38.000072.

Pharr, M., Jakob, W. and Humphreys, G., 2017. *Physically based rendering: from theory to implementation.* 3rd ed. Cambridge, MA, USA: Morgan Kaufmann / Elsevier.

Reiner, T., Carr, N., Měch, R., Šťava, O., Dachsbacher, C. and Miller, G, 2014. Dual-color mixing for fused deposition modeling printers. *Computer Graphics Forum,* 33(2), pp. 479–486. https://doi.org/10.1111/cgf.12319.

Simonot, L., Hersch, R.D., Hébert, M. and Mazauric, S., 2016. Multilayer four-flux matrix model accounting for directional-diffuse light transfers. *Applied Optics,* 55(1), pp. 27–37. https://doi.org/10.1364/AO.55.000027.

Song, H., Martínez, J., Bedell, P., Vennin, N. and Lefebvre, S., 2019. Colored fused filament fabrication. *ACM Transactions on Graphics*, 38(5): 141. https://doi.org/10.1145/3183793.

Influence of some material properties on quality of selective laser sintering (SLS) built objects

Li Yang[1], Henrik Pettersson[1], Göran Flodberg[1] and Samuel Löfstrand[2]

[1] Research Institute of Sweden (RISE), Drottning Kristinas väg 61, 11428 Stockholm, Sweden
[2] Addema, Hedenstorpsvägen 9, 555 93 Jönköping, Sweden
E-mails: (li.yang, henrik.pettersson, goran.flodberg)@ri.se; samuel.lofstrand@addema.se

Short abstract

Selective laser sintering (SLS) is considered as one of the most promising additive manufacturing (AM) techniques thanks to its relatively low mechanical anisotropy. In this work, we studied factors that are important for mechanical performance of SLS built objects, using polyamide (PA12) with and without addition of carbon fibres. It was found that in addition to operational parameters of SLS process, a number of materials properties, e.g., light reflectivity (absorption), thermal conductivity, and flowability of the powder materials are important for the tensile strength of the SLS built object. It was also found that different from the mixture of PA12 with carbon fibres (PA12+CF) that has strong light absorption, the PA12 alone has instead strong light reflection which led to insufficient sintering and big pores inside the SLS built object and hence poor mechanical strength.

Keywords: additive manufacturing, 3D printing, porosity of SLS built object

1. Introduction and background

Additive Manufacturing (AM) is a process of joining materials layer-by-layer to make an object using 3D model data. Due to its similarity to digital printing, AM is also called 3D printing. Thanks to its ability to virtually produce parts of any geometrical complexity without tooling, AM technologies enable users to accelerate product development, offer customized products and to increase production flexibility, (Columbus, 2017). There are several kinds of AM technologies, e.g., Selective Laser Sintering (SLS) (Deckard, 1989), multi jet fusion (MJF), Stereo Lithograph Apparatus (SLA), Fused Deposition Modelling (FDM) and Selective Laser Melting (SLM), etc. These AM technologies operate in different ways and use different materials; hence they have been used for different applications.

SLS and MJF are collectively called polymer bed fusion techniques as they build objects by light fusion of polymer powders. In both cases, a thin layer of polymer powder e.g., polyamide 12 (PA12) is first spread over the build platform or the polymer bed. The temperature of a material layer is raised close to its melting point. The extra energy necessary to sinter the selected parts of the powder together is added by a CO_2 laser beam that scans each cross-section in the case of SLS. The platform then moves downwards one layer and the process repeats until the job is complete. In case of MJF, a carriage with inkjet nozzles (which are similar to the nozzles used in desktop 2D printers) passes over the bed, depositing fusing agent (black) on the powder. Then a high-power IR energy source passes over the build bed and sinters the areas where the fusing agent was dispensed. In other words, in MJF the selective sintering is enabled by increased light absorption at positions defined by the black fusing agent. The process repeats until all parts are complete.

Despite significant advances in AM techniques, there are concerns and limitations that prevent AM from widely acceptance in industrial applications. One of the limitations is that AM produced objects have not only low-level mechanical properties but also much wider range of variation compared to the conventional process like injection moulding (Flodberg, Pettersson and Yang, 2018). Injection Moulding (IM) is the

widely used technique for mass production since it can be easily automated. When thermoplastics are used, they are completely melted and injected into a mould. When it has cooled down, it solidifies into a final shape with a consistent material structure. On the contrary, the structure and mechanical properties of an AM produced object are anisotropic, because it is built up layer-by-layer. Interfaces among the layers are usually the weakest link of the object. Hence, its mechanical properties are direction dependent. Another aspect of AM technique is its surface finish compared to injection moulding, e.g., surface smoothness.

The SLS process has been identified as one of the most promising techniques for producing engineering components (Chalancon and Bourell, 2016). The mechanical anisotropy of an SLS printed sample is relatively low, i.e. ~10 %, when pure polymer is used, (Dizon, et al., 2018). In this report, the major material properties that influence quality of 3D printed objects using SLS technology are described, and possible solutions discussed.

2. Materials and methods

2.1 Materials and test samples

Duraform ProX Nylon PA12 was provided by 3D Systems. The standard test samples (dog bones) were produced by Addema using SLS in a HIQ machine from 3D Systems Inc., Valencia, CA, USA. Nitrogen was used as an inert protective atmosphere during production to avoid any oxidation of the PA12 and, thereby, any brittleness. The average particle size of PA12 is 50 mm. The SLS process parameters were set as following: a laser power of 45 W, a scan spacing of 25 mm, a scan speed of 10 m/s and a thickness of 0.10 mm in each material layer. The pre-heating of the powder bed was set at 175 °C. Similarly, the standard test samples made of the blend of PA12 with 48 % mass fraction of carbon fibres (PA12+CF) were also made by Addema using the SLS machine. All the dog bones were made with a mixture of 50 % fresh and 50 % used materials. As reference, dog bones were also produced by injection moulding following ISO 3167 (International Organization for Standardization, 2014) on a BOY 25 EVH injection moulding machine from Dr. BOY GmbH & Co. KG, Neustadt-Fernthal, Germany.

2.2 Measurement of mechanical properties

The tensile tests were performed using a hydraulic actuator with an MTS FlexTest™ 60 digital controller (MTS Systems Corporation, Eden Prairie, MN). The samples were clamped with a vise in a hydraulic actuator with an MTS FlexTest™ 60 digital controller. A contact extensometer was strapped to the samples with rubber bands and the load was measured with a 10 kN load cell. The tests were performed at a rate of 50 mm/min. The data was recorded using MTS Series 793 Control Software.
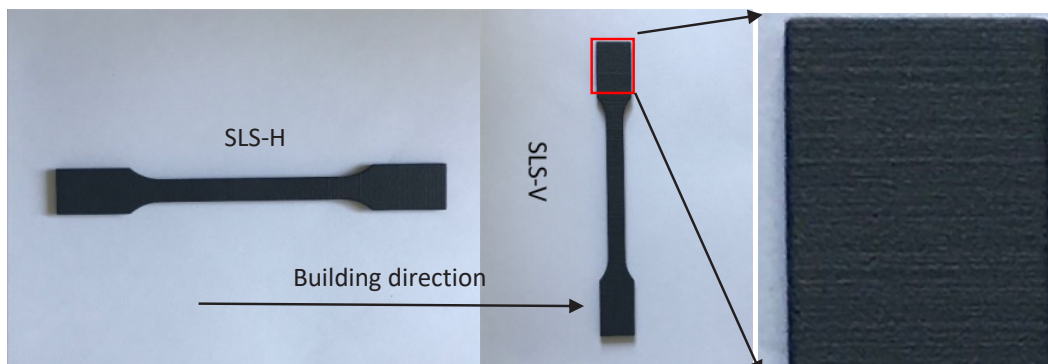

Figure 1: Illustration of the building (SLS sintering) directions in relation to the direction of material application, SLS-H (left),SLS-V (middle), and the amplificated image (right) in which building lines are clearly visible

The measured values, tensile strength, Youngs modulus value, and elongation at break, are listed in Table 1 (Flodberg, Pettersson and Yang, 2018). In the table, the dog bone sample made of conventional technique, injection moulding (IM) is set as reference whose values are set as 100 %. The rest samples are SLS printed with SLS-H and SLS-V standing for building directions of the dog bones in line (vertical) or perpendicular (horizontal) to the direction of material application as illustrated in Figure 1. In addition to the average and the standard deviation of each measured value, their correspondences to the reference are also listed in the parathesis.

Table 1: Mechanical properties of the standard test samples (dog bones)

Material (Processing)	Tensile strength σ_m (MPa)	Youngs modulus E_t (MPa)	Elongation at break ε_b (%)
PA12 (IM) as Ref.	38.90 ± 0.41 (100 %)	$1\,502 \pm 64$ (100 %)	>17
PA12 (SLS-H)	29.05 ± 5.45 (75 %)	$1\,474 \pm 193$ (98 %)	5.8 ± 1.3
PA12 (SLS-V)	30.65 ± 5.31 (79 %)	$1\,726 \pm 110$ (115 %)	2.7 ± 0.5
PA12 + CF (SLS-H)	64.09 ± 0.63 (165 %)	$5\,866 \pm 75$ (391 %)	3.2 ± 0.1
PA12 + CF (SLS-V)	45.99 ± 1.13 (118 %)	$3\,619 \pm 47$ (241 %)	2.3 ± 0.2

3. Results and discussion

3.1 Relationship between porosity in 3D printed structures and variations in mechanical properties

As seen from Table 1, the mean values of the tensile strengths of the 3D printed test samples are about 75–80 % of the reference value. The SLS prints with PA12 powder exhibit little or marginal difference with respect to direction of material application. While the mechanical strengths of SLS prints of PA12+CF are significantly improved by reinforcement of carbon fibres, these test specimen exhibit much stronger directional dependence because carbon fibres have limited reinforcement effect beyond material layers.

One striking observation from Table 1 is the standard deviation (SD) of the tensile strength values. SD is very small for the reference made of IM but becomes very big for the SLS prints with PA12 only. This is an obvious problem for the SLS prints as their mean values are already lower than the reference. However, their corresponding values with carbon fibres are much smaller. This suggests that the origins of strong SD lie in the SLS built structures rather than in SLS technique in general. As seen from Figure 2 (left) that there are plenty of big pores in the structure of the dog bones with PA12 only which is in sharp contrast to the one made of PA12+CF shown in Figure 2 (right). Possible underlying origins of such difference are given in the next subsection.
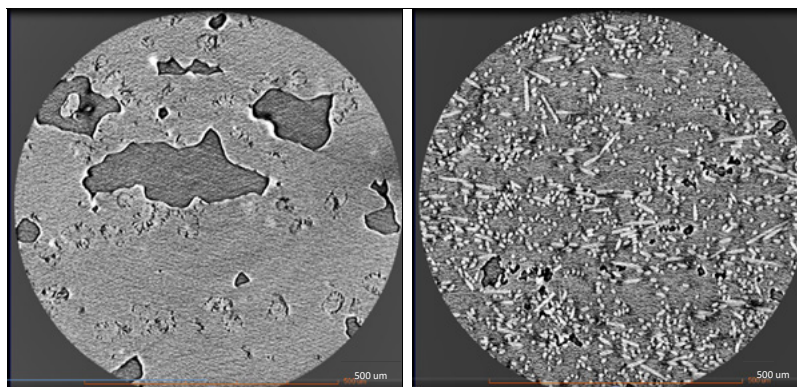
Figure 2: The x-ray tomography images of inner structures of SLS prints; left: with PA12; right: PA12+CF

3.2 Materials properties and operational parameters

The mechanical strength of the SLS built objects depends on sintering of material particles of PA12 with and without addition of carbon fibres. The laser energy density projected onto the powder bed *ED* (J/mm^3) can be estimated by Equation 1 (Chalancon and Bourell, 2016; Nelson, 1993).

$$ED = \frac{P}{s \cdot v \cdot t} \qquad\qquad [1]$$

where *P* (W) is the laser power, *s* (mm) the scan spacing, *v* (mm/s) the scan speed, and *t* (mm) the layer thickness. For a given source of energy (laser), the energy density can be adjusted by adjusting the scanning spacing, scanning speed, and layer thickness. In addition to the energy density provided by the laser, the actual energy received by the layer of powder depends also on the material properties, e.g., light absorption and heat conductivity of the powder. Consider the materials used in this study, PA12 and PA12+CF differ significantly in both light absorption and thermal conductivity. The PA12 is white and has strong light reflectivity to all wavelengths of light. Consequently, only a small portion of energy from the laser beam is absorbed. On the contrary, PA12+CF is black and absorbs most of the energy from the laser beam. Hence, even though the same operational settings were applied to both materials, the differences in light absorption of PA12 compared to PA12+CF caused different sintering effect for the PA12 (white) PA12+CF (black). Due to strong light absorption and much better heat conductivity of carbon fibres, PA12 particles in the material blend PA12+CF received more light energy and were better sintered compared to those of PA12 alone. As a result, voids in the powder layer of PA12+CF collapsed after sintering, while the PA12 particles alone were less well sintered leading to less compact structure as voids remains after sintering. The lack of fusion might have resulted in large pores with diameters of 100 μm close to the surface (Kasperovich, et al., 2016), which were likely to initiate fatigue cracks and, therefore, cause deterioration of the mechanical properties (Damon, et al., 2018).

3.3 Flowability and packability

Good flowability of the material powder is essential for obtaining uniform powder layers, (Spierings, et al., 2016). Powder layers are basic elements of the object built with SLS process. Uniform powder layer is important even for sintering process. As seen from Equation 1, the energy depends on the layer thickness. A non-uniform powder layer will result in non-uniform laser sintering, e.g., over-sintering in positions where powder layer is thinner than intended while under-sintered in positions where powder is thicker than intended. We have demonstrated that by mixing with wood powder, improved flowability of polymer powder can be achieved, leading to uniform material layer thickness and good SLS printability.

4. Conclusions

Mechanical performance of SLS built objects, using polyamide (PA12) with and without addition of carbon fibres, have been studied. It was found that in addition to operational parameters of SLS process, a number of materials properties, e.g., light reflectivity (absorption), thermal conductivity, and flowability of the powder materials are important for the tensile strength of the SLS built object. It was also found that different from the mixture of PA12 with carbon fibres (PA12+CF) that has strong light absorption, the PA12 alone has instead strong light reflection which led to insufficient sintering and big pores inside the SLS built object and hence poor mechanical strength.

Acknowledgements

References

Chalancon, A. and D. Bourell, D., 2016. Measured energy densities for polyamide 12 and comparison of values calculated for laser sintering. In: D.L. Bourell, R.H. Crawford, C.C. Seepersad, J.J. Beaman, S. Fish and H. Marcus, eds. *Proceedings of the 27th Annual International Solid Freeform Fabrication Symposium – An additive Manufacturing Conference*. Austin, Texas, USA, 8–10 August 2016.

Columbus, L. The state of 3D printing, Forbes, 2017. *Forbes,* [online] Available at: <https://www.forbes.com/sites/louiscolumbus/2017/05/23/the-state-of-3d-printing-2017/#173fdf9157eb> [Accessed February 2021]. Available from: https://www.forbes.com/sites/louiscolumbus/2017/05/23/the-state-of-3d-printing-2017/#173fdf9157eb.

Damon, J., Dietrich, S., Vollert, F., Gibmeier, J. and Schulze, V., 2018. Process dependent porosity and the influence of shot peening on porosity morphology regarding selective laser melted AlSi10Mg parts. *Additive Manufacturing*, 20, pp. 77–89. https://doi.org/10.1016/j.addma.2018.01.001.

Deckard, C.R., Board of Regents, The University of Texas System, 1989. *Method and apparatus for producing parts by selective sintering*. U.S. Pat. 4,863,538.

Dizon, J.R.C., Espera Jr., A.H., Chen, Q. and Advincula, R.C., 2018. Mechanical characterization of 3D-printed polymers. *Additive Manufacturing*, 20, pp. 44–67. https://doi.org/10.1016/j.addma.2017.12.002.

Flodberg, G., Pettersson, H. and Yang, L., 2018. Pore analysis and mechanical performance of selective laser sintered objects. *Additive Manufacturing*, 24, pp. 307–315. https://doi.org/10.1016/j.addma.2018.10.001.

International Organization for Standardization, 2014. *ISO 3167:2014 Plastics – Multipurpose test specimens*. Geneva; Switzerland: ISO.

Kasperovich, G., Haubrich, J., Gussone, J. and Requena, G., 2016. Correlation between porosity and processing parameters in TiAl6V4 produced by selective laser melting. *Materials & Design*, 105, pp. 160–170. https://doi.org/10.1016/j.matdes.2016.05.070.

Nelson, J.C., 1993. *Selective laser sintering: a definition for the process and an empirical sintering model*. Ph.D. thesis. University of Texas at Austin.

Spierings, A.B., Voegtlin, M., Bauer, T. and Wegener, K., 2016. Powder flowability characterisation methodology for powder-bed-based metal additive manufacturing. *Progress in Additive Manufacturing*, 1, pp. 9–20. https://doi.org/10.1007/s40964-015-0001-4.

J. Feldmann, D. Spiehl and E. Dörsam: Paper embossing tools: a fast fabrication workflow using image processing ...

5A

Paper embossing tools: a fast fabrication workflow using image processing and stereolithography additive manufacturing

Jakob Feldmann, Dieter Spiehl and Edgar Dörsam

Technical University of Darmstadt, Department of Mechanical Engineering, Institute of Printing Science and Technology, Magdalenenstr. 2, 64289 Darmstadt, Germany
E-mails: feldmann@idd.tu-darmstadt.de; spiehl@idd.tu-darmstadt.de; doersam@idd.tu-darmstadt.de

Short abstract

In conventional fabrication, embossing tools for paper and cardboard are made from metals in an engraving or milling process. The conventional processes are time and cost consuming as there are often multiple iteration loops necessary to create the final design of the embossing tools. A cheaper and especially faster way to produce these tools is needed to make embossments profitable for individual or small small-scale manufacturing. To demonstrate an alternative approach, a workflow was developed to generate embossing tools using stereolithography additive manufacturing. The benefits of the chosen 3D printing method are discussed and a new data preparation workflow to generate layer data from two-dimensional logo designs, which can be directly processed to create fully functional embossing dies, is presented. Additively manufactured embossing tools were tested and their properties are discussed. Embossing tools produced using the proposed workflow were successfully used for embossing of paper in a quantity of up to 500 pieces without failure of the tool or visible wear.

Keywords: 3D printing, additive manufacturing, stereolithography, rapid tooling, embossing tools, heightmap image processing

1. Introduction and background

In recent years an increasing trend of substitution of packages made from plastics and other non-biodegradable materials by such made from paper and cardboard can be seen. With increasing environmental awareness of companies and customers we can expect even further development in paper based packaging (Schüler, 2020) and a higher demand for paper and cardboard packaging for the end user market. Package design is an important part of the presentation of a product, being often the first perception a potential customer will receive. High significance is therefore given to the refinement and finishing of boxes and packages made from paper. Next to general shape and print, a common method of refinement of the appearance of a product is achieved through adding visual and haptic details by embossing the packaging (Emblem and Emblem, 2012). Embossing enables the local raise of areas of the substrate or label of the container in specific shapes to highlight, for example, writing or brand logos and allows reflective contrasts in combination with print (Foil Division, Aluminium Association, 2009) and therefore enhancement of visual impact and luxurious touch when handling the product (Kirwan, 2013). Further, embossed features can be utilized for marking and warning labels as well as for braille writing (Wilken, 2013). Embossed surfaces pose as an additional means of challenge in the manufacturing process and are thus also used as a method of protection against counterfeiting of packages (Werblow, 2009).

Paper and cardboard embossments are realized using embossing tools consisting of a female and male die, which represent inversions of one another, as shown in Figure 1. Placed between the dies the often temperature and moisture conditioned substrate is formed into the desired shape by application of pressure, with the male die driving material into the shape of the female die resulting in the raise of the substrate

(Wilken, 2013). In conventional production these tools are manufactured from metal (most commonly brass or steel) in high precision milling or engraving processes (Anon, 2019). Targeting a preferably broad and clear embossment while also not exceeding the maximum formability of the used substrate the final shapes of the embossing tools are often created in an iterative process, where tools are altered until they meet the desired requirements. Often, the production site of the tools is not in-house with the embossing process, so shipment with each iteration step adds to the overall duration of the creation of new tools. In combination with the already time-consuming milling manufacturing, the current workflow of design and production of new paper and cardboard embossing tools poses a bottleneck in the chain of processes when commissioning the fabrication of a new packaging or stationery layout. Significantly longer lead times and higher preparation costs make embossing under normal circumstances unprofitable for small quantities and short short-term production.
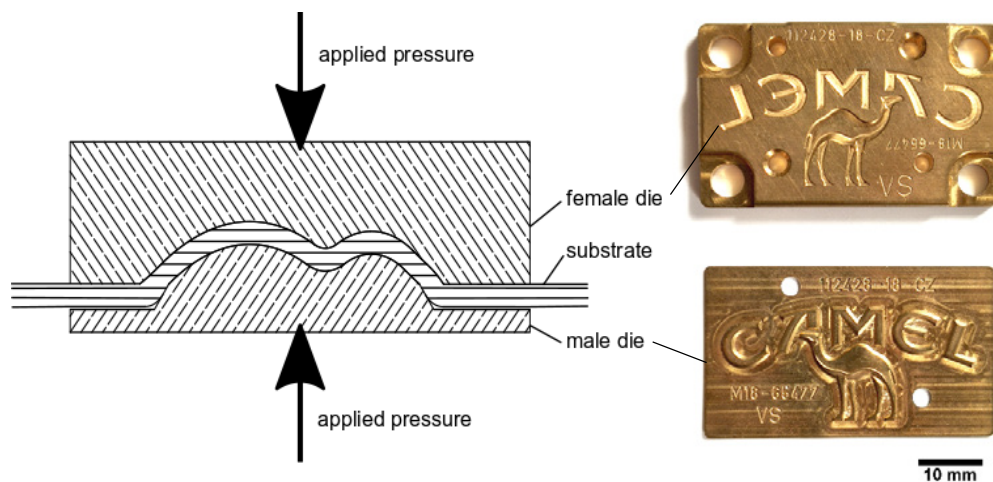

Figure 1: Schematic cross cross-sectional view of the embossing process and photographs of examples for conventionally manufactured embossing dies from brass used to emboss a brand logo; identification marks (numbers) which are not embossed can be seen too

The introduction of additive manufacturing (AM) to design and production processes has led to a rethinking in the fabrication of tools. Under the term rapid tooling (RT) use of AM for fast and often individual fabrication of tools representing a pattern, mold or an impression of a final part is summarized (Gibson, Rosen and Stucker, 2015). The long lead times and high cost of conventional fabrication of tools for paper and cardboard embossing make RT for these tools very attractive, as it bears potential to substantially reduce manufacturing duration and therefore shorten the entire process chain. Replacing the traditional manufacturing of paper embossing tools with AM technology also allows the iteration process to be shortened and redesigned and facilitates further automation of the steps from initial design to final embossed result.

We have chosen stereolithography (SL) as AM technology for the fabrication of embossing tools. SL offers the lowest machine, material and running costs as well as the lowest environmental impact for the geometrical accuracy range delivered (Li, et al., 2017). Former studies utilized *Fused Filament Fabrication* with an even lower cost for the manufacturing of paper embossing tools, where general functionality could be demonstrated but resolution was found to be insufficient for embossments with higher details and higher demands for surface finish (Delić, et al., 2017; Žarko, et al., 2017). SL, or often called *vat polymerization*, utilizes a near ultra violet (UV) light source to initiate local polymerization of a photopolymer resin. By local exposure and thus polymerization and solidification of the cross section of a part in a layer wise repeating process, a three-dimensional object can be obtained. Often, the only moving part of the process is the axis moving the build platform with the part layer wise up or down placing it among the additive manufacturing processes with the highest part resolution and precision (Kim and Oh, 2008) and the lowest surface roughness (Li, et al., 2017).

Masked stereolithography (MSLA) represents a variant of SL technology where the selective exposure of the resin vat is implemented using a UV back lit LCD. Print data is thus only represented by a raster image of the respective layer part cross-section and the light exposure time, which allows for a simple data preparation based on image processing. Figure 2 shows a schematic view of the components and the working principle of an MSLA system.
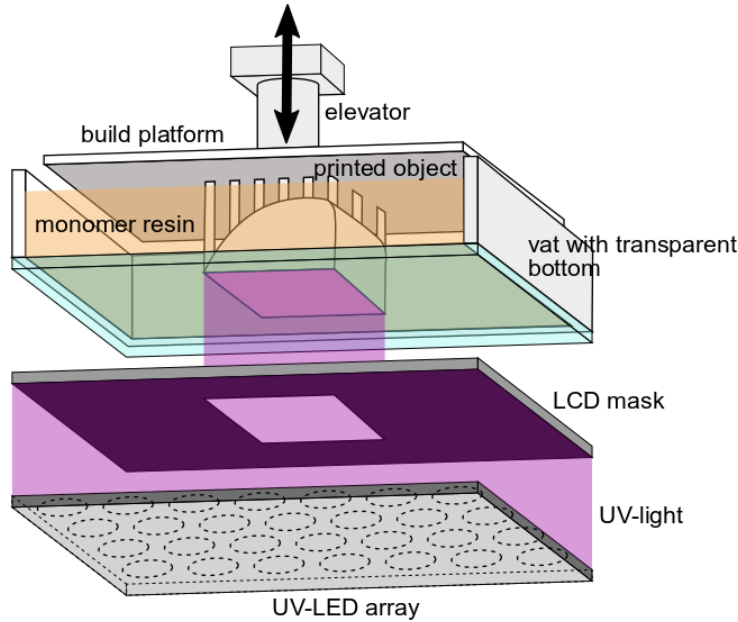
Figure 2: Partially exploded view of the MSLA printing process, showing the printed object is built by layer wise exposure with UV-light; the UV-light source (here UV-LED array) is masked via an LCD mask to match the respective layer cross section, after each subsequent layer the build platform is raised by a predefined layer height to allow for monomer resin to flow underneath the printed object to be processed in the following layer

In standard additive manufacturing pre-processing of a virtual three three-dimensional model of the intended part is needed. These models are either created with help of CAD software or captured using 3D scanning technologies. Next, models are converted into a triangulated surface model (most commonly an *STL* or a *3MF* file) to be used to compute individual layer data using preparatory software for additive manufacturing, the so-called *slicing process* (Gibson, Rosen and Stucker, 2015).

The proposed workflow for the creation of paper embossing tools utilizes an alternative approach for AM data preparation. In the industry it is common practice to depict designs of logos and other possible embossments for paper in form of images rather than 3D data (Anon, 2019). Heights and depths of these reliefs are often represented as different shades of gray in a two-dimensional grayscale heightmap. The proposed data preparation for AM ties in with these conventional methods and builds on these already existing data. Thus, a preparatory digital workflow creating 3D printing layer data from two two-dimensional input heightmaps was developed.

2. Technology and methods

2.1 Additive manufacturing technology

For this work a stereolithography machine with masked UV-LED array technology (*Zortrax Inkspire*, Zortrax, Poland) with a pixel resolution of 1 440 × 2 560 and a display size of 74.67 mm × 132.88 mm resulting in a pixel size of approximately 50 µm was utilized. Although variable, the layer height was set to the recommended minimal thickness by the manufacturer of 25 µm.

For all embossing tools commercially available *tough* SL resin (*Grey Tough Resin*, Prusa Research, Czech Republic) was used. For better adhesion to the build platform the first 8 layers of each tool were printed with higher exposure time of 60 seconds per layer. All other layers were exposed for 8 seconds to UV-light during the build process. After printing all tools were rinsed in isopropyl alcohol for at least 15 minutes to remove uncured resin residue, dried and post-treated in an UV-curing chamber (*Form Cure*, Formlabs, USA) for 30 minutes at 40 °C.

2.2 Data preparation workflow

The data preparation workflow was realized using *Python 3.8* programming language. The objective was to enable the user to create AM layer data that can be directly used for fabrication without the need for any additional preparatory software. For that, the input heightmap image needs to be processed and general tool dimensions, such as tool geometries and features like holes and bore countersinks need to be defined. This data is used to directly derive MSLA layer images and machine code, thus material and process dependent print parameters, such as layer height, exposure time and general printer geometry, are needed as third and last input data set.

Image data processing is done in two subsequent steps. First, the input heightmap, representing the relief geometry of the female embossing die, is converted into a heightmap depicting the male die surface through a modified minimum image filter. The filter is modified to create a uniform offset perpendicular to the relief surface (normal tool offset) which can be computed using the previously defined tool dimensions, containing information about tool offset and total embossing depth. In a second step, based on this male relief image a third heightmap is generated representing further elevation plateau for the male relief. This male elevation is needed to leave a defined gap (tool gap) between the fully closed dies for the substrate not to be deformed in areas other than where the embossment is intended. Height and slope of this male elevation are again defined in the tool geometry data. Figure 3 shows an exemplary female heightmap, its derived images and a schematic view of their respective embodiment as relief surfaces in the final tool.
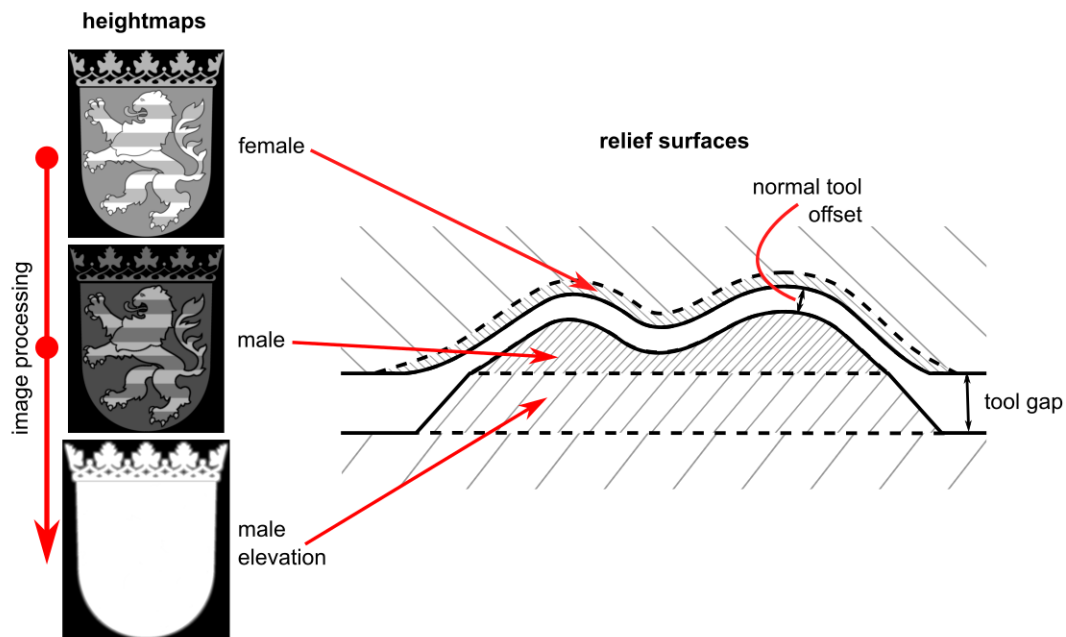
Figure 3: Exemplary image processing chain from female to male and male elevation heightmap (left) and schematic cross sectional view of the embossing tool, where representative female, male and male elevation relief surfaces derived from these heightmaps are highlighted (right); the normal tool offset describes the constant offset between female and male relief surface, while the tool gap depicts the distance between the dies outside of the embossing geometry established by the male elevation

Using a threshold algorithm, individual relief layer image data can be obtained from the heightmap images, slicing the relief into discrete layers according to the chosen embossing depth and layer height.

Next to the relief, layer images containing all other features of the embossing are computed. For this purpose, cross section images of the tool blocks are derived from the predefined tool dimensions, consisting of the measurements of the tool as well as features such as holes, counter sink bores, chamfer radii and identification marks.

To conclude the layer image preparation, the relief and tool block layer images are combined using Boolean operations for each layer.

Depending on the chosen export file format an according machine code (*gcode*) is created from the print parameter data and a print data file, which can be directly processed by the chosen MSLA system is compiled. The whole workflow from the given input data (female heightmap, tool dimensions and print parameters) to the print data file ready to be sent to the SL system is shown in Figure 4 as a program flow chart.
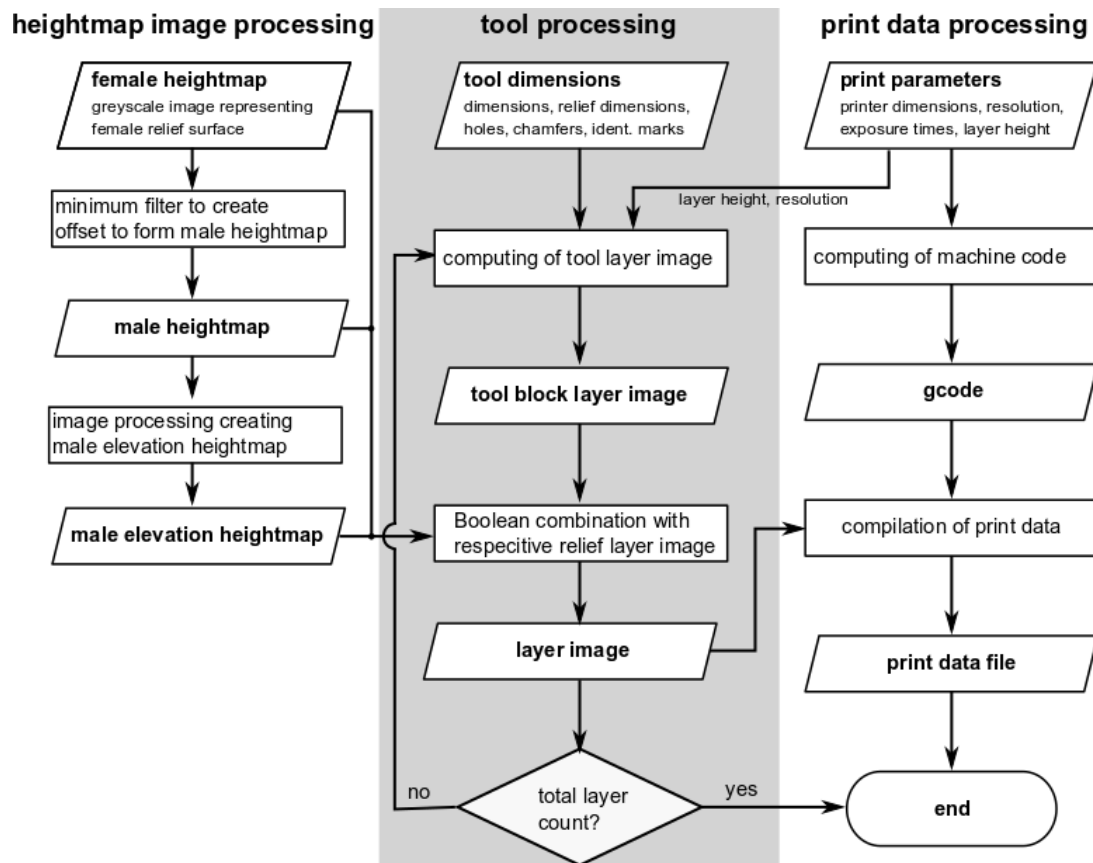
Figure 4: Program flow chart of the data preparation for AM of paper embossing tools; the three main processes (heightmap image, tool and print data processing) are highlighted and marked accordingly

2.3 Embossing and examination

In total 25 embossing tools of different designs for paper and cardboard were produced using the here presented digital preparation and additive manufacturing workflow. All tools were tested with loads between 1 and 30 kN on an embossing press (*Geba 6*, Baier, Germany) using different substrates (GC1 255, GC1 355, GC1 450 and GD2 300). Both embossing dies were centered to one another using centering pins and fixed to the press with double-sided adhesive tape. Embossing results were visually examined and detailed images were taken using a microscope (*Leica DM4000 M*, Leica, Germany).

3. Results and discussion

It has become apparent, that heightmaps are fully usable for the conception process of new embossment reliefs. Neither heightmaps nor embossment geometry can contain any undercuts, so that heightmaps can be used to depict all possible paper embossing reliefs. The presented workflow enables a fast data preparation for 3D printing starting from a single heightmap in less than 10 minutes. The image processing developed was shown to be suitable for the derivation of male and male elevation heightmap from the female heightmap input file.

Additive manufacturing of both dies of a tool can be realized in the same printing process, if both are small enough to fit together on the build platform. Embossing tools are usually flat and wide sheet dies, thus, as AM processing time is proportional to the height of the printed object, flat dies can be produced in a short amount of time. Additionally, by design no support material is needed and dies can be printed flat, directly onto the build platform. Printing time is therefore very short and dies with a thickness of 5 mm, as used in this research, can be produced in under one hour at an estimated material cost of 3 € per die. The absence of support structures also offers the advantage that, apart from a rinse in isopropyl alcohol and curing under UV light, no further post-treatments are necessary. Figure 5 summarizes the time needed for typical production steps for the conventional manufacturing of embossing dies and compares them to the here presented workflow.
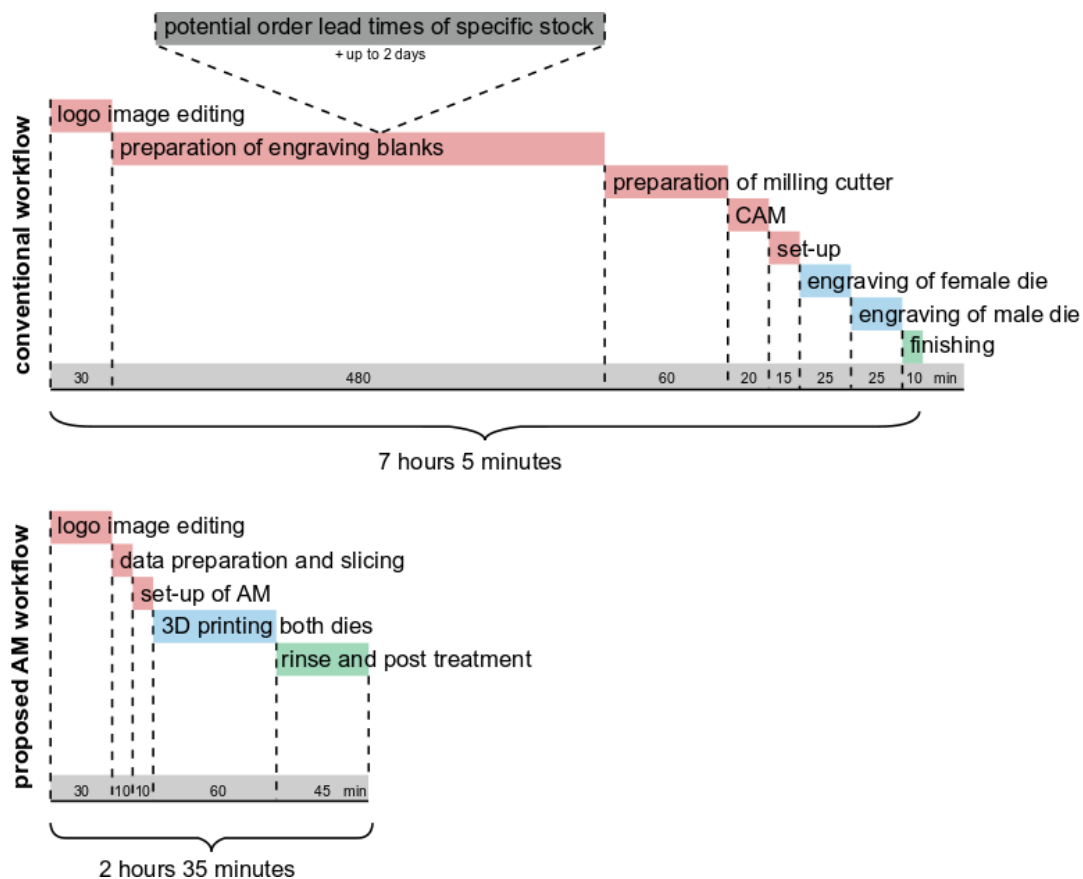
Figure 5: Gantt chart showing production steps and times of an exemplary embossing tool of 50 mm × 30 mm × 5 mm size manufactured using conventional engraving and MSLA; fabrication times for conventional embossing tools in industrial facilities are highly dependent on the available stock of semi-finished metal blocks and the lead times of potential necessary orders, further a high workload in only one of the departments in the process chain of fabrication steps can delay the whole production of the tool, a main time advantage of AM is therefore represented by the fact, that the whole tool can be produced in one process without the need of special confectioned stock material or tooling

Tools produced using AM technology were successfully used for the embossing of paper and cardboard and could handle loads of up to 30 kN without failure. However, small elevations and raised edges can be susceptible to abrasion and wear when handling the tool. Figure 6 shows an embossing result of a tool manufactured in the described workflow as well as both dies of the tool.
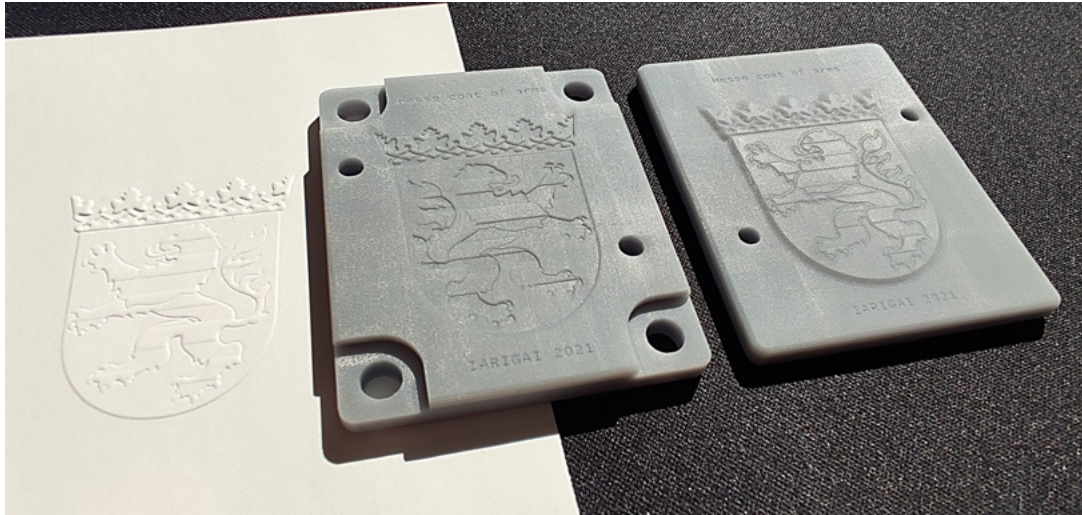
Figure 6: Embossment, female and male dies of finished tool produced using the proposed workflow and AM technology, holes for fixing as well as aligning the dies to each other have been incorporated in the tool, as substrate GC1 255 cardboard was used and 8 kN force was applied onto the two dies; the width of the embossment measures 30 mm and the embossment depth is 0.5 mm

A set of dies produced using the proposed workflow were successfully tested for embossing of cardboard in a quantity of 20 000 pieces. The tool showed no visible wear after the test and could likely be used for further embossing.

Resolution of the embossing dies is depending on the used MSLA system. Details as fine as 50 µm could be created using the here presented setup. Microscopy of the tool shows that individual voxels can be identified in the dies. These get transferred as a fine pattern onto the substrate during the embossing process and are especially noticeable in the area of slopes in the relief. In these areas, the substrate undergoes the greatest deformations, which leads to the greatest material flow and molding to the embossing relief. In addition, the AM process shows a significant stair casing effect exactly at such gradients, which further amplifies this phenomenon. However, neither the voxel resolution nor the pattern on the embossed substrate are visible to the unaided eye. The voxel size of the AM process and its influence on the tool and embossing result is visible in the microscopic images depicted in Figure 7, but it lies below the critical optical resolution of the human eye.

However, if desired there are several possible approaches to increase surface smoothness for embossing tools manufactured using MSLA technology: Using an MSLA machine with a higher pixel resolution would allow for smoother surfaces and smaller details but would increase the overall cost of the set-up. Further, such machines have typically much smaller build volumes, making them often unsuitable for the intended use case.

A second approach without the need for any hardware changes is the use of anti-aliasing of each layer image in the data processing. This method blurs visible steps created by individual pixels, which lets surfaces appear smoother but geometrical accuracy can be reduced due to faded details of the produced part. Additionally, post-processing steps could be added to the workflow allowing for a coating of the dies to increase the surface hardness and lower presence of unwanted voxel patterns.
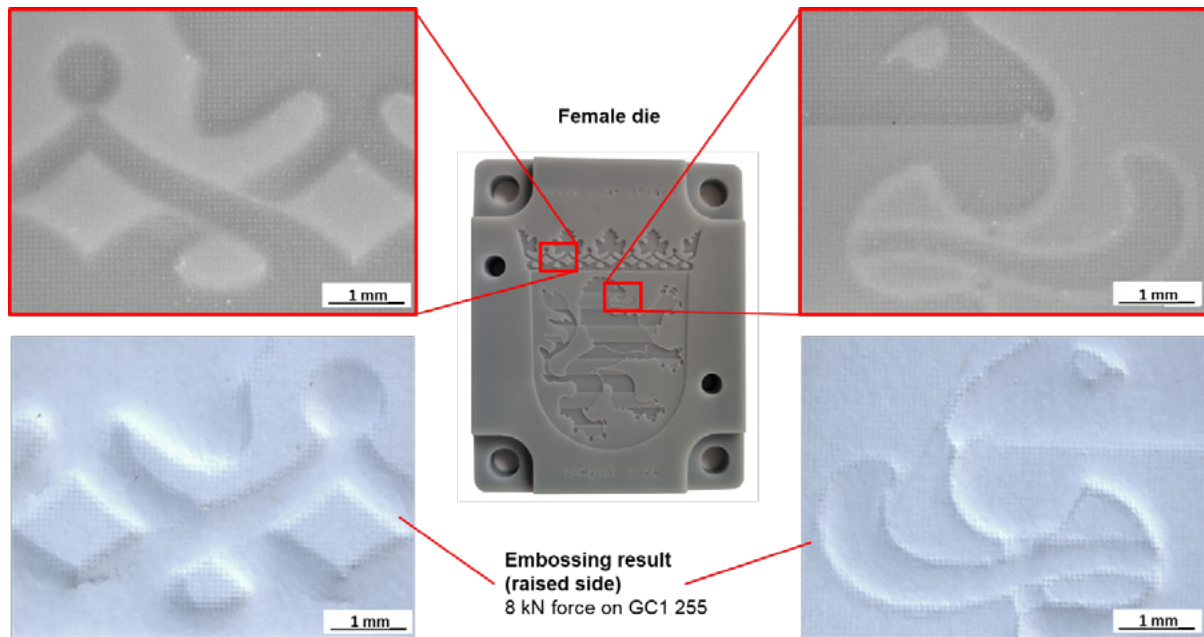
Figure 7: Additive manufactured female embossing die (center) and microscopic detailed views of two features of the tool (top) and their respective result in the embossed cardboard (bottom); in the detailed views of the tool the voxel resolution of the AM process can be seen, these voxel patterns transfer onto the substrate especially at slopes in the embossing relief

4. Conclusions

The here proposed method of fabrication of paper and cardboard embossing tools has been shown as an effective as well as cost and time efficient concept. Conception of new embossing tools can be fully done in a digital workflow, which allows for previews of the tool before the start of the actual manufacturing process and opens the path to future automation. Further, the conception could be integrated in the existing digital preparation of print media. The data workflow shown is based on heightmaps which are already used for design purposes of embossing tools. Here, 3D printing data can be directly derived from these heightmaps without any further preparatory step, shortening set up times for the production of new embossing tools. Male and female dies can be manufactured using stereolithography additive manufacturing in a short amount of time with much lower investment and material costs than conventional engraving. Functionality of the 3D printed embossing tools could be evaluated with 20 000 test embossings in cardboard, after which the dies have shown no visible wear. The used MSLA printing process serves as a system with high resolution, capable of the demanded high accuracy, level of detail and surface finish. However, for even higher resolution MSLA systems with smaller pixel sizes and thinner layer heights can be found on the market. In summary the proposed workflow shows potential for use in the production of low quantity or individual embossments with short lead times. Thus, it can also be used to aid the design process for conventional tooling, as new embossment drafts can be quickly tested on the intended substrate. This allows for an evaluation of the real appearance and feel, before production of cost and time-consuming metal tools is started.

Future research could focus on selection of resin materials for the AM fabrication process. Through a suitable choice of materials, longer service lives and higher load capacities of dies are conceivable – making the presented workflow not only suitable for low quantity manufacturing but also attractive for large scale production.

Acknowledgements

References

Anon, 2019. *ESUpedia: Stanzwerkzeuge für die Karton- und Wellpappenverarbeitung*. Fachverband deutscher Stanzformhersteller e.V.

Delić, G., Vladić, G., Pál, M., Banjanin, B. and Dedijer, S., 2017. Performance evaluation of paper embossing tools produced by fused deposition modelling additive manufacturing technology. *Journal of Graphic Engineering and Design*, vol. 8(, no. 2), pp. 47–54. http://doi.org/10.24867/JGED-2017-2-047.

Emblem, A. and Emblem, H. eds., 2012. *Packaging technology: fundamentals, materials and processes*, Oxford, Philadelphia, PA, USA, Woodhead Publishing. ISBN: 978-0-85709-570-1.

Foil Division, Aluminium Association, 2009. Foil, Aluminium. In: K.L. Yam, (ed.) *The Wiley encyclopedia of packaging technology*. 3rd ed. Hoboken, NJ, USA; John Wiley & Sons, pp. 527–532.

Gibson, I., Rosen, D. and Stucker, B., 2015. *Additive manufacturing technologies: 3D printing, rapid prototyping and direct digital manufacturing.* 2nd ed. New York, NY, USA: Springer.

Kim, G.D. and Oh, Y.T., 2008. A benchmark study on rapid prototyping processes and machines: quantitative comparisons of mechanical properties, accuracy, roughness, speed, and material cost. In: *Proceedings of the Institution of Mechanical Engineers, Part B: Journal of Engineering Manufacture*, 222(2), pp. 201–215. http://doi.org/DOI: 10.1243/09544054JEM724.

Kirwan, M.J. ed., 2013. *Handbook of paper and paperboard packaging technology.*, 2nd ed. Chichester, West Sussex, UK: Wiley-Blackwell.

Li, Y., Linke, B.S., Voet, H., Falk, B., Schmitt, R. and Lam, M., 2017. Cost, sustainability and surface roughness quality – a comprehensive analysis of products made with personal 3D printers. *CIRP Journal of Manufacturing Science and Technology*, 16, pp. 1–11. http://doi.org/10.1016/j.cirpj.2016.10.001.

Schüler, K., 2020. *Aufkommen und Verwertung von Verpackungsabfällen in Deutschland im Jahr 2018: Abschlussbericht.* Mainz, Germany: GVM Gesellschaft für Verpackungsmarkforschung mbH, im Auftrag des Umwelt Bundesamt.

Werblow, S., 2009. Anti-counterfeiting packaging. In K.L. Yam, ed. *The Wiley encyclopedia of packaging technology*. 3rd ed. Hoboken, NJ, USA; John Wiley & Sons, pp. 46–48.

Wilken, R., 2013. Verfahren der Papierbearbeitung. In: J. Blechschmidt, ed. *Papierverarbeitungstechnik*. München, Germany: Carl-Hanser Verlag, pp. 130–241.

Žarko, J., Vladić, G., Pál, M. and Dedijer, S., 2017. Influence of printing speed on production of embossing tools using FDM 3Dd printing technology. *Journal of Graphic Engineering and Design*, 8(1), pp. 19–27. http://doi.org/10.24867/JGED-2017-1-019.

C.F. Weber, D. Spiehl and E. Dörsam: Comparing gloss meters for gloss measurements on metallic embellishments from the printing industry

5B

Comparing gloss meters for gloss measurements on metallic embellishments from the printing industry

Carl Fridolin Weber, Dieter Spiehl and Edgar Dörsam

Technical University of Darmstadt, Department of Mechanical Engineering, Institute of Printing Science and Technology, Magdalenenstr. 2, 64289 Darmstadt, Germany

E-mails: weber@idd.tu-darmstadt.de; spiehl@idd.tu-darmstadt.de; doersam@idd.tu-darmstadt.de

Short abstract

In the printing industry the gloss of metallic embellishments is usually assessed using traditional gloss meters that measure the specular gloss under an angle of 20°, 60° and 85°. However, the specular gloss does not give enough information about the appearance to judge e.g., the image forming capability of a glossy surface. Hence, a more sophisticated gloss meter is used in this study and compared with a conventional gloss meter. For samples with metallic embellishment, it is shown that using a more sophisticated gloss meter that measures more aspects of gloss, judgement about the image forming capability of a surface is easier. It is also investigated how specular gloss measurements of the two gloss meters differ and how the relative standard variation of specular gloss measurements correlates with the glossiness of a surface being examined.

Keywords: gloss measurement, gloss meters, metallic embellishments

1. Introduction and motivation

In the packaging industry, the appearance of the final product is important because it influences the customer at the point of sale (Laine, Leppänen and Nurmi, 2009). According to Hunter and Harold (1987), object appearance is evaluated in terms of i.a. color properties as well as spatial properties that relate to geometric attributes, such as gloss, turbidity, translucency and texture. Geometric attributes are, different to color, associated to the spatial distribution of light by the object.

To the authors knowledge, in the printing industry usually gloss meters are used that only examine the specular gloss of a print product. The schematic of a specular gloss meter and the portion of reflection that is measured as specular gloss measured at a specular angle of 20° can be seen in Figure 1. Most specular gloss meters measure gloss at a specular angle of 60° as a standard method, the measurement at a specular angle of 20° is used for high gloss finishes and the specular angle of 85° is used to evaluate low-gloss surfaces. The aperture size AP1 is the same for measurements at 20°, 60° and 85°. The aperture size AP2 differs for the different angles. In Weber, Spiehl and Dörsam (2021) measurement of specular gloss is described in detail.

When using a gloss meter that only measures specular gloss, certain nuances of the gloss cannot be measured. Additionally, correlation between human visual gloss sensation and specular gloss measurement is reported to be rather poor (Leloup, et al., 2014). This can lead to mistakes in the communication about gloss between producer and customer. A resulting insufficient fulfillment of customer needs regarding gloss can lead to expensive reclamations (Schröder, 2004).

Fortunately, more sophisticated gloss meters have been introduced. These measure the bidirectional reflectance distribution function (*BRDF*) and thus, characterize the directional selective reflectance properties of a surface (Leloup, et al., 2014). Using the *BRDF*, aspects of gloss such as haze and the distinctness of

image (*DOI*) can be evaluated. The haze is related to a milky appearance adjacent to reflected highlights. *DOI* is a measure for the perceived sharpness or waviness of an observed mirror image (Kigle-Boeckler, 1995; Konica Minolta, n.d.).

Scales for specular gloss are based on high polished black glass with a refractive index of 1.567 for the sodium D line for which a specular gloss value of 100 gloss units (GU) is assigned for every angle according to ASTM D523–14 (American Society for Testing and Materials, 2018a). For common print products it would not be expected to obtain gloss values higher than 100 GU for any geometry. Since the reflectance factor of metal is much higher than the reflectance factor of dielectric materials, the measured gloss values can become greater than 100 GU for metallic surfaces (Rich, et al., 2017). In the printing industry, such kind of metallic surfaces are made as embellishments using printing inks containing metallic flake pigments that can be applied by offset-, flexo-, gravure-, screen-, pad-, and ink jet printing (Wißling, 2013; Prolss, Trummer, and Kröll, 2009). Metallic embellishments can also be produced by foil fusing, cold foil stamping, hot foil stamping or bronzing (Morlok and Beckmann, 2009; Rosenberg, 2000).

In this study, a specular gloss meter commonly used in the printing industry is compared to a more sophisticated gloss meter. First, the different readings for metallic embellishments are shown. Then the specular gloss values of the two instruments are compared in terms of inter-instrument conformity and intra-instrument relative standard deviation.
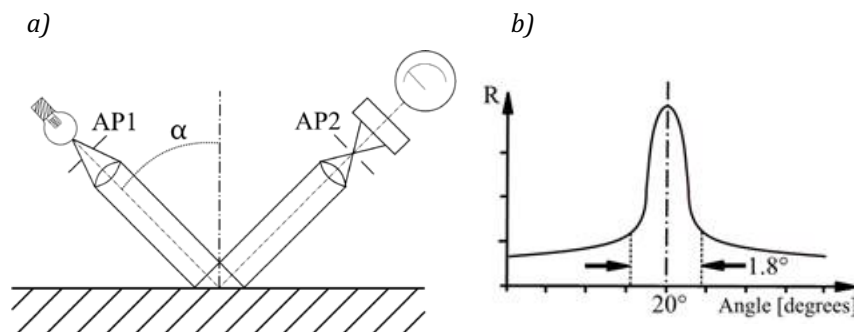

Figure 1: Part (a) shows the principle of a specular gloss meter, where α is the angle of the measurement geometry that is 20°, 60° and 85° for conventional gloss meters, AP1 is the light source aperture and AP2 the receptor aperture of a gloss meter; part (b) shows the portion of reflected light in a range of 1.8° in plane of the measurement direction that is measured as specular gloss for measurements at the specular angle of 20°, R denotes the amount of reflection of light for a specific angle; after Kigle-Boeckler (1995)

An examination of literature was conducted looking for research on gloss measurement of metallic surfaces. Heinzler, Piepenbrink and Doege (2020) compared a traditional and a more sophisticated gloss meter for the examination of specular gloss on chromed surfaces. It was shown that both instruments are suitable for the examination of specular gloss on chromed surfaces, that measurement results are reproducible and that measurement results of both instruments are comparable. Rich, et al. (2017) performed a study about the agreement of visual assessment and the measurement of the reflectivity of printed metallic surfaces. Various types of specular reflectance instruments, including two gloss meters were used. It was i.a. shown that measured gloss does not linearly follow the appearance of highly reflective specular surfaces. Bertholdt and Müller (2014) produced metallic prints in various printing processes with different printing inks on different substrates, characterized them visually and by colorimetry and glossmetry, and investigated them with regard to their corrosion resistance and rub resistance. It was i.a. shown that multi-angle spectrophotometers are not well-suited for the characterization of metallic gloss and that gloss meters are better suited. Rosenberg (2000) investigated methods of metallization by printing and showed that the gloss can be examined using a goniospectrophotometer and by plotting the measured brightness as a function of the measurement angle.

156

2. Materials and method

The traditional gloss meter used in this study is the micro-TRI-gloss model 4446 from BYK-Gardner. It measures specular gloss on the 20°, 60° and 85° angle as described in Silvennoinen, Peiponen and Myller (2008) and Hanson (2006) in detail. The more sophisticated one is the IQ-S from Rhopoint Instruments, distributed by Konica Minolta. It allows for the measurement of the specular gloss at the 20°, 60° and 85° angle. Since at 20° +/- 7.25° instead of a photo diode a 512 element linear diode array (LDA) is placed, a partial one-dimensional BRDF can be measured. This allows for the evaluation of more aspects of gloss than just the specular gloss at 20°. The IQ-S and the micro-TRI-gloss are shown in Figure 2 a. The calibration standards of the instruments are shown in Figure 2b. While the micro-TRI-gloss is calibrated only on a black glass standard, the IQ-S is calibrated on both a black glass standard and a mirror standard. For measurements with the IQ-S it can be chosen whether the reference standard used for the measurements it the black glass standard or the mirror standard. In automatic mode, the device chooses the reference standard according to the reflectivity of the sample. The device-specific gloss readings of the standards are shown in Table 1. In this study, the specular gloss values from the angles of 20°, 60° and 85° are referred to as $gloss_{20}$, $gloss_{60}$ and $gloss_{85}$.
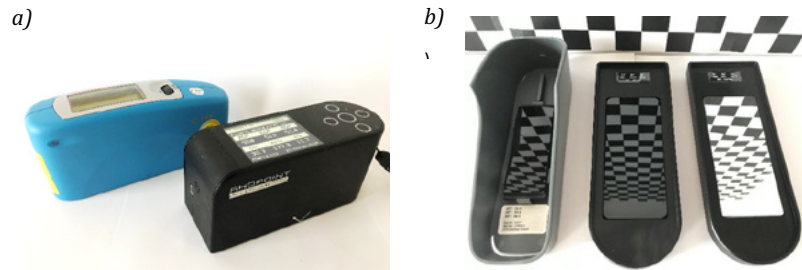

Figure 2: Part (a) shows the instruments micro-TRI-gloss (left) and IQ-S (right); part (b) shows the calibration standards of the instruments; they were photographed in front of a reflective pattern to show their reflective surface, the left one is used for calibrating the micro-TRI-gloss, the two on the right for calibrating the IQ-S

Table 1: Device-specific gloss readings of the micro-TRI-gloss and IQ-S on the device specific calibration standards with device specific calibration values

Instrument	micro-TRI-gloss	IQ-S	
Calibration standard	Black glass standard	Black glass standard	Mirror standard
$gloss_{20}$[GU]	92.9	104	1938
$gloss_{60}$[GU]	95.4	101.6	930
$gloss_{85}$[GU]	99.3	99.8	147.7

From the data of the LDA the specular gloss value at 20°, haze, *DOI*, reflected image quality (*RIQ*), *RSPEC*, log haze and compensated haze can be obtained. The specular gloss at 20° is calculated as follows:

$$gloss_{20}[\text{GU}] = 100 \cdot \frac{\sum R_{19.1°-20.9°} \, (\text{sample})}{\sum R_{19.1°-20.9°} \, (\text{standard})} \qquad [1]$$

where *R* is the intensity reading of a pixel of the LDA. *Sample* is the object that is measured and *standard* refers to the calibration standard. The dash *(-)* between two angles denotes that all readings between the angles are summed up. The haze is calculated as shown in Equation [2] and complies to ASTM E430-19 (American Society for Testing and Materials, 2019). Often it is also called linear haze. It is measured as haze unit [HU] as follows:

$$haze_{E430}[\text{HU}] = 100 \cdot \frac{\sum R_{17.2°-19.0°} \, (sample) + \sum R_{21.0°-22.8°} \, (sample)}{gloss_{20}(standard)[GU]} \qquad [2]$$

According to ASTM D4039-09 (American Society for Testing and Materials, 2015), the difference between the gloss measurements at 20° and 60° can be used to calculate the haze for high-gloss nonmetallic specimens:

$$haze_{D4039}[\text{HU}] = gloss_{60}(\text{sample})[\text{GU}] - gloss_{20}(\text{sample})[\text{GU}] \qquad [3]$$

In this haze measurement mode advantage is taken over the difference in the sizes of detector aperture to measure specular and off-specular reflection by subtracting the measurement value measured on smaller detector at the specular angle of 20° from the greater detector at the specular angle of 60° (Westlund and Meyer, 2001; Fensterseifer, 2021). However, when using this mode of haze measurement, the haze is zero if the 20° gloss is higher than the 60° gloss, which applies to many high gloss metallic surfaces. In literature there could be found no explanation why this test method cannot be used for printed metallic gloss samples that do not result in a haze value of zero.

The *DOI* is measured according to ASTM D5767-18 (American Society for Testing and Materials, 2018b). The *DOI* ranges from 0 to 100 while 0 means that the sharpness of an image of objects produced by the reflection is poor while a value of 100 means that the reflection is very sharp. The *DOI* is calculated using the following formula:

$$DOI[\%] = 100 \cdot (1 - \frac{\sum R_{19,65°-19,80°}(\text{sample}) + \sum R_{20,20°-20,35°}(\text{sample})}{\sum R_{19.95°-20.05°}(\text{sample})}) \qquad [4]$$

The RIQ can only be measured using the devices of the IQ-series from Rhopoint. It is described as an updated version of the *DOI* that is more sensitive to appearance differences due to substrate alignment, coating formulation, substrate and application technique. It also ranges from 0 to 100. The k is a coefficient unknown to the customer of the device.

$$RIQ[\%] = \text{k} \cdot \sum R_{(14.0°-26.0°)}(\text{sample}) \qquad [5]$$

Other values not discussed yet that can be obtained using the IQ-S are the *RSPEC*, log haze and compensated haze. The *RSPEC* is the value of the pixel of the LDA that measures the highest intensity of reflection, which is also the highest value of the measured *BRDF*.

The log haze is preferred for dielectric materials to the linear haze because for those materials it corresponds better to human perception. In the industry, for high gloss metallic surfaces the linear haze is preferred (Fensterseifer, 2021).

For the compensated haze, the luminosity of the diffuse reflection of a surface is subtracted from the haze. This allows for comparing the haze of surfaces independent of their color (Konica Minolta, n.d.). However, the compensated haze is usually not used to examine the appearance of metallic surfaces (Fensterseifer, 2021).

All samples used in this study are rectangular. Gloss measurements of each sample were taken ten times. Five times in printing direction and five times cross to printing direction. In each direction, four measurements were taken near the edges of the sample and one in the center. From the ten measurements of each sample the arithmetic mean and the relative standard deviation was calculated. The measurement values were processed and analyzed using MathWorks MatLab R2019a. For the IQ-S the calibration standard that was chosen as a reference standard for the measurements was the mirror standard.

Before the measurement procedure, calibration of the devices took place once. At one single day all measurements with the micro-TRI-gloss were taken. Another single day, the measurements with the IQS were taken.

Samples were provided by the Heidelberger Druckmaschinen AG and H.C. Moog. Heidelberger Druckmaschinen AG provided samples produced by foil fusing, foil stamping, flexo and offset printing. H.C. Moog provided samples produced by gravure printing.

The authors do not know the exact equipment used by the providers for printing the samples.

3. Analysis and discussion

In Figure 3, eight samples with metallic embellishment can be seen. Sample 1 is made by foil fusing, samples 2 and 3 by cold foil stamping, sample 4 by gravure printing, samples 5 to 7 by flexo printing and sample 8 by offset printing. It can be seen that samples 1, 2 and 3 appear brighter than the other samples. Sample 4 reflects the chessboard pattern in the background the clearest and seems to have the best image forming capability. The glossiness of sample 8 seems to be the lowest. Table 2 shows the measured specular gloss values of the eight samples using the micro-TRI-gloss. These reflect that samples 1, 2 and 3 are the glossiest and that sample 8 has the lowest gloss but they e.g. do not reflect the outstanding image forming capability of sample 4. To take this into account, more aspects of the gloss have to be measured, which is possible using the IQ-S. Gloss values measured using the IQ-S are shown in Table 3. These do not only include specular gloss values but also haze values after ASTM E430, *DOI*, *RIQ* and the *RSPEC*. Here, the high *DOI* and *RIQ* values of sample 4 reflect its high image forming capability which is superior to samples 1, 2 and 3 that have a higher specular gloss.
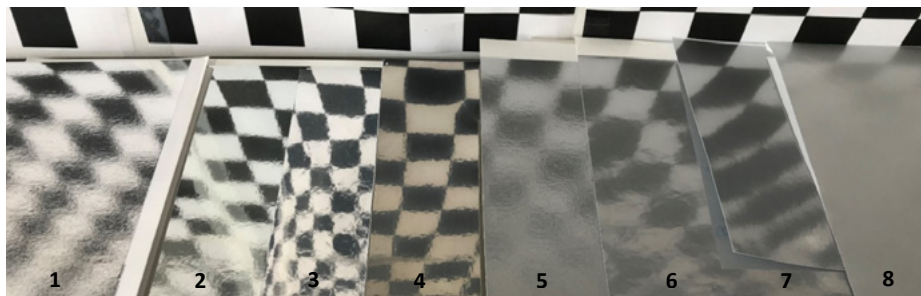

Figure 3: Printed metallic gloss samples made by foil fusing (1), cold foil stamping (2, 3), gravure printing (4), flexo printing (5 to 7) and offset printing (8); the samples were photographed in front of a chessboard pattern

Table 2: Arithmetic mean of the specular gloss values of the samples in figure 3 measured with the micro-TRI-gloss; the sample numbers correspond to the numbers in Figure 3

Method of application	Foil fusing	Cold foil stamping	Cold foil stamping	Gravure printing	Flexo printing	Flexo printing	Flexo printing	Offset printing
Sample number	1	2	3	4	5	6	7	8
$gloss_{20}$ [GU]	570	1063	748	466	85	161	185	12
$gloss_{60}$ [GU]	515	549	698	506	193	239	258	53
$gloss_{85}$ [GU]	93	107	130	130	71	93	92	67

In order to make a more thorough comparison of the two gloss meters, the specular gloss readings of 48 samples with metallic embellishment are compared. Additionally, the relative standard deviation of the measurements from each sample is calculated and compared to the arithmetic mean gloss value of the respective sample. Of the 48 metallic samples 13 are produced by offset printing and 35 are printed by flexo printing. The comparisons of the specular gloss readings are shown in Figure 4. Every data point corresponds to one sample of which the mean gloss value was calculated as described in Chapter 2. Specular gloss readings of the micro-TRI-gloss are on the abscissa and specular gloss readings of the IQ-S on the ordinate.

Table 3: *Arithmetic mean of the gloss values of the samples in figure 3 measured with the IQ-S;*
the sample numbers correspond to the numbers in Figure 3

Method of application	Foil fusing	Cold foil stamping	Cold foil stamping	Gravure printing	Flexo printing	Flexo printing	Flexo printing	Offset printing
Sample number	1	2	3	4	5	6	7	8
$gloss_{20}$ [GU]	687	1081	1028	627	106	203	233	17
$gloss_{60}$ [GU]	563	645	747	535	191	240	261	53
$gloss_{85}$ [GU]	83	94	112	122	57	75	77	57
$haze_{E430}$ [HU]	522	143	320	162	172	167	159	22
DOI [%]	21	31	26	51	18	21	21	1.4
RIQ [%]	3.7	12.0	7.8	29.2	1.4	4.1	4.0	1.3
$RSPEC$ [-]	109	210	179	176	17	33	37	2.6

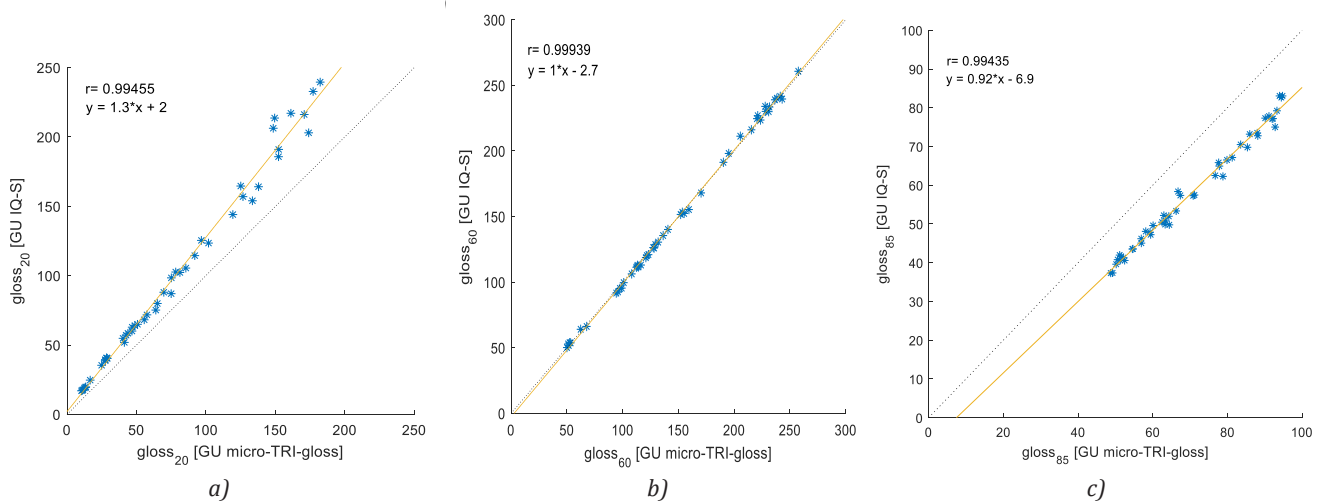a)   b)   c)

Figure 4: *Part (a), (b) and (c) shows the specular gloss values measured at 20°, 60° and 85°, respectively;*
the dotted line shows the 1ˢᵗ median; specular gloss readings of the micro-TRI-gloss are on the abscissa
and specular gloss readings of the IQ-S are on the ordinate

In Figure 4b, it can be seen that the specular gloss values measured with the two instruments at 60° only slightly differ. Because the difference is so small it can be attributed to a small statistical variability. For the IQ-S, the gloss values measured at 20° are higher than those of the micro-TRI-gloss and those measured at 85° are lower. This can be seen in the comparison in Figure 4a and 4c. The differences between the measured specular gloss values are both systematical and statistical. This means that when speaking about gloss units the instrument used for the measurement has to be always specified.

Next, the relative standard deviation of the 10 measurements taken from each of the 48 offset and flexo printed samples is examined. The average of all relative standard deviations and the maximum relative standard deviations of all specular gloss values measured at 20°, 60° and 85° using the micro-TRI-gloss and the IQ-S can be seen in Table 4. The relative standard deviation of the measurements with the IQ-S is larger than that of the micro-TRI-gloss what shows that the micro-TRI-gloss is more precise in the measurement of specular gloss.

Table 4: Relative standard deviations of the measurements of specular gloss at 20°, 60° and 85° using the IQ-S and the micro-TRI-gloss; measurements were taken on 48 offset and flexo printed metallic samples

Measurement angle	20°	60°	85°
micro-TRI-gloss max relative standard deviation	13.5 %	6.8 %	7.2 %
micro-TRI-gloss average of all relative standard deviations	6.2 %	3.3 %	2.6 %
IQ-S max relative standard deviation	20.7 %	8.0 %	7.9 %
IQ-S average of all relative standard deviations	7.4 %	3.8 %	3.7 %

Figure 5 compares the 20° mean specular gloss value of every of the 48 flexo and offset printed samples with the respective relative standard deviation within the ten measurements of every sample. It can be seen that the relative standard deviation correlates positively with the specular gloss value. A reason for this is that the glossier a surface the more intense the reflection in direction of the photo resistor. If the instrument is not perfectly planar adjusted to the surface, a greater part of the reflected light does not reach the photo resistor of the gloss meter (Fensterseifer, 2021). To compensate for the larger statistical error of gloss measurements on high gloss surfaces, it is recommended to take more measurements compared to low gloss surfaces before calculating the arithmetic mean.

Heinzler Piepenbrink and Doege (2020) reported an average relative standard deviation of 0.4 % for gloss measurements at 20° on chromed surfaces using a micro-TRI-gloss. It is likely that the reported relative standard deviations in this study are higher due to the texture and the anisotropy of the prints that influence the gloss values.
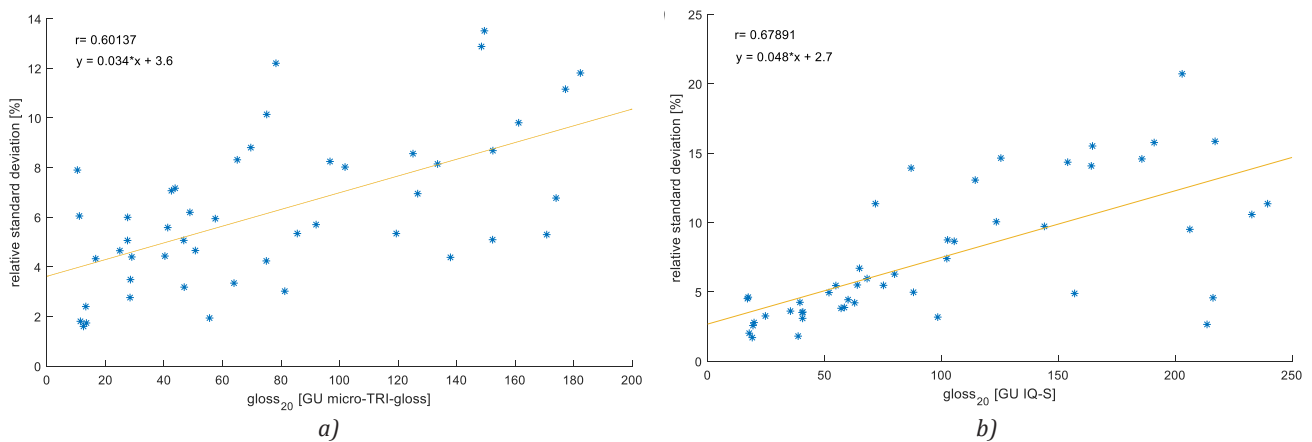

Figure 5: The 20° mean specular gloss value of every of the 48 flexo and offset printed samples is compared with the respective relative standard deviation of the ten measurements of every sample; part (a) shows measurements and relative standard deviations of the micro-TRI-gloss and part (b) shows measurements and relative standard deviations of the IQ-S

Several reasons can be found why the measured specular gloss values of the two devices differ. First, the measurements taken on a printed sample on two different locations are not the same due to the texture of the paper, disorderliness of the metallic pigments, irregularities due to the printing process. This is apparently the greatest contributor to the standard deviation of measurements taken on one sample. Hence, the results about the differences in the relative standard deviation of the measurements have to be treated with caution. Nonetheless, this would not lead to a systematic difference between the measurements.

Second, at the 20° angle the IQ-S is equipped with a LDA but the micro-TRI-gloss with a conventional photo diode. These different types of sensors lead to different results. The authors do not know how this difference in the sensors exactly influences the measurement results.

Third, the IQ-S is differing from the micro-TRI-gloss because it is not only calibrated on a black glass standard but also on a high gloss mirror standard. This additional standard can lead to different measurement results.

Fourth, the black glass standards themselves can differ not only in roughness but also in distribution of black pigments on the glass (Frankhuizen, 2015; Fensterseifer, 2021).

Fifth, according to Frankhuizen (2015) for gloss meters variations in aperture sizes of 30 % can be observed. We do not know the difference of the aperture sizes between the IQ-S and the micro-TRI-gloss but it can be assumed that they are not identical in construction. The difference in construction of gloss meters from different companies was also reported by Ye, Banach and Arney (2006).

Sixth, BYK Gardner and Rhopoint Instrument gloss meters use a single LED to approximate CIE C and human photopic response. If these spectra do not match there could be a source of inter instrument difference (Burrows, 2021).

It was not possible yet to measure the spectra of the two gloss meters to check whether the spectra of the instruments differ.

Seventh, the IQ-S dynamically adjusts integration time of the LDA to achieve high measurement resolution in all ranges, for instance it makes a very long integration time sweep to capture near specular haze signals on painted surfaces. The sensor of the IQ-S is selected to have a highly linear response independent of integration time (Burrows, 2021).

To the authors knowledge there is no dynamic adjustment for measurements of the micro-TRI-gloss. This difference could be a source of differences of measured gloss values.

Differences of measurements of gloss meters including the micro-TRI-gloss and the IQ-S were also examined in Leloup, et al. (2016). However, in this paper only the measurements at 60° are compared and it is shown that for deeper insight into the effect of the differences in the gloss meters ray tracing simulation and a deeper understanding of the construction of the gloss meters would be necessary.

4. Conclusion

In this study, the gloss measurements of metallic embellishments from the printing industry using two different gloss meters were compared. It was investigated how the relative standard deviation of specular gloss measurements change with the glossiness of a surface. The glossier a surface, the higher the relative standard deviation. It could also be shown that it is possible to evaluate more aspects of gloss using the IQ-S, compared to the micro-TRI-gloss. Using these additional measurement results, conclusions about the image reflecting capability of a surface can be drawn. How these additional measured aspects of gloss correlate precisely with human perception of metallic embellishments has to be examined in further studies. In addition, other gloss meters will be investigated in the future to determine their usefulness in the study of metallic gloss.

Acknowledgements

References

American Society for Testing and Materials, 2015. *ASTM D4039 – 09: Test method for reflection haze of high-gloss surfaces*. West Conshohocken, PA, USA: ASTM.

American Society for Testing and Materials, 2018a. *ASTM D523 – 14: Test method for specular gloss*. West Conshohocken, PA, USA: ASTM.

American Society for Testing and Materials, 2018b. *ASTM D5767 – 18: Test method for instrumental measurement of distinctness-of-image (DOI) gloss of coated* surfaces. West Conshohocken, PA, USA: ASTM.

American Society for Testing and Materials, 2019. *ASTM E430 - 19: Test methods for measurement of gloss of high-gloss surfaces by abridged goniophotometry*. West Conshohocken, PA, USA: ASTM.

Bertholdt, U. and Müller, A., 2014. *Material-, Verfahrens-, Veredelungs- und Klimaeinflüsse auf die Ausprägung von Metallic-Effekten im Druck: Fogra Forschungsbericht 50.039*. München, Germany: FOGRA.

Burrows, T., 2021. *Personal note to C.F. Weber*. (Personal communication, 23 July 2021).

Fensterseifer, F., 2021. *Personal note to C.F. Weber*, (Personal communication 7 April 2021).

Frankhuizen, N., 2015. A terminology and metrology view on gloss. *Polymers Paint Colour Journal*, 205: 4613, pp. 24–25.

Hanson, A.R., 2006. *Good practice guide for the measurement of gloss: measurement good practice guide No. 94*. Teddington, Middlesex, UK: National Physical Laboratory.

Heinzler, F.A., Piepenbrink, M. and Doege, T., 2020. Glanzmessung an verchromten Kunststoffbauteilen. *Journal für Oberflächentechnik*, 60, pp. 18–23. http://doi.org.https.jxnydx.proxy.chaoxing.com/10.1007/s35144-020-0610-7.

Hunter, R.S. and Harold, W.H., 1987. *The measurement of appearance*. 2nd ed. New York: John Wiley & Sons.

Kigle-Boeckler, G., 1995. Measurement of gloss and reflection properties of surfaces. *Metal Finishing*, 93(5), pp. 28–31. https://doi.org/10.1016/0026-0576(95)90685-B.

Konica Minolta, n.d. Understanding gloss with the Rhopoint IQ-S. *Konica Minolta* [online]. Available at: <https://assets.thermofisher.com/TFS-Assets/ANZ/brochures/konica-minolta-understanding-gloss.pdf> [Accessed 27 March 2021].

Laine, J., Leppänen, T. and Nurmi, O., 2009. *The influence of special effects on the perception of printed products*: *research report VTT-R-04966–09*. VTT Technical Research Centre of Finland.

Leloup, F.B., Obein, G., Pointer, M.R. and Hanselaer, P., 2014. Toward the soft metrology of surface gloss: a review. *Color Research and Application*, 39(6), pp. 559–570. https://doi.org/10.1002/col.21846.

Leloup, F.B., Audenaert, J., Obein, G., Ged, G. and Hanselaer, P., 2016. Repeatability and reproducibility of specular gloss meters in theory and practice. *Journal of Coatings Technology and Research*, 13(6), pp. 941–951. https://doi.org/10.1007/s11998-016-9813-5.

Morlok, F. and Beckmann, T., 2009. *extra: Enzyklopädie der experimentellen Druckveredelung*. Basel, Switzerland: Birkäuser.

Prolss, D., Trummer, S. and Kröll, A., Eckart GmbH., 2009. *Ink jet printing ink containing thin aluminum pigments and method.* WIPO WO2009/010288A2.

Rich, D.C., Marcus, R., Lovell, V. and Kreutz, T., 2017. Modeling the appearance of metal-like packaging printing. *Color Research and Application*, 42(1), pp. 38–49. https://doi.org/10.1002/col.22035.

Rosenberg, A., 2000. *Visuelle und messtechnische Bewertung von Metalliceffekten bei Drucken: Fogra Forschungsbericht 52.029*. München, Germany: FOGRA.

Schröder, U., 2004. Glanzmessgeräte richtig einsetzen und einkaufen. *Welt der Farben*, 7/8.

Silvennoinen, R., Peiponen, K.-E. and Myller, K., 2008. *Specular gloss*. Amsterdam, Oxford: Elsevier.

Weber, C.F., Spiehl, D. and Dörsam, E., 2021. Comparing measurement principles of three gloss meters and using them for measuring gloss on metallic embellishments produced by the printing industry. In: *Lux junior 2021: 15. Internationales Forum für den lichttechnischen Nachwuchs*. Ilmenau, Germany, 4–6 June 2021. TU Ilmenau, Germany. https://doi.org/10.22032/dbt.49339.

Westlund, H.B. and Meyer, G.W., 2001. Applying appearance standards to light reflection models. In: *ACM SIGGRAPH 2001: Proceedings of the 28th annual conference on Computer graphics and interactive techniques*. Los Angeles, CA, USA, 12–17 August 2001. New York, NY, USA: ACM. https://doi.org/10.1145/383259.383318.

Wißling, P., 2013. *Metalleffekt-Pigmente.* 2nd ed. Hannover, Germany: Vincenz Network.

Ye, L., Banach, S. and Arney, J., 2006. Interpretation of gloss meter measurements. *Journal of Imaging Science and Technology*, 50(6), pp. 567–571. https://doi.org/10.2352/J.ImagingSci.Technol.(2006)50:6(567).

Feasibility of low-cost color sensors in Graphic Communications virtual classroom learning

Bethany Wheeler and Shu Chang

Department of Graphic Communications, The Wilbur O. and Ann Powers College of Business, Clemson University, Clemson, South Carolina, USA

E-mails: bawheel@g.clemson.edu; schang2@clemson.edu

Short abstract

This work presents the process of selecting and assessing a low-cost color sensor suitable for illustrating essential concepts within pre-established graphic communications curricula for virtual learning. The suitability of the device was determined based on its ability to evaluate concepts presented in the curriculum, such as the whiteness and opacity of the substrates; and the optical density, tone reproduction, color balance, hue error, grayness, and overprint trapping of inks. Many of these evaluations require measurement of color and optical density. The selected sensor provides measurement of CIE $L*a*b*$. Established conversions can then translate the CIE $L*a*b*$ values into optical densities. The evaluations performed by the low-cost color sensors were compared to those from a standard device, X-Rite eXact, for the purpose of explaining similar observations. The comparison was conducted in the virtual classroom, with the actual learning delivery and device exploration taking place in parallel. The initial collection of data from the virtual classroom indicates statistically significant differences between the low-cost device and X-Rite eXact; however, the concept illustration was not impeded by the differences.

Keywords: portable color sensors, colorimetric measurement, densitometric measurement, virtual learning, virtual classroom

1. Introduction

Classroom learning and instruction changed drastically over the course of the last year due to the widespread Coronavirus pandemic. In most circumstances, in-person teaching was no longer an option due to the health and safety concerns of students, faculty, staff, and their families. These concerns drove many academic institutions to offer online courses exclusively and launched faculty into virtually delivering course content with no alternative. In a discipline such as graphic communications or printing, where hands-on interaction with tools and equipment is one of the main focuses of the curriculum, this sudden shift presented a whole new set of challenges.

This work aims to identify a portable and affordable color measurement device for virtual classroom use and to assess its feasibility with respect to class curriculum requirements. Measurement devices sampled in this work are classified as portable color sensors. They are affordable, with a cost similar to textbooks, and are easy for students to acquire and use. Past research has assessed the performance of similar sensors in terms of success rates of identifying the color of established color chips and has indicated the attractiveness of these sensors for applications not requiring high accuracy (Kirchner, et al., 2019). Research containing color elements has used these portable color sensors to document changes. For example, the Nix Pro color sensor was used by Post and Schlautman (2020) to categorize flower petals' colors as defined by Royal Horticultural Society (RHS) Colour Chart, and by Stiglitz, et al. (2016) to examine soil color relative to Munsell color codes. Typically, the primary users of these devices are graphic designers, photographers, interior designers, paint suppliers, and contractors, etc.

This paper will focus on the capability of the device to define color using standards such as CIE *L*a*b** and optical density. The goal is for the low-cost sensors to provide a comparable understanding of concepts introduced in our curriculum. Examples of these concepts include color and color difference (Δ*E**), tone reproduction, whiteness and opacity, color balance, and even hue error, grayness, and overprint trapping, typically measured for process colored prints. In the existing in-person curriculum, the X-Rite eXact and X-Rite i1io spectrometers have been the standard instruments. As it is not feasible to provide every student with a standardized spectrophotometer for at-home use, an affordable replacement becomes a must.

The hypothesis of this study is that one or more low-cost color sensors would exhibit sufficiency in the demonstration of colorimetric concepts, such as CIE *L*a*b** color space and color difference (Δ*E**). In addition, the conversions of CIE *L*a*b** values to optical densities are of sufficient accuracy to reflect some of the effects caused by the print process. The goal is for the low-cost sensors to present similar outcomes when contrasted to the X-Rite eXact. For instance, can the low-cost sensor differentiate colors in the definition of CIE *L*a*b**? Can optical densities estimated from the CIE *L*a*b** values discern a difference between dot area coverage when there are changes in the print system? Can the low-cost sensors be a reliable tool in the print evaluations in the curriculum? This study focuses on determining what the low-cost sensor can do and to what extent.

This paper presents the content according to the following categories: selecting a low-cost color sensor, sensor feasibility determination, and results and discussion. This paper will also share the initial outlook on the accuracy and variation of the low-cost devices when compared to the standardized measurement systems.

2. Selecting a low-cost color sensor

In the simplest form, color sensors emit a known amount of light and return a measurement of the light that is reflected back off of a given object. These devices use red, green, and blue filters to measure tri-stimulus (RGB) values that are similar to the way humans perceive color (Mouw, 2019). Densitometers, on the other hand, are blind to color. They emit light onto the object being measured through red, green, or blue filters at specific wavelengths and return density measurements by taking the negative log of the reflected light. By limiting the color (or wavelength) of light, the object being measured can reflect, it is easier to detect subtle changes in the presence of inks (Lakacha, 2013). For example, when measuring the magenta density of an object or the density of magenta ink, the green filter within the densitometer is used. Magenta absorbs green light, so when the green filter is used, the reflectance of a magenta object is minimal. Density values are useful in print evaluation because there is a correlation between the density and the ink film thickness. Spectrophotometers can be used to achieve even more precision as this type of instrument uses narrow filters to split the emitted light into thin bands that record the reflectance at certain intervals, typically every 10 or 20 nanometers. The resulting measurements describe the object's color and reflectance across the entire measured spectrum and can be used to generate spectral curves (Seymour, 2017; Myers, 2021).

Prior to introducing the devices into the curriculum, two low-cost sensors, Color Muse, or "Muse" in this paper, and Nix Mini 2, or "Nix", were examined. Both of the sensors tested represent the base model for each respective manufacturer. Brief device specifications for both Muse and Nix, as well as the X-Rite eXact Advanced or "eXact", can be found in Table 1 (Color Muse, 2020; Nix, 2020; X-rite eXact, 2020).

Table 1: Device Specifications (per published technical specifications)

Characteristics	Color Muse colormuse.io	Nix Mini 2 nixsensor.com	X-Rite eXact xrite.com
Price (in US Dollars)	$59.99	$99.00	~$8350.00
Optical geometry	45°/0°	45°/0°	45°/0°
Illuminants	A, **D50**, D65, F2, F7	**D50**	**D50**, D55, D65, D75
Observer functions	**2°**, 10°	**2°**	**2°**, 10°
Measurement conditions	Closer to M0 than M1	Similar to M2	M0, M1
Measurement size	4 mm	15 mm	1.5 mm, 2 mm, 4 mm, 6 mm

Table 1 indicates that the three devices have some commonalities that are shown in bold. All three devices have an Optical geometry of 45°/0°, Illuminants of D50, and the Observer functions of 2°. Therefore, these settings were used as the standards in this research. One difference among the devices is the size of the apertures 4 mm, 15 mm, and a range between 1.5 mm to 6 mm for Muse, Nix, and eXact, respectively. The other key difference between the devices is the Measurement condition, as the eXact's measurement conditions are set to CIE standards where the Muse and Nix are approximations.

To compare the Muse and Nix devices, measurements were taken from cyan, magenta, yellow, and black ("CMYK") ink patches as well as solid overprint combinations, red, green, and blue ("RGB"). Measurements of CIE $L*a*b*$ data of CMY ink and RGB overprints indicated that both low-cost sensors showed significant color differences with respect to eXact. In Table 2, ΔE_{00} were calculated (using ColorTools, a Microsoft Excel Add-in) by comparing the CIE $L*a*b*$ data obtained with each sensor to those with the eXact (Edgardo, 2021). Table 2 indicates that Muse differed from eXact by 2.7 ΔE_{00} and Nix by 1.4 ΔE_{00}, with a standard deviation of 1.0 ΔE_{00} and 0.8 ΔE_{00}, respectively. As indicated in Table 2, the color differences between Nix and eXact appeared smaller for most of the six colors sampled. Ultimately, the Nix was selected as the sensor for testing in the virtual classroom. Since these low-cost sensors perform the functions of a colorimeter, only CIE $L*a*b*$ data were relied upon for the selection.

Table 2: Color differences of Muse and Nix when compared to X-Rite eXact (ΔE_{00})

Color	Muse	Nix
Cyan	2.3	3.0
Magenta	3.3	0.6
Yellow	1.0	1.2
Red	3.0	1.1
Green	3.8	1.1
Blue	2.6	1.5
Mean	**2.7**	**1.4**
Standard deviation	**1.0**	**0.8**

3. Sensor feasibility determination

Nix feasibility testing was implemented in six of the eight labs in the semester. The concepts tested with Nix included visualizing CIE *L*a*b** space, whiteness and opacity of substrates, opacity of inks, tone reproduction, dot gain, print contrast, hue error/grayness, trapping, gray balance, color balance, and color differences. Nix measured CIE *L*a*b** values. Other print evaluations required optical densities, which were obtained through conversion from CIE *L*a*b**. Formulas used to calculate CMKY optical densities from CIE *L*a*b** data can be found on the attached formula sheet.

Nix measurements were conducted by 46 students in the Fall 2020 semester and 38 students in the Spring 2021 semester. The eXact measurements were conducted by the teaching assistant and the instructor. This paper will focus on the two lab assignments that evaluate CIE *L*a*b** color space and tone reproduction as examples.

3.1 Visualizing *CIE L*a*b** color space

"Getting Started with Colorimeters and *L*a*b**" is the introductory laboratory to help students visualize the color space. The assignment was designed to prepare students to use the Nix device and to provide a basic understanding of the CIE *L*a*b** color space and the meaning of neutral. Although a standardized test target like the FOGRA Media Wedge can be used here, the test target presented in Figure 1 was divised as to present a simplified introduction of the CIE *L*a*b** concept. Figure 1 consists of process-colored inks (CMYK), overprint patches (RGB), a lightness scale, and pseudo-*L*a*b** cross-section. The pseudo-*L*a*b** cross-section contains some extremely saturated colors (that may range substantially on the *L** axis). Therefore, it does not represent a true *a*b** cross-section at a given *L**. The lightness scale *L** contains three levels of grays. Samples used to provide this data were produced on the same paper stock in one run (per semester).

Figure 1: Getting Started with Colorimeters and L*a*b* test target

In this assignment, students are provided with an Excel Data Template and a printed Test Target (Figure 1). Students are instructed to install the Nix Digital smartphone app, pair the Nix device, and to record the CIE *L*a*b** values for the instructed patches. The students then apply Equation [1]: 1976 ΔE^*_{ab} to calculate the color difference (ΔE^*_{ab}) between the measurements from their Nix and a sample of data collected using an eXact provided by the instructors.

$$\Delta E^*_{ab} = \sqrt{(L^*_2 - L^*_1)^2 + (a^*_2 - a^*_1)^2 + (b^*_2 - b^*_1)^2} \qquad [1]$$

3.2 Tone reproduction

Tone reproduction is used in many areas to characterize the print production process. The laboratory of "Banded Roll" intends to illustrate the selection process of an anilox roll that would provide the optimal ink volume to the impression of the images in flexographic printing. Different ink coverage would behave differently in the print process and would be reflected in the outcome of tone reproduction, dot gain, and print contrast. With this laboratory, samples of tone scales (0 % to 100 % dot coverage) were produced with an anilox roll which is a combination of five bands for five different ink volumes; thus, the term banded roll.

For this assignment, students measured tone scales for all five bands from a press sample (all samples were produced in the same press run). The five bands carried 0.95, 1.58, 2.10, 2.61, and 3.01 bcm/in^2 (billion of cubic microns per square inch area). The flexographic plate was imaged at 150 LPI line screen. The data template converted the CIE $L*a*b*$ values to CMYK density and applied the Equation [2]: Murray-Davies Dot Area Formula listed below. The students completed charts for the tone reproduction, dot gain, and print contrast to make recommendations for which band to use for the given substrate.

$$Dot\ Area = \frac{1 - 10^{-Density_{tint}}}{1 - 10^{-Density_{solid}}}$$
[2]

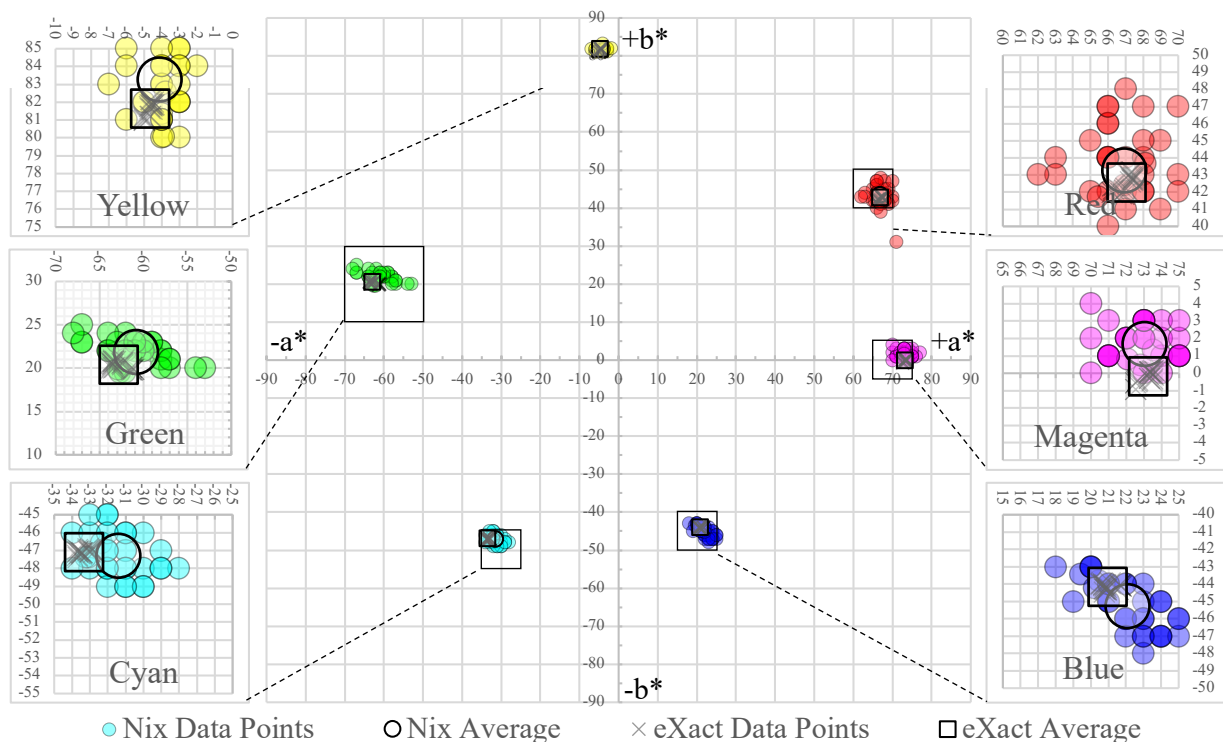## 4. Results and discussion

4.1 Visualinzing color space

Figure 2: Comparing Nix a*b* values (small semi-transparent colored circles) to eXact (×'s); the enlargements associated with each color show larger variations from Nix data

Figure 2 depicts CIE $L*a*b*$ data collected from the "Getting Started with Colorimeters and L*a*b*" laboratory. Nix $a*b*$ data (small semi-transparent colored circles) was collected by 34 students and is compared to 20 eXact $a*b*$ data points (×'s) that were collected by one user with four devices and five samples.

Figure 2 compares data from Nix to those from eXact (×'s) on an *a** (horizontal axis) and *b** (vertical axis) plane for the colors of CMYRGB. Collections of colored circles, or data points, mark a region of *a** and *b** values for the corresponding color. For example, the cyan circles (in Figure 2) are grouped around ~ −33 *a** and ~ −47 *b**. The square boxes around each data cluster indicate roughly the spread of the data from the measurements. All squares are 10 by 10 units, except green, which is 20 by 20 units, underlining a larger variation from the green data.

The enlargements of each color group shown in Figure 2 emphasize the approximate regions that the measurements that each CMYRGB color occupies. The larger circle and square near the center of each color group locate the mean *a** and *b** values for the Nix and eXact, respectively. For example, the cyan data in the bottom left enlargement shows the mean *a** and *b** are −31.4 and −47.3 respectively for the Nix while −33.34 and −47.06 respectively for the eXact. Figure 2 also highlights the smaller variation of eXact than Nix, as the × data points from eXact are tighter than those from the Nix data.

Table 3 presents a statistical comparison between Nix and eXact. Table 3 contains data collected in the Spring 2021 semester. The 34 independent sets collected for the Nix were, presumably, collected by 34 unique students using 34 unique samples and devices; the 20 measurements analyzed for the eXact were collected on four different devices, each measuring five samples, all performed by the same user. The table shows the mean values, deviations, and ranges of *a** and *b** for CMYRGB, as well as of *L** for three gray patches labeled as Light, Medium, and Dark, respectively. The Nix data are in the top three rows and eXact in the next three rows. The bottom row of the table displays the results from a two-sample *t*-testing to identify the differences between the Nix data and the eXact data.

Table 3: Statistical analysis of Nix compared to eXact;
spring 2021: Nix (34 independent sets), eXact (20 Measurements 4 devices 5 samples)

		Cyan		Magenta		Yellow		Red		Green		Blue		Light	Medium	Dark
		a*	*b**	*a**	*b**	*a**	*b**	*a**	*b**	*a**	*b**	*a**	*b**	*L**	*L**	*L**
Nix	Mean:	−31.4	−47.3	73.0	1.7	−4.1	83.3	66.9	43.3	−60.9	21.9	22.1	−45.2	76.4	48.3	23.3
	Deviation:	1.5	1.2	1.8	1.0	1.2	2.2	2.0	3.1	3.5	1.4	1.8	1.4	1.1	1.3	1.4
	Range:	6.0	4.0	7.0	4.0	5.0	9.0	9.0	17.0	15.0	5.5	7.0	5.0	4.0	5.0	6.0
eXact	Mean:	−33.3	−47.1	73.2	−0.2	−4.7	81.6	67.0	42.6	−62.8	20.4	20.9	−44.1	78.6	49.7	24.3
	Deviation:	0.3	0.1	0.4	0.3	0.2	0.4	0.4	0.4	0.9	0.4	0.4	0.2	0.2	0.3	0.3
	Range:	0.9	0.5	1.1	1.1	0.6	1.2	1.3	1.3	2.5	1.2	1.2	0.5	0.7	1.0	1.0
	p-value:	0.00	0.31	0.48	0.00	0.02	0.00	0.69	0.20	0.00	0.00	0.00	0.00	0.00	0.00	0.00

Close observation of the table reveals that for all CMYRGB and *L** sampled, Nix consistently attains larger deviations and range of values than eXact. For example, while eXact measurements produce deviations in the fractional values, Nix's deviations are all over one. This is particularly striking for the color green, where Nix has a deviation of 3.5 and a range of 15. This is consistent with the visibly larger *a** spread of green values in Figure 2. Similar observations of other colors also highlight the eXact's superior performance over Nix.

The two-sample t-test compares the mean values of Nix and eXact. The Null hypothesis assumes that the two means are equal. If the p-value is less than or equal to 0.05, or less than or equal to 5 % probability, then the Null hypothesis is rejected, and the two means are declared to be different. As exhibited in the bottom row of the table, 11 of 15 of the Null hypotheses are rejected. Therefore in these 11 cases, the data from Nix and eXact are proven to be statistically different.

For the concept demonstration, however, students can visualize the differences in colors presented by the patches in the test target presented in Figure 1. In addition, the students can measure the CIE $L*a*b*$ values associated with each patch to visualize $a*$ changes and $b*$ changes individually or jointly. The differences detected in the statistical analysis is insignificant towards the demonstration of CIE $L*a*b*$.

4.2 Tone reproduction

Tone reproduction curves are used frequently to examine the dot gain effects caused by the print process. In the banded roll assignment, the intention is to identify the anilox roll that provides a tone reproduction curve near a one-to-one input dot-to-output dot coverage ratio.

For this assignment, the substrate and procedures were standardized, so the Nix data presented in Figure 3 represents a collection of density values (total 60 submissions) by students in both Fall 2020 and Spring 2021. There was no significant difference between the data collected in each semester. The eXrite means were obtained by averaging five measurements taken on five different eXact devices by the instructors and six students in Spring 2021.

Figure 3 depicts tone reproduction curves from Nix's CIE L*a*b* measurements, converted to densities. Figure 3a on the left shows an example of Nix's measurements in gray-filled circles that are plotted to the left of each vertical marker and eXact's in gray-filled squares that are ploted to the right of each vertical marker (Note that the symbols are semi-transparent - as the data points stack on top of each other, they overlap and darken). The example in Figure 3a is for the anilox band that carries 0.95 bcm/in² volume of ink. eXact data in Figure 3a in gray-filled squares are tightly super-positioned on each other, indicating consistent results from measurement to measurement. In contrast, the gray-filled circles of Nix data scattered over a 20 % to 30 % range.
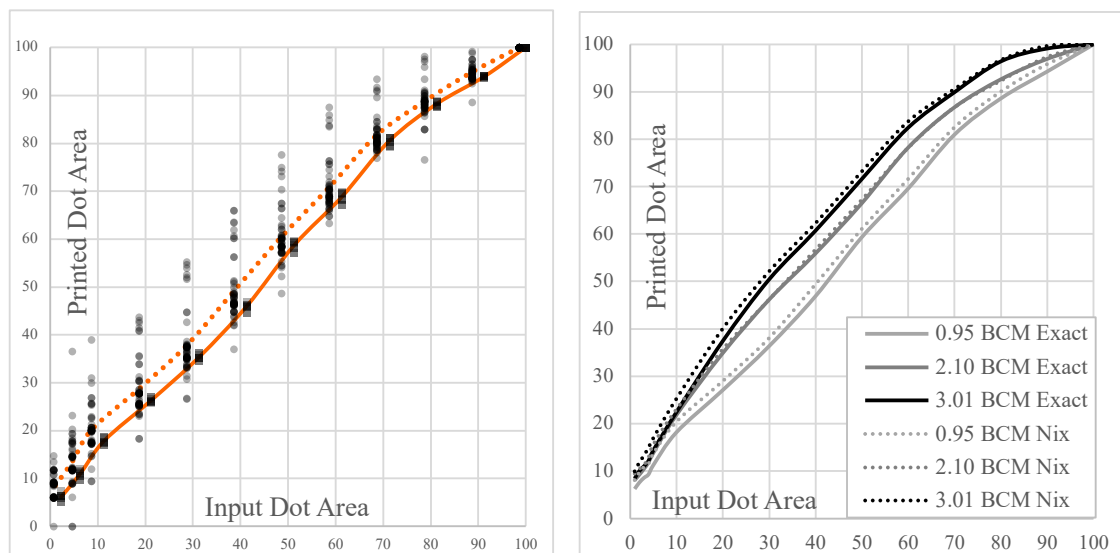
a): Tone reproduction data and average curves for 0.95 bcm/in² band

The data are scattered for Nix measurements (circles) compared to eXact (squares)

b): Tone reproduction average curves 0.95 bcm/in², 2.10 bcm/in² and 3.01 bcm/in²

Averaged output dot areas to show the dot gain effect from increasing input ink volumes from anilox rolls

Figure 3: Tone reproduction data captured Fall 2020 and Spring 2021

Figure 3b on the right replots the tone reproduction curve from the 0.95 bcm/in2 band with the mean values from both Nix and eXact. Also included in Figure 3b are the tone reproduction curves from both the 2.01 bcm/in2 and 3.01 bcm/in2 anilox bands. Figure 3b shows that the tone reproduction curves from

eXact underline the effects of increasing dot gains as the ink volume from the anilox band increases. The tone reproduction curves from Nix in Figure 3b also present a message that is consistent with that of the eXact. We do notice a statically significant difference by applying the Student's t-test throughout the majority of the data points. Although data points are scattered and different from eXact, the Nix appears to be sufficient in differentiating the individual bands from one another and allowed the students to make expected recommendations.

5. Conclusion

The work presented here supported the hypothesis that low-cost sensors can provide sufficient accuracy for virtual classroom use. The examples shown here for "visualizing color space" and "tone reproduction" illustrate that reasonable and consistent outcomes can be expected from the Nix for the curriculum cases. For example, Nix can provide data that allows students to grasp the CIE $L*a*b*$ model conceptually, and the converted CMYK density can show the overall trend to allow students to distinguish the effects of dot gain and ink film thickness. On the contrary, Nix does not perform with the accuracy and precision that is necessary in most color measurement environments outside the classroom. When high sensitivity is called for, Nix becomes ineffective in showing the differences in the prints, as it lacks the precision that standardized devices like the eXact provide. In conclusion, low-cost devices such as Nix can be utilized as a tool for most print evaluations in the online curriculum.

References

Color Muse, 2020. *Compare color sensors*. [online] Available at: <colormuse.io/compare.html> [Accessed 2 November 2020].

Edgardo, G., 2021. *Color calculations in Excel*. [online] Available at: <rgbcmyk.com.ar/en/xla-2/> [Accessed 15 March 2021].

Kirchner, E., Koeckhoven, P. and Sivakumar, K., 2019. Predicting the performance of low-cost color instruments for color identification. *Journal of the Optical Society of America A*, 36(3), pp. 368–376. doi.org/10.1364/josaa.36.000368.

Lakacha, A., 2013. A functional comparison of the densitometer and spectrophotometer. *Techkon,* [blog] 7 May. Available at: <techkonusa.com/a-functional-comparison-of-the-densitometer-and-spectrophotometer> [Accessed June 1 2021].

Myers, B.L., 2021. What is a spectrodensitometer? *Techkon,* [blog] 20 June. Available at: <techkonusa.com/what-is-a-spectrodensitometer> [Accessed 20 June 2021].

Mouw, T., 2019. Colorimeter vs. spectrophotometer. *X-rite,* [blog] 7 October. Available at: <xrite.com/blog/colorimeter-vs-spectrophotometer> [Accessed June 2021].

Nix, 2020. *Compare Nix color sensor devices.* [online] Available at: <nixsensor.com/compare-nix/#1519315093017-f21bfe20-6786> [Accessed 2 November 2020].

Post, P.C. and Schlautman, M.A., 2020. Measuring camellia petal color using a portable color sensor. *Horticulturae* 6(3): 55. https://doi.org/10.3390/horticulturae6030053.

Seymour, J., 2017.Of colorimeters and spectrophotometers. *John the Math Guy* [blog] 13 July. Available at: <johnthemathguy.blogspot.com/2017/07/of-colorimeters-and-spectrophotometers.html> [Accessed 16 July 2020].

Stiglitz, R., Mikhailova, E., Post, C., Schlautman, M. and Sharp, J., 2016. Evaluation of an inexpensive sensor to measure soil color. *Computers and Electronics in Agriculture*, 121, pp. 141–148. https://doi.org/10.1016/j.compag.2015.11.014.

X-Rite eXact, 2020. *eXact Advanced Spectrophotometer Specifications.* [online] Available at: <xrite.com/categories/portable-spectrophotometers/exact-advanced> [Accessed 2 November 2020].

Appendix – Formulas:

CIE $L^*a^*b^*$ to CMYK Density:

$$f(x) = f(y) + a^*/500$$
$$f(y) = (L^* + 16)/116$$
$$f(z) = f(y) - b^*/200$$

X/X_n

Where $f(x) < 24/116$, $X/X_n = (f(x) - (16/116)) * 108/841$

Where $f(x) > 24/116$, $X/X_n = f(x)^3$

Y/Y_n

Where $f(y) < 24/116$, $Y/Y_n = (f(y) - (16/116)) * 108/841$

Where $f(y) > 24/116$, $Y/Y_n = f(y)^3$

Z/Z_n

Where $f(z) < 24/116$, $Z/Z_n = (f(z) - (16/116)) * 108/841$

Where $f(z) > 24/116$, $Z/Z_n = f(z)^3$

$$R = 1.4391 * X/X_n - 0.2202 * Y/Y_n - 0.2027 * Z/Z_n$$
$$G = -0.731 * X/X_n + 1.686 * Y/Y_n + 0.0801 * Z/Z_n$$
$$B = -0.0064 * X/X_n + 0.0171 * Y/Y_n + 1.1995 * Z/Z_n$$

Density Cyan $= -\log_{10} R$
Density Magenta $= -\log_{10} G$
Density Yellow $= -\log_{10} B$
Density Black $= -\log_{10} Y/Yn$

The binding of children's book in Greece (1990–2015)

Evgenia Pagani

National and Kapodistrian University of Athens, Department of Primary Education
E-mail: jen.pag@hotmail.com

Short abstract

Binding is recognized as an important factor of the identity and continuity of the printed book, but it is also evolving into a qualitative reference point for the content of the book. The choice of the binding method determines the aesthetics of the children's book, its perceptual value and its resistance to wear and tear. In addition, the raw materials are chosen in order for the book to be protected by the unconscious handling of the child and with emphasis on the protection and physical integrity of the child as well. The article focuses on the binding methods that were used in children's books published in Greece, from 1990 to 2015. There seems to be a strong relationship of each binding method with specific sub-genres of the children's book, supporting the view that the binding can also predispose the reader's attitude towards the book, creating ideological extensions for its content.

Keywords: bookbinding, materiality, children's book, Greece

1. Introduction and background

The cover, the back cover, the spine and the body of the book are the protectors of its content. The physical wear and tear of materials seems like wounds of a warrior fighting till the end to save what valuable he possesses. Time may alter materials but is not capable of changing the meaning, as the materiality of the book assures the reader that in each reading, the content will come to life as before (Yannicopoulou, 1998, p. 43). The materiality of the book is a vital and fascinating place for a child, "a small consolation, at today's zenith of the technological explosion" (Dimiroulis, 2002, pp. 205–221). The infant, in his first contact with the book, participates in a special type of "reading", with all his senses. He tries to touch, smell, tear or even chew the book pages, literally expressing "the love for reading". On the other side, adults produce books that encourage chewing and other physical activities as forms of "reading", generally accepting them as permissible reading experiences for infants (Beveridge, 2017). The book materiality protects the printed "memory" and this is as important as the decisive choice of its physical form. *Paratext* creates "a zone between text and off-text, a zone not only of transition but also of transaction", strategically composed to influence the reception and interpretation of the text by its audience. According to Genette (1997, pp. 2–4, 344), *paratext* is divided to *epitext* and *peritext*. *Peritext* includes all kinds of features that are evident to a reader holding the book. These include the publishers' choices about the format, the book series, the cover, the title page, the typesetting, the printing, and the front matters of the book, such as the book title, the copyright page, etc. (Doonan, 1993, p. 84).

Genette (1997, pp. 34, 410) attaches great importance to publishing options as "no reader should be indifferent to the appropriateness of particular typographical choices, even if modern publishing tends to neutralize these choices by a perhaps irreversible tendency toward standardization". However, he describes *peritext* as "an assistant, just an 'accessory' of the text". McKenzie (1981, pp. 81–125) explicitly disagrees and expresses his appreciation for bibliographic data recognizing their contribution to the construction of meaning. He states that it is not possible to separate the meaning of the text from its physical form. The set of all bibliographic elements, such as typography, the page design, the raw materials, the format of the

book, is not a marginal *addendum*, but guides the reading experience. However, the importance of *peritext* of the children's book is questioned more than in any other book genre, as the children's book is constantly exposed to "devices" other than narrative (Higonnet, 1990, pp. 47–49). The *peritext* of children's book is part of the text and at the same time outline its "implied reader". The form of a book – the cover and back cover, the title, the illustrations etc. –, provides indications of the type of the implied reader and create similar expectations (Pantaleo, 2017, p. 84; Oikonomidou, 2016, p. 68).

In children's literature, the brevity of average text emphasizes the materiality features of the book, which define the approach of its "reading" (Gavriilidis, 2018, p. 113 et seq.; Yannicopoulou, 1998, pp. 43–45). The materiality of the children's book provides young "readers" with a field of exploration, but especially, the choice of the binding method and the raw materials determine the aesthetics of the children's book, its perceptual value and its resistance to wear and tear (Bann, 2006, p. 144; Ambrose and Harris, 2011, p. 9 et seq.). Yannicopoulou (2008, pp. 327–328) states that binding is evolving into a qualitative reference point for the content of the book, as the beauty of its cover indicate what is written on its pages. Furthermore, Al-Yaqout (2011, pp. 57–77) recognizes the bookbinding as an important factor of the identity and continuity of the printed book. Despite the fact that some children's books completely pass over the binding stage and take the format of a leaflet for the purpose of a creative narrative, the available methods of assembling the printed sheets include different methods of bookbinding. The perfect, notch or sewn binding with soft-cover (paperback book) are popular methods and evaluation elements for the printed book. On the other side, the quality features of the perfect, notch or sewn binding with hardcover (hardback book) protect the verbal and visual text over time and add aesthetic and commercial value. The spiral binding is most commonly used for leaflets, annual reports, etc. but is used sometimes for binding children's books as well. Different sub-genres of the children's book seem to be more or less related either to paperback, hardback or spiral bound book, determining a frequency of their use according to the type of the book and/or the age of the reader. Therefore, the variety of the binding methods and the raw materials used may be proved an important factor in the ever-evolving and playful nature of the printed children's book, contributing to its multimodality through materiality.

2. Materials and methods

The research was based on the principles of descriptive statistics and secondary quantitative method. The characteristics of children's book published from 1990 to 2015 in Greece were selected by statistical methods and numerical data, collected from descriptive data of the bibliographic database "Βιβλιονέτ" ["Biblionet"]. The research was carried out on the "Home Page" of the database (http://www.biblionet. gr/). Printed books were searched under the term "Βιβλίο" ["Book"] in the field "Είδος:" ["Type:"], in subject categories under the prefix "Παιδικό, -ά, -ές" ["Children's"] or "Βιβλία για παιδιά" ["Books for children"] e.g. "Children's books, Greek", "Animals - Books for children". The research was repeated for each time period "from 1990 to 1995", "from 1996 to 2000", "from 2001 to 2005", "from 2006 to 2010" and "from 2011 to 2015". The conclusions were based on the frequency of each variable "μαλακό εξώφυλλο" ["softcover"], "σκληρό εξώφυλλο" ["hardcover"], "σπειροειδής" ["spiral binding"], "πανόδετο" ["cloth book cover"] and "δερματόδετο" ["leather book cover"], per subject category of the children's book. However, the database did not provide more information about the perfect, notch or sewn binding methods that were used in books, as well as board books were inaccurately recorded as "hardcover" books, so the assumptions were based on the variables that were available.

The "IBM Statistical Package for Social Sciences – SPSS Statistics 20" software was used for the quantitative data analysis. The data are presented in frequency tables and visually in bar charts and/or frequency polygons, providing important indications of trends in the printed form of the children's book in Greece, from 1990 to 2015.

2.1 The sample size

The total research sample is 33 385 children's books. The research sample is 2 122 children's books for the period 1990–1995, 6 297 for the period 1996–2000, 8 027 for the period 2001–2005, 9 925 for the period 2006–2010 and 7 014 for the period 2011–2015 (Table 1 and Figure 1):

Table 1: The research sample (Source: Biblionet)

	1990–1995	1996–2000	2001–2005	2006–2010	2011–2015
N book titles (all genres) [1]	16 002	33 139	44 188	53 351	36 435
N_{i*} children's books [2]	2 180	6 682	9 199	12 097	8 301
v children's books in multiple subject categories	138	952	2.964	5.267	3.089
N_i **children's books** [3]	**2 122**	**6 297**	**8 027**	**9 925**	**7 014**
$R(N_i)$ standard deviation	*± 23*	*±7 9*	*± 247*	*± 439*	*± 257*
Relative frequency F_i (**N_i/N**)	0.13	0.19	0.18	0.18	0.19
$R(F_i)$ standard deviation	*0.014*	*0.02*	*0.05*	*0.08*	*0.07*
*Percent F_i% (**N_i/N**)%*	13.26	19.00	18.16	18.60	19.25
$R(F_{i\%})$ standard deviation	*0.14*	*0.24*	*0.56*	*0.82*	*0.70*
Percent F_i%	–	+ 5.74	– 0.84	+ 0.44	+ 0.65

[1] All book titles registered in the "Biblionet" database are included, regardless of the book genre (adult and children's books).

[2] Initial sample size, including book entries in multiple subject categories of the children's book.

[3] The final sample size was calculated after clearing the multiple children's book subject category entries.
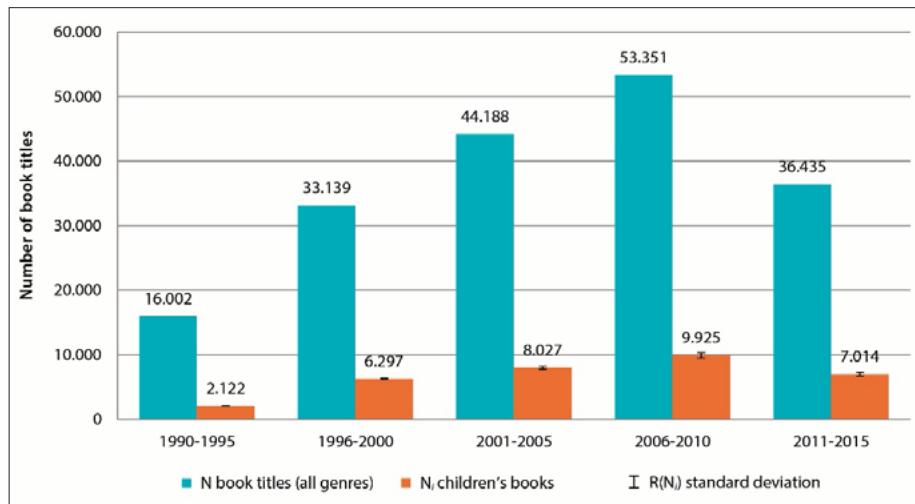

Figure 1: The research sample of children's books in relation with the book titles (all genres)
as collected from the bibliographic database "Biblionet"

3. Results and discussion

3.1 The binding methods

From 1990 to 2015, the highest average frequency of 87.96 % of softcover binding in children's and young adult's Greek literary books, confirmed that literature explicitly dictates standardization in its form, with the verbal text setting stricter terms for its effective modality. In the case of the bookbinding method, an older age of the reading audience, the wider content, the need for a sustainable domestic production and a lower book price, minimized the variety of the cover type in the literary books.

Children's activity books showed, also, a high frequency of softcover, marginally exceeding 80 %. Coloring pages, stickers and toys were offered to the child from the age of three in a softcover book. Despite the young age of the reading audience, the almost ephemeral use of the activity book led to the most economical and easy-to-use, soft cover. Completing the activities usually meant fulfilling the purpose of the book, with many actions being completed once. The child both reconstructed the materiality of the activity book, through the reconstruction of the content -such as coloring or collage of images- and disassembled it, by removing stickers or cutting paper designs from entire pages (Figure 2).
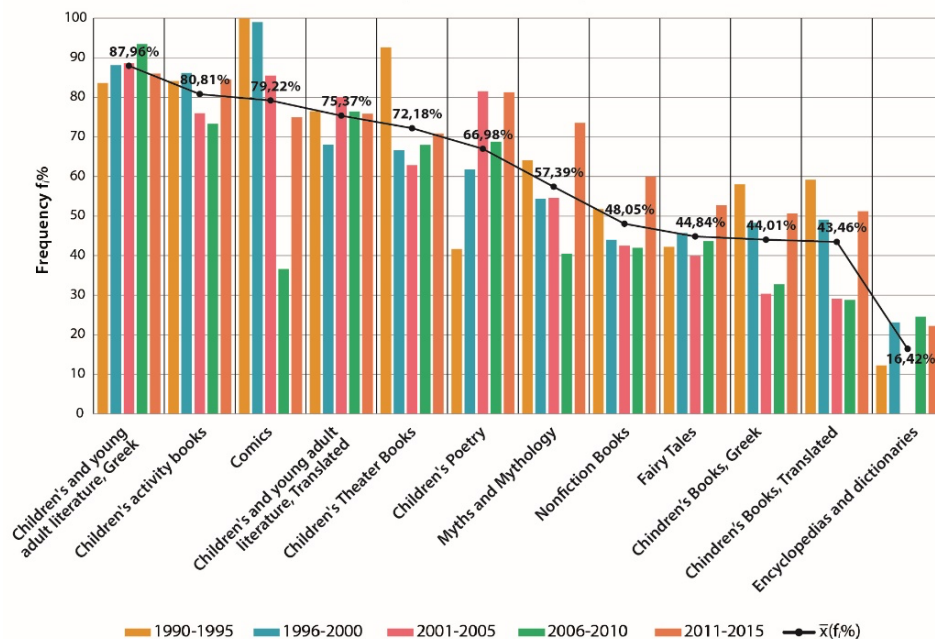

Figure 2: The softcover binding in children's book in Greece (Source: Biblionet)

On the other hand, reference books avoided the soft cover, in 82.66 % of their titles, as unsuitable to keep the knowledge they contained intact over time. The books in the "Encyclopedias and Dictionaries" subject category were used repeatedly, with the child looking at them each time to get the answer to a question. Reference books usually stood on library shelves for longer time periods, and a hardcover protected encyclopedias and dictionaries while giving them an elegant appearance or uniformity in their voluminous works. The hardcover kept the body of the book almost intact, helping the child's smaller hands to hold it while reading or allowing the pages to fully open when placing the book on a surface – with the help of the extra weight of binding. For the above reasons, about half of the books in the subject categories "Children's books, Translated", "Children's books, Greek" and "Fairy tales" preferred to be bound on a hardcover. Numerous preschool books and fairy tales were available in hardcover, providing young children with the necessary help and guidance, as well as the book with the necessary protection from wear and tear. In particular, the compact surface of the front hardcover and the back hardcover supported the reading of rich illustrated books. The hardcover allowed the footer of the book to rest on the reader's body or on a surface,

accepting all the pressure of the contact without the risk of damaging the inner pages of the book. At the same time, its construction prevented a larger than 180° opening, with the pages finding the necessary support from both sides, keeping the visual art of the book in the right place for its pleasure by the reader.

Sometimes the material used on the hard cover was extended to the inside pages of the book to reach even the toddler. The "board book" category carried the rigid cardboard material to the pages of the book, bypassing any rule of the traditional book format. At other times, the special construction of the book was able to incorporate innovative elements, enhancing the reading experience and igniting every sense of the child. In particular, the board book ensured a safe contact with the child, which would not be possible or would soon be disturbed, in the case of reproduction of a codex book. The edges of the paper could cause dangerous abrasions, while at the same time the paper was easily torn by the unconscious treatment of the younger child. The board material reconciled a two-way catastrophic encounter, putting its materiality at the disposal of the reading experience, in order to achieve the early and gradual development of the child's relationship with his book (Figure 3).
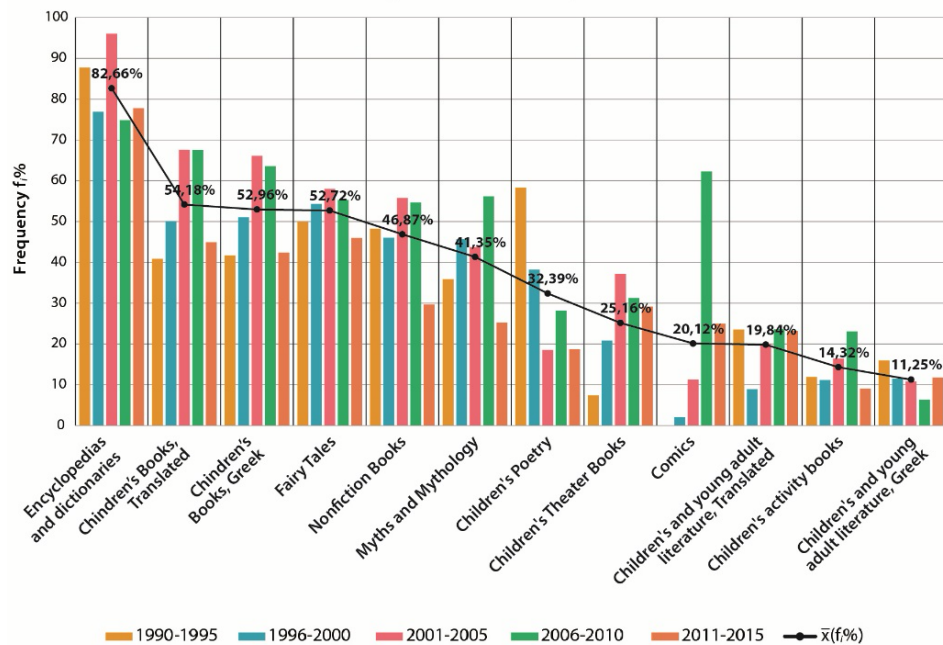

Figure 3: The hardcover binding in children's book in Greece (Source: Biblionet)

In the case of spiral bookbinding, the pages were held in a body with a metal or plastic material. Independence enabled the pages to move in the trajectory of a helical "thread" and to stand parallel, at a distance from each other in a spread. The line of the spine that intersected the narrative space in the other bookbinding methods, turned into a gap that clearly separated the contents of two facing pages, breaking the flow of the content. For this reason, the average frequency of spiral bookbinding was very limited, less than 1 %, in the children's books published in Greece, from 1990 to 2015. The need for independent pages with stickers, stencils and all other kinds of activities, as well as the opening of the pages by 360° and the possibility of detaching individual pages, justified the slightly stronger presence of the spiral bookbinding, only of 3 %, in the books of the subject categories "Children's activities" and "Non-fiction books" (Figure 4).
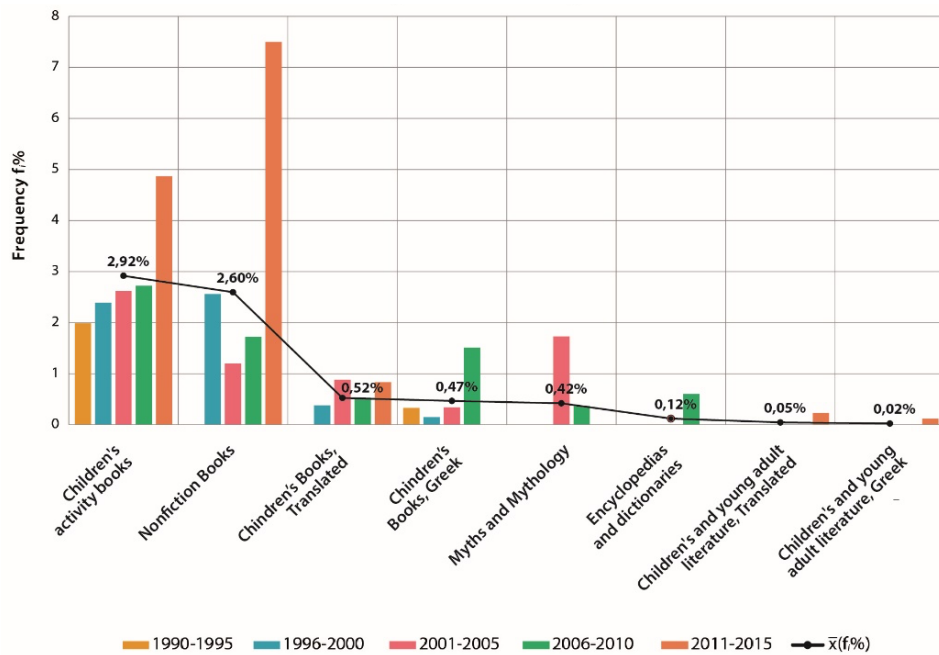
Figure 4: The spiral binding in children's book in Greece (Source: Biblionet)

Since 1990, the usual ratio of the softcover to hardcover children's books was 2:1. However, in 2001, there has been a change in the choice of publishers regarding the format of the children's book, as the frequency curves of softcover and hardcover binding converged for the first time. By 2005, the hardcover binding dominated more than half of the children's books published over a five-year period.

From 2001 to 2010, a large number of illustrated books, under the subject categories "Children's books, Translated" and "Children's books, Greek", led to an exponential growth of hardcover children's books. From 2011 to 2015, the dominance of softcover children's books reached the highest levels of all time. There was also a slight increase in the use of spiral bookbinding, which is consistently the choice for only a small number of children's books (Figure 5 and Table 2).
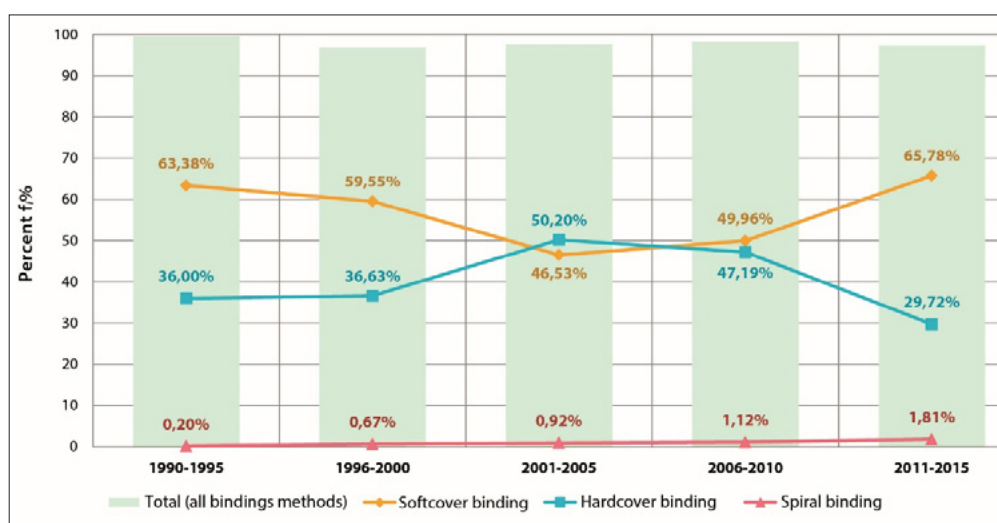

Figure 5: The binding methods used in children's book in Greece

Table 2: The binding methods used in children's book in Greece (Source: Biblionet)

Binding method	1990–1995			1996–2000			2001–2005			2006–2010			2011–2015			Average percent frequency $\bar{x}(f_{i\%})$
	Frequency v_i	Relative frequency f_i	Percent f_i %	Frequency v_i	Relative frequency f_i	Percent f_i %	Frequency v_i	Relative frequency f_i	Percent f_i %	Frequency v_i	Relative frequency f_i	Percent f_i %	Frequency v_i	Relative frequency f_i	Percent f_i %	
	v_1=2.180			v_2=6.682			v_3=9.199			v_4=12.097			v_4=8.301			$\bar{x}(f_{i\%})$
Softcover binding	1382	0.63	63.38	3979	0.60	59.55	4281	0.47	46.53	6044	0.50	49.96	5460	0.66	65.78	57.04
Hardcover binding	785	0.36	36.00	2448	0.37	36.63	4618	0.50	50.20	5708	0.47	47.19	2467	0.30	29.72	39.95
Spiral binding	4	0.00	0.20	44	0.01	0.67	85	0.01	0.92	135	0.01	1.12	150	0.02	1.81	0.94
Total	2171	0.00	99.58	6471	0.97	96.85	8983	0.98	97.65	11887	0.98	98.27	8078	0.97	97.31	

3.2 Other materials

During book history, leather and fabric materials were the usual that adorned the hardcover of books, while paperback appeared much later. From 1990 to 2015, the children's book in Greece presented only a few hardcover books made of leather or fabric – less than 0.1 %, as their decoration was expensive and not as effective as the full color printing of a paper cover. The younger reading audience did not usually appreciate the austerity of an otherwise elegant leather-bound edition, which was more often associated with collectible books and voluminous works.

On the contrary, the board book showed the way of utilizing the materials in adapting the form of the book to the needs and possibilities of the child. A variety of materials enhanced the soft texture feel or added other properties to the book, such as waterproofing. The book made of fabric and plastic sacrificed its usual materiality to reach its reader, as a primary aim to teach him its conventions and to acquaint him with the presence of its modalities. The fabric and plastic pages were turned, crumpled, bitten and left at the disposal of any unconscious treatment of the child, ensuring the safety of both parties. Cloth and plastic material are used to protect the infant from skin injuries or choking, bringing him close to the book from an early age, as part of his daily activities – playing, sleeping or bathing.

4. Conclusions

The softcover, the hardcover and the spiral binding fulfilled a practical and functional role in the children's book in Greece. The pages of the children's book accommodate its verbal and visual mode – as well other modes –, which created their synergetic meaning through the sequential browsing of the pages that have been gathered in one body. In this way, each binding method protects different narrative spaces and directs the child to handle the book in a specific way, guiding him to the reading experience. In general, binding serves the portability of the book, determines its aesthetics and wear resistance, but also affects the cost of the production process and the viability of the publication. However, the strong relationship of each binding method with specific sub-genres of the children's book supports the view that the binding method can also predispose the reader's attitude towards the book, creating ideological extensions for its content.

References

Al-Yaqout, G., 2011. From slate to slate: what does the future hold for the picturebook series? *New Review of Children's Literature and Librarianship*, 17(1), pp. 57–77. https://doi.org/10.1080/13614541.2011.573679.

Ambrose, G. and Harris, P., 2011. *The fundamentals of creative design*. 2nd ed. Lausanne, Switzerland: AVA Publishing.

Bann, D., 2006. *The all new print production handbook*. Mies, Swirzerland: RotoVision.

Beveridge, L., 2017. Chewing on baby books as a form of infant literacy: books are for biting. In: P. Nodelman, N. Hamer and M. Reimer, eds. *More words about pictures: current research on picture books and visual/verbal texts for young people*. London & New York: Routledge, pp. 18–30.

Dimiroulis, D., 2002. *Paralláx: sýmmeikta gia ti logotechnía kai ti glóssa.* Athens, Greece: Psichogios Publications. [In English: *Parallax: literature and language*].

Doonan, J., 1993. *Looking at pictures in picture books*. Stroud, Gloucestershire, UK: Thimble Press.

Gavriilidis, S., 2018. *Ekdótes, vivlía, paidiá*. Athens, Greece: University Studio Press. [In English: *Publishers, books, children*].

Genette, G., 1997. *Paratexts: thresholds of interpretation*. Cambridge, New York & Melbourne: Cambridge University Press.

Higonnet, M.R., 1990. The playground of the peritext. *Children's Literature Association Quarterly*, 15(2), pp. 47–49. https://doi.org/10.1353/chq.0.0831.

McKenzie, D.F., 1981. Typography and meaning: the case of William Congreve. In: G. Barber and B. Fabian, eds. *Buch und Buchhandel in Europa im achtzehnten Jahrhundert, Wolfenbütteler Schriften zur Geschichte des Buchwesens,* 4. Hamburg, Germany: Hauswedell, pp. 81–125.

Oikonomidou, S., 2016. *To paidí píso ap' tis léxeis: o ennooúmenos anagnóstis ton paidikón vivlíon*. Athens, Greece: Gutenberg Publications. [In English*: The child behind the words: the implied reader of children's books*].

Pantaleo, S., 2017. Paratexts in picturebooks. In: B. Kümmerling-Meibauer, ed. *The Routledge companion to picturebooks*. Oxon & New York: Routledge, pp. 73–88.

Yannicopoulou, A.A., 1998. *Apó tin proanágnosi stin anágnosi: odigós gia goneís kai ekpaideftikoús*. Athens, Greece: Kastanioti Publications. [In English: *From pre-reading to reading: a guide for parents and teachers*].

Yannicopoulou, A.A., 2008. *Sti chóra ton chromáton: to sýnchrono eikonografiméno paidikó vivlío.* Athens, Greece: Papadopoulos Publishing. [In English: *In the land of colors: the modern illustrated children's book*].

Combining graphic design and mathematics

Konstantinos Kyriakopoulos, Sofia Strati and Chrysoula Gatsou

University of West Attica, School of Applied Arts & Culture, Department of Graphic and Visual Communication Design
E-mails: kkyriakop@uniwa.gr; sost@uniwa.gr; cgatsou@uniwa.gr

Short abstract

This paper's research objective is to investigate the usefulness of sciences and in particular mathematics, in art. Further, to emphasize that also in arts which is considered an abstract "process" rules, and guidelines play a quite significant role towards the creation of harmony in a part of art. Finally, the purpose of the paper is to reveal the commonly hidden values of science in art and design. For this reason, the paper investigates the way that sciences and in particular mathematics affect or influence art and design. Specific examples are presented such as Golden Ratio, Canon of Polykleitos, Vitruvius Man, Fibonacci sequence, Byzantine art, Layout dimensions with Golden Ratio, The use of Golden Ratio in Typography, Fractals' theory in art. In addition, the significance of the human body dimensions measure of any artistic creation, is presented. In this case, the body dimensions of Greek goddess Aphrodite is analysed.

Keywords: mathematics, design, architecture, golden ratio

1. Introduction

This research paper focuses on the combination of mathematics and art. It is exploring the relation between numerical ratios on one hand, and art and design in general on the other. In addition, it is shown how mathematical proportions between parts of the human body are used as a measure in art. The goddess Aphrodite was the pre-eminent model of such proportions, as rendered by artists during the centuries. People believe that the skills needed to be a designer are not related to mathematics. However, there is a combination between them, in design concepts, such as symmetry, which is based in mathematics as the string that holds together presentation, measuring and angles.

Here is a list of some careers combining art and math skills:
- 3D modelling
- animation
- web design
- product design
- graphic design
- video game design

Common examples that combine mathematics in art and design are presented in further sections.

2. The "Golden Ratio" in Greek art and architecture

The origins of the early western theory of beauty can be found in the works of many early Greek philosophers. Pythagoras and other philosophers from the pre-Socratic period noticed the strong relationship between mathematics and beauty. They observed that objects that were proportionally created, according to the golden ratio, look more attractive. Pythagoras (560–480 BC), the great Greek geometer first studied

and was especially interested in the Golden Ratio, defined as follows: "*A rectangle with golden ratio proportions, with side a greater and side b smaller, when placed next to a square with sides a of length, will produce a similar rectangle with golden ratio, with larger side a + b and smaller a. The reason it offers is expressed in the decimal system as 1.6180339887498948482 ...*" He proved that the proportions between the parts of the human body were based in this Ratio (Figure 1) and it could improve the appearance and functionality in architecture. Pythagoras' discoveries on the proportions of the human figure had a tremendous effect on Greek art. Every part of the major Greek buildings, down to the smallest detail of decoration, was constructed upon this proportion. The sculptor Phidias was the first to use the term *Golden Ratio*. The Greek letter Phi (φ), is used to represent the "Golden Ratio" geometric relation: φ = 1.6180339887498948482 ... (Liu and Sumpter, 2018).

Figure 1: The Venus de Milo statue proportions adheres, strictly to the Golden Ratio (1.6180339887)
(Anon, 2009)

The Parthenon (Figure 2)was designed according to the above mathematical ratio and using the "root five rectangle," a rectangle with an irrational side the square root of 5, became an example of the use of proportion in architecture, like many other Greek temples in ancient Greece.

Figure 2: Parthenon was perhaps the best example of a mathematical approach to art; image taken by Solstad (2005)

Architecture in ancient Greece and in other countries (e.g. in India – Taj Mahal) was based in this principle. Modern research has even introduced the idea that people whose facial features are symmetrical and proportionate according to the golden ratio are considered more attractive than those who do not have mathematical symmetry.
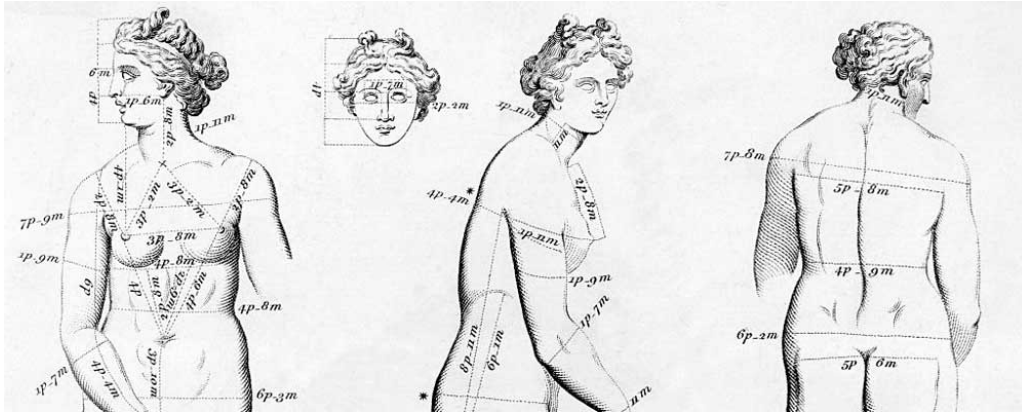
3. Canon of Polykleitos

Figure 3: The canon of Polykleitos and its application to the iconography of Aphrodite, image: Lifejournal.com

Every component of Greek thought translates into a measurable analogy. Pythagoras was the first to give a visible geometric ratio, based on harmonious numbers. Artists then used these harmonious relations based on pure geometric shapes and applied the Golden Ratio in painting, sculpture and architecture, to create dazzling compositions. The first application of the Golden Ratio is credited to Polykleitos, a famous Greek sculptor, widely regarded as one of the fathers of the classic Greek sculpture style (Figure 3). His work is admired in many museums all over the world. His work on symmetry regarding the sculpting of the male form, known as "Canon of Polykleitos", represented his thoughts on aesthetics and artistic perfection. It is a male figure proportions model in the upright posture (Meisner and Araujo, 2018).

He believed that all parts of the body appearing in a sculpture should be clearly distinct from one another, and proportioned using mathematics. For example, the size and proportion of the first knuckle of the little finger would be the basis for the proportions of the rest of the fingers, the finger would be the basis of the proportion of the palm of the hand, and so forth. The tip of the finger was used as a square unit of measurement. Nude as a measure in art, projects mathematical proportions that accurately determine perfection of the work and consequently beauty. His work in determining the best ways to reach a perfect balance in sculpture is still influential today. In fact, his son, grew up to be a famous architect, influenced by his father's work on proportion. Many artists followed that rule over the centuries obsessed with the numerical perfection of human proportions (Moon, 1995).

4. Vitruvius
The Roman Vitruvius (80 BC – 15 BC) in his ten books entitled "De Architectura" described architectural rules based on human sizes. In his third book, Vitruvius states that temples must be constructed using the proportions of the male body which is a model of proportion.

The most elaborate image of all, Como Vitruvius, painted by Cesarino in 1521, depicts an ugly male figure with a very small head and very large legs (Figure 4).
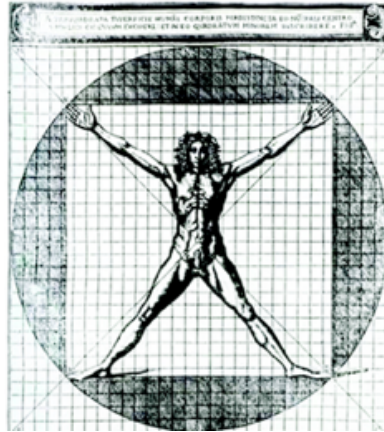
Figure 4: Homo ad circulation and ad quadratum by C. Cesarino in The Ten Books of Vitruvius Architecture (Vitruvius Polio, 1521)

The next architect after Vitruvius, who describes the rhythms in architecture following the same point of view was Leon Batista Alberti (1452 AD). He theoretically connected the proportions of a geometric shape, a musical scale or a mathematical sequence, and formed the background of architectural theory in his "Ten Books of Architecture". He sought harmonious rules in his architectural works and correlated the harmonic proportions in geometry, in numbers and in the harmony of music, with those of the human body.

The rule of the golden ratio was applied also in music, which gave amazing results based on the Fibonacci sequence, rooted in the same proportion (Clark, 1956).

5. Fibonacci sequence

In the following sequence of numbers 0, 1, 1, 2, 3, 5, 8, 13, 21, 34, 55... the pattern is a Fibonacci sequence (Figure 5). When these numbers are translated into shapes various patterns emerge including spirals, flowering, and branching. Once the Fibonacci sequence was discovered, these numbers were divided back to as close to zero as they could, in order to form the golden ratio, basis of the following shape which is the template for the perfect spiral.

Spirals, appear quite frequently in design (Figures 6 and 7). Arranged in other ways, Fibonacci numbers form the basis of stars and many other geometric shapes. Even the human face closely follows this pattern. Historical architecture such as the Pyramids and the Parthenon, if one examines them closely, also contain the Fibonacci sequence (Gary, 2018).
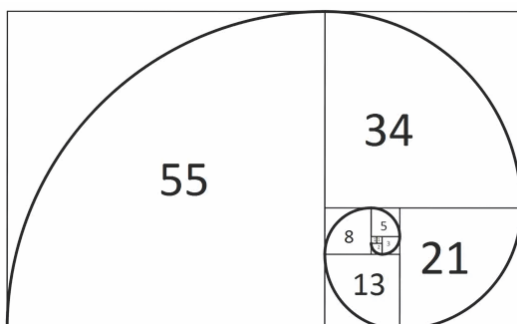

Figure 5: The Fibonacci sequence

Figure 6: The Golden Number, Rectangle, Ratio, and Spiral in Boticelli's The Birth of Venus Composition 1.618 (Botticelli, n.d.)

Figure 7: Golden ratio staircase inside the Vatican, Vatican Museum: Golden Ratio offers a unity of science (Vatican Museums, 2021)

6. Renaissance

The artist who renders the forms must not ignore the elements of the human body. Michelangelo, an artist and pioneer in the performance of nudity, uses the term "Dipendenza" to express the relationship between form and ratio. This is understandable if one examines the change in the ratio observed between the Greek and the Gothic idea in the performance of the female body. A constant measure of comparison is the distance between the breasts, but also the distance from the lower part of the chest to the navel and from there to the division of the legs. These proportions are reverently observed in all forms of the classical era and in most of their imitations until the 1st century (Clark, 1956).

Da Vinci is very well known for the incorporation of the golden ratio into his work (Figure 8). In order to fit the body in a circle, the body must be in a posture with the legs outstretched so that it is one-fourteenth smaller than if they were together.
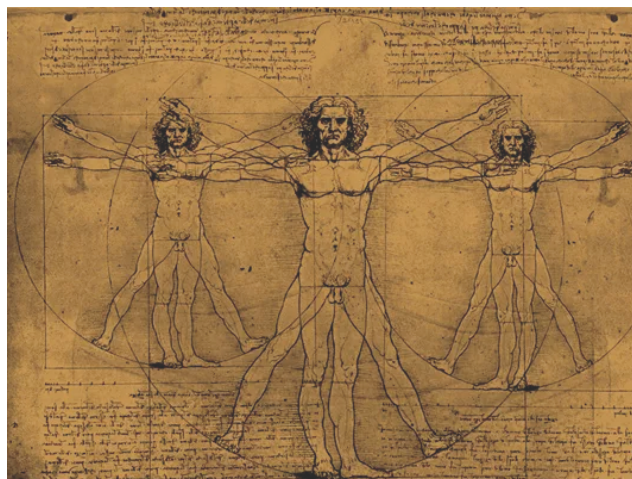
Figure 8: Leonardo Da Vinci famously incorporated the golden ratio into his work (Henryson, 2015)

Examining the drawing one can see that the combination of the position of human arms and legs can create sixteen different postures. The posture with the arms outstretched and the legs together is inscribed in the square. The posture with the arms slightly raised and the legs open is inscribed in the circle. This illustrates the theorem that when alternating between two positions, the apparent center of the figure appears to be moving, but in reality the navel of the figure which is the actual center of gravity remains stationary.

The re-discovery of the mathematical proportions of the human body in the 15th century by da Vinci and others is considered one of the great achievements that led to the Italian Renaissance. Da Vinci's design combines a careful reading of the ancient text with his own observations of true human bodies. When designing the circle and the square he rightly observed that the square may not have the same center as the circle, at the navel, but somewhere lower in the anatomy. This arrangement is a novelty in da Vinci's design and sets it apart from previous illustrations.

The design itself is often used as an implied symbol of the essential symmetry of the human body, and by extension the Universe as a whole.

Da Vinci applied perfect proportions to many of his works, including the *"Mona Lisa"* and *"Leda with the Swan"*, as well as his famous *"Vitruvius man"* and overall in his *"Aphrodite".*

Figure 9: The Man of Vitruvius, Leonardo da Vinci, 1490 (Serious Puzzles, 2021)

Figure 10: Hans Memlinc, Eve, from collection of Museum of History and Art, Vienna (Memlinc, 1485)

The large frescoes in the churches, the paintings and the statues, during the Renaissance, the imposing temples were achieved thanks to the studies of perspective and its mathematical formulation. Durer's engraving, known as Nemesis or Large Fortune was made in 1501 (Gobrich, 2003). The artist had studied Vitruvius and applied his methods. His work is characterized by his dedication to the ancient forms that he associated with his system. The squares and circles he used in his works were influenced from the classical proportions, applications from the memories of Apollo Belvedere and Medici Venus, figures that were "perfected in his mind" by carefully examining the beautifully formed bodies of Greek sculpture. Artists or writers of art who took seriously the ancient copies of naked Aphrodite came to the conclusion that there was a basis of construction stated in terms of measurement.

In order to highlight the difference, it is worth making a reference to a typical 15th century Gothic nude, a work by Memlinc in Vienna (Figure 10), in which the basic shape remains oval, but the oval has inflated incredibly, and the "spheres" are rendered extremely small. The distance between the breasts is narrow, the navel is exactly twice the body than in the classic shape. The great elongation of the body becomes more noticeable because the extended surface does not have any ribs or muscles. Gothic nudity is commonly referred to as "naturalistic", but in Memlinc Eve the artist's goal was to produce the form that would meet the ideal of beauty of his time, the kind of shape that men admired.

The same elongation happens in typography in Byzantine curves, in Hagia Sophia, Gothic (oblong) etc. In Figure 11 an example from the mediaeval illuminated manuscript is presented.

Figure 11: The Garden of Eden from the Très Riches Heures du duc de Berry,
illustrated by Limbourg brothers in 1405–1409, photo by R.M.N. / R.-G. Ojéda (Galagher, 2016)

7. Layout dimensions with Golden Ratio

The term "layout" in web design or graphic design is used to describe the arrangement of visual elements on a page and organizing the art composition to achieve specific communication objectives. The Golden Ratio rule can be used to define the widths of panels, sidebars or even height of the views (Figure 12). For example, a layout with 96 cm width requires height of 59 cm, because 96 dividing by 1.618 equals 59.
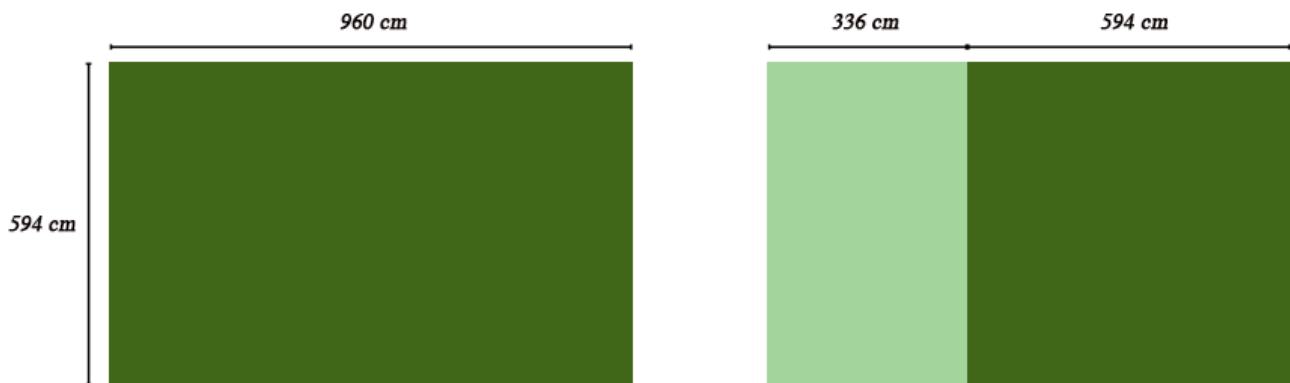

Figure 12: Layout using Golden Ratio

Defining spacing between content is usually done by standard padding and margin to define the gutters and spacing between the content blocks irrespective of what the layout sizes are. Managing these positive spaces or negative spaces often define the final result. However, one can make use of golden ratio to ensure that the inter-layout spaces are proportional and calculated.

8. The use of Golden Ratio in typography – Icon/Logo

Golden ratio can be used as a guide to determine the optimal sizes of different text hierarchies in graphic design (Figure 13). In a body text of 10 px, the heading text size can be 16 px (10 multiplying by 1.618).
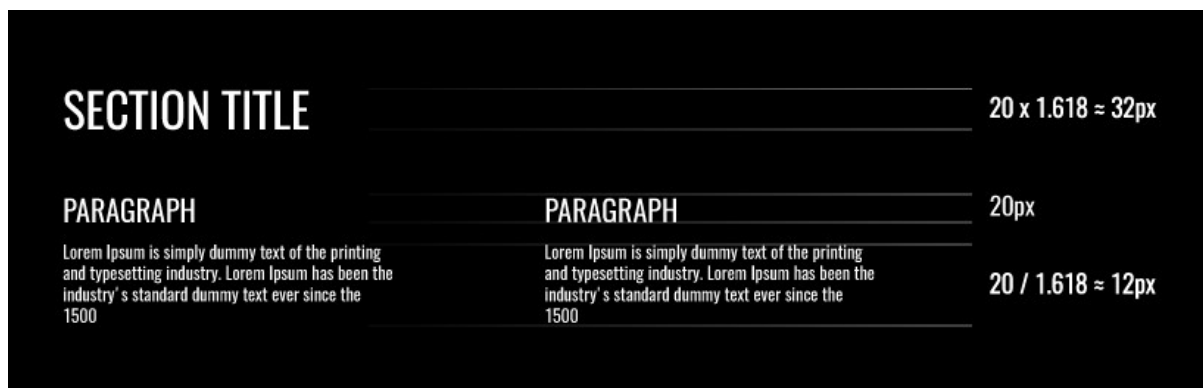
Figure 13: Golden Ratio in typography (CourseHero.com, n.d.)

Designers use shapes like triangles, squares, circles to create an icon or a logo. Using the golden shapes properly, a designer can harness balance that can turn a good layout into a great one (Figure 14).
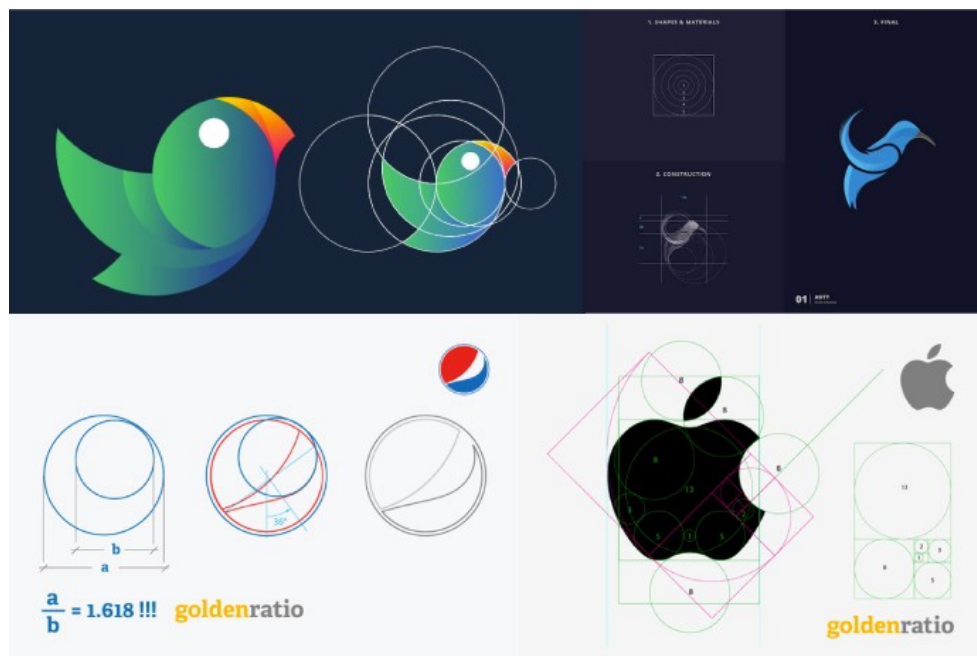

Figure 14: Images taken from Google for illustration purposes that (arguably) use the golden ratio

Even if designers do not use mathematics in their creations, the result in their work reflects the use of mathematics, such as geometric proportions, symmetry, balance, correct use of positive and negative space. You can also notice that the correct use of the text, readable in plenty of white space, means the use of mathematics.

9. Fractals

Fractals (fractus or fractio) are repeating geometric patterns combined to a form that can be noticed regardless of scale. Its two basic characteristics are: similarity and non-integral dimension. Similarity examples are the "Cantor powder" (Figure 15) and the "Van Koch" curve (Figure 16). Fractals can be created via mathematics, but can also appear in nature e.g. leaves, snowflakes, geological structures, and ice crystals (Panagopoulos, 2014; Field and Golubitsky, 1992). Designers use fractals in many cases from clothing design to website backgrounds (Figure 17).
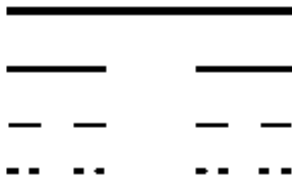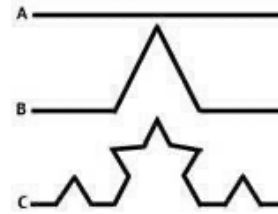
Figure 15: Cantor powder
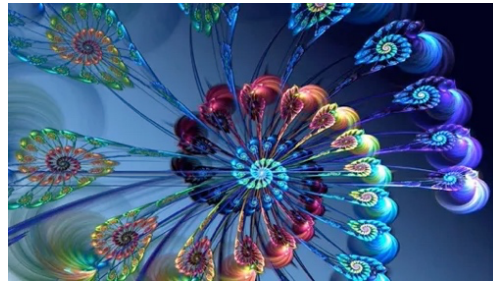

Figure 16: Van Koch curve

Figure 17: Fractals are mathematical sequences (Peacock Digital, 2021)

10. Conclusion

Mathematics coexists with art and design because the human brain appreciates and understands consistency. Natural balance and visual harmony are brought in by the use of golden ratio in artistic composition, thereby giving an undeniable aesthetic appeal. Pythagoras developed the theory of proportions expressed by the relation φ = 1.6180339887498948482 .... This is the relation that defines the golden ratio. The Canon of Polykleitos and the mathematical analogies of the ancient Greeks were used by the artists of the classical period who created works of unparalleled aesthetics and perfection. Aphrodite of Milos complies with these exactly rules of mathematical proportions. This rule of proportions was studied in the Roman period by Vitruvius. It was also adopted by Renaissance artists, offering works of high aesthetic value. The proportions of the human body are the measure of any artistic creation, determining the form and style of art works and a part of our society's cultural identity. Thus, the disproportions observed in the depictions of the naked body by Gothic artists are observed in gothic architecture, as well as in their alphabet. A common feature of all, the narrow and elongated rendering of the form. Something similar can be seen in the architecture and also in the typography of Byzantines where the curve, indicative of their culture, dominates. The Golden Ratio is a tool that every designer should use. This combination is common in the iconography of Aphrodite, where it is usually applied. It is for this reason, that symmetry, balance, and proportion are such important parts of a design. The results will likely be more aesthetically pleasing as well as being easier to use.

It is also why patterns frequently appear in art and design. Fractals are patterns that exist in nature. A graphic design or a website that seems to be troubling to look at, that means that the designer failed in one of these areas. It is one thing when this is done deliberately, e.g. painting something that lacks symmetry for effect. Unfortunately, when it is simply the result of poor execution, it becomes problematic.

References

Anon., 2009. *Posts tagged 'golden ratio'*. [online] Available at: <https://canukeepup.wordpress.com/tag/golden-ratio/> [Accessed February 2021].

Botticelli, S., n.d. *The birth of Venus*. Uffizi, Florence. [online] Available at: <https://en.wikipedia.org/wiki/The_Birth_of_Venus> [Accessed February 2021].

Clark, K., 1956. *The nude: a study of ideal art*. London, UK: The reprint Society, pp. 12–14, 207.

CourseHero, n.d. *Question: Search the internet regarding "Golden Ratio"*. [online] Available at: <https://www.coursehero.com/tutors-problems/Math-Other/28100491-Search-the-internet-regarding-Golden-Ratio-Explain-its-history-sig/> [Accessed February 2021].

Henryson, M., 2015. The math that every designer needs to know. *Creative bloq*, [blog] 2 October. Available at: <https://www.creativebloq.com/design/math-every-designer-needs-know-91517049> [Accessed February 2021].

Field, M. and Golubitsky, M., 1992, *Symmetry in Chaos: a search for pattern in mathematics, art and nature*. New York and London: Oxford University Press.

Galagher, P., 2016. The Limbourg Brothers beautiful illustrations for 'Très Riches Heures du Berry' 1416. *Flashbak* [blog], 29 February. Available at: <https://flashbak.com/the-limbourg-brothers-beautiful-illustrations-for-tres-riches-heures-du-berry-1416-56244> [Accessed February 2021].

Gobrich, E., 2003. *To chronikó tis téchnis*. Athens, Greece: National Bank Educational Foundation, p. 224. [In English: *The chronicle of art*].

Liu, Y. and Sumpter, D., 2018. Is the golden ratio a universal constant for self-replication? *PLoS ONE*, 13(7): e0200601. https://doi.org/10.1371/journal.pone.0200601.

Meisner, G. and Araujo, A., 2018*. Golden ratio: the divine beauty of mathematics.* Caracas: Race Point Publishing, pp. 73–79, 83–85, 151–153.

Memlinc, H., 1485. *Adam and Eve (detail).* [painting, triptych] GG_939, Kunsthistorisches Museum, Vienna.

Moon, W.G. ed., 1995. *Polykleitos, the Doryphoros, and tradition*. Madison, WI, USA: The University of Wisconsin Press, pp. 26–28.

Panagopoulos, M., 2014. Fractal.Téchnes kai epistímes mazí. *Fractal: geometría ton ideon,* [blog] 11 July. Available at: <https://www.fractalart.gr/fractal-τέχνες-και-επιστήμες-μαζί-2/> [Accessed February 2021]. [In English: Fractal. Arts and sciences together]*.

Peacock Digital, 2021. *Peacock digital painting 5D DIY paint by Diamond kit*. [online] Available at: <https://originalpaintbydiamond.com/products/5d-diy-diamond-painting-colors-fluorescent-flower-full-square-diamond-embroidery-flower-kits-pictures-of-crystals-home-deocr-xsh-26> [Accessed February 2021].

Serious Puzzles, 2021. *Da Vinci: Vitruvian man*. [online] Available at: <https://www.seriouspuzzles.com/jigsaw-puzzles/by-theme/art/da-vinci/> [Accessed February 2021].

Solstad, O., 2005. *Parthenon*. [image online] Available at: <https://www.flickr.com/photos/brandnewbrain/8704717> [Accessed February 2021].

Vatican Museums, 2021. *Vatican Museums virtual tour*. [online] Available at: <https://joyofmuseums.com/museums/europe/italy-museums/rome-museums/vatican-museums/> [Accessed February 2021].

Vitruvius Polio, M., 1521. *De Architectura libri Dece*. Como: Gottardo de Ponte. [In English: *The teen books on architecture*].

6B

K. Abdel Aal, M. Ailinger and N. Willenbacher: The influence of the pastes' slip and wetting properties on the printing …

The influence of the pastes' slip and wetting properties on the printing of fine features in flatbed screen printing of silicon solar cell metallization

Karim Abdel Aal, Max Ailinger and Norbert Willenbacher

Karlsruhe Institute of Technology (KIT)
E-mails: karim.abdelaal@kit.edu; max.ailinger@partner.kit.edu; norbert.willenbacher@kit.edu

Short abstract

The decreasing width of printed lines in the front side metallization of silicon solar cells requires carefully tailored silver pastes. Recent development of a highspeed video imaging system for monitoring the screen printing process enables basic research to identify how different rheological and wetting properties of the paste affect fine-line printing. An in-depth understanding of these phenomena will facilitate further paste development utilizing established and innovative formulation concepts. In the presented study different pastes have been developed varying only in their slip velocity and wetting to the substrate, whereas other rheological paste parameters are kept in a narrow range. The slip velocity is determined using a rotational rheometer, whereas the contact angle of the vehicle system to the substrate characterizes the wetting behaviour of the paste. Printing trials with these pastes utilizing high speed video imaging during printing together with a subsequent laser scanning microscopy analysis of the printed lines allows to identify the influence of the varied parameters on the paste spreading during printing and the overall paste transfer. Based on the gained insights guidelines for the development of advanced solar cell metallization pastes will be suggested.

Keywords: solar cell metallization, paste formulation, fine feature printing, flatbed screen printing

1. Introduction and background

In silicon solar cell front side metallization, it is of utmost importance to be able to print fine lines in the low micron range with a high aspect ratio in order to minimize shading losses (Yüce, König and Willenbacher, 2018; Aleem, et al., 2019)rheology and screen-printed line morphology is essential. Three model pastes with similar silver content and corresponding vehicles differing in their thixotropic agent content were investigated. Rheological properties (yield stress, viscosity, wall slip velocity, structural recovery, and fracture strain. Due to high printing speeds and the robustness of the process, flatbed screen printing is widely used in the printing of solar cell front side contacts and has been adopted by the industry (Tepner, et al., 2020). During the last couple of years research pushed the printable line width down in the range of 30 to 20 μm while current efforts aim at pushing the limit even further (Clement, et al., 2019). Printing these feature sizes demands careful adjustment of the metallization paste properties. However, in most published studies, pastes differing in various parameters at the same time usually induced by creating a variation through means of adding a thinner are printed and the final printing result is evaluated. Other research focuses on improving the print results through the modulation of the slip properties by applying different screen coatings or changing the screen layout (Ney, et al., 2019; Tepner, et al., 2019). Since most pastes are developed in industry, the scientific research published on the influence of different paste constituents or paste rheological and wetting properties is very limited. The silver pastes are based on organic solvents and use rheology control additives like thickeners or thixotropic agents to modify the flow properties (Yüce, König and Willenbacher, 2018)rheology and screen-printed line morphology is essential. Three model pastes with similar silver content and corresponding vehicles differing in their thixotropic agent content were investigated. Rheological properties (yield stress, viscosity, wall slip velocity, structural recovery, and fracture strain. There is a lack of fundamental understanding about what is happening dur-

ing the printing process and how this is affected by the paste rheology as well as its wetting of the screen and substrate. To close this gap of knowledge, recently conducted studies used highspeed camera setups to disclose the mechanisms making up the printing process (Abdel Aal and Willenbacher, 2020). Continuing this approach will make it possible to identify the relevant rheological paste parameters for optimized screen printing. A clearly identified target range for the relevant paste parameters facilitates further paste development using conventional or innovative formulation approaches. Therefore, in this study different front side metallization pastes have been developed differing solely in their wetting and slip properties while maintaining the other rheological paste properties constant. Pastes varying in those parameters are formulated, rheologically characterized and printed. The printed structures and the videos monitoring the paste transfer during printing are analysed and discussed. This will show the influence of the varied parameters on the printing process in detail, and particularly on the overall paste transfer, the printed line height uniformity and the number of defects as for example line interruptions.

2. Materials and methods

2.1 Paste chemistry

The vehicles of the pastes are based on commonly used solvents for the formulation of front side metallization pastes, inter alia, Texanol, Terpineol, Benzyl alcohol and Triacetin. The pastes contain the particles Processed Silver Powder K7418P (Metalor Technologies) and lead-free glass frit PSGS-2016 (BASS Co., Ltd.) with a total volume fraction of 48 vol.% corresponding to 90 ± 1 % mass fraction. To modify the paste's rheology the typical additive Thixatrol Max (Elementis Specialties, Inc.), based on castor oil derivatives, and a mixture of short and long chain polymers, e.g. various molecular weight grades of ethyl cellulose are used. Paste preparation followed the typical route of speed mixing and subsequent three roll milling similar to the procedure described in (Yüce, et al., 2019). The slip velocity is derived from video assisted measurements on a rotational rheometer at a constant shear stress of 350 Pa using steel rheometer plates. The procedure is identical to the one described in (Xu, Fieß and Willenbacher, 2017). The fracture strain in uniaxial elongational deformation is measured using a tensile testing machine at a separation speed of 10 mm/s. The elongational deformation is monitored using a highspeed camera and the break-up distance is determined from image analysis.

2.2 Printing

Printing was done on a modified Ekra E2 lab scale printer equipped with an EoSens Mini1 highspeed camera to capture the printing process with high temporal and spatial resolution. The camera is equipped with a customized adapter containing a Nikon "LU Plan ELWD 20x/0.4A" objective to allow for the necessary magnification while taking pictures at 1000 frames per second. The printing setup comprises a diamond squeegee and screens (430-13/17" combination screen (synthetic material & steel) fabric, 22.5° mesh angle and 9 ± 1 μm EOM). The nominal line width of the test pattern is 30 μm. The varied parameters are the squeegee pressure (49 to 98 N/cm), the squeegee speed (200 to 400 mm/s) and the snap off distance (1 to 3 mm). The lines are printed on transparent glass (Soda-lime glass, Theodor Schmid GmbH, Karlsruhe, Germany) substrates similar as described in Abdel Aal and Willenbacher, (2020) study. The percentage of interruptions in the printed lines as well as the resulting line width and height was determined by laser scanning microscopy using a VK-X100 3D Laser Microscope (Keyence).

3. Results and discussion

Following the formulation and characterization of the pastes, the printing properties were tested in printing trials at different printing parameters. The number of line defects like interruptions and the variation in wet line height and width was evaluated based on laser scanning microscopy. The number of interruptions can be seen as a measure for the line quality since interruptions prevent the current flow and thereby create dead areas on the solar cell surface, leading to a huge loss in efficiency. The cross-sectional area of the line (width x height) can be taken as a measure for the overall paste laydown which is supposed to be maximized to deposit enough material to achieve a low resistance. At the same time a high aspect ratio (width / height) is desired to minimize the shadowed area, which cannot generate electricity. In this abstract, the rheological paste characterization, the line quality and the paste laydown will be discussed. In the end a qualitative outlook on what can be learned in terms of paste spreading by analysing the high-speed videos is given.

3.1 Rheological paste characterization

A number of different pastes have been developed, which can be classified as follows: In series A the wetting of the vehicle system and thereby its slip velocity on steel plates is varied over a wide range between 0,07 and 2,7 mm/s. Paste B shows no slip at an applied shear stress of 350 Pa, but poorer wetting of the substrate compared to paste A3. Since the slip velocity at 350 Pa is 0 mm/s, paste B is not shown in Figure 1a. An overview of the slip and wetting properties is shown in Figure 1, whereas the other parameters are summarized in Table 1. The viscosity ($\eta_{solvent} \approx 0{,}02$ Pa·s, $\eta_{10} \approx 81$ Pa·s), the yield stress (≈ 615 Pa) and fracture strain ($\varepsilon \approx 5$) are essentially kept constant.
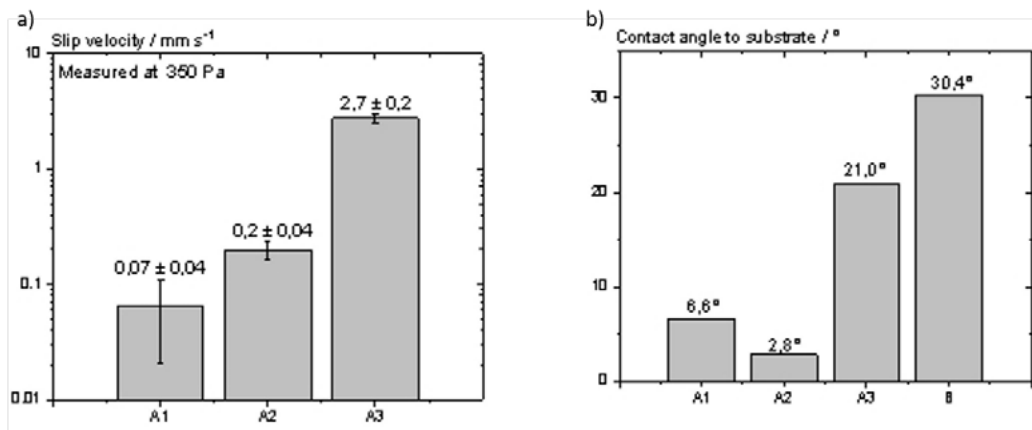

Figure 1: Pastes slip velocity values for paste series A and wetting of the glass substrate for paste series A and paste B

Table 1: Formulated paste properties kept in the same range

Pastes	Pure Solvent Viscosity 25°C / Pa·s	Low Shear Viscosity (10 s⁻¹) / Pa·s	Yield Stress / Pa	Fracture strain / -
A1	0.043	100 ± 14	605 ± 53	6.3 ± 0,4
A2	0.015	71 ± 4	774 ± 37	4.7 ± 0,7
A3	0.006	85 ± 4	443 ± 27	4.2 ± 0,6
B	0.018	69 ± 1	637 ± 20	3.8 ± 0,4

3.2 Line quality

Figure 2 shows the fraction of interruptions versus the slip velocity. Obviously, the fraction of interruptions is decreasing with increasing slip velocity of the paste. This finding indicates, that high slip facilitates filling of the mesh during the printing process. This is particularly important, where there are wire crossings in the pattern, since those areas are prone to mesh marks or interruptions when printing features in the low micron range. Printing with an intermediate speed of 300 mm/s did lead to fewer interruptions. This indicates that optimizing the printing speed is crucial for the creation of interruption free lines in solar cell manufacturing.
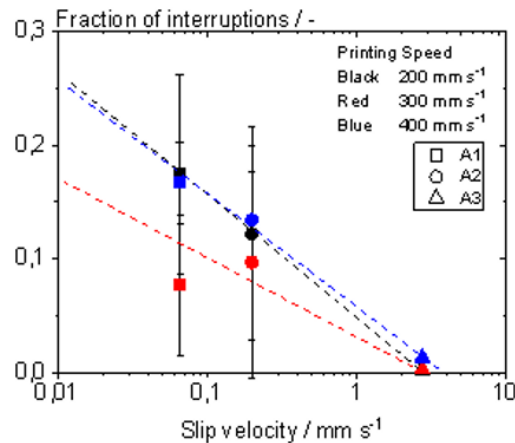

Figure 2: Fraction of interruptions in the printed lines versus slip velocity of the applied paste

3.3 Paste transfer

In Figure 3 the cross-sectional area of the printed lines as a measure of the overall paste laydown is shown versus the slip velocity and the wetting of the substrate by the applied paste.
Previous studies which did not consider the wetting of the paste to the substrate lead to the anticipation that achieving a higher paste laydown can be correlated with an increased slip velocity (Durairaj, et al., 2010; Zhou, et al., 2017). Contrary to expectations we did not find such a correlation here. Instead, we found a very clear correlation showing that an increased paste laydown is achieved for pastes showing a better wetting of the substrate. Investigating the width and the height of the printed features separately showed that the line height increases strongly with the pastes wetting of the substrate, while the width is not affected. The observed effect is more pronounced at lower printing speed.
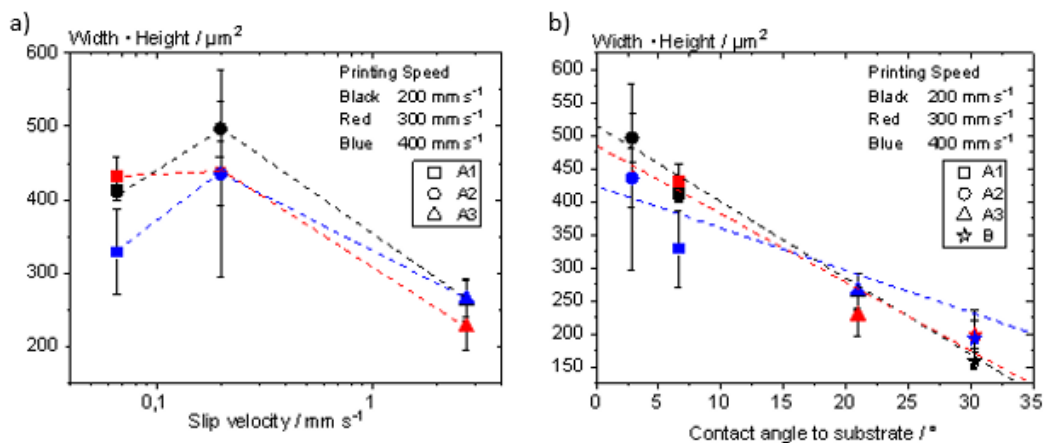

Figure 3: Width x Height as a measure for the total paste laydown versus the slip velocity (a)
and the contact angle to the substrate (b)

A better wetting might lead to an increased counteracting force pulling the paste out of the pattern, while the screen is snapping off. This in turn facilitates the emptying of the screen and enables a higher paste transfer. The finding indicates that the applied solvent chemistry has to be carefully matched to the targeted substrate when formulating the paste in order to achieve best printing results.

3.4 Paste spreading

The paste spreading and retraction behavior during the printing process was monitored and evaluated based on the analysis of the videos. An example of the paste spreading during the cling period is shown in Figure 4 for a paste A1 and paste A3, videos were taken for the same printer settings (300 mm/s printing speed, 2 mm snap off, 74 N/cm squeegee pressure). As can be seen in Figure 4, the spreading of paste A3 directly beneath the squeegee during printing is significantly more pronounced than with paste A1. An analysis of the printed lines reveals differences in the achievable line width. Line A1 has a width of 39.21 ± 1.24 μm, while A3 ends up at 47.99 ± 4.64 μm at a nominal screen opening width of 30 μm. These differences are due to the spreading that already occurs during the squeegee passage while printing and lead to the formation of wider lines despite the poorer wetting of the A3 solvent to the substrate. With regard to the achievable line height, comparable values are measured for both pastes A1 is 11.47 ± 0.64 μm and A3 is 10.84 ± 0.90 μm (9 ± 1 μm EOM). However, there are major differences in the percentage of interruptions. While the lines of paste A1 have 14.19 ± 1.85 % interruptions for the printing parameters given here, paste A3 has 0 % interruptions. The measured values indicate that the paste, which is characterized by an increased slip velocity, can be pressed through the mesh more easily. The consideration and targeted adjustment of paste slip is therefore essential in the design of screen-printing pastes, especially for the printing of ultra-fine features.

Further results of the printing experiments and video analysis will be discussed in order to elucidate the role of wall slip, i.e. wetting of screen and substrate as well as paste cohesion on the quality of the printed lines and the influence of paste spreading and retraction during the printing process. The difference that results when varying the different print parameters is also discussed.
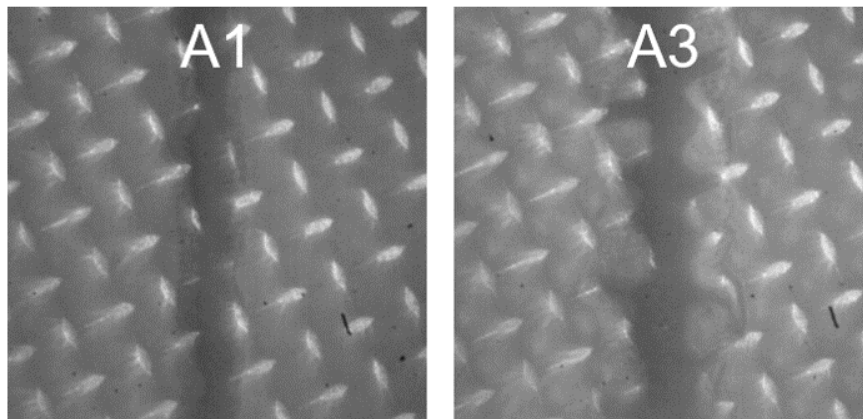

Figure 4: Example of paste spreading as revealed via highspeed video analysis during printing of different metallization pastes

4. Conclusions

The presented study shows how a variation in the wetting properties of the paste isolated from the other rheological paste properties affect the final print result. Line quality in terms of the avoidance of line interruptions is strongly affected by the pastes slip velocity facilitating the filling of the mesh during printing. The overall paste transfer is contrary to expectations not dominated by the pastes slip velocity but by its

wetting of the substrate. The gained insights indicate, that the wetting to the substrate plays a crucial role in order to achieve high lines, while the final line width is not affected. Slip velocity and wetting of the involved surfaces has to be carefully considered when choosing the solvents for formulating the pastes vehicle system. These insights will facilitate further front side metallization paste development for fine-line printing in the low micron range.

References

Abdel Aal, K. and Willenbacher, N., 2020. Front side metallization of silicon solar cells – a high-speed video imaging analysis of the screen printing process. *Solar Energy Materials and Solar Cells*, 217: 110721. https://doi.org/10.1016/j.solmat.2020.110721.

Aleem, M., Karuppanan, K.K., Raghu, A.V., Satheesan, N., Krishnan, B. and Pullithadathil, B., 2019. Optimal design of narrow line-width front contact grid pattern for silicon solar cells and low-cost fabrication of electroless nickel plated imprint lithography hard stamp. *Advanced Engineering Materials*, 21(12): 1900734. https://doi.org/10.1002/adem.201900734.

Clement, F., Linse, M., Tepner, S., Wengenmeyr, N., Ney, L., Krieg, K., Lorenz, A., Pospischil, M., Bechmann, S., Oehrle, K., Steckemetz, S. and Preu, R., 2019. "Project FINALE" - screen and screen printing process development for ultra-fineline contacts below 20μm finger width. In: *Proceedings of the 36th European Photovoltaic Solar Energy Conference and Exhibition*. Marseille, France, 9–13 September 2019. pp. 255–258. https://doi.org/10.4229/EUPVSEC20192019-2DO.5.1.

Durairaj, R., Man, L.W., Ekere, N.N. and Mallik, S., 2010. The effect of wall-slip formation on the rheological behaviour of lead-free solder pastes. *Materials and Design*, 31(3), pp. 1056–1062. https://doi.org/10.1016/j.matdes.2009.09.051.

Ney, L., Tepner, S., Wengenmeyr, N., Linse, M., Lorenz, A., Bechmann, S., Weber, R., Pospischil, M. and Clement, F., 2019. Optimization of fine line screen printing using in-depth screen mesh analysis. In: L. Tous, G. Beaucarne, G. Schubert and J. Hoornstra, eds. *AIP Conference Proceedings 2156: Proceedings Of The 8th Workshop On Metallization And Interconnection For Crystalline Silicon Solar Cells*. Konstanz, Germany, 13–14 May 2019. https://doi.org/10.1063/1.5125871.

Tepner, S., Wengenmeyr, N., Ney, L., Linse, M., Pospischil, M. and Clement, F., 2019. Improving wall slip behavior of silver pastes on screen emulsions for fine line screen printing. *Solar Energy Materials and Solar Cells*, 200:109969. https://doi.org/10.1016/j.solmat.2019.109969.

Tepner, S., Ney, L., Linse, M., Lorenz, A., Pospischil, M. and Clement, F., 2020. Studying knotless screen patterns for fine-line screen printing of Si-solar cells. *IEEE Journal of Photovoltaics*, 10(2), pp. 319–325. https://doi.org/10.1109/JPHOTOV.2019.2959939.

Xu, C., Fieß, M. and Willenbacher, N., 2017. Impact of wall slip on screen printing of front-side silver pastes for silicon solar cells. *IEEE Journal of Photovoltaics*, 7(1), pp. 129–135. https://doi.org/10.1109/JPHOTOV.2016.2626147.

Yüce, C., König, M. and Willenbacher, N., 2018. Rheology and screen-printing performance of model silver pastes for metallization of Si-solar cells. *Coatings*, 8(11): 406. https://doi.org/10.3390/coatings8110406.

Yüce, C., Okamoto, K., Karpowich, L., Adrian, A. and Willenbacher, N., 2019. Non-volatile free silver paste formulation for front-side metallization of silicon solar cells. *Solar Energy Materials and Solar Cells*, 200: 110040. https://doi.org/10.1016/j.solmat.2019.110040.

Zhou, Y., Tong, H., Liu, Y., Yuan, S., Yuan, X., Liu, C., Zhang, Y., Chen, G. and Yang, Y., 2017. Rheological effect on screen-printed morphology of thick film silver paste metallization. *Journal of Materials Science: Materials in Electronics*, 28(7), pp. 5548–5553. https://doi.org/10.1007/s10854-016-6219-1.

The effect of halftoning on the appearance of 3D printed surfaces

Fereshteh Abedini, Sasan Gooran and Daniel Nyström

Media and Information Technology Division, Department of Science and Technology, Linköping University, Norrköping, Sweden
E-mails: fereshteh.abedini@liu.se; sasan.gooran@liu.se; daniel.nystrom@liu.se

Short abstract

Managing the final appearance of 3D surfaces is an interesting and essential topic in 3D printing applications. Knowledge about the parameters which influence the 3D surface reproduction quality enables engineers to achieve the final appearance as accurately as designed. Many studies have been conducted to explore numerous parameters that affect the quality of 3D surface reproduction. This work contributes to verifying the role of halftoning in increasing the 3D surface visual quality and the control over the surface appearance of a 3D printed object. The results show that applying different halftones according to the geometrical characteristics of the 3D surface could emphasize or diminish the perceived 3D geometrical structures of a shape. The experimental results are in line with the simulated outputs reported in previous work. Our findings might introduce a new approach towards having more control over 3D appearance reproduction without changing the material or printer settings.

Keywords: 3D printing, halftoning, surface appearance

1. Introduction and background

Printing devices have a limited number of inks which makes it difficult to reproduce images as accurately as desired; thus, continuous tone images should be halftoned prior to printing. Digital halftoning is a technique to reproduce different shades of colours using only limited number of inks. Halftoning leverages the fact that the human eye performs as a low pass filter and small dots are not visible to the eye from a normal viewing distance. Therefore, halftoning algorithms provide methods to optimally place dots in a way that the quantization error is shifted to a higher frequency which is not visible to the human eye.

In 2D printing, digital halftoning plays a crucial role in creating visually pleasant results. In order to improve print quality, different halftoning techniques have been developed for conventional 2D printing. Screening, error diffusion, and iterative methods are the three main categories of 2D halftoning. Studies have shown that halftoning has a constructive impact on the visual quality in printing. Screening halftoning methods are based on a threshold comparison. Therefore, they are computationally simple, but the resulting outputs suffer from several artifacts. Error diffusion and its different improved versions generate results of higher quality than screening, but still, they exhibit some artifacts in the output. Compared to screening and error diffusion, iterative halftoning methods create results of the highest quality at the cost of computational complexity.

Like in 2D printing, halftoning plays an important role in enhancing the quality of surface reproduction in 3D printing applications. However, compared to 2D printing, it still requires more development. Most of the existing 3D halftoning algorithms are extensions of their 2D counterparts, i.e., the main idea of 3D halftoning methods has been borrowed from the 2D halftoning approaches. In 2D halftoning the neighbouring pixels lie on a 2D plane, while in 3D halftoning the neighbourhood voxels form a 3D surface. As a result, the neighbourhood processing in 3D halftoning is more complex compared to 2D halftoning.

Brunton, et al. (2015) introduced a novel traversal algorithm to adapt 2D error diffusion to the 3D domain. Mao, et al. (2017) developed 3D direct binary search (DBS) halftoning algorithm based on the 2D DBS which can be used with available 3D printing technology to reproduce 3D surfaces. Abedini, et al. (2020) have extended a search-based 2D halftoning algorithm called iterative method controlling the dot placement (IMCDP) to the 3D domain. The aforementioned 3D halftoning methods rely on the main idea of their 2D versions, however, the researchers have modified the way of choosing the neighbouring voxels and assigning weights to them to adapt them to 3D surfaces.

Emerging 3D printing technology has paved the way towards reproduction of complex 3D surfaces. One of the crucial tasks in graphical 3D printing applications is to control the appearance of the printed objects in order to reproduce 3D surfaces as accurately as designed. Many researchers have focused on different approaches to improve the visual quality of 3D surface reproduction and create surfaces with customizable and controllable appearance.

Some recent works have focused on controlling the roughness as one of the 3D surfaces' attributes which contributes to the appearance. Roughness is introduced to the surface due to the layered manufacturing process of 3D printing. Luongo, et al. (2020) studied the use of greyscale patterns to change and control the roughness of the 3D printed parts with a DLP printer. In Ahn, et al. (2009) and Wang, et al. (2019) the authors investigated the effect of printing parameters such as nozzle temperature, layer thickness, surface orientation, platform temperature, printing speed, print direction, etc. on generating surface roughness in an FDM process. They have shown that controlling printing settings and material properties are parameters that affect the appearance of the reproduced surfaces.

The authors Gooran and Abedini (2020) have introduced halftoning as a parameter that could affect the appearance of the reproduced surfaces. It has been shown that it is possible to vary the resulting surface appearance of 3D objects by applying different halftone patterns onto the 3D surface. They argued that halftoning a 3D surface according to its 3D geometrical structure and the structure of the texture being mapped on it affects the visual quality of the surface reproduction.

In the current work, the goal is to validate the effect of halftoning on the final surface appearance of the 3D shapes reported in previous work (Gooran and Abedini, 2020). We utilized a 3D colour printer to apply halftones with different dot sizes and alignments on the 3D shape. The aim is to control the 3D surface appearance by using different halftone patterns while considering the 3D geometrical characteristics of the shape.

2. Materials and methods

2.1 Methodology

Among different halftoning methods, iterative algorithms reproduce results of the highest quality. IMCDP is an iterative halftoning technique that has been proposed by Gooran (2004) and has been extended to the 3D domain by Abedini, et al. (2020).

The 2D IMCDP starts with a blank image of the same size as the original image. The algorithm searches for the position of the pixel holding the maximum value in the original image; then, a black dot (a "1") is placed at its position in the blank image. The effect of this quantization is fed back to the halftoning process by subtracting the low pass filtered version of the halftoned image from the low pass filtered version of the original image. In the next iteration, the position of the pixel with the second maximum value determines

the location of the next "1" in the halftoned image. The algorithm continues until the predetermined number of black dots is placed and the halftoned image is created.

The low pass filter being used in IMCDP is a Gaussian filter as represented in Equation 1:

$$f_{1^{st}G}(m, n) = Ke^{-\frac{1}{2\sigma^2}\left(\frac{m^2}{k_1} + \frac{n^2}{k_2}\right)}$$ [1]

where m and n denote the position of the pixel under operation and σ is the standard deviation of the Gaussian function. The parameters k_1 and k_2 decide the symmetry of the applied filter. Assigning $k_1 = k_2$ results in symmetric halftone structure while, $k_1 \neq k_2$ creates halftone structures with nonsymmetric alignments. To be more precise, setting $k_1 > k_2$ makes the clusters grow faster in the horizontal direction, while $k_1 < k_2$ makes the halftone alignment vertical. There is also the possibility of generating line halftones in other directions by rotating the filter.

Applying the filter based on Equation 1 generates first order FM halftone. In first order FM halftoning, the size of the dots is constant and different absorptances are generated by varying the frequency of distribution of the dots. In this type of halftone, the quantization error is shifted to higher frequencies and as a result, the halftones exhibit blue noise characteristics. Another important feature of IMCDP is the possibility to generate second order FM halftones with green noise properties by modifying the filter as shown in Equation 2 (Gooran and Kruse, 2015). In second order FM halftones, both the size and the frequency of dots are variable, and the quantization error is shifted to mid-high frequencies.

$$f_{2^{nd}G}(m, n) = K\left(e^{-\frac{1}{2\sigma_1^2}(m^2 + n^2)} - e^{-\frac{1}{2\sigma_2^2}\left(\frac{m^2}{k_1} + \frac{n^2}{k_2}\right)}\right)$$ [2]

By using the filter in Equation 2, single dots are first placed homogeneously based on σ_1, then they start to form clusters and σ_2 decides on the final size of the clustered dots ($\sigma_1 > \sigma_2$). Different choices of σ_1 and σ_2 generates halftones with different clustered dot sizes.

When extending the 2D IMCDP to the 3D domain, the original pipeline of 3D IMCDP is similar to 2D IMCDP. However, the way of applying the Gaussian filter has been modified (Abedini, et al., 2020). In 3D IMCDP, the neighbouring voxels are located within a box of size $m \times m \times m$ centered at the under-operation voxel and weights are assigned to the voxels based on their 3D Euclidean distances to the central point.

It has been shown that in adapting 2D IMCDP to halftone 3D surfaces, a 2D Gaussian function outperforms a 3D function as the low pass filter (Abedini, et al., 2020). This means that in 3D IMCDP, weights are generated by a 2D Gaussian filter, but the 3D Euclidean distances still determines the distribution of the weights within the voxels in a neighbourhood.

As mentioned above, it is possible to create halftones of different dot sizes, shapes, and alignments only by changing the filter parameters in 3D IMCDP. Figure 1 shows examples of different halftone patterns produced by 3D IMCDP. The 3D shape is a box with some sinusoidal structures on top with variation of the 3D geometrical structures along the x-axis. As can be seen in this figure, different halftone structures change the appearance of the image (or the texture) on the 3D shape. For example, applying halftones with line structures in x-direction (parallel to the variation of the 3D structure) attenuates the perceived 3D geometry of the shape. That is the reason that the mapped image in Figure 1a appears to have less 3D structure. On the contrary, applying line halftones perpendicular to the variation of the 3D structure emphasizes the perceived geometry of the 3D shape in the appearance of the mapped image (Figure 1b). Figure 1c shows the result of symmetric first order halftoning, which does not aim to diminish or emphasize the 3D structure in the appearance of the shape.

2.2 Print setup

The goal of the current work is to evaluate the effect of using different halftone structures on the perceived appearance of 3D surfaces without changing the printer parameters or materials. A colour fused filament fabrication 3D printer, DaVinci Colour 3D printer PartPro200xTCS from XYZPRINTING was used. The DaVinci Colour 3D printer combines inkjet technology with 3D printing. It uses CMYK inkjet printing technique to apply ink to a colour-absorbing PLA filament.

a)   *b)*   *c)*
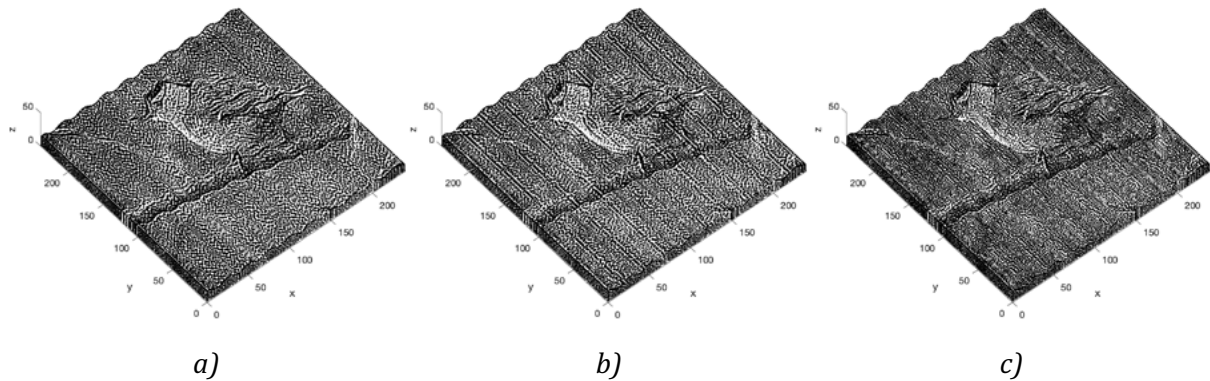
Figure 1: Different possible halftones generated by IMCDP;
(a) second order halftone: σ_1 = 1.3, σ_2 = 0.7 and k_1 =1 & k_2 = 2,
(b) second order halftone: σ_1 = 1.3, σ_2 = 0.7 and k_1 = 2 & k_2 = 1,
(c) first order halftone: σ = 1.3

It is worth mentioning that the DaVinci Colour 3D printer does not allow us to have full control on the voxel level. Therefore, we simulated a thin box with sinusoidal structures on top with constant absorptance. The 3D model has been created in Blender software. The 3D shape has been halftoned using the algorithm described in Section 2.1 with second order FM using two different clustered dot sizes and alignments using MATLAB. Then, the top view of the 3D halftoned shape has been projected on the *x-y* plane. The resulting 2D image has been mapped onto the top face of the 3D model using closest mapping and sent to the printer.

3. Results and discussion

To verify the effect of halftone patterns on the perceived appearance and to compare the simulated halftone outputs with experimental results, a box with sinusoidal structures on the top face has been considered as the 3D shape. The shape with constant absorptance of 0.3 has been halftoned using the filter in Equation 2. The two extreme cases, i.e., halftones with line structure parallel and perpendicular to the 3D geometrical structures, have been examined. Figure 2 shows the halftoned 3D shapes. According to the simulation results, it can be seen that halftones with lines parallel to the variation of the 3D geometrical structure of the shape has diminished the perceived 3D structures of the shape (Figure 2a) while using halftones with perpendicular lines has emphasized it (Figure 2b).

Since the DaVinci Colour 3D printer does not enable voxel-wise control, the 2D projection of the top face of the simulated halftoned shape has been mapped as an image texture on the top face of the 3D model and sent to the printer. Figure 3 shows examples of the 2D projection of the shapes in Figure 2 on the x-y plane. We used low resolution bitmap images in Figure 2 and 3 to make sure that the halftone structures are clearly visible.

To have a better indication of the results, a Gaussian filter with standard deviation of 4 is applied to the halftoned shapes of Figure 2. Figure 4 illustrates the filtered version of the halftoned shapes. The param-

eters for the Gaussian low pass filter were found experimentally, merely to illustrate the effect, and it is not based on the printer characteristics or the actual low pass characteristics of the human visual system. Comparing the halftoned shapes represented in Figure 4, the shape to the left is perceived as more homogeneous and less structured compared to the shape to the right.

Figure 5 shows images of the resulting printouts under daylight illumination. According to our observations, different halftone structures could diminish or emphasize the perceived 3D geometrical structures of the printed surface. In Figure 5, the surface to the right has been halftoned with line patterns perpendicular to the variation of the 3D structures. Comparing to the surface in the middle, which has been halftoned with symmetric halftone alignment, the one to the right is perceived more structured. As Figure 5 illustrates, line halftones parallel to the variation of the 3D structures reduce the perceived waviness of the printed shape. That is, the shape is perceived as less wavy or of lower frequency from right to left. This could also be interpreted as the shape is perceived as a flatter surface when being halftoned by line patterns parallel to the variation of the 3D structures. It is worth noting that the viewing angle for the real prints in Figure 5 is set to be the same viewing angle for the simulation results in Figure 2.

Moreover, to evaluate the effect of clustered dot size on changing the perception of the 3D geometrical structures, we applied halftones with smaller cluster dot size to the same 3D shape. Figure 6 shows the results for two different choices of standard deviations. In this figure, the applied halftone pattern has larger clustered dots in the pair to the left. As can be seen in Figure 6, the difference between halftones with parallel and perpendicular alignment is not easily noticeable when using smaller clusters. This means that the alignment of line halftones has less impact on the appearance of the 3D surface when the clustered dot size is smaller.
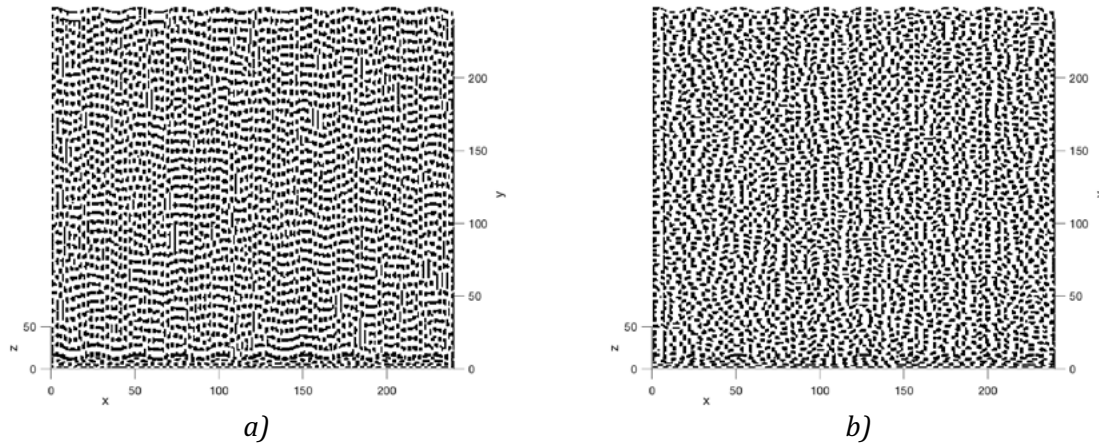

a)   *b)*

Figure 2: 3D shape, absorptance 0.3, halftoned with filter parameters as σ_1 = 1.9, σ_2 = 1 and:
(a) k_1 = 1 & k_2 = 3 (line halftone parallel to the 3D structure variation),
(b) k_1 = 3 & k_2 = 1 (line halftone perpendicular to the 3D structure variation)
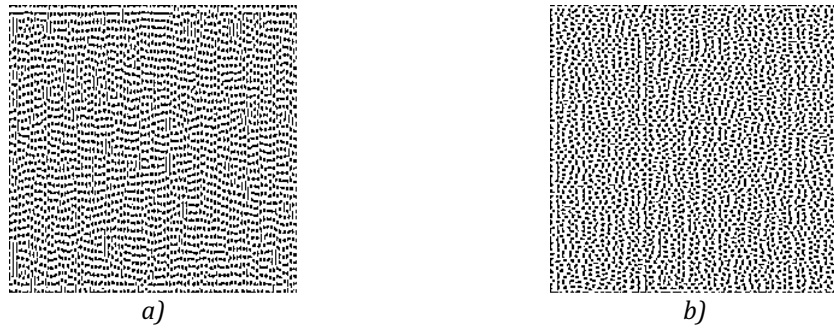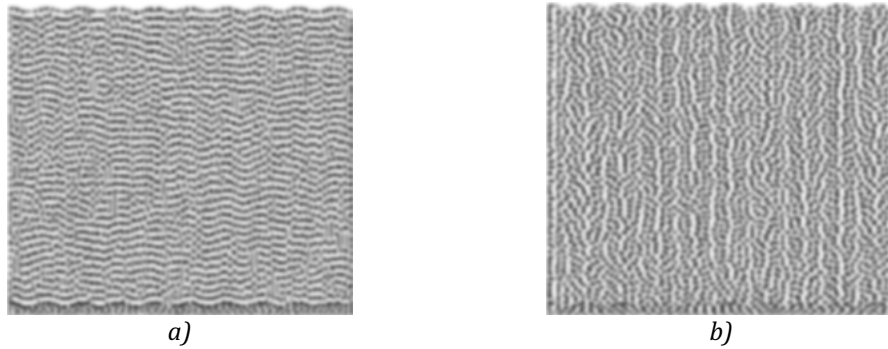
a)

b)

Figure 3: 2D top face views, absorptance 0.3, halftoned with filter parameters as: σ_1 = 1.9, σ_2 = 1 and:
(a) k_1 = 1 & k_2 = 3 (line halftone parallel to the 3D structure variation),
(b) k_1 = 3 & k_2 = 1 (line halftone perpendicular to the 3D structure variation)

a)

b)

Figure 4: 3D views, low pass filtered version of halftoned shapes in Figure 2;
(a) k_1 = 1 & k_2 = 3 (line halftone parallel to the 3D structure variation),
(b) k_1 = 3 & k_2 = 1 (line halftone perpendicular to the 3D structure variation)

Figure 5: Print results, 3D views; filter parameters as σ_1 = 1.9, σ_2 = 1,
left: parallel, middle: symmetric alignment, right: perpendicular halftones to the 3D structure variation
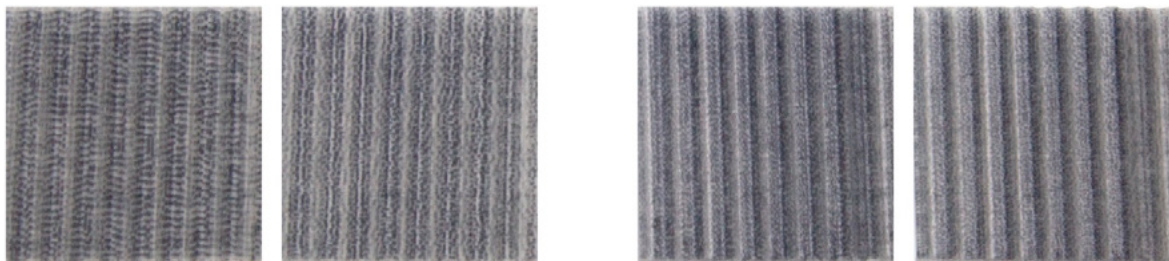
Figure 6: Print results, 3D views; left pair: larger clustered dot size, right pair: smaller clustered dot size;
in each pair, the shape to the left is halftoned with line patterns parallel to the variation of the 3D structure and the
shape to the right is halftoned with line patterns perpendicular to the variation of the 3D structure, the larger clusters
have greater effect on changing the appearance of the 3D geometrical structure

4. Conclusions

In this work, we studied the effect of halftoning on perception (or misperception) of the surface geometry of 3D printed objects. To investigate the influence of halftoning on geometric surface characteristics, halftone patterns with different structures have been applied to a 3D surface. We validated the effect of halftoning in altering the appearance of 3D geometrical structure of printed surfaces by comparing the experimental 3D prints with simulation results from previous work. The 3D printouts are similar to the simulation results. It has been shown that halftones with structures parallel to the variation of the 3D structure of the object attenuate the perceived waviness of the 3D geometry, while halftones with perpendicular lines emphasize it. However, we have not had full control over each voxel with the available 3D printer (DaVinci Colour 3D printer), hence, we believe that the role of halftoning would be even more noticeable if different halftone patterns could be applied to the 3D printed object at a voxel level.

Acknowledgements

References

Abedini, F., Gooran, S. and Nyström, D., 2020. 3D halftoning based on iterative method controlling dot placement. In: *NIP and Digital Fabrication Conference: Printing for Fabrication*. Online 19-21 October 2020. Society for Imaging Science and Technology. pp. 69–74. https://doi.org/10.2352/ISSN.2169-4451.2020.36.69.

Ahn, D., Kweon, J.-H., Kwon, S., Song, J. and Lee, S., 2009. Representation of surface roughness in fused deposition modeling. *Journal of Materials Processing Technology*, 209(15-16), pp. 5593–5600. https://doi.org/10.1016/j.jmatprotec.2009.05.016.

Brunton, A., Arikan, C.A. and Urban, P., 2015. Pushing the limits of 3D color printing: error diffusion with translucent materials. *ACM Transactions on Graphics*, 35(1): 4. https://doi.org/10.1145/2832905.

Gooran, S., 2004. Dependent color halftoning: better quality with less ink. *Journal of imaging science and technology*, 48(4), pp. 354–362.

Gooran, S. and Abedini, F., 2020. 3D Surface Structures and 3D Halftoning. In: *NIP and Digital Fabrication Conference: Printing for Fabrication*. Online 19-21 October 2020. Society for Imaging Science and Technology. pp. 75–80. https://doi.org/10.2352/ISSN.2169-4451.2020.36.75.

Gooran, S. and Kruse, B., 2015. High-speed first- and second-order frequency modulated halftoning. *Journal of Electronic Imaging*, 24(2): 023016. http://dx.doi.org/10.1117/1.JEI.24.2.023016.

Luongo, A., Falster, V., Doest, M.B., Ribo, M.M., Eiriksson, E.R., Pedersen, D.B. and Frisvad, J.R., 2020. Microstructure control in 3D printing with digital light processing. *Computer Graphics Forum*, 39(1), pp. 347–359. https://doi.org/10.1111/cgf.13807.

Mao, R., Sarkar, U., Ulichney, R. and Allebech, J.P., 2017. 3D halftoning. In: *IS&T International Symposium on Electronic Imaging, 2017*. Burlingame, CA, USA, 29 January – 2 February 2017. Society for Imaging Science and Technology, pp. 147–155. https://doi.org/10.2352/ISSN.2470-1173.2017.18.COLOR-048.

Wang, P., Zou, B., Ding, S., 2019. Modeling of surface roughness based on heat transfer considering diffusion among deposition filaments for FDM 3D printing heat-resistant resin. *Applied Thermal Engineering*, 161(10–11): 114064. https://doi.org/10.1016/j.applthermaleng.2019.114064.

Index of authors